A study of conjugated polymers and their applications in light-emitting diodes

Dailey, Stuart

ABSTRACT

The initiation of research into conjugated polymer electroluminescent devices in Durham is reported. The apparatus required for the fabrication and characterisation of polymer light-emitting diodes (LEDs) is outlined, and the essential assumptions and calculations required to determine their efficiency, brightness and colour are summarised.

Optical and electrical characterisation of a range of polymers is reported, including polypyridine (PPY) and a range derivatives, poly(*p*-phenylene vinylene) (PPV) and poly(2-methoxy, 5-(2'ethyl-hexyloxy)-*p*-phenylene vinylene) (MEH-PPV). The optical properties of PPY in solution, film and dilute solid state are characterised. The conjugation length of PPY is investigated by deliberate disruption of the conjugation by the inclusion *meta*-links in the otherwise *para*-linked polymer. The effect of altering the chemical structure of PPY is investigated by the study of some PPY derivatives including random and regular copolymers. The consequences of using precursor polymers, especially the effects of conversion on indium tin oxide coated substrates are investigated using absorption and luminescence spectroscopy and capacitance-voltage analysis.

Electroluminescence from a number of conjugated polymers is reported and the efficiency, spectral output and device characteristics are presented. The formation of Schottky barriers in some polymer devices is investigated using quasi-static capacitance-voltage measurements.

Improvements in the quantum and power efficiency of polymer LEDs have been achieved using two hole-transporting polymers, poly(vinyl carbazole) and the doped, conducting form of polyaniline. A substantial improvement in quantum efficiency has also been demonstrated when PPY is used as an electron-transporting layer in PPV and MEH-PPV based light-emitting diodes. The variation in quantum efficiency and emission spectrum with the ratio of the thickness of the two polymer layers is reported and analysed.

A STUDY OF CONJUGATED POLYMERS AND THEIR APPLICATIONS IN LIGHT-EMITTING DIODES

By

Stuart Dailey

A thesis submitted to the Faculty of Science, at the University of Durham, for the degree of Doctor of Philosophy.

University of Durham

Department of Physics

1998

CONTENTS

FIGURES

TABLES

DECLARATION

The material in this thesis has not been submitted for examination for any other degree or part thereof at the University of Durham or any other institution. The material in this thesis is the work of the author except where formally acknowledged by reference.

ACKNOWLEDGEMENTS

The largest thank you must go to my parents without whom (rather obviously and otherwise) I would never have got to this stage. They have provided excellent support of every kind throughout my education and they have my fullest gratitude.

I would like to thank my supervisors, Dr A.P. Monkman and I.D.W. Samuel for their help and assistance throughout my time in Durham. Also a big thank you to the technical staff in both mechanical workshops and the electronics workshop for their assistance in technical and football related matters.

For help in retaining some semblance of sanity, thanks must go to a large number of people. Thanks to Marianne for being there, and sometimes being in the same country. A big thank you to everyone I've played football and cricket within my time in Durham, including the boys on the Staff Football Team and the Graduate Society Cricket Team. A big "cheers" to all the friends I've made, and special greetings go to (in alphabetical order) Aidie, Brian, Chris, Debbie, Dirk, Eggie, Ian D, Ian P, John C, Marek, Nancy-Ann, Nige, Phil, Sergei, Simon, Smallus, Steve, Tallus, Tom and Yasu.

Finally, thanks go to the OEM group, to Bill and Ben (the Flower Pot Men) for useful discussions and to my friend of misery and his dog, Shep.

Chapter 1 Introduction

The field of conjugated polymer electroluminescence is a fast-moving and active area of research. The main drive behind this research is the exploitation of the novel properties of conjugated polymers in electro-optic devices. Conjugated polymers can be used in a variety of ways to produce a range of devices. The main direction of research with conjugated polymers is their use in electroluminescent devices. A wide range of polymers have been used as the active layer in polymer light-emitting diodes (LEDs) and much progress has been made in the efficiency and lifetime of their operation. Eight years after the initial report of polymer electroluminescence in 1990 [1], the first commercial screens using conjugated polymers have recently been announced.

Polymer LEDs have several processing advantages over conventional inorganic LEDs. Polymers can be used to cover large areas and hence provide a means of developing flat, large area displays with large viewing angles. They are processable directly from solution, producing robust, high quality thin films without the need for complex fabrication procedures. An added benefit is the "tuneability" of the polymers; the physical properties and emission wavelength can be modified by relatively simple chemistry.

Several techniques can be used improve the efficiency and lifetime of polymer LEDs. Firstly, the photoluminescence quantum yield (PLQY) of the polymers used has increased dramatically; therefore more energy is recovered via radiative rather than non-radiative decay. Hole transport layers and electron injection from metals with low work functions have also resulted in an increase in efficiency, although these metals tend to be very reactive. Electron-transporting polymers (ETPs) can facilitate the use of higher work function (lower reactivity) metals and also improve the efficiency and lifetime of polymer LEDs.

Detailed description of work in this field is provided by the numerous review papers have been published summarising work in this area. A brief description of current research into polymer electroluminescence is given below.

Burroughes *et al* reported the discovery of polymer electroluminescence in *Nature* in 1990 [1]. The report centred on single layer devices using poly(*p*-phenylene vinylene) (PPV) as the active layer. The discovery was confirmed by Braun *et al* [2]

who reported electroluminescence from a single layer device using a soluble derivative of PPV, poly(2-methoxy, 5-(2'ethyl-hexyloxy)-*p*-phenylene vinylene) or MEH-PPV. Following the initial discovery, the range of luminescent polymers studied has increased dramatically. Hole and electron transporting polymers have been used to increase the efficiency of operation and the emission of the LEDs has been altered with microcavities (see for example references [3, 4]). With reports of lasing from conjugated polymers (see for example references [5, 6]) and from polymers in microcavities (see for example reference [7]) and with improvements in material quality, the production of electrically driven microcavity lasers using conjugated polymers may be possible.

A substantial review of a number of polymers and the present situation in conjugated polymer research is provided by Kraft *et al* [8]. Another substantial review is provided by Dodabalapur [9]. Microfabrication and photoprocessing of polymer devices [10-12] has demonstrated the processing flexibility of the polymers. The physical nature of the polymers has enabled the fabrication and operation of a device on a flexible substrate [13]. Integrated three-colour light emitting diodes using polymers have also been reported [14]. Other intriguing device structures using polymers include an integrated organic field effect transistor and LED [15] and devices operated under alternating current [16].

The present study involved the initiation of research into polymer electroluminescence in Durham, starting with single layer device structures using PPV and developing the research into multilayer device structures. Considerable experience already present in conducting forms of polyaniline was applied to hole-transporting polymer applications. Synthesis of a pure form of another luminescent polymer, poly(2,6-pyrdinediyl) (PPY), led to it's use as the active layer in single and multilayer device structures and also its novel use as an efficient electron-transporting polymer in polymer light-emitting diodes. Luminescent derivatives of PPY were characterised and some were used as the active layer in light-emitting diodes. A novel precursor route MEH-PPV was also characterised and used in LEDs.

Chapter 2 outlines the nature of the bonding which gives rise to the behaviour of organic semiconductors. A theory describing a simple conjugated polymer, Su Schreiffer and Heeger theory, is outlined and used to illustrate the origin of the band gap and the density of states which arises. Extensions to this theory, which facilitate the description of a wider range of polymers, are outlined. The theory of the

photoluminescence and electroluminescence of the polymers, and the link between the two processes is explored. The theory of device operation is discussed, and the nature of the interactions between the polymer layers and the other parts of an electroluminescent device are discussed in terms of a literature mini-review.

Chapter 3 provides an account of the experimental techniques and essential assumptions and calculations required for polymer LED characterisation. The experimental details and apparatus used for the optical characterisation of the studied polymers are presented. The fabrication techniques used for sample preparation are examined and a summary of polymer film preparation is given. The measurement techniques and calculation procedures for the spectral, efficiency and brightness characterisation of polymer LEDs are summarised and information necessary for colour co-ordinate calculation and conversion is provided.

The first chapter of results, Chapter 4, presents the optical characterisation of the polymers used. The optical characterisation provides insight into the nature of the ground and excited states of the polymers and also provides information regarding the reproducibility, batch to batch variation and the conversion processes of polymers. It can also provide insight into the effect of changing the chemical structure and environment of the polymer.

The second chapter of results, Chapter 5, presents measurements of single polymer layer diodes. The efficiency, spectrum and colour of devices using a range of polymers is reported and the effect of using different metals is investigated. Capacitance-voltage analysis of diodes using PPV, PPY and MEH-PPV as the active layer is reported.

The final chapter of results, Chapter 6, deals with improvements to LED operation created through the use of multiple polymer layers. Efficiency improvements using poly(vinyl carbazole) and thin films of conducting polyaniline as hole-transporting polymers are reported. Application of PPY as an efficient electron-transporting polymer, in a bilayer structure, with a number of luminescent polymers is reported. The effect of device structure on the efficiency and emission of the bilayer devices is investigated, and a model for the operation of the device is outlined.

REFERENCES

[1] J. H. Burroughes, D. D. C. Bradley, A. R. Brown, R. N. Marks, K. Mackay, R. H. Friend, P. L. Burn and A. B. Holmes, Nature, **347** , 11 October 1990 (1990), 539-541.

[2] D. Braun and A. J. Heeger, Appl. Phys. Lett., **58** , 18 (1991), 1982-1984.

[3] M. S. Weaver, et al., Thin Solid Films, **273** , (1996), 39-47.

[4] A. Dodabalapur, L. J. Rothberg, R. H. Jordan, T. M. Miller, R. E. Slusher and J. M. Phillips, J. Appl. Phys., **80** , 12 (1996), 6954-6964.

[5] M. A. DiazGarcia, F. Hide, B. J. Schwartz, M. R. Andersson, Q. B. Pei and A. J. Heeger, Synth. Met., **84** , 1-3 (1997), 455-462.

[6] G. Wegmann, H. Giessen, D. Hertel and R. F. Mahrt, Solid State Communications, **104** , 12 (1997), 759-762.

[7] N. Tessler, G. J. Denton and R. H. Friend, Nature, **382** , 22 August 1996 (1996), 695-697.

[8] A. Kraft, A. C. Grimsdale and A. B. Holmes, Angewandte Chemie-International Edition In English, **37** , 4 (1998), 402-428.

[9] A. Dodabalapur, Solid State Communications, **102** , 2-3 (1997), 259-267.

[10] M. L. Renak, G. C. Bazan and D. Roitman, Adv. Mat., **9** , 5 (1997), 392.

[11] D. G. Lidzey, M. A. Pate, M. S. Weaver, T. A. Fisher and D. D. C. Bradley, Synth. Met., **82** , 2 (1996), 141-148.

[12] S. Noach, E. Z. Faraggi, G. Cohen, Y. Avny, R. Neumann, D. Davidov and A. Lewis, Appl. Phys. Lett., **69** , 24 (1996), 3650-3652.

[13] G. Gustafsson, G. M. Treacy, Y. Cao, F. Klavetter, N. Colaneri and A. J. Heeger, Synth. Met., **57** , 1 (1993), 4123-4127.

[14] C. C. Wu, J. C. Sturm, R. A. Register and M. E. Thompson, Appl. Phys. Lett., **69** , 21 (1996), 3117-3119.

[15] A. Dodabalapur, Z. Bao, A. Makhija, J. G. Laquindanum, V. R. Raju, Y. Feng, H. E. Katz and J. Rogers, Appl. Phys. Lett., **73** , 2 (1998), 142-144.

[16] A. J. Epstein, et al., Synth. Met., **78** , (1996), 253-261.

Chapter 2 Theory

SIMPLE ARGUMENTS

Polymers are regular arrangements of multiple monomer units producing a larger, repeating system. For example the monomer unit vinyl chloride polymerises via radical polymerisation to produce poly(vinyl chloride) or PVC.

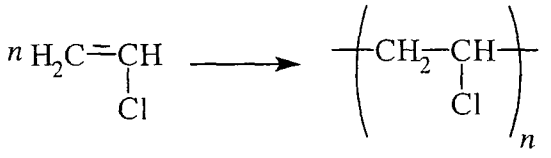

Figure 2-1 *Polymerisation of vinyl chloride to form PVC*

Conjugated polymers are polymeric systems with alternating single and double (or any other unsaturated multiple bond) bonds. The simplest example of a conjugated polymer is poly(acetylene) (PA). It can be represented with or without the hydrogen atoms, as shown in Figure 2-2 (a) and Figure 2-2 (b) respectively.

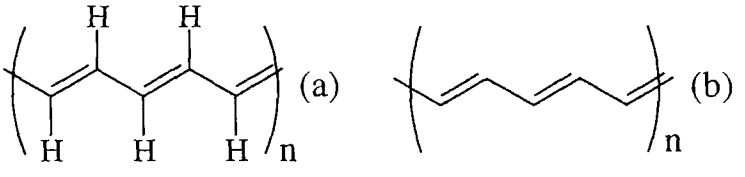

Figure 2-2 *Poly(acetylene)*

The bonding in conjugated polymers is a result of the formation of hybridised orbitals and unsaturated multiple bonds, which are created by the bonding of sp^2 and sp hybridised orbitals and any remaining p orbitals.

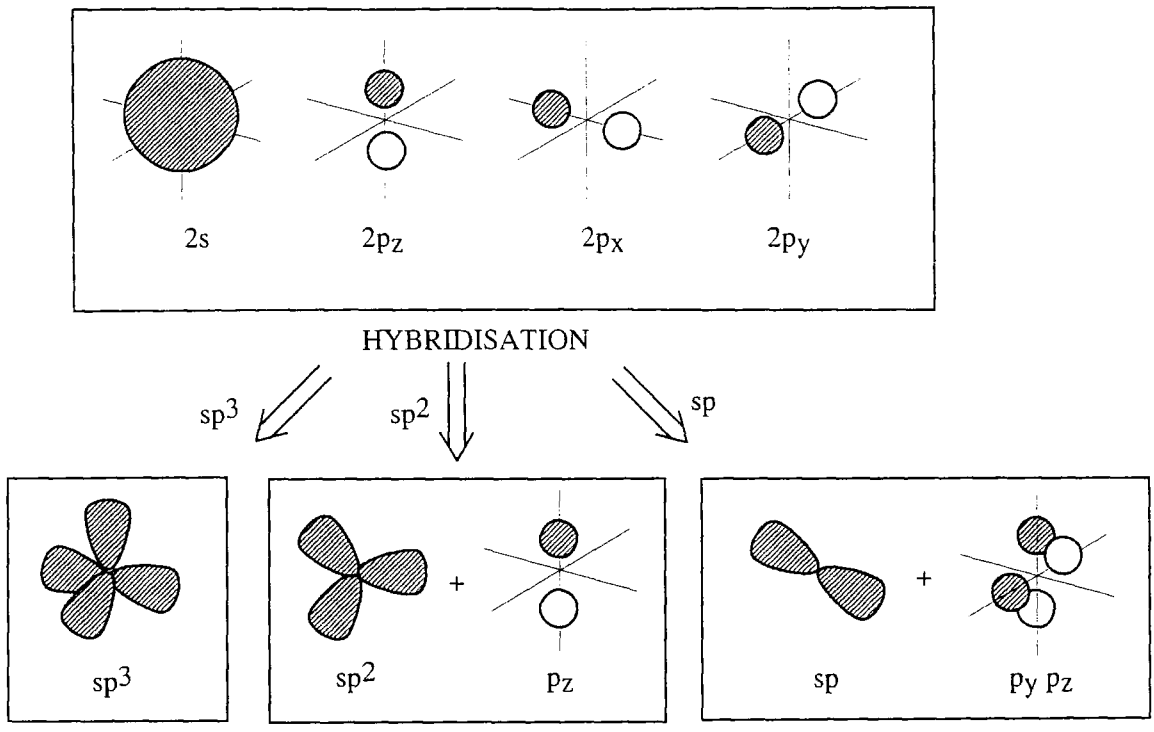

Figure 2-3 *Hybridisation of 2s and 2p orbitals. Shading and non-shading represent opposite phases of the orbital wavefunction (opposite phases on hybrid orbitals are not shown) (after reference* [1]*)*

The energy levels of the hybrid orbitals are shown schematically in Figure 2-4.

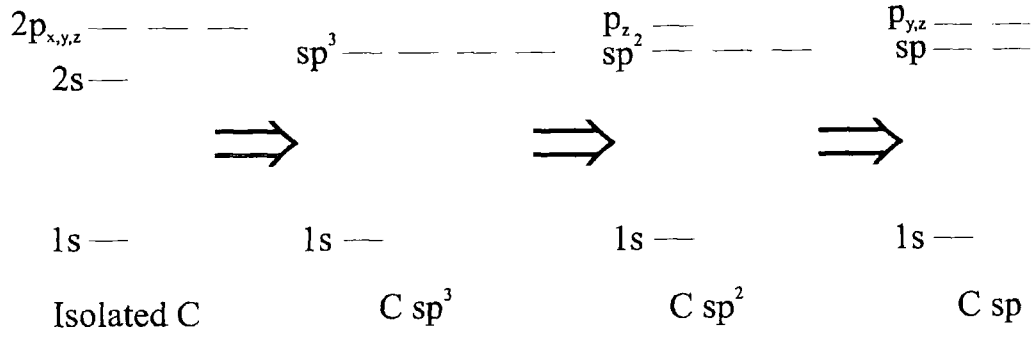

Figure 2-4 *Energy levels of hybridised carbon orbitals*

The sp^2 hybrid orbitals can bond to other carbon atoms along the chain or to other atoms, for example hydrogen. This bonding produces sigma (σ) bonds.

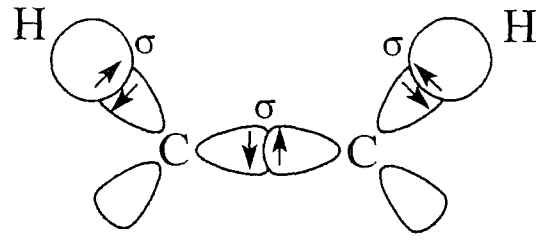

Figure 2-5 *sp^2 σ bonding (after reference* [1])

The sp^2 hybrid orbital can σ-bond to another carbon atom, allowing the remaining p_z orbital to bond with another orbital of similar symmetry. This interaction of a remaining p orbital produces a π bond.

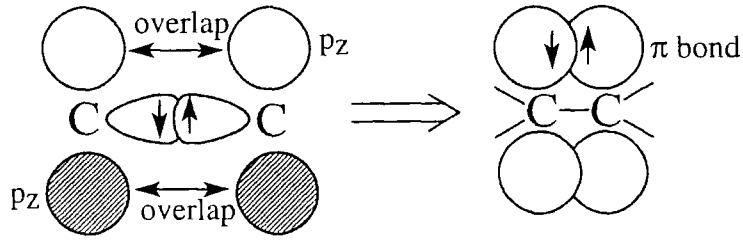

Figure 2-6 *Formation of a π bond (after reference* [1])

The formation of both a pi and a sigma bond in this system creates a carbon-carbon *double bond.* Any molecule with a multiple bond is said to be *unsaturated.* An example of a compound which has a carbon-carbon double bond is ethene, which has two carbon atoms each with 2 sigma bonded hydrogen atoms. The presence of a double bond shortens the distance between the carbon atoms.

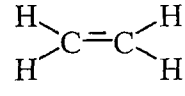

Figure 2-7 *Ethene*

The energy level picture for this bonding is shown in Figure 2-8.

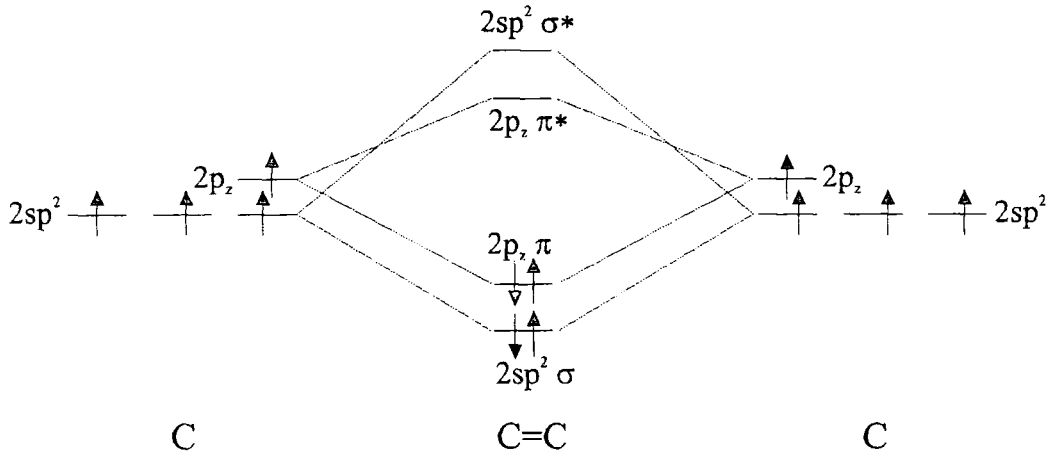

Figure 2-8 *Energy level diagram of a carbon-carbon double bond*

Several elements are capable of forming pi bonds and hence are capable of supporting multiple bonds, for example nitrogen, oxygen and sulphur. These elements can form sp^x hybrids and have been used in polymeric systems, for example nitrogen in poly(pyridine-2,5-diyl). The electron configuration in the hybridised orbitals of these elements results in one or more (non-bonding) pairs of electrons. This is referred to as a lone pair and this results in a region of high electron density. The lone pair does not interact with the pi orbitals in the ring, although it is free to interact with other species, transition metals being one obvious example (see for example reference [2]).

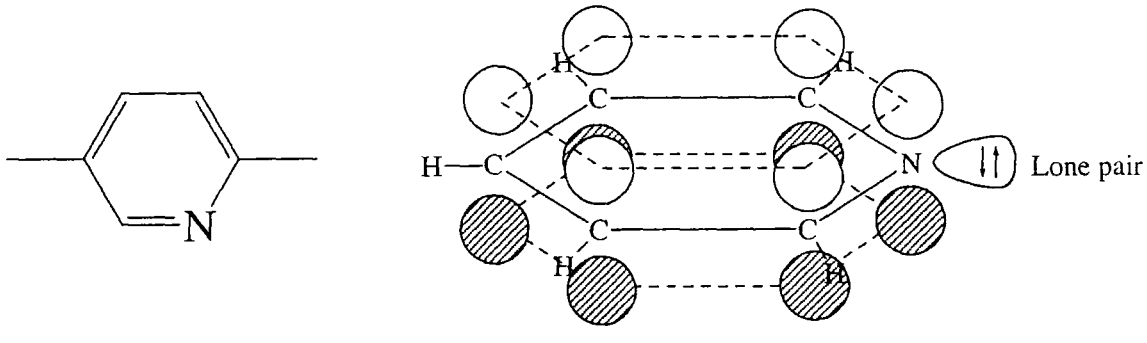

Figure 2-9 *Structure of a pyridine monomer (after reference* [1]*)*

In a phenylene (or benzene) ring, the situation is more complex. The sp^2 hybrids form sigma bonds in the ring. The remaining p_z orbitals can then overlap to form pi bonds.

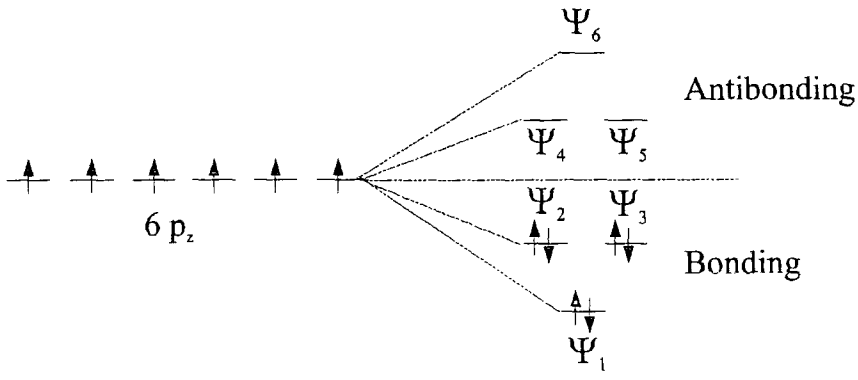

Figure 2-10 *Molecular orbitals in benzene (after reference* [1]*)*

The electron arrangements for the bonding and antibonding molecular orbitals $\Psi_{1\text{-}6}$ are shown below.

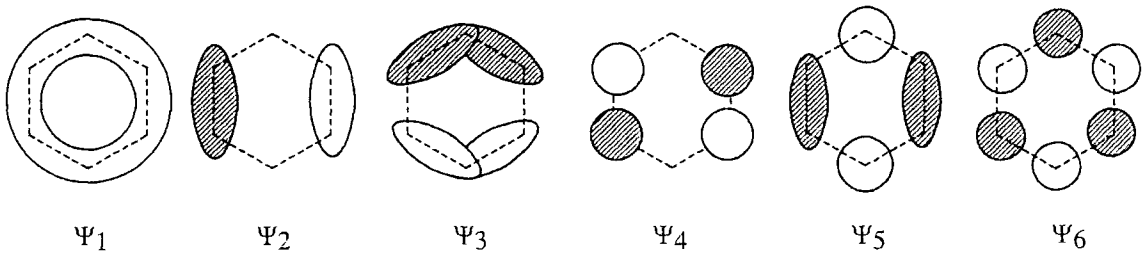

Figure 2-11 *Pi molecular orbitals in benzene (after reference* [1]*)*

A simple example of a conjugated polymer is *trans*-poly(acetylene) (*t*-PA), which has a linear chain of carbon atoms, each of which is attached to a hydrogen atom and two other carbon atoms. The sp^2 orbitals form sigma bonds and the remaining p_z orbitals can overlap to form pi bonds through the system. If this happens, as shown in Figure 2-12, then the pi bonds produce a bond order of 1.5 for carbon atoms along the chain. (A bond order of 1 would arise for a single bond, and a bond order of 2 would arise for a double bond, hence a bond order of 1.5 is midway between the two. It is a similar case to that of benzene and can be considered either as a single bond plus half a bond, or as a resonance hybrid between two forms, for example the two Kekulé structures in the case of benzene).

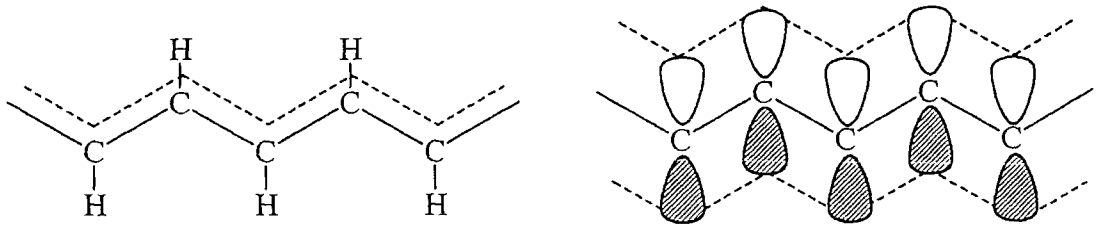

Figure 2-12 *Undimerised trans poly(acetylene)*

The overlap and interaction of the pi orbitals results in band structure due to the Coulomb interaction of the carbon-carbon lattice and the electrons in the system. Each state of a given quantum number is spread in energy thus forming a band, the width of which is governed by the strength of the overlap interaction between neighbouring groups (atoms). As the number of groups (orbitals) increases, the pi bonding and non-bonding orbitals lose their discrete energies and a band of energy levels is formed. The pi bonding orbitals are occupied, whereas the pi antibonding orbitals are empty, leading to the formation of a half-filled valence band capable of supporting metallic conduction, and the system can be considered as a 1-dimensional metal. This system is susceptible to a distortion, which reduces the energy of the system and opens a gap in the electronic states. This is known as a *Peierls distortion* (or *transition*) [3]. This distortion reduces the symmetry of the system and reduces the overall energy by lowering the energy of the filled (pi-bonding) states whilst raising the energy of the empty (pi-antibonding) states. The pi-bonding states are completely filled, the pi-antibonding states are completely empty and an energy gap now exists between the states, producing a polymer which is a semiconductor. This occurs in conjugated polymers (for example PA) and the distortion produces a polymer with alternating single (long) and double (short) bonds. The polymer is said to be *dimerised.*

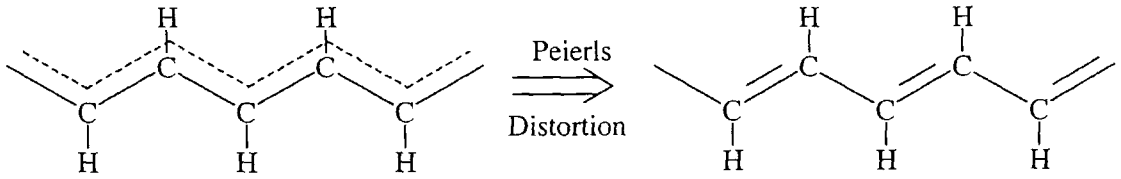

Figure 2-13 *Peierls transition of PA*

Dimerised PA has two ground states, differentiated by the direction of the bond alternation. These ground states are degenerate in energy. It exhibits a band gap and is a semiconductor.

Conjugated polymers behave like wide gap semiconductors due to the Peierls distortion. Pi-bonding orbitals (π), which, due to their occupation, are designated highest occupied molecular orbitals (HOMOs), can interact to produce the lower energy band. This lower energy band is called the valence band as in inorganic systems. The pi-antibonding orbitals (π^*), known as lowest unoccupied molecular orbitals (LUMOs), can interact to form the higher energy conduction band. Due to the molecular orbital origin of the valence and conduction bands, a transition across the

band gap can be referred to as a π-π^* transition. The top of the valence band and the bottom of the conduction band correspond to the HOMO and LUMO level respectively. The band gap can then be referred to as the HOMO-LUMO gap.

A more rigorous treatment of the electronic structure of conjugated polymers can be provided by Su, Schrieffer and Heeger (SSH) theory [4] and by various models which treat electron-electron interaction in the polymer systems as non-trivial (i.e. not as a perturbation to the system).

SU, SCHRIEFFER AND HEEGER (SSH) THEORY

Su, Schrieffer and Heeger (SSH) theory [4-7] provides a theoretical framework for some conjugated polymers. It explores the origin of the band gap and of electrically neutral pseudo particles with spin ½ (solitons) which have been found in poly(acetylene) in electron spin resonance experiments.

The theory assumes dimerisation of the poly(acetylene) chain and relatively weak *inter*-chain coupling (i.e. a one-dimensional system). The σ electrons in the system are considered to be tightly bound and hence move adiabatically with the CH groups (i.e. the Born-Oppenheimer approximation is utilised to separate the motion (wavefunction) of the heavy CH groups and the lighter π electrons).

The sigma bonds in poly(acetylene) are treated as springs, forming a semi-rigid "lattice" such that the energy of the σ bonds (E_σ) is given by Equation 2-1. K is the effective σ-bond spring constant and u_n is a configuration co-ordinate for displacement of the n^{th} CH group along the molecular symmetry axis.

$$E_\sigma = \frac{1}{2}\sum_n K(u_{n+1} - u_n)^2$$

Equation 2-1

The π electron interaction is treated in the tight-binding or Hückel-type approximation such that the σ bonds are assumed to be fixed and the energy of the π electrons (orbitals) is calculated separately. In this case the energy of the π orbitals (electrons) can be written as

$$E_\pi = -\sum_n t_{n,n+1}(c^\dagger_{n+1,s}c_{ns} + c^\dagger_{ns}c_{n+1,s}),$$

Equation 2-2

where $t_{n+1,n}$ is the hopping integral and is given, expanded to the first order, by

$$t_{n+1,n} = t_0 - \alpha(u_{n+1} - u_n),$$

Equation 2-3

t_0 is the hopping integral for the undimerised chain, α is the electron-lattice displacement (phonon) coupling constant and $c^\dagger_{ns}$ and c_{ns} create and destroy π electrons, of spin s, respectively on the n^{th} CH group.

The kinetic energy of the nuclear motion is given by

$$E_K = \frac{1}{2}\sum_n M\dot{u}_n^2 ,$$

Equation 2-4

where M is the mass of the CH group. The SSH Hamiltonian (H_{SSH}) is produced by the addition of Equation 2-1, Equation 2-2 and Equation 2-4 to give Equation 2-5.

$$H_{SSH} = +\frac{1}{2}\sum_n K(u_{n+1} - u_n)^2 - \sum_{ns} t_{n+1,n}(c^{\dagger}_{n+1,s}c_{ns} + c^{\dagger}_{ns}c_{n+1,s}) + \frac{1}{2}\sum_n M\dot{u}_n^2$$

Equation 2-5

It is important to note that the Coulomb interactions between π electrons are ignored in this Hamiltonian, and it has been observed that "if the π-π Coulomb interactions are very strong, our approach is invalid and one should start from the large-U limit for the π electrons" [6], where "large-U" refers to the size of the on site Hubbard potential. This is one of the failings of SSH theory, although a modification to SSH theory was produced in an effort to address this (see for example reference [8] page 778). Polymers are different from conventional semiconductors. In inorganic semiconductors, it is plausible to treat electron-electron interaction as a perturbation, but a polymeric system is usually strongly correlated with a moderate to large on site Hubbard repulsion. The lack of treatment of the electron-electron interaction in SSH theory, produces some incorrect results [9, 10].

Continuing from the SSH Hamiltonian, we can determine the effect of bond alternation on the ground state energy. If we constrain the lattice displacements to be

$$u_n = (-1)^n u ,$$

Equation 2-6

then we can write the SSH Hamiltonian for a fixed chain of N monomer units in a ring geometry of length L (=Na) as

$$H^d(u) = -\sum_{ns}\left[t_0 + (-1)^n 2\alpha u\right]\times\left(c^{\dagger}_{n+1,s}c_{ns} + c^{\dagger}_{ns}c_{n+1,s}\right) + 2NKu^2 .$$

Equation 2-7

Using the reduced zone scheme, the valence and conduction band operators are defined by

$$c^v_{ks} = \frac{1}{\sqrt{N}}\sum_n e^{ikan}c_{ns}$$

$$c^c_{ks} = \frac{-i}{\sqrt{N}}\sum_n e^{ikan}(-1)^n c_{ns}$$

Equations 2-8

Inverting the transformations in Equations 2-8 and substituting in Equation 2-7 gives a Hamiltonian in k space such that

$$H^d = \sum_{ks}\left[2t_0\cos(ka)\left(c_{ks}^{c\dagger}c_{ks}^{c} - c_{ks}^{v\dagger}c_{ks}^{v}\right) + 4\alpha u\sin(ka)\left(c_{ks}^{c\dagger}c_{ks}^{v} + c_{ks}^{v\dagger}c_{ks}^{c}\right)\right] + 2NKu^2$$

$$H^d = \sum_{ks}\left[\varepsilon_k\left(c_{ks}^{c\dagger}c_{ks}^{c} - c_{ks}^{v\dagger}c_{ks}^{v}\right) + \Delta_k\left(c_{ks}^{c\dagger}c_{ks}^{v} + c_{ks}^{v\dagger}c_{ks}^{c}\right)\right] + 2NKu^2$$

Equations 2-9

The lowermost of Equations 2-9 arises when we define ε_k as the unperturbed band energy in the reduced zone and Δ_k as the gap parameter as shown in Equations 2-10.

$$\varepsilon_k = 2t_0\cos(ka)$$
$$\Delta_k = 4\alpha u\sin(ka)$$

Equations 2-10

We can then define new operators in order to diagonalise H^d.

$$a_{ks}^{v} = \alpha_k c_{ks}^{v} - \beta_k c_{ks}^{c}$$
$$a_{ks}^{c} = \alpha_k^{*} c_{ks}^{c} + \beta_k^{*} c_{ks}^{v}$$
$$|\alpha_k|^2 + |\beta_k|^2 = 1$$

Equations 2-11

Substituting for c_{ks} in the lowermost of Equations 2-9, and requiring H^d be diagonal in the a operators, produces

$$H^d = \sum_{ks} E_k\left(a_{ks}^{c\dagger}a_{ks}^{c} - a_{ks}^{v\dagger}a_{ks}^{v}\right) + 2NKu^2,$$

Equation 2-12

where

$$E_k = \left(\varepsilon_k^2 + \Delta_k^2\right)^{1/2}.$$

Equation 2-13

Equation 2-12 can be further simplified by defining the occupation number operator $n=a^{\dagger}a$ to give Equation 2-14.

$$H^d = \sum_{ks} E_k\left(n_{ks}^{c} - n_{ks}^{v}\right) + 2NKu^2$$

Equation 2-14

The ground state energy of the system, as a function of configuration co-ordinate u, can then be calculated for one π orbital per atom (on average) in the reduced zone scheme, where the occupation number operators are given as

$$n_{ks}^{c} = 0$$
$$n_{ks}^{v} = 1 \quad ,$$

Equations 2-15

and the ground state energy is given by

$$E_0(u) = -2\sum_k E_k + 2NKu^2 .$$

Equation 2-16

Changing the sum to an integral over the first Brillouin zone ($-\pi/2a \leq k \leq \pi/2a$) produces

$$E_0(u) = -\frac{2L}{\pi}\int_0^{\pi/2a}\left[\left(2t_0\cos ka\right)^2 + (4\alpha u\sin ka)^2\right]^{1/2} dk + 2NKu^2 .$$

Equation 2-17

We can define

$$z = \frac{t_1}{t_0} = \frac{2\alpha u}{t_0} ,$$

and using $L=Na$ and $cos^2(ka) \equiv 1-sin^2(ka)$ we can rewrite Equation 2-17 as

$$E_0(u) = -\frac{4Nt_0}{\pi}\int_0^{\pi/2}\left[1-\left(1-z^2\right)\sin^2 ka\right]^{1/2} a\,dk + 2NKu^2$$
$$= -\frac{4Nt_0}{\pi}E\left(1-z^2\right) + \frac{NKt_o^2z^2}{2\alpha^2} \quad ,$$

Equation 2-18

where $E(1-z^2)$ is the elliptical integral and for small z can be expanded as shown in Equation 2-19.

$$E\left(1-z^2\right) \cong 1 + \frac{1}{2}\left(\frac{\ln 4}{|z|} - \frac{1}{2}\right)z^2 + \ldots .$$

Equation 2-19

The energy per CH group is then given as

$$\frac{E_0(u)}{N} = \frac{-4t_0}{\pi}\left[1 + \frac{1}{2}\left(\frac{\ln 4}{|z|} - \frac{1}{2}\right)z^2\right] + \frac{Kt_0^2z^2}{2\alpha^2} .$$

Equation 2-20

This energy per CH group as a function of the configuration co-ordinate, u, is shown in Figure 2-14.

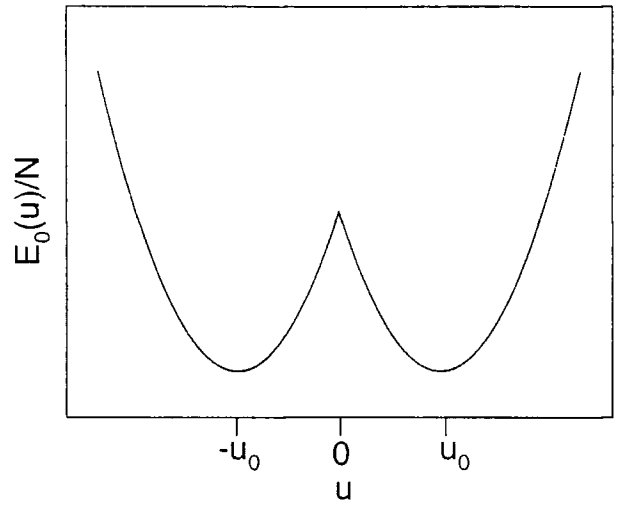

Figure 2-14 *Ground state energy $E_0(u)$ per CH unit as a function of configuration co-ordinate u*

The energy of the Undimerised system (where $u=0$) is higher than the two stable dimerised phases, denoted $A(u_0)$ and $B(-u_0)$, in accordance with a Peierls transition. The two dimerised phases describe two phases of the same energy, differing only in the direction of the bond alternation, a *degenerate ground state*. The configurations of these phases are shown below.

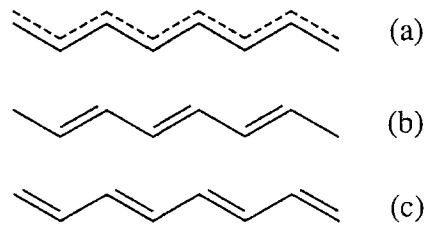

Figure 2-15 *Phases of PA, undimerised (a), phase A (b) and phase B (c)*

The energy as a function of wavevector can also be calculated. The single particle eigenstates can be calculated using the transformation coefficients

$$\alpha_k = \left[\frac{1}{2}\left(1+\frac{\varepsilon_k}{E_k}\right)\right]^{1/2}$$

$$\beta_k = \left[\frac{1}{2}\left(1+\frac{\varepsilon_k}{E_k}\right)\right]^{1/2} \operatorname{sgn} k$$

Equation 2-21

and recalling Equations 2-8, to give

$$\psi_k^v = \left[\frac{1}{2}\left(1+\frac{\varepsilon_k}{E_k}\right)\right]^{1/2} \chi_k^v - i\,\mathrm{sgn}\,k\left[\frac{1}{2}\left(1-\frac{\varepsilon_k}{E_k}\right)\right]^{1/2} \chi_k^c$$

$$\psi_k^c = \left[\frac{1}{2}\left(1+\frac{\varepsilon_k}{E_k}\right)\right]^{1/2} \chi_k^c - i\,\mathrm{sgn}\,k\left[\frac{1}{2}\left(1-\frac{\varepsilon_k}{E_k}\right)\right]^{1/2} \chi_k^v$$

Equation 2-22

These eigenfunctions have eigenvalues as shown below.

$$E_k^v = -E_k, E_k^c = +E_k\,.$$

Equations 2-23

If we consider the undimerised ($u=0$) case then Δ_k ($=4\alpha u \sin ka$) $\rightarrow 0$, $E_k \rightarrow \varepsilon_k$, and the energy of the "bands" is given by Equations 2-24.

$$E_k^{0v} = -\varepsilon_k = -2t_0 \cos ka$$

$$E_k^{0c} = \varepsilon_k = 2t_0 \cos ka$$

Equations 2-24

The E-k diagram is shown for the undimerised case in Figure 2-16.

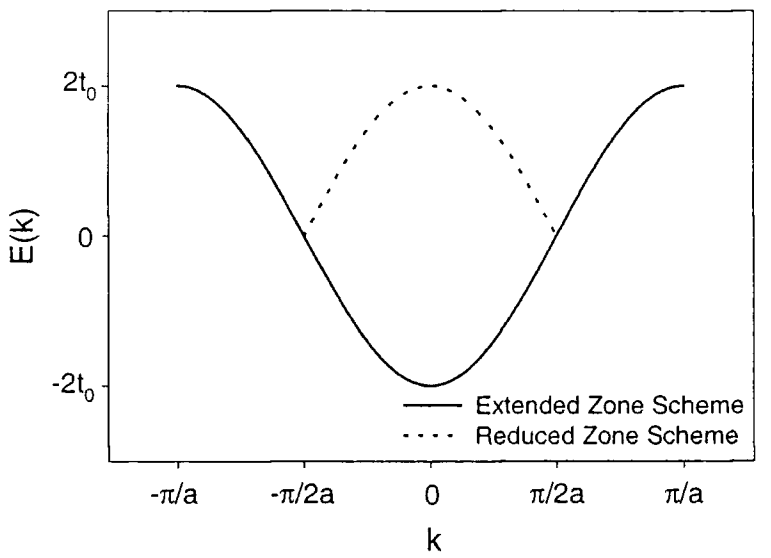

Figure 2-16 *Energy as a function of wavevector for an undimerised polyacetylene chain*

In the dimerised case, Equation 2-13 holds, so that the energy of the conduction and valence bands, given by the eigenvalues in Equations 2-23, is as shown in Equation 2-25.

$$E_k^v = E_k = \left(4t_0^2 \cos^2 ka + 16\alpha^2 u^2 \sin^2 ka\right)^{1/2}$$
$$E_k^c = -E_k = -\left(4t_0^2 \cos^2 ka + 16\alpha^2 u^2 \sin^2 ka\right)^{1/2}$$

Equation 2-25

The E-k diagram for the dimerised case is shown in Figure 2-17.

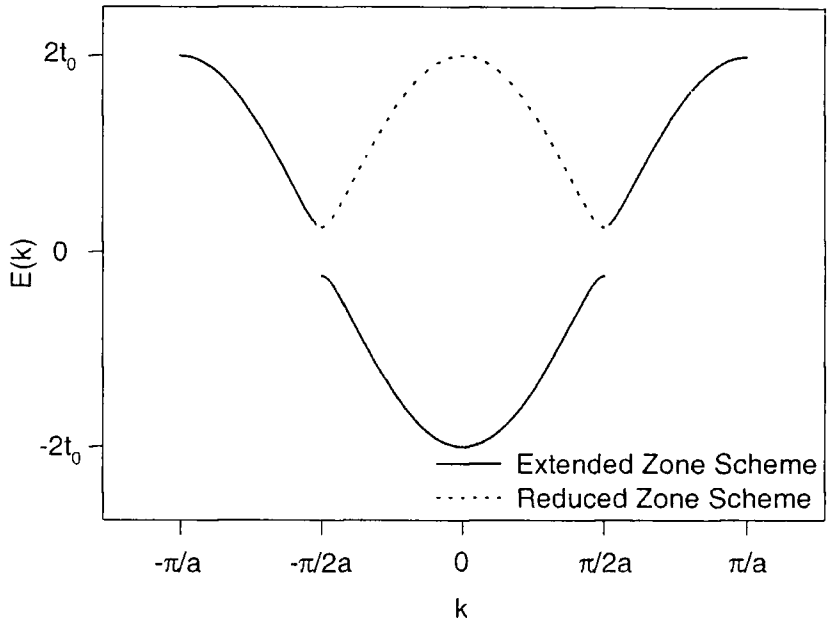

Figure 2-17 *Energy as a function of wavevector (E-k) diagram for a perfectly dimerised polyacetylene chain*

As can be seen from Figure 2-17, the Peierls theorem holds for the dimerised poly(acetylene) chain. The Peierls distortion produces a band gap at $k=\pm\pi/2a$. Figure 2-14 shows the ground state energy for PA is the dimerised form and that the formation of this lower energy ground state produces the band gap. The density of states distribution for the dimerised case can be calculated from Equation 2-26.

$$\rho_0 = \frac{L}{2\pi \left| dE_k / dk \right|}$$

Equation 2-26

If we recall Equation 2-13, differentiate and use Equation 2-13 once again, we obtain Equation 2-27.

$$\frac{dE_k}{dk} = \frac{a \sin(ka)\cos(ka)\left[(4\alpha u)^2 - \left(2t_0\right)^2\right]}{E_k}$$

Equation 2-27

Using Equation 2-13 to the power 4, using Equations 2-10 and recalling that

$$\sin^2\theta + \cos^2\theta \equiv 1$$

Equation 2-28

gives Equation 2-29.

$$E_k^4 = (2t_0)^4\cos^2(ka) + (4\alpha u)^4\sin^2(ka) + \sin^2(ka)\cos^2(ka)\left[2(2t_0 4\alpha u)^2 - (2t_0)^2 - (4\alpha u)^2\right]$$

Equation 2-29

Squaring the numerator of Equation 2-27 and taking the square root gives

$$\frac{dE_k}{dk} = \frac{a\left[\sin^2(ka)\cos^2(ka)\left[(4\alpha u)^4 - 2(2t_0 4\alpha u)^2 + (2t_0)^4\right]\right]^{1/2}}{E_k}.$$

Equation 2-30

Rearranging Equation 2-29 and substituting into Equation 2-30 produces

$$\frac{dE_k}{dk} = \frac{a\left[(2t_0)^4\cos^2(ka) + (4\alpha u)^4\sin^2(ka) - E_k^4\right]^{1/2}}{E_k}$$

Equation 2-31

Rearranging Equations 2-10 and Equation 2-13, substituting into Equation 2-31, recalling Equation 2-28 and factorising gives

$$\frac{dE_k}{dk} = \frac{a\left[\left(4t_0^2 - E_k^2\right)\left(E_k^2 - (4\alpha u)^2\right)\right]^{1/2}}{E_k}.$$

Equation 2-32

If we consider the perfectly dimerised case, such that $u=u_0$ then we can define $\Delta=4\alpha u_0=2t_1$ and $E=E_k$, using Equation 2-26 and remembering $L=Na$, we can obtain the density of states for the dimerised chain, shown as Equation 2-33.

$$\rho_0(E) = \frac{N}{2\pi}\times\frac{|E|}{\left[\left(4t_0^2 - E^2\right)\left(E^2 - \Delta^2\right)\right]^{1/2}}$$

Equation 2-33

The density of states as a function of energy can be seen in Figure 2-18.

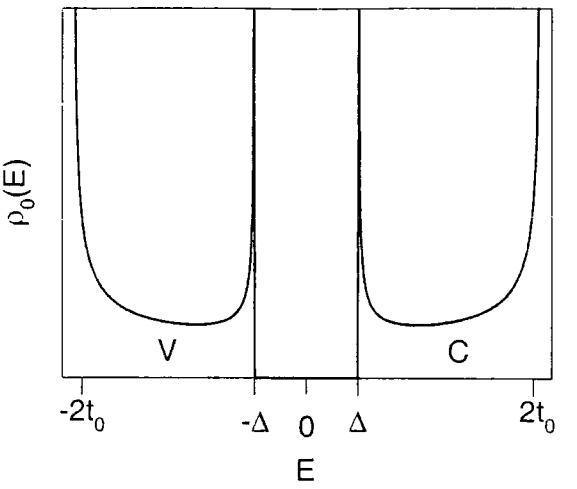

Figure 2-18 *Density of states of a perfectly dimerised polyacetylene chain*

The density of states for the conduction (C) and valence (V) bands, shown in Figure 2-18, has a singularity at the band edges.

EXTENSIONS TO SSH THEORY

Electron-electron Interactions

Su, writing in the Handbook of Conducting Polymers [11], gives an account of electron-electron interactions and their effect on SSH theory. This is a brief summary of that section.

Kivelson [12] and Subbaswamy [13] have proposed an additional term, in addition to the SSH Hamiltonian, to take on site electron-electron repulsion into account. The addition involves the on-site Hubbard repulsion term, U.

$$H_1 = U\sum_n \left(C_{n\uparrow}^{\dagger} C_{n\uparrow} - \frac{1}{2} \right) \left(C_{n\downarrow}^{\dagger} C_{n\downarrow} - \frac{1}{2} \right)$$

Equation 2-34

This becomes [11]

$$H_1^{'} = U\sum_n (-1)^n \delta C_{n\downarrow}^{\dagger} C_{n\downarrow} - U\sum_n (-1)^n \delta C_{n\uparrow}^{\dagger} C_{n\uparrow} + U\delta^2$$

$$\left\langle C_{n\uparrow}^{\dagger} C_{n\uparrow} - C_{n\downarrow}^{\dagger} C_{n\downarrow} \right\rangle = 2(-1)^n \delta$$

Equation 2-35

By analogy with the Peierls instability, the system is unstable with respect to formation of a spin density wave (for further information, see for example references [13-15]). In

the presence of both a bond dimerisation, u, and spin density wave, δ, the electronic energy gap is given by E_g.

$$E_g = 2\Delta = 4\left(4\alpha^2 u^2 + \frac{U^2\delta^2}{4}\right)^{1/2}$$

Equation 2-36

The total energy per site is

$$E_0(u,\delta) = \frac{-2}{\pi}\left(U^2\delta^2 + 4t_0^2\right)^{1/2} E(1-z^2) + 2Ku^2 + U\delta^2$$

$$z^2 = \frac{(U\delta)^2 + 16\alpha^2 u^2}{(U\delta)^2 + 4t_0^2}$$

Equation 2-37

Hence there is a new contribution to the band gap and the ground state energy, caused by the electron-electron interactions in the system. The size of the effect of these interactions depends upon the size of the on-site Hubbard potential, U. In this simple case, the band gap is widened by electron-electron interactions, but the situation can be far more complex, and the effect of electron-electron interaction is a matter for lively debate (see for example reference [16]).

Non-degenerate Ground State Polymers

SSH theory can be extended to allow for non-degenerate ground state polymers, such as *cis*-polyacetylene (*cis*-PA). The two phases, A and B, of *cis*-PA are shown below. Phase A has a lower ground state energy than phase B.

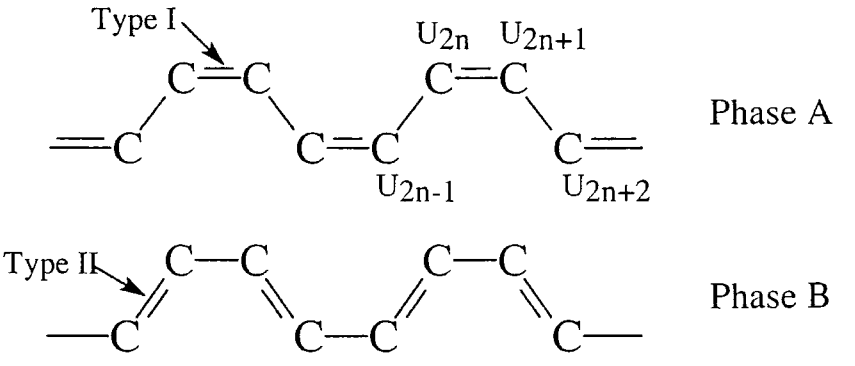

Figure 2-19 *Two non-degenerate phases of cis-polyacetylene*

An extension to allow for the lack of degeneracy can be considered in a continuum [17] or in a discrete case [18]. Following reference [18], the effects of the loss of degeneracy can be considered. Figure 2-19 illustrates the two phases of *cis*-PA and the two types of bond present. A type I bond has an overlap integral t_1 and phonon

coupling constant α_1, and correspondingly a type II bond has an overlap integral t_2 and phonon coupling constant α_2. It is assumed that $t_1 > t_2$ and $\alpha_1 > \alpha_2$. The Hamiltonian of the system is

$$H = -\sum_{n,\sigma}\left[t_1 + \alpha_1\left(u_{2n} - u_{2n+1}\right)\right]\left(C_{2n+1}^{\dagger}C_{2n} + H.C.\right) + \left[t_2 + \alpha_2\left(u_{2n+1} - u_{2n+2}\right)\right]\left(C_{2n+2}^{\dagger}C_{2n+1} + H.C.\right)$$
$$+ \frac{K}{2}\sum_i\left(u_{i+1} - u_i\right)^2 + \frac{M}{2}\sum_i \dot{u}_i^2$$

Equation 2-38

The static system energy is considered ($\Rightarrow \dot{u}_i \to 0$), using the Born-Oppenheimer approximation and the energy per CH group is given by

$$\frac{E_0}{N} = -\frac{4}{\pi}\left(t_0 + \Delta\alpha u\right)E\left(1 - z^2\right) + 2Ku^2$$
$$= -\frac{4}{\pi}\left(t_0 - \Delta\alpha u\right)\left(1 + \frac{1}{2}\left[\ln\left|\frac{8\left(t_0 + \Delta\alpha u\right)}{4\alpha_0 u + \Delta t}\right| - \frac{1}{2}\left[\frac{4\alpha_0 u + \Delta t}{2\left(t_0 + \Delta\alpha u\right)}\right]^2\right]\right) + 2Ku^2,$$

Equations 2-39

where

$$z = \frac{4\alpha_0 u + \Delta t}{2\left(t_0 + \Delta\alpha u\right)}$$
$$t_0 = \frac{t_1 + t_2}{2}, \Delta t = t_1 - t_2, \alpha_0 = \frac{\alpha_1 + \alpha_2}{2}, \Delta\alpha = \alpha_1 - \alpha_2$$

Equations 2-40

The energy per CH unit as a function of configuration co-ordinate is shown in Figure 2-20.

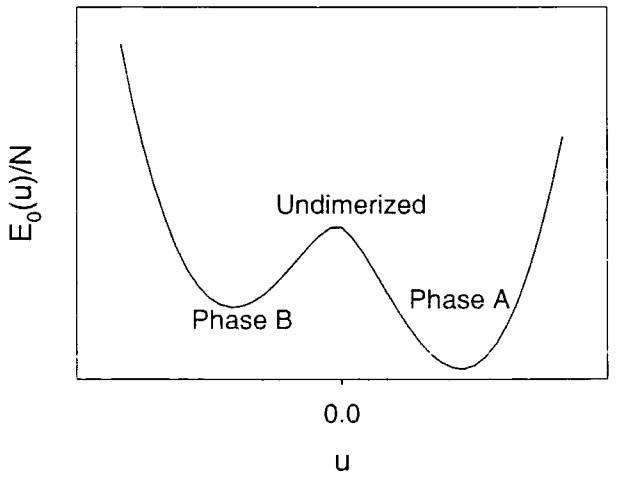

Figure 2-20 *Ground state energy versus configuration co-ordinate for cis-PA*

The one electron energy spectrum is given by

$$\varepsilon(k) = \pm\varepsilon = \pm\left[k^2\left(V_F + \frac{\Delta\alpha}{2\alpha_0}a\Delta_0\right)^2 + \left(\Delta_0 + \Delta_e\right)^2\right]^{1/2},$$

Equation 2-41

and the energy gap, Δ_0, satisfies the equation

$$\Delta_0 = \left[\frac{2\alpha_0^2\left(\Delta_0 + \Delta_e\right)}{\pi k t_0^*} - \frac{\alpha_0\Delta\alpha\left(\Delta_0 + \Delta_e\right)^2}{4\pi k\left(t_o^*\right)^2}\right] \times \ln\frac{W^*}{\left|\Delta_0 + \Delta_e\right|} + \frac{\alpha_0\Delta\alpha}{\pi k}.$$

$$\left\{W^* = 4t_o^*, t_0^* = t_0 + \Delta\alpha\Delta_0/4\alpha_0\right\}$$

Equation 2-42

This is a condition where the band gap is partially due to the intrinsic Peierls gap, stabilised by the π-electrons (Δ_0), but there is also an external contribution from the semi-rigid σ lattice (Δ_e). If the values of Δt (Δ_e) and $\Delta\alpha$ are chosen carefully, this system can produce a state with degenerate energy, but this is not the same as *trans*-PA due to the different energy spectra of the two resulting configurations.

Poly(*p*-phenylene vinylene) (PPV) and poly(pyridine-2,5-diyl) (PPY) are polymers with a non-degenerate ground state.

Interchain Coupling

Lu in reference [19] gives a summary of the contribution to the interchain interaction descriptions in polyacetylene and gives a brief account of the effect of the interchain interaction in a framework by Baeriswyl and Maki [20] and also cites other work in this area. In this framework, two polyacetylene chains are considered to interact, and are denoted by a chain index, j=1,2. There is an additional term in the SSH Hamiltonian which governs the interchain interactions, with a transverse hopping integral ($t_\perp$) and each chain is described by an SSH Hamiltonian. Generally, $t_\perp$ is smaller than t_0. In PA, $t_\perp \approx 0.1$eV [21] and $t_0 \approx 2.5$eV [4]. In PPV $t_\perp \approx 0.15 t_0$ [22].

$$H_\perp = -t_\perp \sum_n \left(c_{1n}^\dagger c_{2n} + H.c.\right)$$

Equation 2-43

$$H_j = \frac{1}{2}K\sum_n \left(u_{j,n+1} - u_{j,n}\right)^2 - \sum_n \left[t_0 - \alpha\left(u_{j,n+1} - u_{j,n}\right)\right]\left(c^{\dagger}_{j,n+1}c_{j,n} + H.c.\right)$$

Equation 2-44

The overall Hamiltonian of the system is described by the sum of the individual Hamiltonians.

$$H = H_1 + H_2 + H_{\perp}$$

Equation 2-45

The bond alternation of the two chains can produce two types of ordering. If the two chains are in phase then the energy spectrum is shifted by $\pm t_{\perp}$. This produces the in phase 'ferromagnetic' ordering. If the two chains are out of phase then the energy of the system is modified to

$$E_k = \tilde{E}_k = \left[E_k^2 \pm 4t_0 t_{\perp}\cos(ka) + t_{\perp}^2\right]^{1/2}$$

Equation 2-46

and the ground state energy (in the weak coupling limit, $\Delta_0 << 2t_0$) is reduced by ΔE.

$$\Delta E = -\frac{Nt_{\perp}^2}{\pi t_0}$$

Equation 2-47

Thus, energetically, the antiphase 'antiferromagnetic' ordering is favoured in *trans*-polyacetylene.

ELECTRON-ELECTRON COULOMB INTERACTIONS

Although there is an extension, described above, to SSH theory which takes into account electron-electron interactions, this extension only takes into account the on-site Coulomb interactions and not the longer range off-site Coulomb interaction. There is a large number of papers attempting to deal with both on and off-site Coulomb interactions in polymeric systems. Lu on page 66 of reference [19] gives a considerable list of references and an insight into the range of techniques employed in this field. Many different calculation schemes are used to provide mostly numerical data for various polymer systems. Hartree-Fock [14, 23, 24], extended Hubbard [25], Pariser-Parr-Pople (PPP) [26-31] and modified SSH Hamiltonian [10, 32] models have successfully been applied to polymeric systems. Screened Coulomb interactions in these systems have also been studied [16, 33].

In essence, these models provide a method to model the interaction of the π-electrons to a certain degree. For example the PPP and extended Hubbard models have a similar form for the electron-electron interactions.

$$H_{ee} = U\sum_{i} n_{i,\uparrow} n_{i,\downarrow} + \frac{1}{2}\sum_{i,j} V_{i,j}\left(n_i - 1\right)\left(n_j - 1\right)$$

Equation 2-48

The on-site Coulomb interaction, U, is similar in both cases, but the off-site Coulomb interaction, V, is different. In the extended Hubbard model only nearest neighbour interactions are taken into account whereas in the PPP model, a form of long range potential is used, for example an Ohno or Mataga-Nishimoto potential. The inclusion of electron-electron interactions increases the complexity of the system and hence a simple qualitative description of the evolution of the band gap and the charge transport in conjugated polymers is achieved by consideration of the SSH model. The increase in complexity from the single electron SSH model also means that shorter oligomeric systems have to be considered in PPP-like models, to reduce computation time, rather than the almost infinite system considered in the case of the SSH framework. However, due to the relatively short conjugation lengths found in most conjugated polymers, these models can provide a suitable framework for investigation of the electronic states of specific polymers. This leads to improved understanding of the physical nature of the system which often provides valuable insight.

One of the main reasons behind the formulation of SSH theory was the effort to explain the existence of chargeless particles with spin ½ discovered in electron-spin resonance experiments. SSH theory extends beyond the explanation given above, to mathematically describe the presence of pseudo particles with properties like those described. In degenerate ground state polymers it is has been shown that conduction occurs due to (charged) *solitons*. In non-degenerate ground state polymers, it is impossible for these solitons to be energetically stable and the corresponding species in these polymers is a *polaron*.

PSEUDO PARTICLES

Solitons

Solitons are mid-gap states only found in degenerate ground state polymers. They form the boundary between the two degenerate phases of a polymer, for example *trans*-polyacetylene. When forming the boundary between the two phases of a polymer, without any associated charge, it is known as a neutral soliton, S^0. An example of a neutral soliton in *trans*-polyacetylene is shown in Figure 2-21.

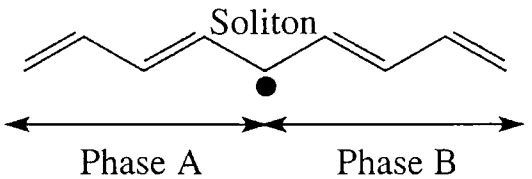

Figure 2-21 *Neutral Soliton in polyacetylene*

Charges can also be found in association with these lattice distortions, forming charged solitons. These species are responsible for conduction in degenerate ground state polymers.

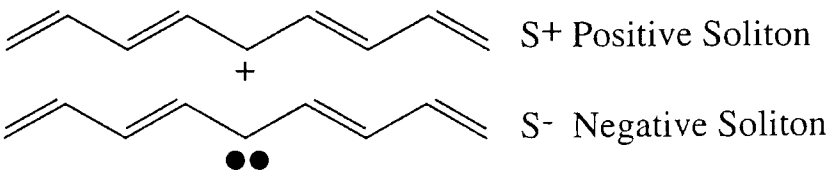

Figure 2-22 *Charged Solitons*

Solitons are mid-gap states, and a schematic representation of their energy levels can be seen in Figure 2-23.

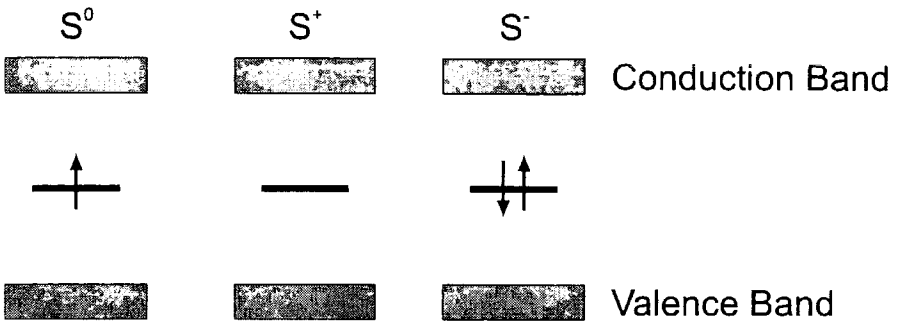

Figure 2-23 *Energy picture of neutral and charged solitons*

Polarons

In non-degenerate ground state polymers, the energy difference between the two phases of the ground state means that a soliton would be energetically unfavourable, i.e. there would be a tremendous increase in energy due to the switch to the alternate (higher energy) phase. Solitons can exist in these systems, but would be accompanied by an anti-soliton, allowing only a limited amount of the higher energy phase. This bound soliton anti-soliton pair is called a *polaron.* Polarons are not mid gap states, but form two energy levels near the conduction and valence bands. Polarons form due to the presence of excess charge on the chain and hence neutral polarons do not form. Further addition of charge to the chain will result in the formation of bipolarons which have a lower energy than the creation of multiple polarons. Bipolarons form two energy levels, closer to the centre of the band gap than the polaron states.

G.J. Ashwell in *Molecular Electronics* [34] gives an account of polaron and bipolaron formation as follows.

"For oxidation, an electron is removed from the π system of the polymer, producing a free radical (2 electrons per π bond). The radical and cation are coupled to each other via local bond rearrangement. This rearrangement will be of a higher energy than the remainder of the chain hence separation of these defects would require a considerable amount of energy, thereby limiting the extent of bond rearrangement. If a further electron is removed then two positive charges are coupled by the bond rearrangement. This is a spinless *bipolaron.* The formation of a bipolaron produces a larger decrease in ionisation energy compared to two polarons and so is thermodynamically more favourable than two polaron states. Further oxidation can

result in production of partially filled bipolaron bands which can display metal-like conductivity. This is at the expense of states at the band edges and the band gap widens."

Polarons are stable in degenerate ground state polymers, but further charge added to the chain will result in the formation of solitons which are free to move along the chain. G.J. Ashwell [34] describes this as follows.

"Degenerate systems can also sustain polaron states, but because of the degeneracy, further doping results in the formation of charged solitons which are not bound to each other (as bond defects have no energy cost in degenerate systems) and so bipolaron states are not formed."

The schematic of a positive polaron and bipolaron in poly(*p*-phenylene) (PPP) is shown below.

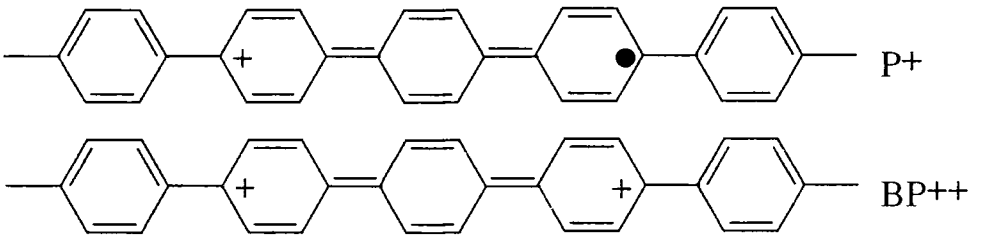

Figure 2-24 *Positive polaron and bipolaron in PPP*

The corresponding schematic for a negative polaron and bipolaron in PPP is shown in Figure 2-25.

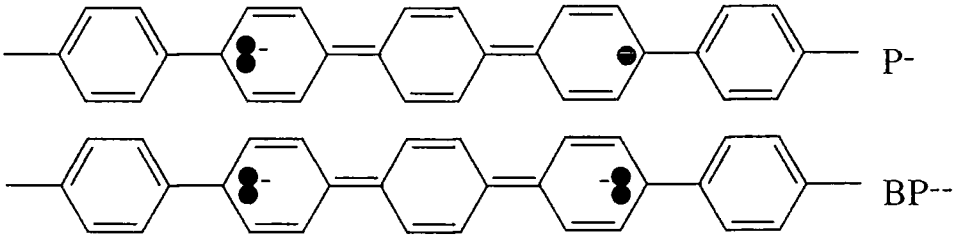

Figure 2-25 *Negative polaron and bipolaron in PPP*

The corresponding energy pictures for polarons and bipolarons are shown in Figure 2-26 and Figure 2-27.

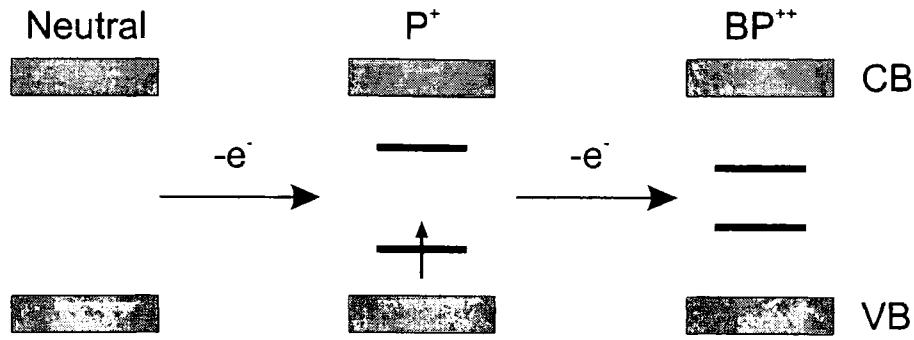

Figure 2-26 *Oxidation of polymer to form positive polaron(P^+) and bipolaron (BP^{++})*

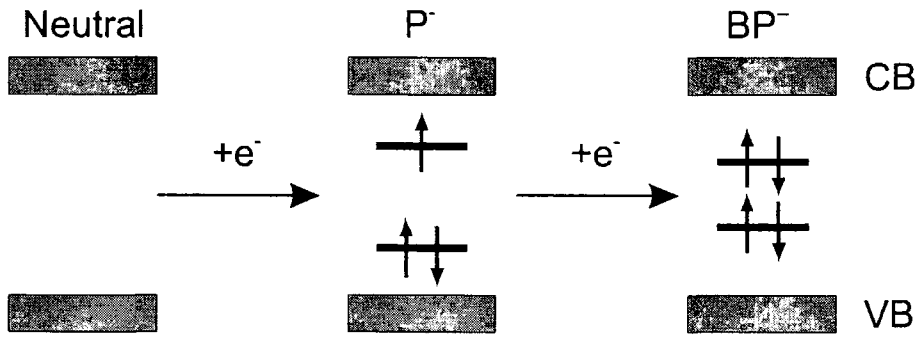

Figure 2-27 *Reduction of polymer to form negative polaron (P^-) and bipolaron (BP^{--})*

A summary of notation for polarons and solitons can be seen in Table 2-1.

Symbol	Description
S^0	Neutral Soliton
S^-	Negative solution
S^+	Positive Soliton
P^-	Negative Polaron
BP^{--}	Negative Bipolaron
P^+	Positive Polaron
BP^{++}	Positive Bipolaron

Table 2-1 *Summary of soliton and polaron notation*

Polarons and bipolarons are essential in the description of polymer light-emitting diode (LED) operation. As mentioned previously, polarons are responsible for charge conduction in non-degenerate ground state polymers. Most luminescent polymers presently studied have a non-degenerate ground state and hence the study of polarons is very important. In addition, there is some suggestion that charge injection in polymer light-emitting diodes, occurs not into the HOMO and LUMO of the polymer, but into polaron levels [35] or that polaron levels can play a significant role in

charge injection [36]. The emitting species in polymer LEDs is thought to be the polaron exciton [37, 38], formed by the combination of oppositely charged polarons.

Solitons, polarons and bipolarons created in a system can be detected and differentiated by the number and energy of sub-gap optical transitions. For example, a neutral soliton will have two possible transitions at energies below the band gap, whereas a charged soliton will have only one. Similarly for polarons, a polaron will have four possible optical transitions whereas a bipolaron will have two possible transitions at different energies. Further details can be found in, for example, reference [39].

Optical measurements can provide valuable insight into the conformation, structure and emission processes of conjugated polymers. This information, in addition to helping to understand the fundamental processes involved, can be used to ascertain and hence improve the performance of the polymers and polymer structures used in light-emitting diodes.

ABSORPTION SPECTROSCOPY

Optical absorption spectroscopy is a probe of the electronic structure of a system. It can also reveal information regarding the physical arrangement and chemical structure of conjugated polymer solutions and films. For example, absorption spectroscopy is a good measure of the extent of conjugation (hence conversion) of precursor PPV. The ratio of the strengths of the absorption of the two main absorption peaks can provide insight into the extent and reproducibility of the conversion process.

An absorption spectrum, as its name suggests, is a measure of the amount of light absorbed at a given wavelength, over a range of wavelengths. The relative amount of absorption at each wavelength is governed by the relative strength (probability) of the optical transition, which is proportional to the overlap between the wavefunctions of the ground and excited states at the corresponding energy. The strength of optical transitions is governed by the Beer-Lambert law.

$$I_l = I_0 e^{-\alpha C l}$$

Equation 2-49 *The Beer-Lambert Law*

I_0 is the incident intensity, I_l is the intensity that emerges from a sample of length l, α is the frequency dependent absorption coefficient, and C is the concentration of the absorbing species. The absorbance, or optical density, of the sample can be defined as

$$A = OD = \log_{10}(I_0/I_l) = \varepsilon C l ,$$

Equation 2-50

where ε is the molar absorption coefficient (or the extinction coefficient) and is equal to the absorption coefficient divided by ln(10). The total intensity of the transition is the integral of the absorption coefficient over the entire range of frequencies it spans.

$$A = \int \alpha d\nu = c\int \alpha d\bar{\nu}$$

Equation 2-51

A is related to the transition dipole moment by

$$A = \left(\pi\nu_{fi}/3\varepsilon_0\hbar c\right)L\left|\mu_{fi}\right|^2,$$

Equation 2-52

where μ_{fi} is the transition dipole moment. Equation 2-52 shows that the intensity of the absorption is proportional to the square of the transition dipole moment. The dimensionless oscillator strength can also be defined by

$$f = \left(4m_e c\varepsilon_0/Le^2\right)A$$
$$= \left(4\pi m_e\nu_{fi}/3e^2\hbar\right)\left|\mu_{fi}\right|^2,$$

Equation 2-53

where intense, allowed transitions have $f\approx 1$ and forbidden transitions have much smaller f values. The transition dipole is related to the overlap of the wavefunctions of the initial and final states, as described in Equation 2-54.

$$\mu_{fi} = \int \psi_f^* \mu \psi_i d\tau$$
$$\mu = \mu_e + \mu_N, \psi_i = \psi_\varepsilon(r)\psi_v(R)$$
$$\Rightarrow \left\langle \varepsilon' v' \middle| \mu \middle| \varepsilon v \right\rangle \approx \mu_{\varepsilon'\varepsilon}\int \psi_{v'}^*(\mathbf{R})\psi_v(\mathbf{R})d\tau_N = \mu_{\varepsilon'\varepsilon}\mathbf{S}_{v'v}$$

Equation 2-54

$S_{v'v}$ is the overlap integral of the initial and final vibrational states. This means that the strength of an optical transition depends on the overlap of the wavefunctions of the two vibrational energy levels, the ground state vibrational level and the excited state vibrational level.

Transitions take place following the Franck-Condon principle, which means that the nuclear conformation readjusts after the electronic transition, and not during it. This is represented by a vertical transition on an energy-nuclear co-ordinate (R) diagram (see Figure 2-28). Excitation takes place from the $v=0$ vibrational level of the ground state, and is most likely to occur from the most probable conformation of the molecule. This point is at the equilibrium nuclear co-ordinate position, R_e, in Figure 2-28. The vertical transitions take place to the excited state vibrational levels with the relative strength of the transition depending upon the overlap of the vibrational wavefunctions.

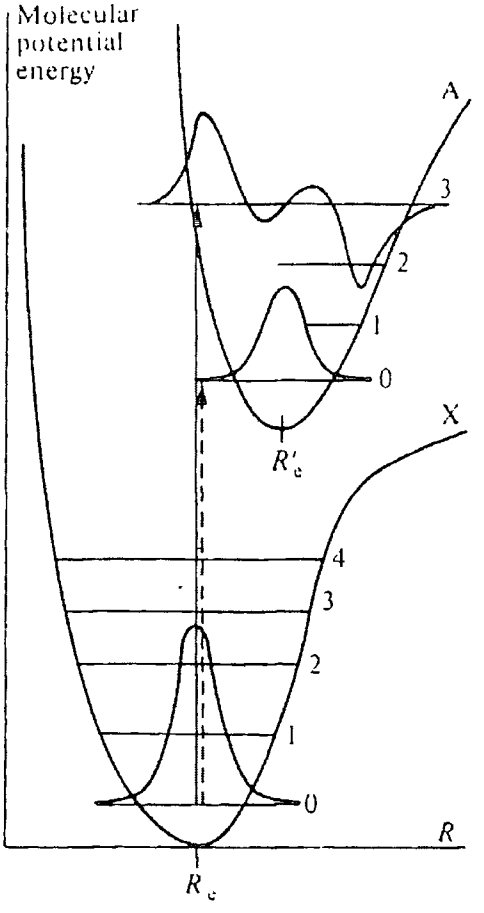

Figure 2-28 *Schematic of optical absorption from reference [40]*

LUMINESCENCE

Luminescence is defined as "the phenomenon of light emission in excess of thermal radiation" [41]. The method of excitation determines the nomenclature used. For example, photoluminescence and electroluminescence arise due to excitation due to photons and an applied voltage respectively.

Photoluminescence

Photoluminescence is the radiative decay of an excitation caused by absorption of a photon. Absorption and photoluminescence spectra, in the simplest case, are very similar, but not identical. In this simplest case, the photoluminescence spectrum is the red shifted, mirror image of the absorption spectrum. The reason for this relationship is shown below.

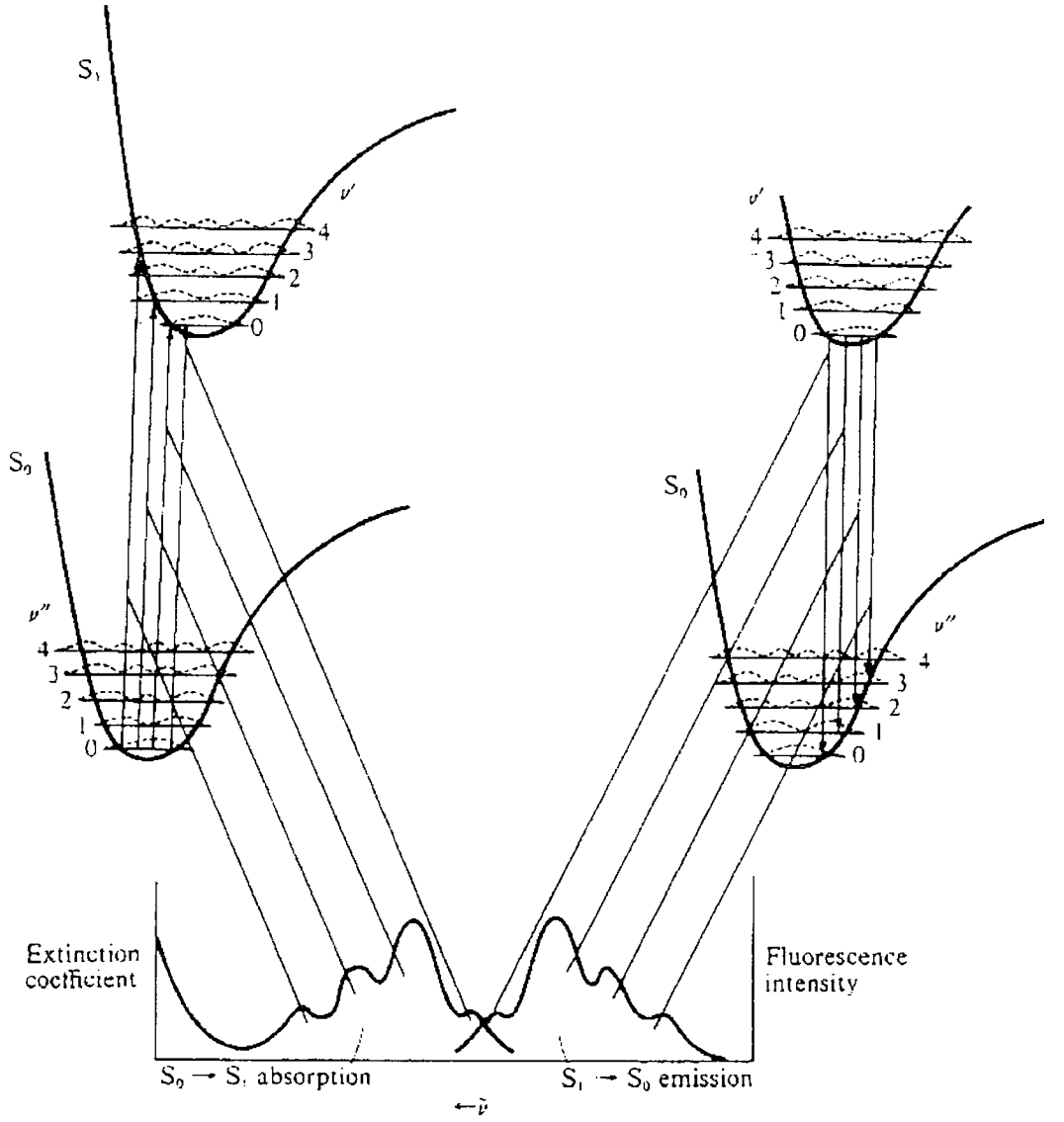

Figure 2-29 *Schematic of the mirror image relationship of absorption and luminescence from reference [42]*

Absorption occurs from the populated $v''=0$ level of the S_0 electronic ground state to the various vibrational levels of the S_1 excited state. The excited state can then undergo radiationless vibrational relaxation, leading to population of the $v'=0$ level of the excited state. Radiative transitions can then occur from this level to the various vibrational levels of the ground state. The origin of the mirror image relationship, that can occur in simple systems, with symmetric vibrational levels, is also illustrated. The relative strengths of the specific transitions in absorption and luminescence will be very similar and hence the spectra should have similar shapes. The vibrational relaxation that occurs, however, will produce a red shift of the emission spectrum compared to the absorption spectrum. In Figure 2-29, the largest shift illustrated is the 0-3 (S_0 $v''=0 \rightarrow$ S_1 $v'=3$) absorption and corresponding 0-3 (S_1 $v'=0 \rightarrow$ S_0 $v''=3$) luminescence

transitions. The shift between the 0-0 transitions should be the smallest and indeed this is the case. These transitions do not completely overlap, however, and there is a shift between the 0-0 absorption and luminescence peaks. This is called the *Stokes shift*. Thus absorption spectroscopy can provide information about the vibrational states of the excited state and luminescence spectroscopy can provide information about the vibrational states of the ground state.

In organic systems, the emission due to fluorescence and phosphorescence occurs due to radiative decay from a singlet and triplet excited state respectively. The difference between these two processes is illustrated as Figures 2-30. Due to the definition of luminescence, fluorescence and phosphorescence are considered to be luminescent processes.

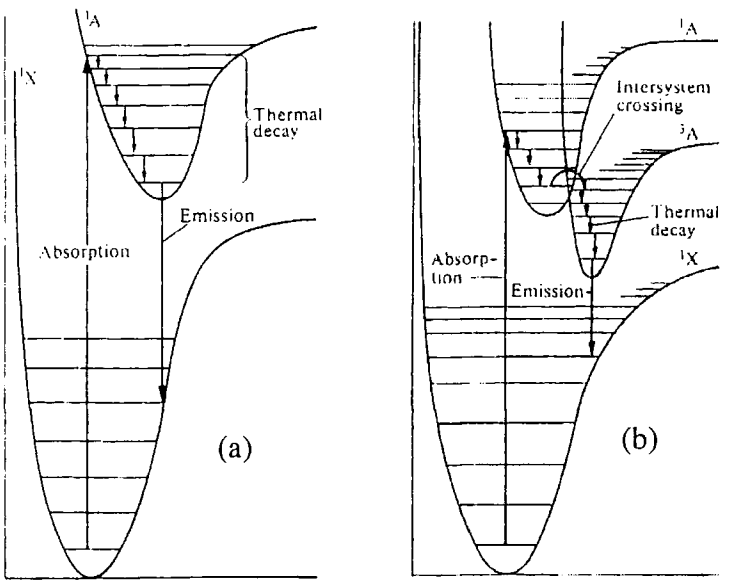

Figures 2-30 a, b *Schematic of (a) fluorescence and (b) phosphorescence from reference [40]*

Absorption and photoluminescence in polymeric systems is more complicated than the situation in simple polyatomic molecules. In a polymer sample, there will be an amount of disorder along a polymer chain. This will produce a distribution of the extent of electron delocalisation along the polymer chain, resulting in a number of chain segments with various *conjugation lengths*. Shorter conjugation lengths produce a larger band gap and longer conjugation lengths produce a smaller band gap. The lowering of the band gap with increasing conjugation length arises due to the linear combination (overlap) of neighbouring π orbitals, producing a decreasing π-π^* energy

difference. During absorption, light of sufficient energy will excite all conjugation lengths, resulting in a broadening of the absorption spectrum. Absorption produces mobile excitations on polymer chains, which can then migrate to a chain segment with a longer conjugation length and decay radiatively, producing emission at a lower energy, red-shifting the photoluminescence and contributing to a seemingly larger Stokes shift. Evidence for this excitation migration is found by time resolved studies of polymer systems (see for example reference [43]).

The energy gap behaviour is essentially linear with 1/n where n is the number of repeat (monomer) units making up the conjugation length. For an infinite conjugation length, there remains an intrinsic band gap, as shown in Figure 2-31.

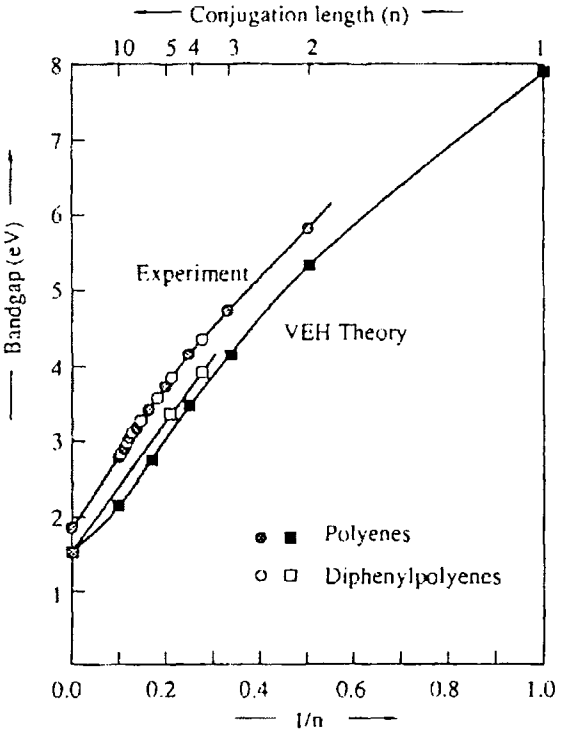

Figure 2-31 *Relationship of the band gap of conjugated polymers with increasing conjugation length from reference [44]. Results are presented for experimental and theoretical (valence effective Hamiltonian, VEH) studies*

Aggregates and Excimers

In concentrated polymer systems, it is possible to form states between different polymer chains. These interchain structures can considerably affect the absorption and emission properties of polymer systems.

Aggregates can be considered as physical dimers, arrangements of two identical molecules spatially close enough to allow overlap of their wavefunctions. The ground

and excited state wavefunctions of the aggregate system are a mixture of the separate molecular wavefunctions. The formation of an aggregate state results in the change of the absorption and luminescence spectra. These changes are material and concentration dependent, but in general, changes can be observed with increasing concentration. New absorption peaks can appear, the maxima of the absorption peaks are red-shifted and broadened, and the most intense transition is the 0-1 rather than the 0-0 transition. The luminescence from aggregate states tends to be broad and featureless, and it can be shifted or split into two shifted peaks, depending on the geometrical arrangement of the dimer. The energy level arrangement of the dimer which produces this effect is shown in Figure 2-32. A more extensive treatment of dimers can be found in reference [42].

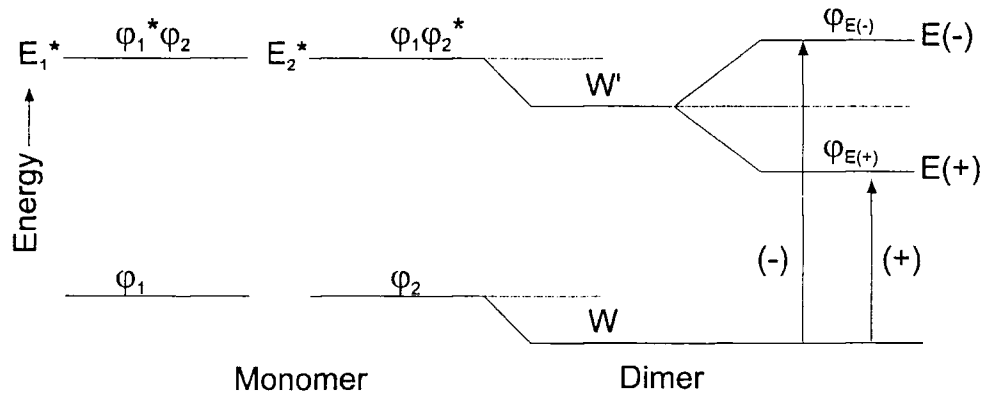

Figure 2-32 *Effect of physical dimer formation on possible optical transitions (after reference [42])*

Excimers are dimers which only exist in the excited state. The ground state of the excimer is dissociative, leading to wavefunction overlap only in the excited state. This means that there is no direct optical excitation of the excimer from the ground state and hence there is no change in the absorption spectrum like that found in the case of aggregates. The emission of the excimer is red shifted, broad and featureless, a consequence of the lack of vibronic states in the repulsive ground state. An example of an excimer transition from a stable excited state to a repulsive ground state is shown in Figure 2-33.

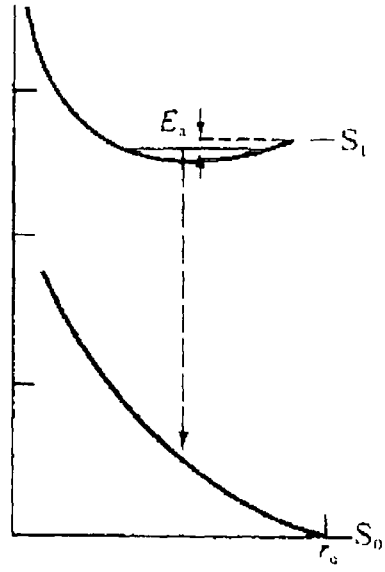

Figure 2-33 *An excimer transition from a stable excited state to an unstable ground state (from reference [42])*

Band Picture of Optical Transitions

In contrast to the molecular picture described above, an alternative method of illustrating the optical transitions in conjugated systems is to use the valence and conduction band picture used in inorganic semiconductors. In this framework, the scheme for photoluminescence is shown below.

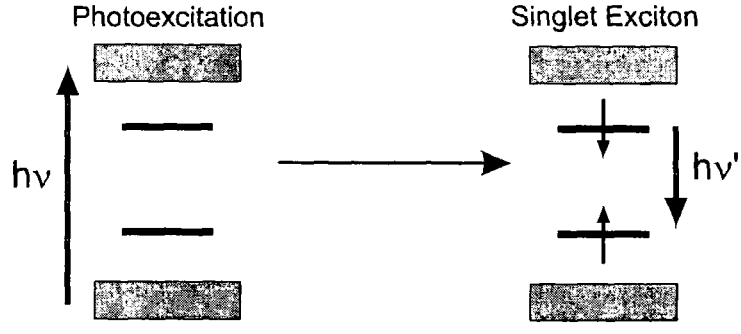

Figure 2-34 *Scheme of photoluminescence in a band picture framework (after reference [45])*

Absorption of a photon promotes an electron from the valence band to the conduction band, leaving a hole in the valence band (forming a negative and positive polaron). The system can then produce a coulombically bound electron-hole pair, an *exciton* (or more correctly in this system, a polaron-exciton). In photoluminescence, this exciton should be singlet, the electron excited from the valence band will leave a hole with the same spin. Thus the exciton level will be populated with two electrons

with opposite spin and hence will be singlet. These singlet excitons can radiatively decay, whereas the radiative decay of triplet excitons to the ground state is not a dipole allowed transition [37].

Photoluminescence Quantum Yield

Photoluminescence quantum yield (PLQY) is a quantitative measure of the radiative decay processes following an optical excitation. PLQY (Φ_{PL}) is defined as the ratio of the number of photons emitted by the material to the number of photons absorbed by the material. The PLQY value is usually quoted as a fraction or as a percentage.

$$\Phi_{PL} = \frac{n_{emitted}}{n_{absorbed}}$$

Equation 2-55

The PLQY of solutions can be measured by comparing the integrated emission spectrum of the solution with that of a standard solution of known PLQY, measured under identical optical conditions. The measurement of the PLQY of films is complicated by the complex angular light distribution. Although film PLQY can be obtained in the manner described above, more accurate results can be obtained through the use of an integrating sphere. An integrating sphere is a hollow sphere with an internal coating of a diffuse, reflecting material. A measurement proportional to the total amount of light generated by excitation of the sample inside the sphere is made through an aperture in the sphere. This method produces an accurate measurement of the PLQY of a film sample. A rigorous account of the procedure and corrections needed for these measurements can be found in reference [46].

Accurate measurement of the PLQY of films is important as it is one of the major factors affecting the operating efficiency of light-emitting diodes, and the PLQY provides a theoretical upper limit for the efficiency of electroluminescence. Values of PLQY in solution and film are, in the majority of cases, dissimilar (see for example, references [43, 47-49]), hence the necessity of integrating sphere measurements.

Electroluminescence

Electroluminescence occurs following the injection of charge carriers into a material, the migration of the charges under an applied electric field and subsequent radiative recombination. The first step in this process is charge injection. In the

simplest view, electrons are injected into the conduction band (LUMO band), and holes are injected into the valence band (HOMO band). Hole injection can also be considered as electron removal from the valence band. The next step is charge migration. In organic systems with a non-degenerate ground state, charge is transported in the form of negative or positive polarons in the case of electrons and holes respectively. Polarons tend to be more mobile than bipolarons, and hence transport is predominantly due to polarons. The polarons migrate under the effect of the applied field and can meet up with an oppositely charged polaron to form a polaron-exciton. Unlike photoluminescence, however, there is no spin correlation to ensure the sole production of singlet excitons. The injection of charges with random signs will statistically produce both singlet and triplet excitons. Triplet excitons are more likely to form as there are 3 triplet exciton states and only one singlet exciton state. These states are shown below.

$$\text{singlet} = \frac{1}{\sqrt{2}}\left[(\uparrow\downarrow) - (\downarrow\uparrow)\right]$$

$$\begin{aligned}\text{triplet} &= (\uparrow\uparrow) \\ &= \frac{1}{\sqrt{2}}\left[(\uparrow\downarrow) + (\downarrow\uparrow)\right] \\ &= (\downarrow\downarrow)\end{aligned}$$

Equation 2-56

The emitting species is often the same for photoluminescence and electroluminescence, and the relationship between the two processes, in a simple system, is shown in Figure 2-35.

Due to this relationship, and the preferential generation of triplet excitons, the theoretical maximum quantum efficiency of polymer light-emitting diodes is thought to be a quarter of the photoluminescence quantum yield of the polymer. In some systems, the electroluminescence and photoluminescence spectra differ and it is uncertain whether this relationship still holds. High fields are often required for charge injection in polymer LEDs, and this may affect the emitting species. The emitting species may also change completely, producing radically different emission spectra, although the nature of any new species has not been investigated in this study.

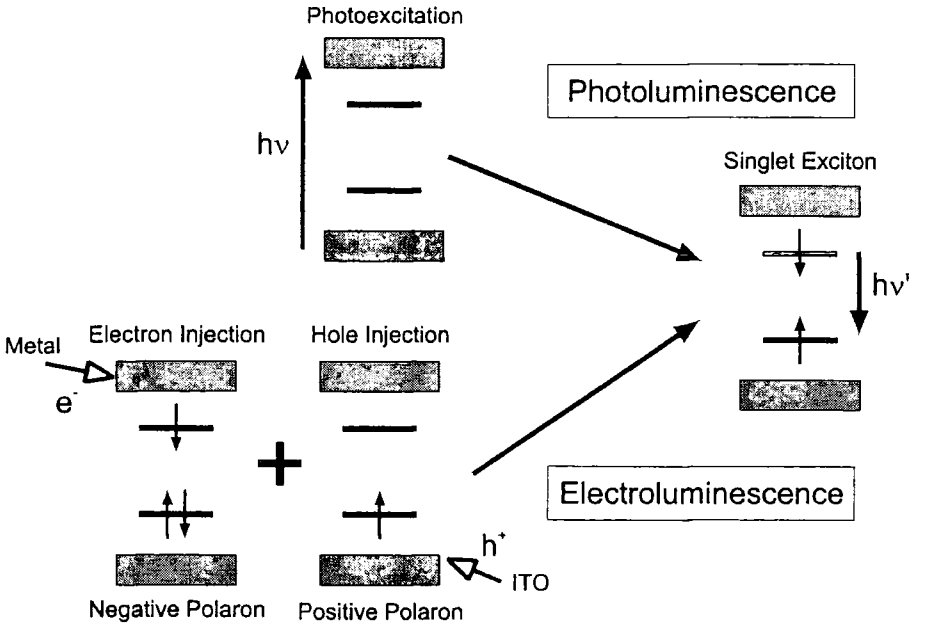

Figure 2-35 *Relationship between photoluminescence and electroluminescence. The formation of triplet polaron-excitons is not shown.*

SUMMARY

Optical characterisation of the polymers in this study is useful for several reasons. Absorption and photoluminescence spectroscopy can provide information about the electronic states of the polymers, in both concentrated and dilute systems. They can help to determine the nature of the ground and excited states (and hence the absorbing and emitting species), probe the extent and reproducibility of the thermal conversion of precursor route polymers and examine differences in related polymers.

Photoluminescence spectroscopy is an almost essential tool in the investigation of polymer electroluminescence. In the simple device model, the two processes differ only by the method of excitation, the emitting species is thought to be the same. This strong link means that quantitative measurements of the amount of luminescence from a polymer, the photoluminescence quantum yield, can put a theoretical upper limit on the efficiency of the electroluminescence (1/4 that of the PLQY). The maximum theoretical efficiency will only be achieved if hole and electron injection and transport are perfectly balanced, and no other factors are present. Hence the knowledge of spectral and efficiency data for photoluminescence can probe the validity of the simple model and provide insight into the possible limits to efficiency in polymer LEDs.

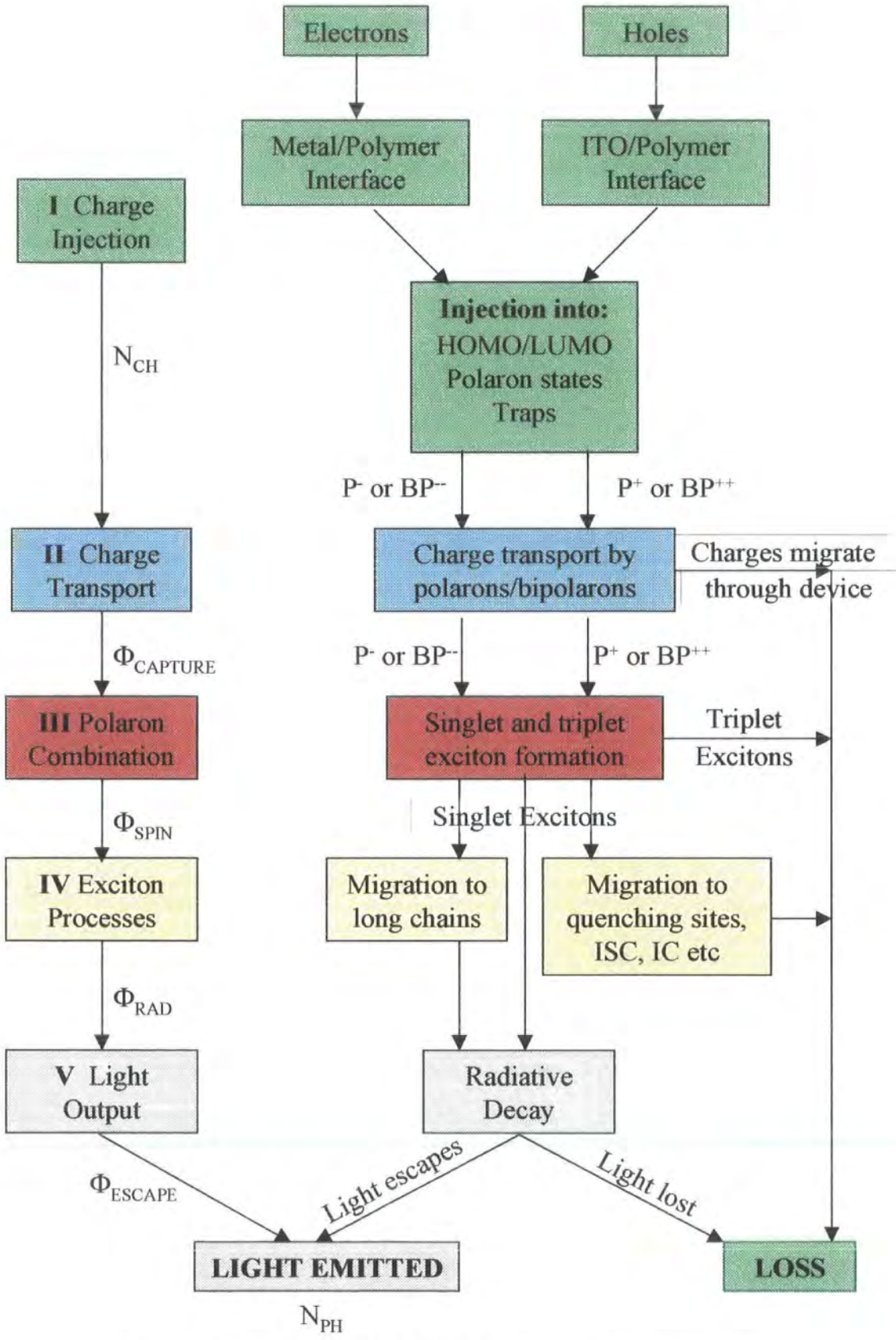

Figure 2-36 *Scheme of polymer light-emitting diode operation*

There are several discrete steps in the evolution of light from polymer light-emitting diodes (LEDs), which are summarised in Figure 2-36. The first step is the injection of charges into the polymer. The efficiency of injection is affected by the material used and the interaction of the material with the polymer. The injected charges are transported through the device, under the effect of the applied electric field. Some of the charges will meet up with opposite charges to form excitons, whereas some will merely migrate through the device, adding to heating effects and reducing the efficiency. A figure of merit can be defined for this process. A fraction of the total number of charges transported through the device will form excitons. This fraction can be represented by a capture quantum efficiency, $\Phi_{CAPTURE}$. Only a quarter of the excitons that are formed will be spin singlet and three quarters will be triplet. The fraction of singlet excitons is reflected by an exciton spin quantum efficiency, Φ_{SPIN}. Triplet excitons decay non-radiatively, and hence limit the efficiency of operation. Once the singlet excitons are created, they can migrate through the polymer. Migration to lower energy (longer conjugation length) chain segments is possible, but migration to quenching sites and other forms of non-radiative decay are also possible. The fraction of singlet excitons which decay radiatively is given by Φ_{RAD}. The light generated by the radiative decay of the singlet excitons can then escape, but some can be lost, for example in self absorption. The fraction of light which escapes the LED is given by Φ_{ESCAPE}. The overall external quantum efficiency, in terms of a ratio of the number of charges injected to the number of photons emitted, is given by Equation 2-57.

$$\frac{N_{ph}}{N_{ch}} = \phi_{CAPTURE}\phi_{SPIN}\phi_{RAD}\phi_{ESCAPE}$$

Equation 2-57

I CHARGE INJECTION

The most commonly held view of charge injection into polymeric systems is that injection occurs from the electrodes directly into the valence and conduction bands of the polymer (see for example references [45, 50]). Conwell and Wu [35] have suggested that tunnelling takes place into polaron levels and not into broad HOMO and LUMO levels and that transport occurs due to hopping among these levels. They cite the primary reason for this injection is the relatively short conjugation lengths producing no broad bands to tunnel into. They state that this decreases injection by a

couple of orders of magnitude, and the short conjugation lengths mean that the mobility is highly field dependent and conclude that Fowler-Nordheim theory is not a good model for polymer light-emitting diodes. This work highlights the complex nature of polymer light-emitting diode operation and is an illustration of the amount of work still to be done to fully understand polymer LEDs.

There are barriers to electron and hole injection into the HOMO and LUMO of the polymer. These arise primarily due to the difference in work functions of the materials used for contacts and the electron affinity and ionisation potential of the polymer, although interface formation does play a role. In a simple view, ignoring the work by Conwell [35], low workfunction metals can be used to inject electrons into the LUMO efficiently, whilst higher workfunction materials are used to inject holes into (withdraw electrons from) the HOMO. Obviously, for light emission, one of the electrodes must be semi-transparent (although a planar arrangement of electrodes has been used to overcome this [51, 52]). The simple injection scheme is shown as Figure 2-37.

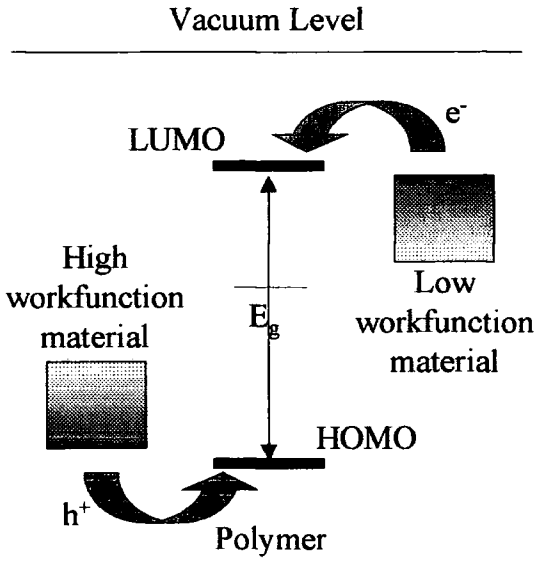

Figure 2-37 *Charge injection into polymer light-emitting diodes*

It can be seen from Figure 2-37 that improved efficiency and a reduced operating voltage should be facilitated by reducing the barriers to charge injection (symbolised by the darker shades in the injection materials in Figure 2-37). XPS, UPS, theoretical and experimental studies of the cathode [53-72] and anode [73-80] have shown the wide range of behaviour that is witnessed in these systems.

Electron Injection

Electron injection is usually achieved in polymer LEDs through the use of non-transparent metal electrodes. Electron injection can usually be improved through the use of metals with a low workfunction [81, 82]. This would bring the Fermi level of the metal closer to the LUMO level of the polymer hence reducing the barrier to electron injection. There are complications, however. Firstly, low workfunction metals tend to be highly reactive with moisture and air, making operation on vacuum or encapsulation essential. Secondly, different metals interact very differently with polymer surfaces, forming a range of interfaces and affecting polymer films to various degrees.

Aluminium Electrodes

Birgerson *et al* [59] have investigated the interfacial region which is created upon aluminium deposition onto polymer surfaces. Aluminium deposited onto most polymer surfaces, by evaporation, produces covalent bonding of the aluminium with the carbon (or nitrogen etc) atoms along the polymer chain. This produces a region of reduced conjugation of approximately 20-30Å, reducing the mobility of the charges in this region. This means, for example in PPV, that there is a large barrier to electron injection due to the difference in workfunction of the materials and a region of low charge mobility near this interface, resulting in devices with reduced efficiency, compared to devices with calcium electrodes.

Calcium Electrodes

There is considerable difference in the performance of calcium contacts in polymer LEDs [81, 82], depending upon the surface to be deposited on and the pressure at which the evaporation is carried out [59].

In very high vacuum metal deposition systems, i.e. better than 10^{-7} mbar, with clean polymer surfaces, "clean" calcium contacts arise. In this regime, there is considerable diffusion of calcium 2+ ions, formed by charge transfer from the calcium to the polymer, into the polymer. These ions interact with the polymer backbone, causing doping [59] and some modifications to the carbon-carbon bond length alternation pattern [57] to a depth of about 20-30Å [59]. The doping results in the formation of bipolaron (bands) [56] through the polymer, increasing the conductivity of the doped region. Application of an electric field, enables calcium ions to diffuse

further into the polymer under the effect of the field, leading to short circuits and device breakdown. The increased conductivity results in charges passing through the polymer without combining with corresponding charges and forming excitons, thus reducing the efficiency of the device [59].

"Dirty" calcium electrodes arise due to the deposition of calcium at pressures of 10^{-6} mbar and above. XPS/UPS studies have shown the formation of oxides of calcium at the metal/polymer interface [58]. These oxides prevent the doping which occurs in better vacuums, and the resulting devices have improved efficiency and lifetime when compared to their "clean" calcium counterparts. A further complication arises when this calcium oxide layer has been formed and a layer of "clean" calcium is deposited at higher vacuum. Upon application of a field in this case, the clean calcium is thought to diffuse through the oxide layer, doping the polymer and producing reduced efficiency and lifetime as before.

The highest performance LEDs are produced when deposition is carried out at a pressure of 10^{-6} mbar, fortuitously the pressure at which most standard laboratory evaporators operate. This deposition forms an oxide layer, protecting the LED from calcium ion diffusion, doping and device failure. A summary schematic of this information can be seen in Figure 2-38.

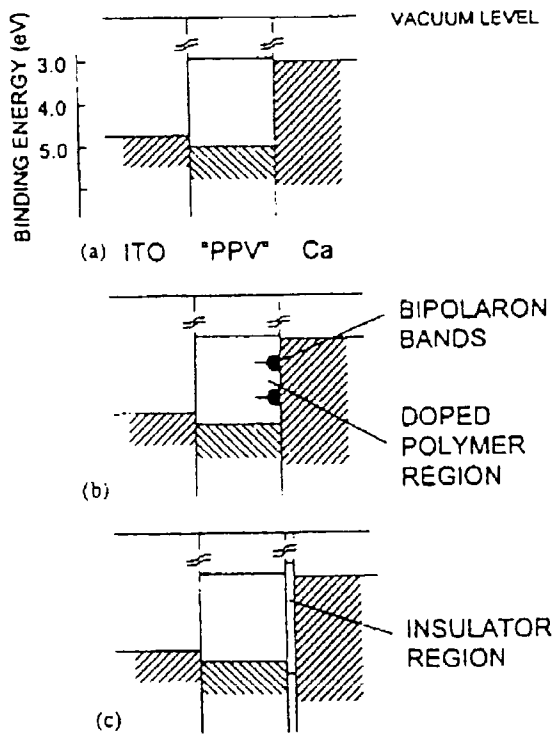

Figure 2-38 *Summary of calcium electrode formation in an ITO/PPV/Ca diode, in a) an ideal case, b) a "clean" calcium case and c) a "dirty" calcium case. The shaded areas indicate regions with a non-zero density of states (from reference [59])*

Magnesium Electrodes

In contrast to the results for calcium, the production of an oxide layer in LEDs with magnesium electrodes seems to have a detrimental effect on LED performance. The turn-on field for device operation increases with the thickness of the oxide layer, suggesting that the oxide layer reduces the efficiency of charge injection and hence the efficiency of the device [59].

Group I Metals

Deposition of sodium, rubidium and potassium results in the uniform doping of the polymer, following charge transfer from the metal to the π-system. Bipolarons are formed and performance would be expected to be similar to that of "clean" calcium [59].

Hole Injection

Hole injection is usually achieved in forward bias through the use of a high workfunction material, for example gold or indium tin oxide (ITO). The hole injecting contact tends to be the (semi) transparent electrode, hence the use of these materials. Polyaniline (PANi) [36, 50, 75, 76, 83-91] and poly(ethylenedioxythiophene) (PEDT or PEDOT) [76, 77] have been used, although the necessity for transparent electrodes limits the thickness and hence the conductivity of the polymer, and therefore ITO is often used in conjunction with the polymer layers. Insulating (emeraldine base) forms of PANi have successfully been used with ITO [36, 75, 86, 89-91], suggesting the conductivity of the polymer is not as important as preventing damage [74, 92] and doping (leading to an essentially ohmic polymer/ITO contact) [93-95] of the emitting polymer caused by ITO. Poly(methyl methacrylate) has also been used as an insulating layer, between the ITO and the polymer layer, improving performance of polymer LEDs [96, 97]. The treatment of the ITO before device manufacture seems to have a substantial effect on the operation of LEDs [73, 78, 80, 98]. Due to the variation in the behaviour of ITO, current-voltage measurements for the purpose of modelling the behaviour of polymer LEDs, should usually be carried out on device structures utilising metal or polymer contacts rather than standard ITO anodes.

II CHARGE TRANSPORT

Paasch [99], and Redecker [100] have shown experimentally and Mizes and Conwell [101] have shown theoretically that charge transport in polymer light-emitting diodes is carried out by polarons and not by electrons and holes. Paasch [99], from theoretical and experimental data, has described a system where immobile bipolarons form a ground state from which mobile polarons can be thermally excited to transport charge via a hopping process. Mizes [101] has concluded, from a theoretical treatment, that chain endings and conjugation breaks stabilise the polarons and hence conduction due to this species is expected. It is also concluded that if these defects were eliminated then conduction would be due to the movement of free charge carriers (i.e. electrons and holes) rather than negatively and positively charged polarons.

Charge Mobility

The hole (positive polaron) mobility in polymers has been shown to be highly field dependent [102, 103]. The mobility of the positive charge carrier is important as most organic materials are very good positive charge carriers and hence the majority charge carrier in organic LEDs tends to be the positive charge carrier (see for example reference [37]). The mobility, $\mu_p(E)$, is proportional to the exponential of the root of the applied electric field (E) and the behaviour can be described by the following equations [103].

$$\mu_p(E) = \mu_p(0)\exp\left(\gamma\sqrt{E}\right)$$

$$\mu_p(0) = \mu_0 \exp\left(\frac{-\Delta}{kT}\right)$$

Equations 2-58

$\mu_p(0)$ is the mobility at zero field, Δ is the activation energy, μ_0 is a prefactor, γ is a material dependent coefficient and the other symbols have their usual meaning.

III POLARON COMBINATION

Charge carriers, in the form of polarons, migrate through the device and meet with their oppositely charged counterparts. The position at which this occurs is governed, to a large degree, by the relative mobilities of the two charges in the material(s) which forms the device [104]. In PPV (and most organic) LEDs, the low electron (negative polaron) mobility means that the region where most combination

takes place is close to the electron injecting contact [37, 104]. When the polarons meet, a polaron-exciton is formed [37, 38], and will be singlet or triplet as described by Equation 2-56.

IV EXCITON MIGRATION

Once the polaron-exciton is formed, it can migrate from short conjugation length chain segments to longer conjugation, lower energy chain segments. Time resolved luminescence measurements (see for example [43, 105-109]) have shown a red-shifting, narrowing of the luminescence spectrum with time, consistent with exciton migration to lower energy chain segments. The migration becomes slower with time, as there are fewer energetically available sites to which the exciton can migrate. During this migration, the exciton can also migrate to quenching sites, reducing the emission efficiency of the polymer [105]. The migration occurs on a sub picosecond timescale [107], and the migration of the charge-neutral exciton is not assisted by the field. This implies that the migration will move the exciton only a short distance away from the position where it was first formed.

V RADIATIVE DECAY

The electron and hole in the singlet exciton can then recombine and emit light. The presence of a metal/polymer interface can have a substantial effect on the emission of polymer films, however [104, 110-112]. Light emission is suppressed near the metal/polymer interface, and the presence of the interface seems to have an effect up to 60nm into the polymer film [104, 110]. As a consequence, the displacement of the emissive region away from the interface and into the bulk should have a positive effect on the radiative efficiency of the polymer.

Not all of the light generated in the polymer film is able to escape, some is waveguided and reabsorbed by the film. The amount of light that actually escapes in the forward direction is believed to be a factor $2n^2$ lower (where n is the refractive index of the polymer) than the amount of light generated inside the film (reference [113] and Chapter 3).

MODELLING OF DEVICE OPERATION

The theoretical modelling of polymer light-emitting diode operation is a growing but complicated field of study. As illustrated previously in this section, the formation of interfaces between polymers and electrodes is complicated and no device

model has yet managed to take interactions beyond the simple misalignment of energy levels into account in a two carrier model. The situation is further complicated by the different behaviour of the various materials in use, and the differences caused by variations in fabrication methods. There have been attempts to produce a novel device model, for example references [114-118], but most device models are based on one of three inorganic based approaches. These approaches are Fowler-Nordheim tunnelling [50, 119-123], Schottky diode [54, 64, 71, 95, 124-131] and space charge limited current [35, 103, 132-134] systems. Comparisons of these systems with experimental data have been carried out, but often very different conclusions have been drawn (see for example references [120, 133, 135, 136]). Modifications to these systems (see for example references [95, 121, 133]) have produced more agreement with experimental data in organic systems, although the application of such models to the complex situations in organic LEDs has yet to be fully justified.

Schottky Barrier Diodes

A Schottky barrier [124] is formed between a metal and a semiconductor when the two are brought into contact. The number of charge carriers in a region close to the metal/semiconductor junction is severely reduced. This is known as the depletion layer. The Fermi levels of the metal and the semiconductor are brought into alignment, and charged donor (n-type semiconductor) or acceptor (p-type semiconductor) ions remain. A schematic of Schottky barriers in n-type and p-type semiconductors is shown in Figure 2-39.

In Figure 2-39, the conduction and valence bands are labelled E_C and E_V, the band gap is E_g, the donor and acceptor levels are labelled E_D and E_A, the Schottky barrier height is ϕ_b, the barrier to electron injection is ϕ_e, the width of the depletion region is w, the built-in voltage (the contact potential difference between the metal and the semiconductor) is V_{SO} and the electron affinity of the polymer (semiconductor) is labelled χ.

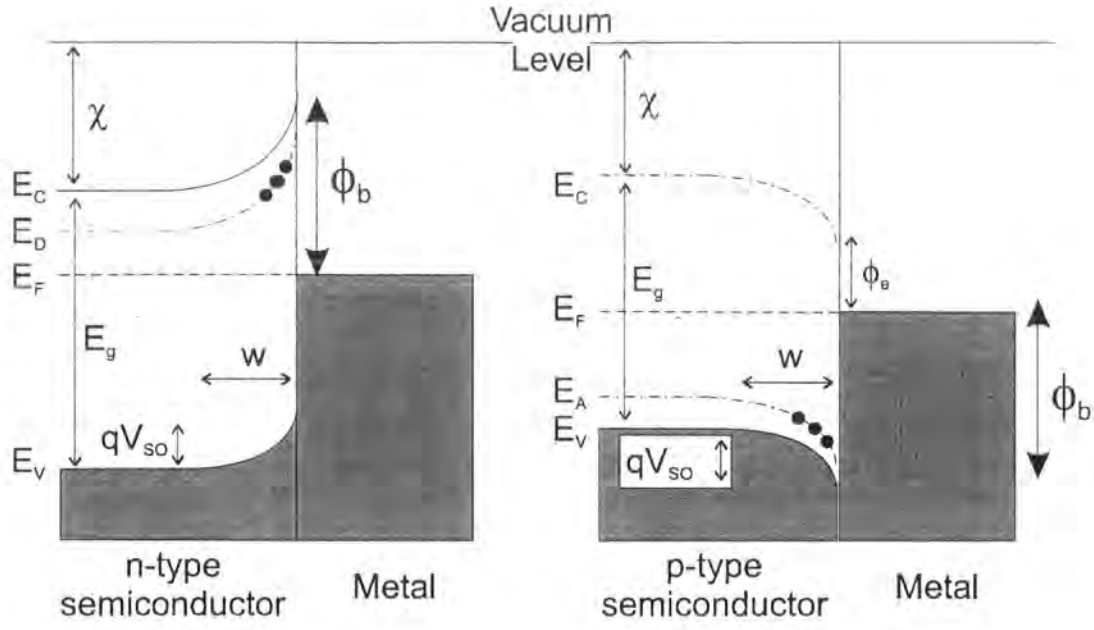

Figure 2-39 *Schottky barrier formation in n- and p-type semiconductors*

The formation of a Schottky barrier produces current density-voltage characteristics governed by

$$J = J_0\left[\exp\left(\frac{qV}{nkT}\right)-1\right].$$

Equation 2-59

The behaviour of J_0 depends whether the current is limited by thermionic emission (Equations 2-60i) or by diffusion (Equations 2-60ii) of charge carriers across the barrier.

$$(i)J_0 = A^*T^2\exp\left(\frac{-q\phi_b}{kT}\right)$$

$$(ii)J_0 = qN_v\mu E_{max}\exp\left(\frac{-q\phi_b}{kT}\right)$$

Equations 2-60

J is the current density which flows at an applied voltage, V, n is the ideality factor, J_0 the reverse saturation current density (given for thermionic and diffusion limited conduction in a p-type semiconductor), A^* the modified Richardson constant, ϕ_b is the difference between the Fermi energy of the metal and the edge of the majority carrier transport band, N_V is the effective density of states in the valence band and E_{max} is the maximum field strength in the space charge layer. All of the other symbols have their usual meaning.

The capacitance of the junction varies with applied voltage, V, and built-in voltage, V_{so}, number of acceptors (p-type), N_A, and the relative permittivity, ε, within the Mott-Schottky relation.

$$C_d^{-2} = \left(\frac{2}{q\varepsilon\varepsilon_0 N_A} \right) (V_{so} - V)$$

Equation 2-61

The width of the depletion region is given by Equation 2-62.

$$w = \sqrt{\frac{2\varepsilon\varepsilon_0 (V_{so} - V)}{qN_A}}$$

Equation 2-62

(Equation 2-59 to Equation 2-62 after reference [127]).

Fowler-Nordheim Tunnelling

At high fields, with large barriers to charge injection, Fowler-Nordheim type tunnelling [119] may be a more applicable theory. A model within the Fowler-Nordheim framework i.e. tunnelling through triangular barriers has been described by Parker [123]. He suggests there is a rigid band structure, with very little band bending (unlike in the case of Schottky barriers) due to the low carrier concentration and immediate depletion of devices made with poly(2-methoxy, 5-(2'ethyl-hexyloxy)-*p*-phenylene vinylene) (MEH-PPV). The application of a large electric field tilts the polymer bands, presenting a reduced barrier thickness through which the charges can tunnel. This is illustrated below for an ITO/Polymer/calcium or aluminium device under high forward bias.

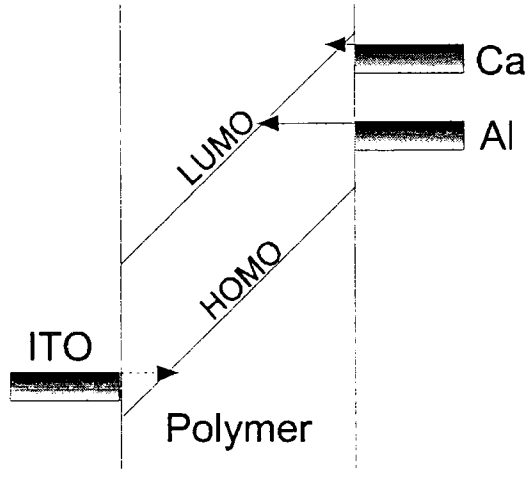

Figure 2-40 *Scheme of Fowler-Nordheim tunnelling (after reference [123])*

This model produces a field (F) dependence of the current (I) governed by the equation

$$I \propto F^2 \exp\left(\frac{-K}{F}\right),$$

Equation 2-63

where, for tunnelling through triangular barriers,

$$K = \frac{8\pi\sqrt{2m^*}\varphi^{3/2}}{3qh},$$

Equation 2-64

and m^* is the effective mass of the injected charge and φ is the barrier height. Fowler-Nordheim plots of $\ln(I/F^2)$ versus $1/F$ are expected to produce a straight line if the theory holds.

Space Charge Limited Current

Within space charge limited current (SCLC) theory, the initial characteristics of the current density (J)-voltage (V) behaviour should be ohmic, i.e. dependent on the carrier density, n, the carrier mobility, μ, and the thickness of the device, d, (Equation 2-65) at low bias.

$$J = qn\mu V / d$$

Equation 2-65

This is due to the fact that the field from the injected charges is negligible compared to the applied bias. As the density of injected charge carriers increases, however, the ohmic conduction breaks down and the current is limited by the space charge effect of the injected carriers, which has an effect comparable to that of the applied bias. The transition from ohmic to SCLC occurs at the space charge limit. The current density is governed by Child's law after this limit.

$$J = \frac{9\varepsilon\varepsilon_0\mu V^2}{8d^3}$$

Equation 2-66

(ε and ε_0 are the permittivity of the polymer and a vacuum). It is possible that the ohmic behaviour is not witnessed due to the high current densities in polymer LEDs, even at low bias [133]. Modifications to SCLC theory to include charge carrier traps have been applied to polymer systems (see for example references [133, 137]).

Summary

The application of inorganic semiconductor models to polymer systems provides numerical results, which should be treated with caution. However, the lack of a coherent model for polymer LED operation makes the use of these models almost essential. Schottky, Fowler-Nordheim and SCLC models can provide insight into the barrier heights and charge mobility of polymers and hence insight into device operation itself. Although results from these models do require cautious treatment, they do provide a relatively simple means of comparison between different groups and materials, which can prove to be invaluable.

REFERENCES

[1] T. W. G. Solomons, *Organic Chemistry*, 5 ed. (John Wiley & Sons, Inc., 1992).

[2] T. Yamamoto, Y. Yoneda and K. Kizu, Macromolecular Rapid Communications, **16** , 8 (1995), 549-556.

[3] R. Peierls, *More Surprises in Theoretical Physics*, 1 ed. (Princeton University Press, Princeton, 1991).

[4] W. P. Su, J. R. Schrieffer and A. J. Heeger, Phys. Rev. Lett., **42** , 25 (1979), 1698-1701.

[5] W. P. Su, J. R. Schrieffer and A. J. Heeger, Phys. Rev. B, **28** , 2 (1983), 1138.

[6] W. P. Su, J. R. Schrieffer and A. J. Heeger, Phys. Rev. B, **22** , 4 (1980), 2099-2111.

[7] A. J. Heeger, S. Kivelson, J. R. Schrieffer and W. P. Su, Reviews of Modern Physics, **60** , 3 (1988), 781-850.

[8] *Handbook of Conducting Polymers*; *Vol. 2*, edited by T. A. Skotheim (Marcel Dekker, New York, 1986).

[9] Z. G. Yu, R. T. Fu, C. Q. Wu, X. Sun and K. Nasu, Phys. Rev. B., **52** , 7 (1995), 4849-4854.

[10] Z. G. Yu, A. Saxena and A. R. Bishop, Phys. Rev. B., **56** , 7 (1997), 3697-3716.

[11] W. P. Su, in *Handbook of Conducting Polymers*; *Vol. 2*, 1 ed., edited by T. A. Skotheim (Marcel Dekker, Inc., New York, 1986), p. 757-794.

[12] S. Kivelson and D. E. Heim, Phys. Rev. B., **26** , 8 (1982), 4278-4292.

[13] K. R. Subbaswamy and M. Grabowski, Phys. Rev. B., **24** , 4 (1981), 2168-2173.

[14] H. Hayashi and K. Nasu, Phys. Rev. B., **32** , 8 (1985), 5295-5302.

[15] C. Kittel, *Introduction to Solid State Physics*, 6 ed. (John Wiley & Sons, Inc., New York, 1986).

[16] X. Sun, Z. Shuai, K. Nasu, D. L. Lin and T. F. George, Phys. Rev. B., **44** , 20 (1991), 11042-11047.

[17] S. A. Brazovskii and N. N. Kirova, JETP Letters, **33** , 1 (1981), 4-8.

[18] C. L. Wang, Z. B. Su and F. Martino, Phys. Rev. B., **33** , 2 (1986), 1512-1515.

[19] Y. Lu, *Solitons & polarons in conducting polymers*, 1 ed. (World Scientific Publishing Co., Singapore, 1988).

[20] D. Baeriswyl and K. Maki, Phys. Rev. B, **28** , 4 (1983), 2068-2073.

[21] D. Moses, A. Feldblum, E. Ehrenfreund, T. C. Chung and A. G. MacDiarmid, Physics Review B, **26** , (1982), 3361.

[22] Z. G. Yu, X. S. Rao, X. Sun and A. R. Bishop, Synth. Met., **85** , 1-3 (1997), 1135-1136.

[23] H. Guo and J. Paldus, International Journal Of Quantum Chemistry, **63** , 2 (1997), 345-360.

[24] A. K. Bakhshi, Journal Of Scientific & Industrial Research, **52** , 6 (1993), 407-422.

[25] F. Guo, M. Chandross and S. Mazumdar, Phys. Rev. Lett., **74** , 11 (1995), 2086-2089.

[26] R. Pariser and R. G. Parr, J. Chem. Phys., **21** , 5 (1953), 466-471.

[27] R. Pariser and R. G. Parr, J. Chem. Phys., **21** , 5 (1953), 767-776.

[28] I. Ohmine and M. Karplus, J. Chem. Phys., **68** , 5 (1978), 2298-2318.

[29] C. Q. Wu, Phys. Rev. B., **47** , 8 (1993), 4204-4214.

[30] M. Chandross, S. Mazumdar, M. Liess, P. A. Lane, Z. V. Vardeny, M. Hamaguchi and K. Yoshino, Phys. Rev. B., **55** , 3 (1997), 1486-1496.

[31] Y. Shimoi and S. Mazumdar, Synth. Met., **85** , 1-3 (1997), 1027-1028.

[32] S. Abe, J. Yu and W. P. Su, Phys. Rev. B., **45** , 15 (1992), 8264-8271.

[33] E. Moore and D. Yaron, Synth. Met., **85** , 1-3 (1997), 1023-1024.

[34] *Molecular Electronics*; *Vol.* , edited by G. J. Ashwell (Research Studies Press Ltd., Taunton, U.K., 1992).

[35] E. M. Conwell and M. W. Wu, Appl. Phys. Lett., **70** , 14 (1997), 1867-1869.

[36] A. J. Epstein, Y. Z. Wang, S. W. Jessen, J. W. Blatchford, D. D. Gebler, L. B. Lin, T. L. Gustafson, T. M. Swager and A. G. MacDiarmid, Macromolecular Symposia, **116** , (1997), 27-38.

[37] D. D. C. Bradley, et al., in *Photochemistry and Polymeric Systems*, 1st ed., edited by M. Kelly, C. B. McArdle and M. J. F. Maunder (The Royal Society of Chemistry, Cambridge, 1993), p. 120-133.

[38] K. Fesser, A. R. Bishop and D. K. Campbell, Phys. Rev. B., **27** , 8 (1983), 4804-4825.

[39] R. H. Friend, D. D. C. Bradley and P. D. Townsend, J. Phys. D.-Appl. Phys., **20** , 11 (1987), 1367-1384.

[40] P. W. Atkins, *Molecular Quantum Mechanics*, 2nd ed. (Oxford University Press, Oxford, 1983).

[41] *The Encyclopaedia of Physics*; *Vol. 1*, edited by R. M. Besancon (Van Nostrand Reinhold, New York, 1990).

[42] M. Pope and C. E. Swenburg, *Electronic Processes in Organic Crystals*, 1st ed. (Oxford University Press, New York, 1982).

[43] I. D. W. Samuel, B. Crystall, G. Rumbles, P. L. Burn, A. B. Holmes and R. H. Friend, Chem. Phys. Lett., **213** , 5,6 (1993), 472-478.

[44] J. M. Andre, J. Delhalle and J. L. Bredas, *Quantum Chemistry Aided Design of Organic Polymers, An Introduction to the Quantum Chemistry of Polymers and its Applications*, Vol. 2, 1st ed. (World Scientific Publishing Co. Pte. Ltd., Singapore, 1991).

[45] A. B. Holmes, et al., Synth. Met., **55-57** , (1993), 4031-4040.

[46] N. C. Greenham, I. D. W. Samuel, G. R. Hayes, R. T. Phillips, Y. A. R. R. Kessener, S. C. Moratti, A. B. Holmes and R. H. Friend, Chem. Phys. Lett., **241** , (1995), 89-96.

[47] J. Stampf, S. Tasch, G. Leising and U. Scherf, Synth. Met., **71** , 1-3 (1995), 2125-2128.

[48] J. W. Blatchford, S. W. Jessen, L.-B. Lin, T. L. Gustafson, D.-K. Fu, H.-L. Wang, T. M. Swager, A. G. MacDiarmid and A. J. Epstein, Phys. Rev. B, **54** , 13 (1996), 9180-9189.

[49] M. Remmers, D. Neher, J. Gruner, R. H. Friend, G. H. Gelinck, J. M. Warman, C. Quattrocchi, D. A. Dossantos and J. L. Bredas, Macromolecules, **29** , 23 (1996), 7432-7445.

[50] A. J. Heeger, I. D. Parker and Y. Yang, Synth. Met., **67** , 1-3 (1994), 23-29.

[51] U. Lemmer, D. Vacar, D. Moses, A. J. Heeger, T. Ohnishi and T. Noguchi, Appl. Phys. Lett., **68** , 21 (1996), 3007-3009.

[52] E. Smela, Y. Kaminorz, O. Inganas and L. Brehmer, Semiconductor Science and Technology, **13** , 4 (1998), 433-439.

[53] M. Fahlman, G. Iucci, W. R. Salaneck and J. L. Bredas, in *SPIE Nonlinear Optical Properties of Organic Materials VIII*, San Diego, California, 1995 , p. 190-199.

[54] Y. Gao, K. T. Park and B. R. Hsieh, J. Appl. Phys., **73** , 11 (1993), 7894-7899.

[55] S. A. Brazovskii and N. N. Kirova, Synth. Met., **57** , 2-3 (1993), 4385-4392.

[56] P. Dannetun, M. Fahlman, C. Fauquet, K. Kaerijama, Y. Sonoda, R. Lazzaroni, J. L. Bredas and W. R. Salaneck, Synth. Met., **67** , 1-3 (1994), 133-136.

[57] R. Lazzaroni, M. Logdlund, A. Calderone, J. L. Bredas, P. Dannetun, C. Fauquet, C. Fredriksson, S. Stafstrom and W. R. Salaneck, Synth. Met., **71** , 1-3 (1995), 2159-2162.

[58] P. Broms, J. Birgersson, N. Johansson, M. Logdlund and W. R. Salaneck, Synth. Met., **74** , 2 (1995), 179-181.

[59] J. Birgerson, M. Fahlman, P. Broms and W. R. Salaneck, Synth. Met., **80** , 2 (1996), 125-130.

[60] W. R. Salaneck and J. L. Bredas, Adv. Mat., **8** , 1 (1996), 48.

[61] M. Fahlman, J. L. Bredas and W. R. Salaneck, Synth. Met., **78** , 3 (1996), 237-246.

[62] E. Ettedgui, H. Razafitrimo, Y. Gao, B. R. Hsieh, W. A. Feld and M. W. Ruckman, Phys. Rev. Lett., **76** , 2 (1996), 299-302.

[63] K. Seki, E. Ito and H. Ishii, Synth. Met., **91** , 1-3 (1997), 137-142.

[64] E. Ettedgui, B. R. Hsieh and Y. Gao, Polymers For Advanced Technologies, **8** , 7 (1997), 408-416.

[65] L. S. Hung, C. W. Tang and M. G. Mason, Appl. Phys. Lett., **70** , 2 (1997), 152-154.

[66] H. Ishii and K. Seki, IEEE Trans. Elect. Dev., **44** , 8 (1997), 1295-1301.

[67] W. R. Salaneck, M. Logdlund, J. Birgersson, P. Barta, R. Lazzaroni and J. L. Bredas, Synth. Met., **85** , 1-3 (1997), 1219-1220.

[68] T. Wakimoto, Y. Fukuda, K. Nagayama, A. Yokoi, H. Nakada and M. Tsuchida, IEEE Trans. Elect. Dev., **44** , 8 (1997), 1245-1248.

[69] P. Broms, J. Birgerson and W. R. Salaneck, Synth. Met., **88** , 3 (1997), 255-258.

[70] E. I. Haskal, A. Curioni, P. F. Seidler and W. Andreoni, Appl. Phys. Lett., **71** , 9 (1997), 1151-1153.

[71] I. H. Campbell, P. S. Davids, D. L. Smith, N. N. Barashkov and J. P. Ferraris, Appl. Phys. Lett., **72** , 15 (1998), 1863-1865.

[72] W. Brutting, E. Buchwald, G. Egerer, M. Meier, K. Zuleeg and M. Schwoerer, Synth. Met., **84** , 1-3 (1997), 677-678.

[73] Y. Park, V. Choong, Y. Gao, B. R. Hsieh and C. W. Tang, Appl. Phys. Lett., **68** , 19 (1996), 2699-2701.

[74] E. Gautier, A. Lorin, J. M. Nunzi, A. Schalchli, J. J. Benattar and D. Vital, Appl. Phys. Lett., **69** , 8 (1996), 1071-1073.

[75] T. Kugler, A. Johansson, I. Dalsegg, U. Gelius and W. R. Salaneck, Synth. Met., **91** , 1-3 (1997), 143-146.

[76] S. A. Carter, M. Angelopoulos, S. Karg, P. J. Brock and J. C. Scott, Appl. Phys. Lett., **70** , 16 (1997), 2067-2069.

[77] Y. Cao, G. Yu, C. Zhang, R. Menon and A. J. Heeger, Synth. Met., **87** , 2 (1997), 171-174.

[78] K. Furukawa, Y. Terasaka, H. Ueda and M. Matsumura, Synth. Met., **91** , 1-3 (1997), 99-101.

[79] R. B. H. Tahar, T. Ban, Y. Ohya and Y. Takahashi, J. Appl. Phys., **83** , 5 (1998), 2631-2645.

[80] F. Nuesch, K. Kamaras and L. Zuppiroli, Chem. Phys. Lett., **283** , 3-4 (1998), 194-200.

[81] D. Braun and A. J. Heeger, Thin Solid Films, **216** , 1 (1992), 96-98.

[82] A. R. Brown, N. C. Greenham, R. W. Gymer, K. Pichler, D. D. C. Bradley, R. H. Friend, P. L. Burn, A. Kraft and A. B. Holmes, Proceedings of Nato ARW, , .

[83] G. Gustafsson, G. M. Treacy, Y. Cao, F. Klavetter, N. Colaneri and A. J. Heeger, Synth. Met., **57** , 1 (1993), 4123-4127.

[84] Y. Yang and A. J. Heeger, Appl. Phys. Lett., **64** , 10 (1994), 1245-1247.

[85] S. Karg, J. C. Scott, J. R. Salem and M. Angelopoulos, Synth. Met., **80** , 2 (1996), 111-117.

[86] H. L. Wang, A. G. Macdiarmid, Y. Z. Wang, D. D. Gebler and A. J. Epstein, Synth. Met., **78** , 1 (1996), 33-37.

[87] J. C. Scott, S. A. Carter, S. Karg and M. Angelopoulos, Synth. Met., **85** , 1-3 (1997), 1197-1200.

[88] Y. Z. Wang, D. D. Gebler, D. K. Fu, T. M. Swager, A. G. MacDiarmid and A. J. Epstein, Synth. Met., **85** , 1-3 (1997), 1179-1182.

[89] Y. Z. Wang, D. D. Gebler, D. K. Fu, T. M. Swager and A. J. Epstein, Appl. Phys. Lett., **70** , 24 (1997), 3215-3217.

[90] A. J. Pal, R. Osterbacka, K. M. Kallman and H. Stubb, Appl. Phys. Lett., **70** , 15 (1997), 2022-2024.

[91] R. Osterbacka, A. J. Pal, K. M. Kallman and H. Stubb, J. Appl. Phys., **83** , 3 (1998), 1748-1752.

[92] C. I. Chao, K. R. Chuang and S. A. Chen, Appl. Phys. Lett., **69** , 19 (1996), 2894-2896.

[93] W. Brutting, M. Meier, M. Herold, S. Karg and M. Schwoerer, Synth. Met., **91** , 1-3 (1997), 163-168.

[94] W. Brutting, M. Meier, M. Herold, S. Karg and M. Schwoerer, Chemical Physics, **227** , 1-2 (1998), 243-252.

[95] S. Karg, M. Meier and W. Riess, J. Appl. Phys., **82** , 4 (1997), 1951-1960.

[96] Y. E. Kim, H. Park and J. J. Kim, Appl. Phys. Lett., **69** , 5 (1996), 599-601.

[97] Y. E. Kim, H. Park and J. J. Kim, Synth. Met., **85** , 1-3 (1997), 1191-1192.

[98] F. Li, H. Tang, J. Shinar, O. Resto and S. Z. Weisz, Appl. Phys. Lett., **70** , 20 (1997), 2741-2743.

[99] G. Paasch, W. Riess, S. Karg, M. Meier and M. Schwoerer, Synth. Met., **67** , 1-3 (1994), 177-180.

[100] M. Redecker and H. Bassler, Appl. Phys. Lett., **69** , 1 (1996), 70-72.

[101] H. A. Mizes and E. M. Conwell, Phys. Rev. Lett., **70** , 10 (1993), 1505-1508.

[102] H. Bassler, Physica Status Solidi B-Basic Research, **175** , 1 (1993), 15-56.

[103] P. W. M. Blom, M. J. M. deJong and M. G. vanMunster, Phys. Rev. B., **55** , 2 (1997), R656-R659.

[104] J. Gruner, M. Remmers and D. Neher, Adv. Mat., **9** , 12 (1997), 964.

[105] R. F. Mahrt, U. Lemmer, A. Greiner, Y. Wada, H. Bassler, E. O. Gobel, R. Kersting, K. Leo and H. Kurz, Journal of Luminescence, **60&61** , (1994), 479-481.

[106] I. D. W. Samuel, G. Rumbles and C. J. Collison, Physical Review B Rapid Communications, **52** , 16 (1995), 11573-11576.

[107] G. R. Hayes, I. D. W. Samuel and R. T. Phillips, Phys. Rev. B., **52** , 16 (1995), 11569-11572.

[108] K. K. Liang, J. H. Hsu, W. S. Fann, S. H. Lin, K. H. Lee, M. K. Leung, K. R. Chuang and S. A. Chen, Synth. Met., **84** , 1-3 (1997), 953-954.

[109] G. R. Hayes, I. D. W. Samuel and R. T. Phillips, Synth. Met., **84** , 1-3 (1997), 889-890.

[110] V. Choong, Y. Park, Y. Gao, T. Wehrmeister, K. Mullen, B. R. Hsieh and C. W. Tang, Appl. Phys. Lett., **69** , 10 (1996), 1492-1494.

[111] V. E. Choong, Y. Park, N. Shivaparan, C. W. Tang and Y. Gao, Appl. Phys. Lett., **71** , 8 (1997), 1005-1007.

[112] H. Becker, S. E. Burns and R. H. Friend, Phys. Rev. B., **56** , 4 (1997), 1893-1905.

[113] N. C. Greenham, R. H. Friend and D. D. C. Bradley, Adv. Mat., **6** , 6 (1994), 491-494.

[114] P. S. Davids, A. Saxena and D. L. Smith, J. Appl. Phys., **78** , 6 (1995), 4244-4252.

[115] H. Bassler, Y. H. Tak, D. V. Khramtchenkov and V. R. Nikitenko, Synth. Met., **91** , 1-3 (1997), 173-179.

[116] D. V. Khramtchenkov, V. I. Arkhipov and H. Bassler, J. Appl. Phys., **81** , 10 (1997), 6954-6962.

[117] P. S. Davids, I. H. Campbell and D. L. Smith, J. Appl. Phys., **82** , 12 (1997), 6319-6325.

[118] J. C. Scott, S. Karg and S. A. Carter, J. Appl. Phys., **82** , 3 (1997), 1454-1460.

[119] R. H. Fowler and L. Nordheim, in *Proceedings of the Royal Society*, London, 1928 , p. 173-181.

[120] L. S. Roman, I. A. Hummelgen, F. C. Nart, L. O. Peres and E. L. Desa, J. Chem. Phys., **105** , 23 (1996), 10614-10620.

[121] M. Koehler and I. A. Hummelgen, Appl. Phys. Lett., **70** , 24 (1997), 3254-3256.

[122] P. S. Davids, S. M. Kogan, I. D. Parker and D. L. Smith, Appl. Phys. Lett., **69** , 15 (1996), 2270-2272.

[123] I. D. Parker, J. Appl. Phys., **75** , 3 (1994), 1656-1666.

[124] W. Schottky, Naturwissenschafen, **26** , (1938), 843.

[125] W. Riess, S. Karg, V. Dyakonov, M. Meier and M. Schwoerer, Journal Of Luminescence, **60** , 1 (1994), 906-911.

[126] D. M. deLeeuw and E. J. Lous, Synth. Met., **65** , 1 (1994), 45-53.

[127] D. M. Taylor and H. L. Gomes, J. Phys. D.-Appl. Phys., **28** , 12 (1995), 2554-2568.

[128] H. L. Gomes and D. M. Taylor, IEE Proceedings-Circuits Devices and Systems, **144** , 2 (1997), 117-122.

[129] R. Singh and A. K. Narula, Appl. Phys. Lett., **71** , 19 (1997), 2845-2847.

[130] S. S. Pandey, M. K. Ram, V. K. Srivastava and B. D. Malhotra, Journal Of Applied Polymer Science, **65** , 13 (1997), 2745-2748.

[131] H. M. Gupta, Physica Status Solidi a-Applied Research, **164** , 2 (1997), 733-745.

[132] P. W. M. Blom, M. J. M. Dejong and J. J. M. Vleggaar, Appl. Phys. Lett., **68** , 23 (1996), 3308-3310.

[133] A. J. Campbell, D. D. C. Bradley and D. G. Lidzey, J. Appl. Phys., **82** , 12 (1997), 6326-6342.

[134] V. N. Savvateev, M. Tarabia, H. Chayet, E. Z. Farragi, G. B. Cohen, S. Kirstein, D. Davidov, Y. Avny and R. Neumann, Synth. Met., **85** , 1-3 (1997), 1269-1270.

[135] H. Kusano, N. Shiraishi, S. Hosaka, I. Kuruma, M. Kitagawa, K. Ichino and H. Kobayashi, Synth. Met., **91** , 1-3 (1997), 341-343.

[136] J. Kalinowski, P. Dimarco, N. Camaioni, V. Fattori, W. Stampor and J. Duff, Synth. Met., **76** , 1-3 (1996), 77-83.

[137] P. E. Burrows, Z. Shen, V. Bulovic, D. M. McCarty, S. R. Forrest, J. A. Cronin and M. E. Thompson, J. Appl. Phys., **79** , 10 (1996), 7991-8006.

Chapter 3 Experimental

POLYMER STRUCTURES AND CONVERSION

The polymers most frequently used in this study are poly(*p*-phenylene vinylene) (PPV), poly(2-methoxy, 5-(2'ethyl-hexyloxy)-*p*-phenylene vinylene) (MEH-PPV) and poly(2,5-pyridinediyl) (PPY). The chemical structure of these polymers is shown in Figure 3-1.

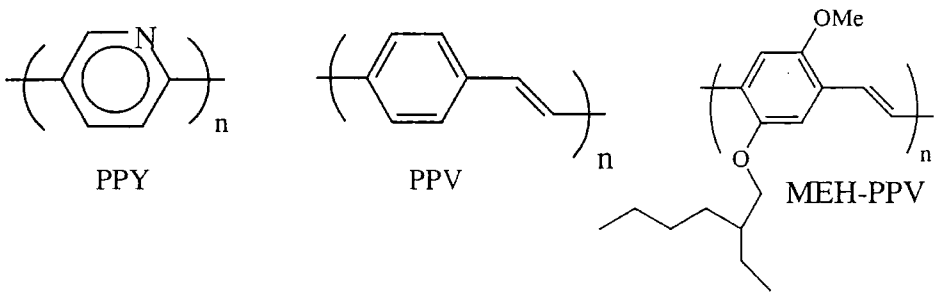

Figure 3-1 *Chemical structure of PPY, PPV and MEH-PPV*

PPV precursor solution in methanol was supplied by Cambridge Display Technology (CDT) (their non-proprietary PPV), solid MEH-PPV was supplied by Hoechst Chemicals, PPY is synthesised in Durham and precursor MEH-PPV solution in THF was supplied by Graham Webster and P.L. Burn of the Dyson Perrins Laboratory, Oxford. PPV is insoluble in common organic solvents, hence the use of a precursor route. There are some advantages to using precursor polymers, hence the study of a precursor of the readily soluble polymer, MEH-PPV. The PPV studied is the tetrahydrothiophenium (THT) leaving group precursor with chloride counterion. Conversion to PPV is carried out in a vacuum of 10^{-5}mbar or better, at 250°C for 10 hours for complete conversion. MEH-PPV precursor conversion is similar, but the conversion temperature is 160°C, and the leaving group is a chloride ion. The use of a precursor MEH-PPV is not essential as soluble MEH-PPV also exists. The use of the precursor route does allow the investigation and direct comparison of the properties of precursor and solution processed polymers and the effects of thermal conversion, however. In both precursor systems, complete conversion of every monomer unit of the polymer chain would not be expected.

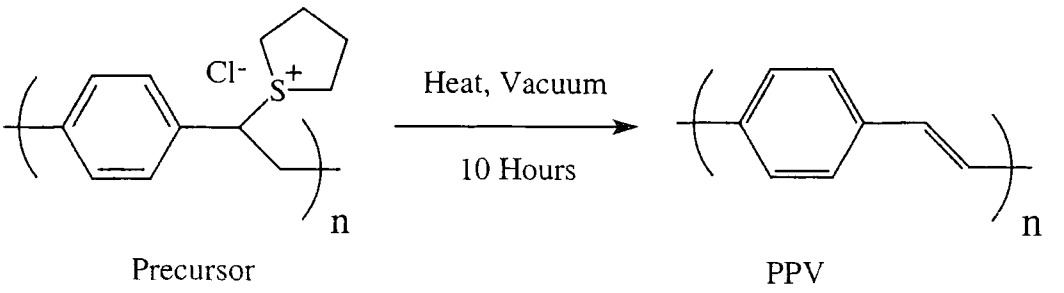

Figure 3-2 *Thermal conversion of PPV precursor to PPV*

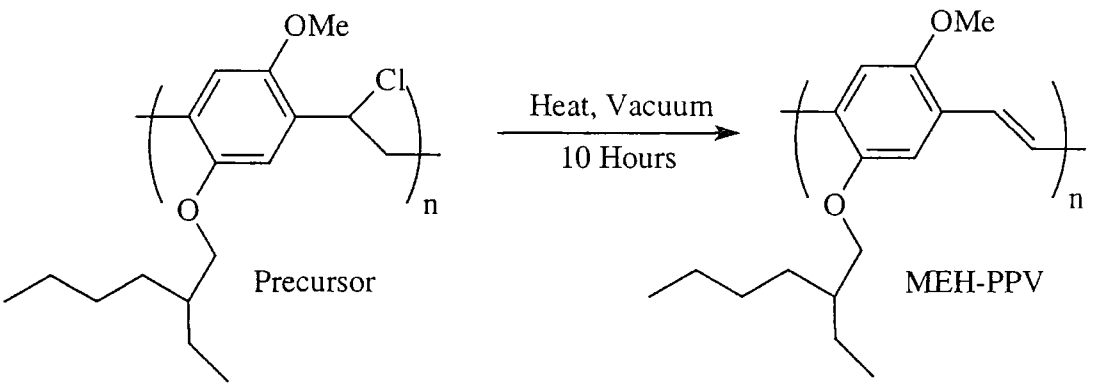

Figure 3-3 *Thermal conversion of MEH-PPV precursor to MEH-PPV*

Polypyridine was prepared by Dr E. Rebourt and Dr L.E. Horsburgh by dehalogenation polycondensation of 2,5-dibromopyridine with a tetrakakis(triphenylphosphine) nickel(0) catalyst following a modified Yamamoto route [1]. The reaction scheme is shown in Figure 3-4.

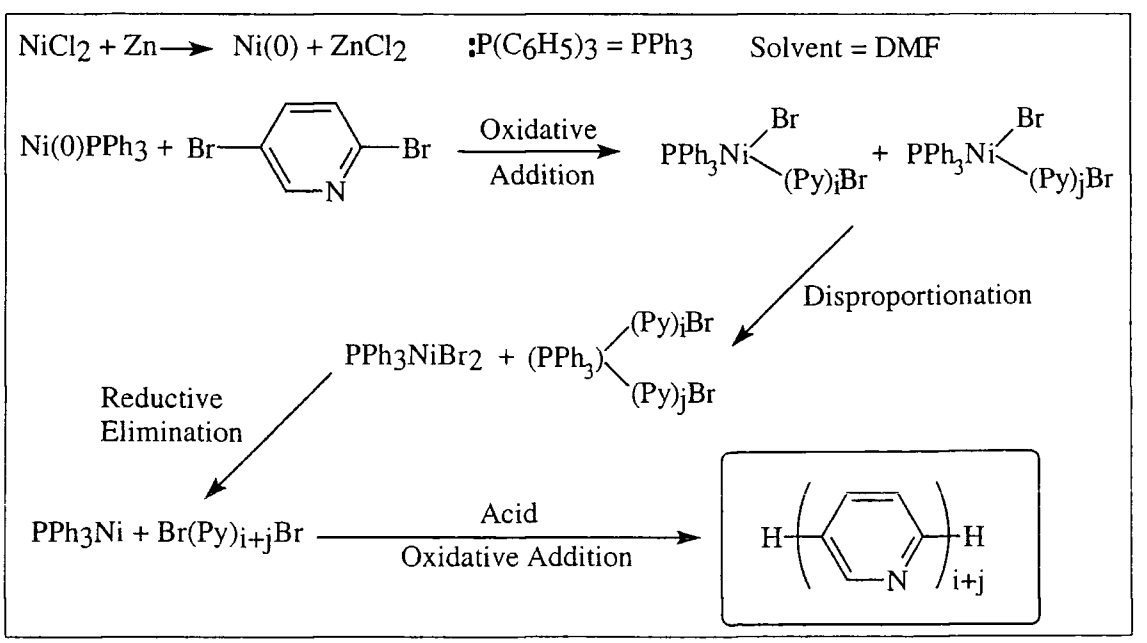

Figure 3-4 *Reaction scheme of the preparation of poly(p-pyridine)*

SAMPLE PREPARATION

Polymer solution samples were filtered, if required, through a 0.45 μm filter before spin-coating or optical measurements were performed.

Optical Absorption and Photoluminescence Samples

Samples for absorption and photoluminescence experiments were prepared from polymer solutions. Solution samples of the soluble polymers were prepared by dissolving polymer powders in chlorobenzene and formic acid for MEH-PPV and PPY respectively. Measurements of solution absorption and luminescence were carried out on solutions contained in quartz cuvettes. Film samples were prepared by spin-coating from solutions of MEH-PPV and PPY, and from precursor solutions of PPV and MEH-PPV in methanol and THF respectively, followed by thermal conversion as required, as described above. The films were formed on quartz or glass substrates.

Electroluminescence Samples

Light-emitting diodes were fabricated by spin-coating the polymer films onto indium tin oxide (ITO) coated glass substrates. Multiple polymer layer device structures were prepared by spin-coating from the various polymer solutions directly onto the previous polymer layers. Thermal conversion was carried out as required, before the addition of any further layers. The diode structure was completed by evaporation of metal electrodes.

Metal Evaporation

Metal electrodes were evaporated onto the polymer layers, usually to a thickness of approximately 100nm, forming the cathode in forward bias. The deposition rate was held at roughly 1Å/s to minimise the effect the evaporation would have on the polymer layer. Calcium electrodes were partially protected from the effects of oxidation by subsequent evaporation of an aluminium capping layer. The arrangement of the metal electrodes is governed by the action of a shadow mask, of my design, which dictates where the metal contacts are formed. The action of the mask defines an active device area of 2 mm^2.

ITO Preparation

ITO is almost exclusively used as the semitransparent electrode, due to its high surface conductivity and high optical transmission (higher than 80% transmission across most of the visible region of the spectrum), shown in Figure 3-5. The ITO used in this study has a sheet resistivity of 20 Ω/square and is obtained in the form of 60×60cm sheets from Balzers. ITO with a sheet resistivity of 30 Ω/square has also been used, and no significant changes were observed.

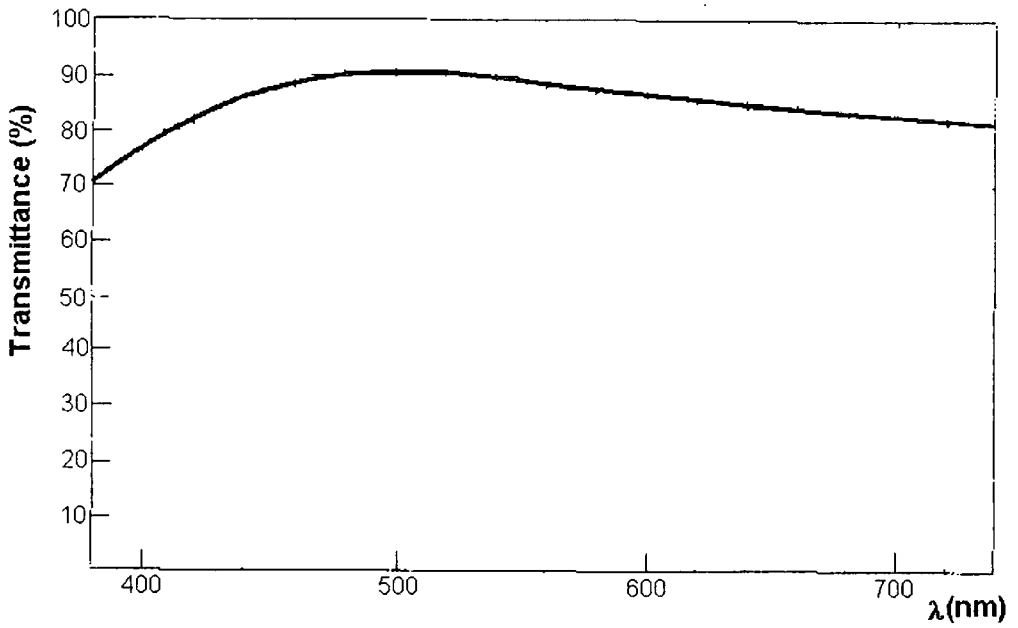

Figure 3-5 *Transmission versus wavelength for Balzers indium tin oxide coated glass (from Balzers Optical Coatings catalogue)*

It is patterned through the use of a positive photoresist, which is applied to a large area of ITO sheet. The ITO sheet is cut into 12mm wide strips using a tungsten cutting wheel and guide. The exterior sections of photoresist, 3mm each side, are defined and removed using a scalpel and stencil, producing a central 6mm section of photoresist with well defined edges. The ITO is removed by placing 12×12mm squares (prepared using the cutting wheel) into an acid etch at a temperature between 45°C and 55°C for two minutes. The acid etch is a mixture of water, hydrochloric and nitric acids in a ratio of 12.5:12.5:1, as recommended by Balzers. The substrate is then placed briefly into deionised water before the photoresist is removed using acetone, before the substrate is repeatedly washed in acetone and propan-2-ol (IPA) in an ultrasound bath. This patterning process is summarised in Figure 3-6. The patterning

produces substrates with well defined edges, and a resistance in excess of 10MΩ/cm in the etched (ITO-less) regions. The remaining ITO has a resistance similar to that of pristine ITO.

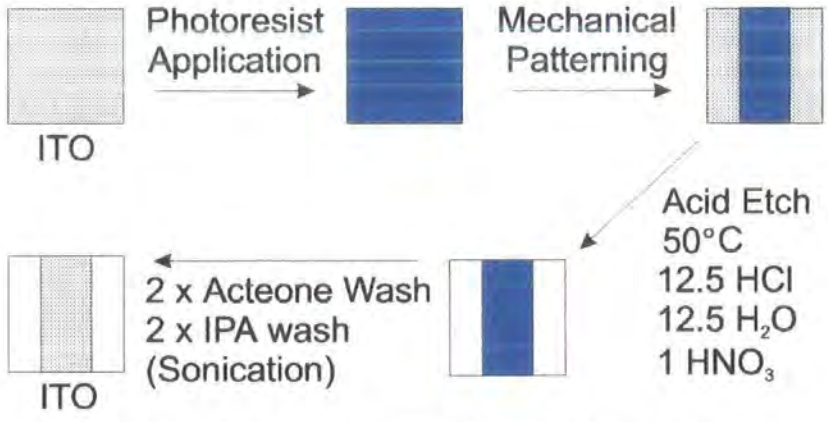

Figure 3-6 *Patterning of ITO coated substrates*

The evaporated metal contacts are positioned to allow electrical connection to be made in the etched region, preventing a short-circuit of the diode. The device structure is shown in Figure 3-7.

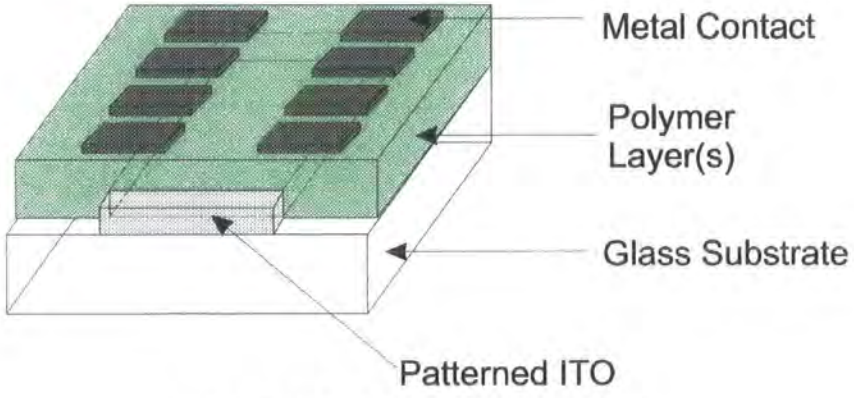

Figure 3-7 *Polymer diode structure*

Electrical connections are made through the use of a matrix of sprung gold pins, in a 3rd generation device holder of my own design and manufacture. The individual diodes are addressed using a self-made switching box to address the individual cathodes (forward bias) and a common ITO anode is used. Light emission occurs through the semitransparent ITO and glass substrate as shown in Figure 3-8.

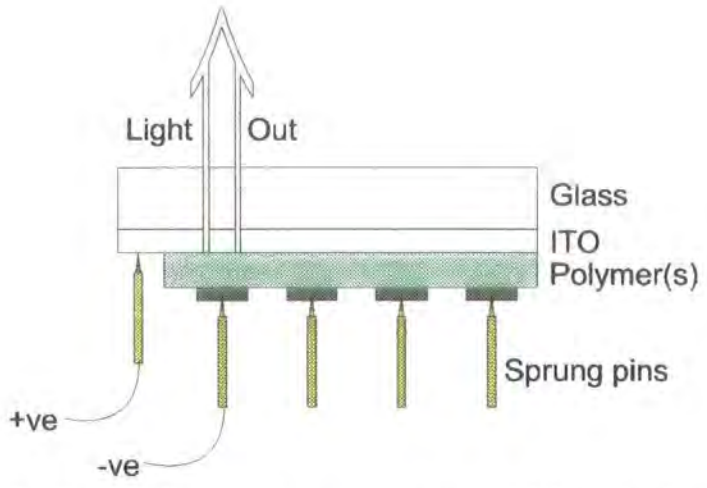

Figure 3-8 *Electrical connections to a polymer LED under forward bias*

Thickness Measurements

Measurements of film thickness were performed using a Tencor Alpha-Step thickness profiler. A small section of polymer film was removed using a scalpel blade and the stylus of the profiler was drawn across the removed section, producing a measure of the thickness of the sample. For multilayer samples, the thickness of both layers was measured before the upper layer was removed, using a suitable solvent, and a measurement of the lower film thickness was performed. A typical trace resulting from an Alpha-Step measurement is shown below.

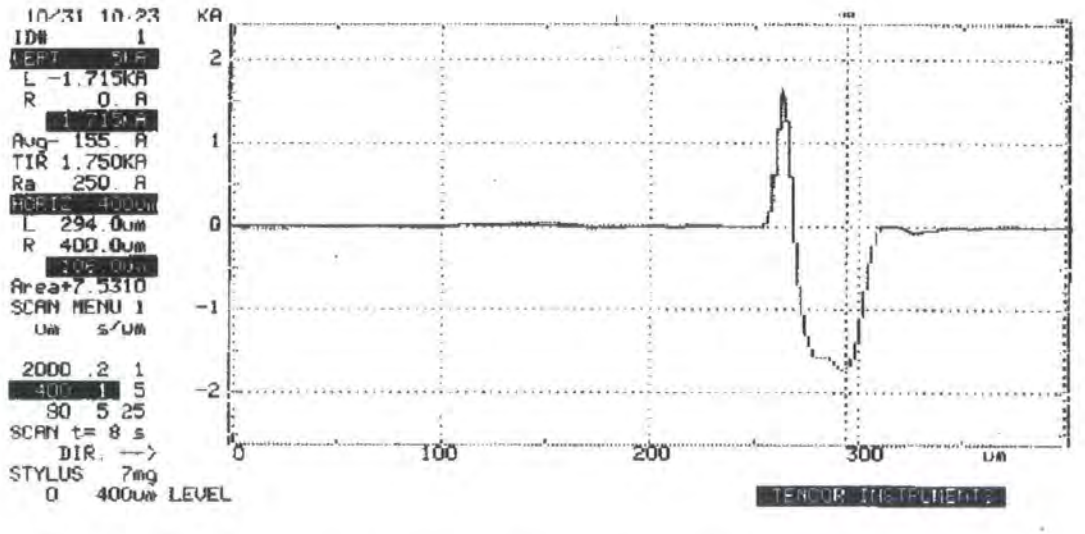

Figure 3-9 *Typical trace from an Alpha-Step thickness measurement*

The trace shows a flat area from around 0μm to 250μm on the x-axis. There is then a large peak of about +170nm before the trace shows a wide depression with a

depth of 171.5nm (as measured). The depression is caused by the action of a scalpel scratch down the surface and the peak is a result of material from this scratch piling up on the side of the scratch.

OPTICAL ABSORPTION AND PHOTOLUMINESCENCE CHARACTERISATION

The absorption spectra of the film and solution samples were measured using a commercial Perkin-Elmer Lambda 19 absorption spectrometer, which is also capable of measuring the reflectivity and transmission of the various samples.

Photoluminescence experiments were carried out using either a commercial fluorimeter, a laser and diode array or a laser/mercury arc lamp and charge coupled device (CCD) and spectrograph system. Most photoluminescence spectra were measured using the mercury arc lamp and a monochromator as the excitation source, and the CCD and spectrograph as the detector (shown schematically in Figure 3-10), in a set-up assembled by myself. The emitted light is collected by optics connected, via a fibre optic cable, to the spectrograph and CCD. An argon ion laser has also been used as an excitation source with this set-up.

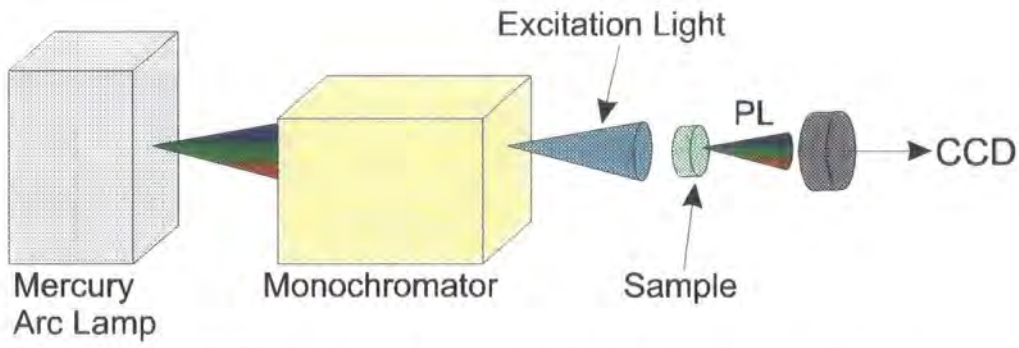

Figure 3-10 *Experimental set-up for photoluminescence experiments*

Two collection geometries were used for photoluminescence experiments. In some measurements, the emitted light was collected on the opposite side to the excitation light, i.e. in transmission. In other measurements the emitted light was collected on the same side of the sample as the excitation, i.e. in reflection. The geometries of the measurements are illustrated in Figure 3-11.

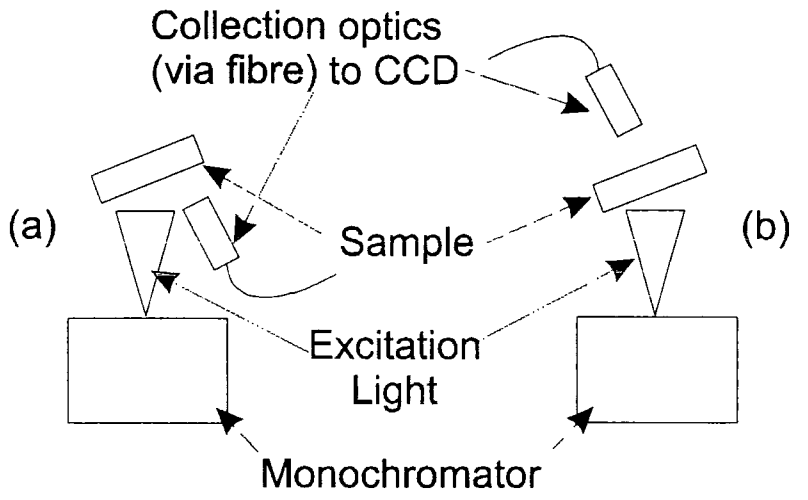

Figure 3-11 *Schematic representation of a) reflection and b) transmission geometries for PL spectra acquisition*

In both transmission and reflection geometries, the sample was offset from 90° to the monochromator and the collection optics were offset from the plane of the excitation light, in order to reduce the collection of excitation and second order light. Collection geometries were chosen and adjusted depending on the nature of the substrate (or sample holder) and the strength of the sample absorption and emission.

Photoluminescence quantum yield measurements of solution and film samples were carried out by M. Halim, using an integrating sphere, as described in Chapter 2 and reference [2].

EXPERIMENTAL SET-UP

The electroluminescence from the polymer light emitting diode is characterised separately for intensity and spectral output. The intensity measurements are carried out simultaneously with the electrical (current-voltage) characterisation. Intensity is measured by a Keithley 2000 Multimeter, as a voltage from a large area ($100mm^2$) silicon photodiode (standard RS photodiode) in a transimpedance amplifier circuit (Figure 3-15). The current-voltage behaviour is measured using a Keithley 2400 Source-Measure unit. Both meters are controlled, via IEEE, by a computer running a self-written program, logging current, voltage and intensity information in a comma delimited ASCII form. The program is capable of multiple runs, at various voltage step delays, and also performing studies of LEDs over time.

The spectral output is measured using a spectrograph attached to either a diode array or CCD, while the diode is held at a constant voltage or current. Most measurements were performed using a CCD. The measurements are made in vacuum to negate any effect oxidation may have on the diodes. The vacuum chamber is self designed and is capable of being transferred directly from a nitrogen glovebox to a vacuum condition.

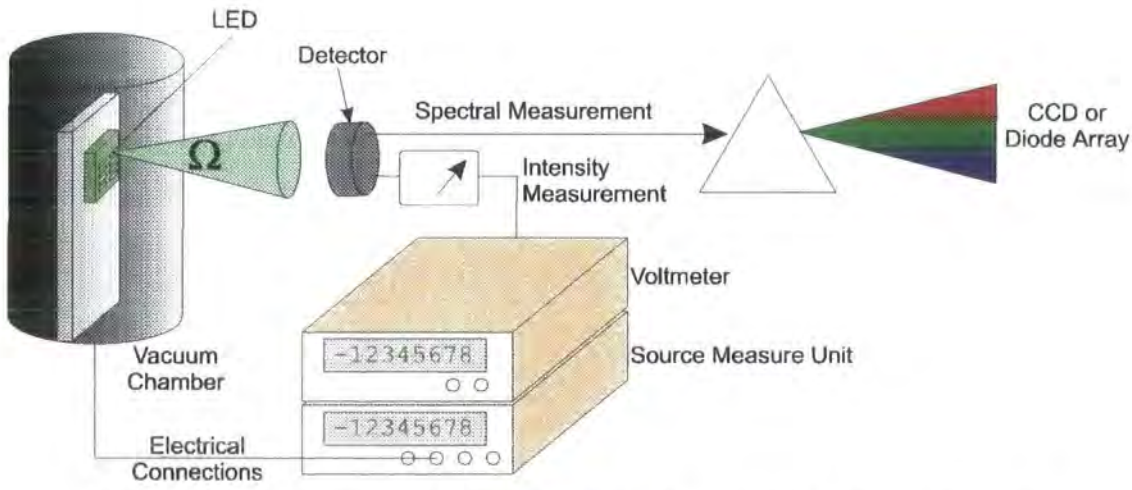

Figure 3-12 *Experimental set-up for electroluminescence characterisation*

The spectral output of the polymer diodes tends to be relatively broad and any conversion from a measured voltage from the large area photodiode to absolute units (watts, candela etc.) must take this spectrum into account.

PRINCIPLES OF CCD IMAGING

The following is a brief introduction to the process of spectral measurement using a charge coupled device (CCD). The information is mostly taken from reference [3].

The charge coupled device or CCD is essentially a large area silicon detector, divided into an array of pixels, defined by a matrix of metal electrodes. The essential feature of the CCD is its ability to store information in the form of electrical charge packets in *potential wells* created in the semiconductor by the influence of overlying electrodes separated from the semiconductor by a thin insulating layer (metal-insulator-semiconductor, or MOS structure). Under the control of external voltages applied to the electrodes, the potential wells, and hence the charge packets, can be shifted through the semiconductor. By introducing the charge packets at one point and detecting them at another, one can create a shift register or delay line. The delay line is not, however, merely a digital structure: the potential wells are capable of storing variable amounts of charge and so the CCD is capable of providing an *analogue* signal delay. Furthermore, charges may be introduced into the potential wells by optical means: light incident on the semiconductor generates charge carriers which can be collected in the potential wells and subsequently clocked out of the structure thereby enabling the CCD to act as an image sensor [3].

The basic structure is illustrated schematically in Figure 3-13 for an n-channel array. For spectral measurement, the emitted light from a source is spatially split into its constituent wavelengths using a diffraction grating. The light falls onto the front face of the CCD, represented by a light spot in Figure 3-13. Photons entering the silicon substrate, either through or between the electrodes (depending upon the electrode material), generate electron-hole pairs by virtue of the photoelectric effect. The minority carriers (*i.e.* electrons), generated within the depletion regions or within a minority carrier diffusion length of the depletion regions, are collected under each ϕ_3 electrode. The number of electrons collected under a given electrode within a given period of time (the integration period) is proportional to the local light intensity. Thus the pattern of charge that collects under the electrodes is an analogue replica of the light intensity across the original image. At the end of the integration period the charge pattern is read out by clocking the array [3]. At the end of the readout period the device is again switched to the integration mode and the cycle is repeated if necessary.

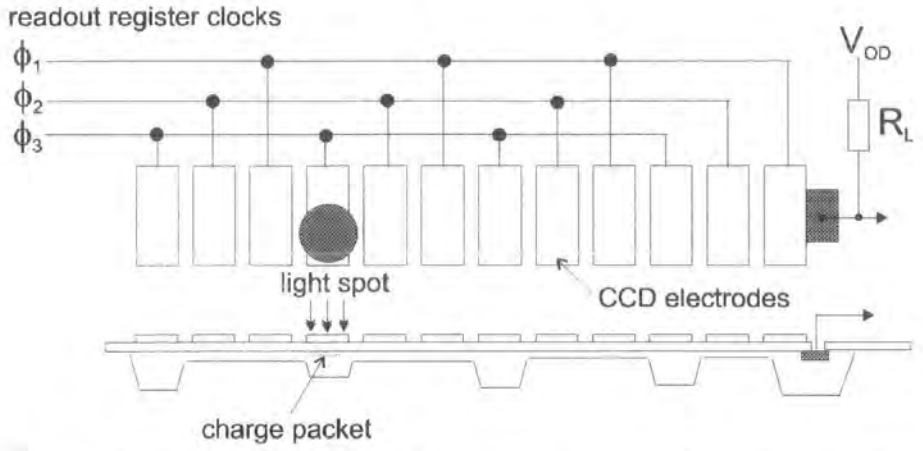

Figure 3-13 *Scheme of CCD detector operation (after reference [3])*

The light emitted by the source is collected using a fibre optic, or collection optics and then focussed onto a grating. As explained above, the grating is used to spatially separate the spectrum emitted by the source. The spectrum can then be measured by a rectangular CCD array (see Figure 3-14).

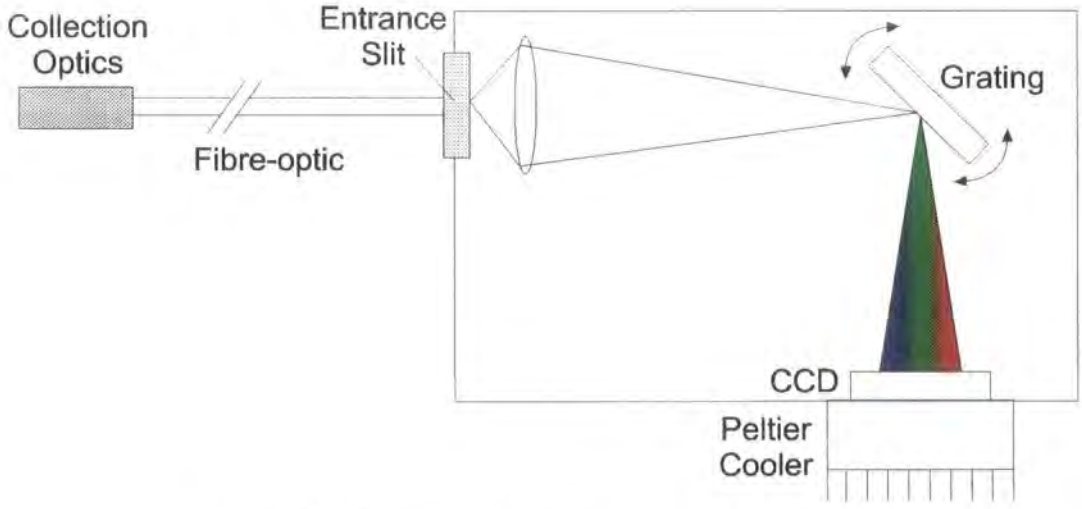

Figure 3-14 *Schematic of CCD/spectrograph set-up*

An entrance slit can be used to vary the overall amount of incident light. Widening the slit produces more incident light but reduces the spectral resolution of the instrument. The collected light is spectrally split by the moveable diffraction grating. The angle of the grating defines the spectral region to be measured. The spectrally resolved light is then incident on the cooled CCD chip. A Peltier cooler reduces the temperature of the CCD chip, reducing the thermal generation of carriers (and hence the noise level), increasing the sensitivity of the instrument.

Thermal Generation

Thermal generation, or dark current, arises from the transition of electrons or holes after they absorb thermal energy from a phonon. This provides an undesired source of charge carriers which cannot be distinguished from the photogenerated carriers. It is this process which can limit the sensitivity of CCD detectors. The probability of thermal generation can be approximated to [3]

$$\ln(U_{gen}) \propto -\frac{A}{T} + B,$$

Equation 3-1

where A and B are constants. As would be expected, the probability of thermal generation increases as the temperature of the detector increases. Cooling the CCD detector reduces the dark current and permits an increase in the integration time or enables the detector to be used for detecting smaller optical signals [3]. A four stage Peltier effect cooling device (for more information see reference [4]) is used with an air heat exchanger in our system. The CCD chip is held in vacuum, and this arrangement leads to a typical operating temperature of the CCD chip of 243K (-30°C).

As stated above, the angle of the grating defines the wavelength range to be measured. In the CCD spectrograph controlling software, the wavelength range is defined by a single parameter, the wavelength at the centre of the wavelength range. The fibre optic, the gratings (300 and 150 lines per mm) and CCD each have a wavelength-dependent response. The 300 lines per mm grating produces a superior wavelength resolution, but has a narrower wavelength range than the 150 lines per mm grating. The complete system, using the fibre optic, was supplied calibrated by Instruments SA, using a standard source at several centre wavelengths. Changing system configurations and changing to unsupported centre wavelengths requires new calibration data files. These were calculated as required by measuring a tungsten lamp spectrum in various configurations and using the previous calibration files to produce new calibration data.

NORMALISATION OF ELECTROLUMINESCENCE SPECTRA

The spectrum measured on the CCD or diode array has intensity proportional to the number of photons in a given wavelength interval, but there can be no quantitative information about the *amount* of light generated by the LED unless the measurement takes place under identical optical conditions. A large area photodiode is instead used

to measure the total amount of light emitted in a known solid angle by the polymer LED, then this quantitative information is added to the qualitative data from the CCD to calculate efficiency etc. This intensity measurement is in terms of a voltage, V_D, from the transimpedance amplifier circuit shown in Figure 3-15. This voltage is proportional to the current generated by light from the light-emitting diode incident on the large area photodiode.

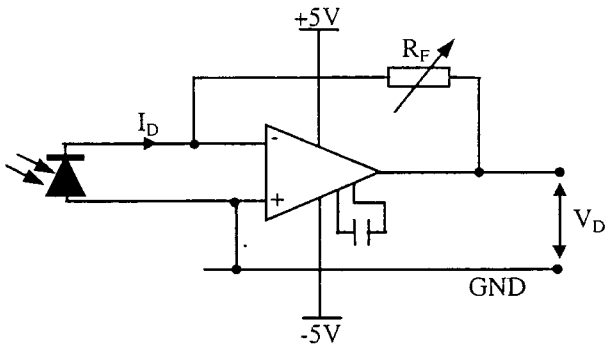

Figure 3-15 *Transimpedance amplifier circuit for the photodiode detector*

In this circuit, the operational amplifier is used as a current to voltage converter. The current, I_D, is linearly related to the incident light level. The measured voltage, V_D, is equal to the product of current and the value of the reference resistor, R_F, as shown in Equation 3-2.

$$V_D = -I_D \times R_F \Rightarrow |I_D| = \frac{V_D}{R_F}$$

Equation 3-2

Once the intensity measurement is performed, a normalised spectrum can be calculated. The electroluminescence spectrum of the sample, $T(\lambda)$, is measured with its intensity proportional to the number of photons emitted by the device, but the spectrum contains no information about the total number of photons emitted. A normalised spectrum, $S(\lambda)$, can be calculated from the intensity measurement and the electroluminescence spectrum. The integral of $S(\lambda)$ is equal to the total number of photons measured by the detector. A number of steps are involved in the calculation of $S(\lambda)$. The first of the steps is the correction for the wavelength response of the silicon photodiode. It corrects the measurement for the response of the silicon to photons of different energies.

Wavelength Response of a Silicon Photodiode

The responsivity ($R_D(\lambda)$ amps per watt) of a standard silicon photodiode is known and is shown as Figure 3-16 (data taken from RS data sheets F 232-3894).

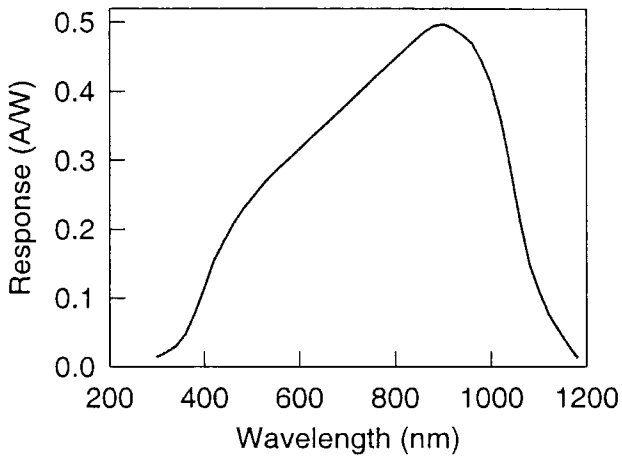

Figure 3-16 *Wavelength response of a silicon photodiode*

The wavelength response of the photodiode can be approximated, in the visible region of the spectrum, by a second order polynomial which is used in efficiency and absolute intensity calculations in the majority of cases (i.e. when the emission spectrum lies within a range of 440nm to 900nm). If a spectrum lies outside this range then a seventh order polynomial can be used. A seventh order polynomial is used as it is the lowest order polynomial to produce a reasonable fit to the response over the entire range of the response. The approximations to the data can be seen as Figure 3-17 (a) and (b).

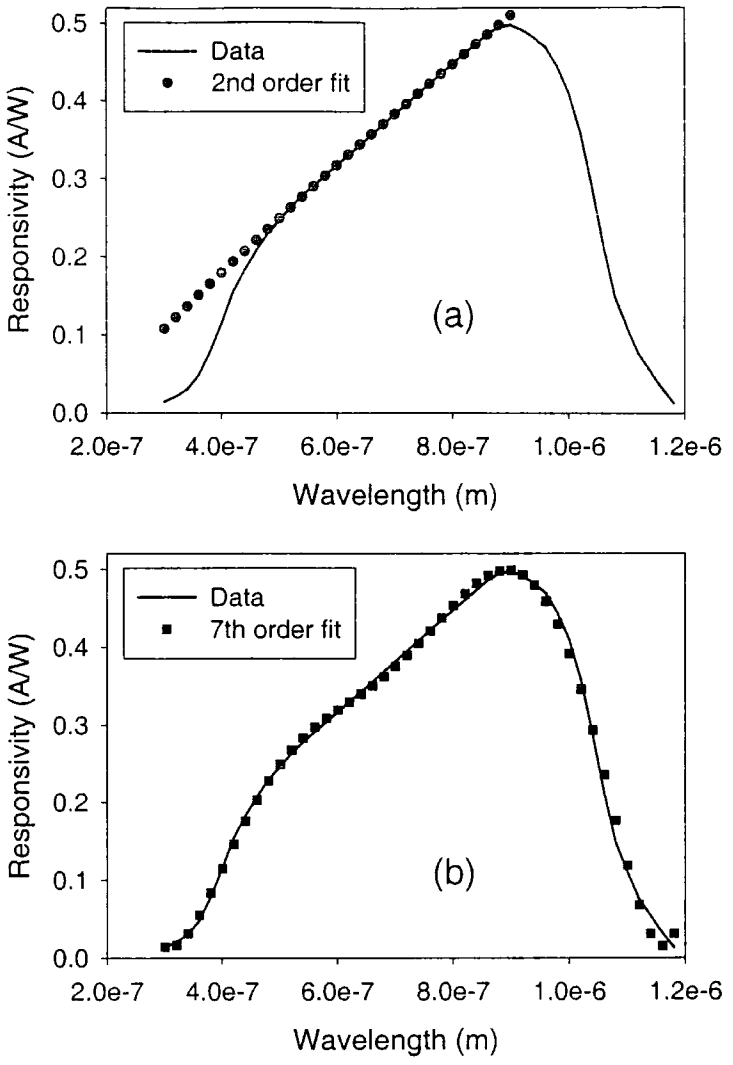

Figure 3-17 **(a)** *2nd order polynomial and* **(b)***7th order polynomial approximations to silicon photodiode response*

The equations used for these approximations are shown as Equations 3-3.

$$y_2 = -9.17965e10x^2 + 7.80834e5x - 0.119066$$

$$y_7 = 5.08611e43x^7 - 9.81884e37x^6 - 1.38876e32x^5 + 5.51266e26x^4 - 6.17115e20x^3 + 3.27231e14x^2 - 8.27777e7x + 7.99188$$

Equations 3-3

Spectra Normalisation

To calculate a spectrum with intensity proportional to amps, $A(\lambda)$, the measured spectrum, $T(\lambda)$ must be multiplied by the energy of a photon of a certain wavelength and also by the response of the photodiode as shown in Figure 3-16.

$$A(\lambda) = T(\lambda) \times R_D(\lambda) \times E(\lambda)$$

Equation 3-4

$E(\lambda)$ is the photon energy and is defined in Equation 3-5.

$$E(\lambda) = h\upsilon = \frac{hc}{\lambda}$$

Equation 3-5

A numerical factor, B, can then be used to normalise the spectrum with respect to the measured current (Equation 3-6). B is calculated from the rearrangement of Equation 3-6.

$$I_D = B\int_0^\infty A(\lambda)d\lambda$$

Equation 3-6

To calculate a normalised spectrum in terms of measured number of photons, $S(\lambda)$, it is necessary to convert from intensity in amps to intensity in number of photons (Equation 3-7).

$$S(\lambda) = \frac{B \times A(\lambda)}{R_D(\lambda) \times E(\lambda)}$$

Equation 3-7

Rearranging Equation 3-6 and using Equation 3-4 and Equation 3-5, Equation 3-7 becomes

$$\boxed{S(\lambda) = \frac{V_D T(\lambda)}{R_F hc}\left(\int_0^\infty \frac{T(\lambda)R_D(\lambda)}{\lambda}d\lambda\right)^{-1}},$$

Equation 3-8

and hence the total number of photons measured by the photodiode per second, L, is given by Equation 3-9.

$$\boxed{L = \int_0^\infty S(\lambda)d\lambda}$$

Equation 3-9

The calculation of S(λ) allows simpler calculation of other values (see for example Equation 3-16 and Equation 3-39).

EFFICIENCY CALCULATIONS

To calculate the quantum efficiency of the diodes it is necessary to make a correction for the light output in the forward direction. This correction arises because

the light output is measured in only a small cone of the total emission volume, in the forward direction. The emission from the diode is assumed to be Lambertian. Experimental evidence for Lambertian emission can be found in reference [5]. A Lambertian source has a flux (in terms of number of photons per unit area per second), measured normal to the diode, of F_0 and a flux at an angle θ to the normal of $F_0 cos(\theta)$ (Figure 3-18).

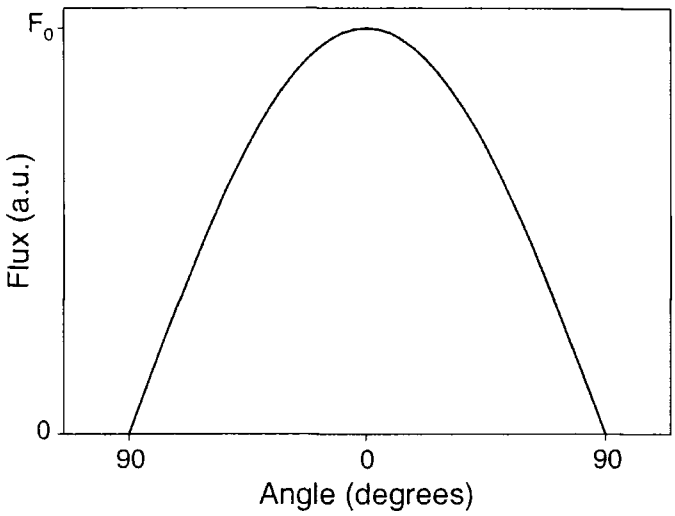

Figure 3-18 *Flux as a function of angle for a Lambertian source*

To correct for this, the following treatment is used (following Greenham *et al* [5]).

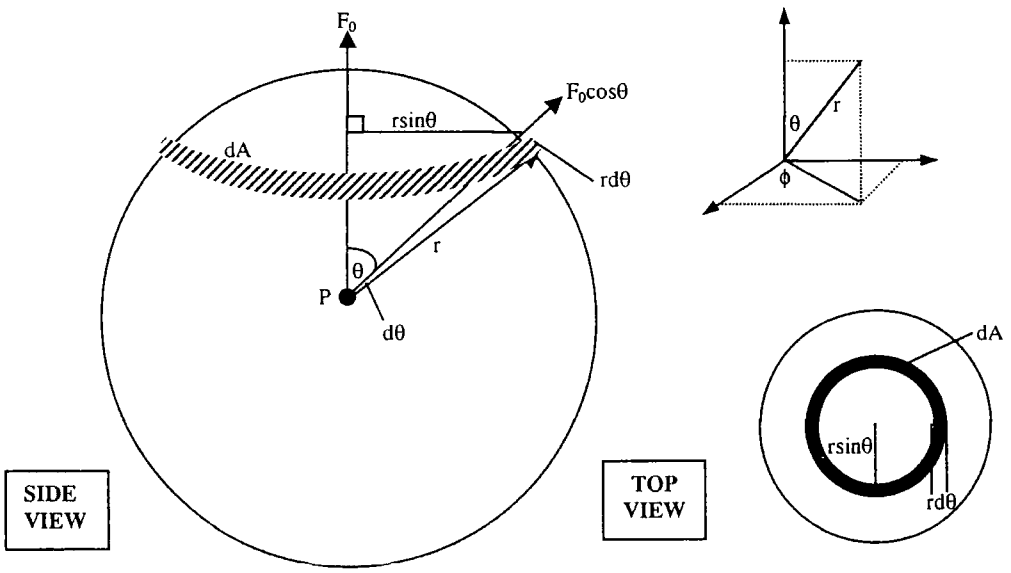

Figure 3-19 *Schematic of the Lambertian point source under consideration*

Consider a source, P, at the centre of a sphere radius r. The surface element dA is described by the rotation of the arc length $rd\theta$ around the polar co-ordinate ϕ, through 2π. The area dA is calculated for small $d\theta$ as the product of the arc length multiplied by the circumference of the circle, illustrated by the top view in Figure 3-19.

$$dA = 2\pi(r\sin\theta)rd\theta = 2\pi r^2\sin(\theta)d\theta$$

Equation 3-10

At $\theta=0$ radians, the flux is F_0.

Assuming Lambertian emission implies that at an angle θ to the normal, the flux $F(\theta) = F_0\ cos(\theta)$. To calculate the total number of photons in forward direction per second, F_T, the emission at an angle θ can be integrated over the forward hemisphere, using the surface element dA such that

$$F_T = \int_A F(\theta)dA = F_o\pi r^2\int_0^{\pi/2} 2\cos(\theta)\sin(\theta)d\theta .$$

Equation 3-11

Using $2\sin(\theta)\cos(\theta) = \sin(2\theta)$

$$F_T = F_0\pi r^2\int_0^{\pi/2}\sin(2\theta)d\theta = F_0\pi r^2\left[-\frac{1}{2}\cos(2\theta)\right]_0^{\pi/2}$$

$$\Rightarrow F_T = F_0\pi r^2$$

Equation 3-12

The experimental arrangement for measuring the light output is shown in Figure 3-20.

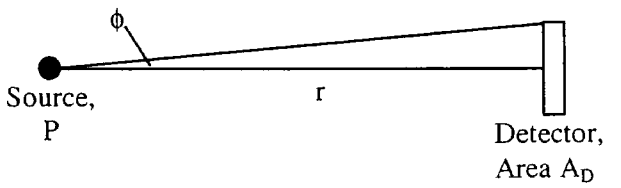

Figure 3-20 *Large distance approximation for LED measurement*

Assuming r is much lager than the area of the detector, L (number of photons incident on the detector, area A_D per second) is measured by the photodiode, but F_0 (the number of photons per unit area per second) is required for efficiency calculations.

So the flux $F_0 = \frac{L}{A_D}$

$$\Rightarrow F_T = \frac{\pi L r^2}{A_D} = \frac{\pi L}{\Omega} = \frac{\pi}{\Omega}\int_0^\infty S(\lambda)d\lambda,$$

Equation 3-13

where $\Omega = \frac{A_D}{r^2}$ is the solid angle of collection.

External Quantum Efficiency

The external quantum efficiency is defined as the ratio of the number of photons emitted in the forward direction to the number of injected charges.

$$E_{ext} = \frac{\text{Photons}_{emitted}}{\text{Charges}_{injected}}$$

Equation 3-14

The number of injected charges is given by

$$N_e = \frac{I_P}{e},$$

Equation 3-15

where e is the magnitude of the electronic charge on the electron (in coulombs) and I_P is the current injected into light emitting diode. So using Equation 3-14,
and Equation 3-15, we can show

$$E_{ext} = \frac{F_T}{N_e} = \frac{e\pi r^2 \int S(\lambda)d\lambda}{I_P A_D}$$

Equation 3-16

and

$$\boxed{E_{ext} = \frac{\pi e V_D}{R_F I_p \Omega hc}\int_0^\infty T(\lambda)d\lambda\left(\int_0^\infty \frac{T(\lambda)R_D(\lambda)}{\lambda}d\lambda\right)^{-1}}.$$

Equation 3-17

Due to the ratio V_D/I_p which appears in Equation 3-17, plots of measured intensity versus current produce a slope proportional to the efficiency of the device. This means that for identical spectral outputs, the ratios of the slopes of the current-intensity graphs are a measure of the ratios of the external quantum efficiencies of the devices. The higher the gradient of these curves, the higher the quantum efficiency, as illustrated in Figure 3-21.

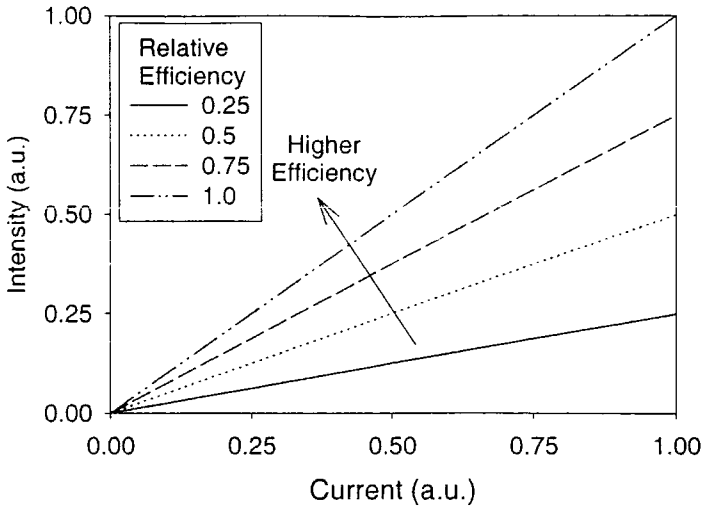

Figure 3-21 *Current-intensity curve illustrating efficiency relationship*

The calculation of external quantum efficiency is carried out using a Sigmaplot (Jandel Scientific graph plotting program) transform, Eext.xfm, shown in Appendix 1.

Internal Quantum Efficiency

Internal quantum efficiency is defined as the ratio of the number of photons created in the device to the number of charges injected into the device.

$$E_{\text{int}} = \frac{\text{photons}_{created}}{\text{charges}_{injected}}$$

Equation 3-18

The relationship between the internal and external efficiencies is shown in Equation 3-19.

$$E_{\text{int}} = 2n^2 \times E_{ext}$$

Equation 3-19

This relationship arises due to the following considerations (following Greenham *et al* [5]). Firstly the emission inside the polymer film is assumed to be isotropic.

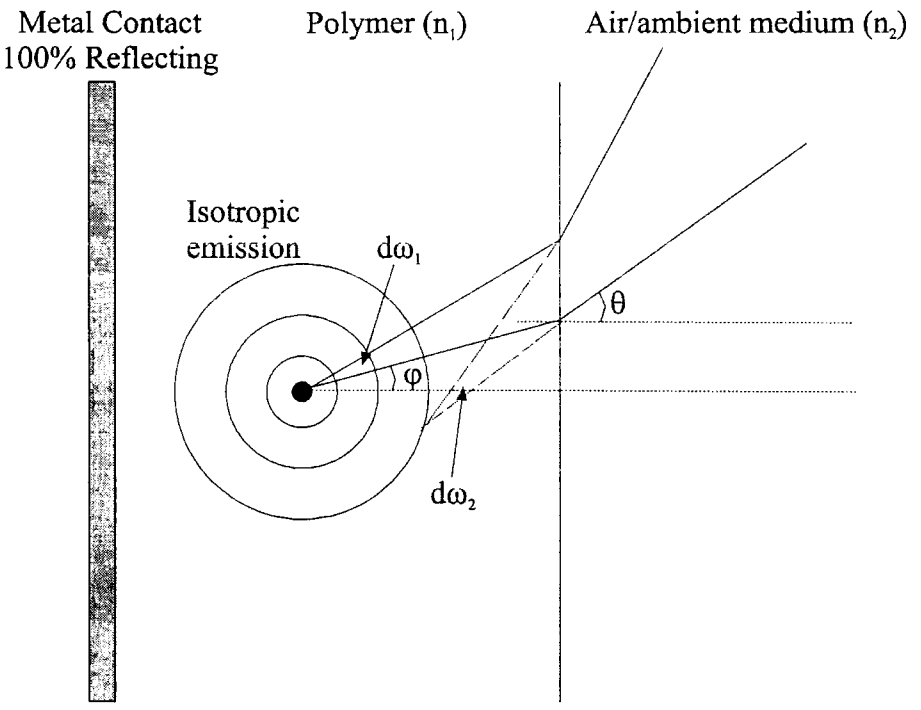

Figure 3-22 *Scheme of light emission inside a polymer film*

Using Snell's law,

$$n_1 \sin\varphi = n_2 \sin\theta ,$$

Equation 3-20 *Snell's Law*

assuming the refractive index of the ambient medium (n_2) is 1, setting $n_1=n$ and differentiating gives Equation 3-21.

$$n\cos\varphi d\varphi = \cos\theta d\theta$$

$$\frac{d\varphi}{d\theta} = \frac{\cos\theta}{n\cos\varphi}$$

Equation 3-21

Taking Snell's law, squaring both sides and using the identity $sin^2\varphi=1-cos^2\varphi$ we can obtain Equation 3-22.

$$n^2(1-\cos^2\varphi) = \sin^2\theta$$

$$\Rightarrow n\cos\varphi = (n^2 - \sin^2\theta)^{\frac{1}{2}}$$

Equation 3-22

Combining Equation 3-21 and Equation 3-22 gives Equation 3-23.

$$\frac{d\varphi}{d\theta} = \frac{\cos\theta}{\sqrt{n^2 - \sin^2\theta}}$$

Equation 3-23

Considering the 3-dimensional system and using the equation relating a solid angle to a plane angle (in spherical polar co-ordinates, using dγ rather than dθ as a co-ordinate) gives

$$d\Omega_1 = \sin\varphi d\varphi d\phi$$
$$d\Omega_2 = \sin\theta d\theta d\phi \text{'}$$

Equation 3-24

and using Snell's law again gives Equation 3-25.

$$\frac{d\Omega_1}{d\Omega_2} = \frac{d\varphi d\phi}{nd\theta d\phi}$$
$$= \frac{\cos\theta}{n\sqrt{n^2 - \sin^2\theta}}$$

Equation 3-25

We measure light only in the forward direction such that θ=0°, which simplifies Equation 3-25.

$$\frac{d\Omega_1}{d\Omega_2} = \frac{1}{n^2}$$
$$\Rightarrow d\Omega_2 = n^2 \times d\Omega_1$$

Equation 3-26

The metal contact is assumed to be 100% reflecting such that any light at θ=0° or θ=180° is detected at the detector, hence a factor ½ is used in Equation 3-27. If the light detected per steradian is equal to L/Ω (where L is the number of photons incident on the detector per second) then the number of photons emitted in total over 4π steradians of isotropic emission inside the polymer layer, F'_{int} is found to be

$$F'_{\text{int}} = \frac{4\pi}{2} L = 2\pi L .$$

Equation 3-27

Finally, we make the correction for the modification of the size of the solid angle caused by refraction at the polymer/ambient interface. This refraction causes the flux per solid angle measured outside the polymer to be smaller than inside as the solid angle is a factor n^2 larger (Equation 3-26). If we set $d\Omega_2=\Omega$ and use Equation 3-26 and Equation 3-27, we get Equation 3-28.

$$F_{\text{int}} = \frac{2\pi L}{d\Omega_1} = \frac{2\pi n^2 L}{d\Omega_2} = 2n^2 \times \frac{\pi L}{\Omega}$$

Equation 3-28

Comparing Equation 3-13 and Equation 3-28 the relationship between internal and external measurements can be seen.

$$F_{\text{int}} = 2n^2 \times F_T$$
$$E_{\text{int}} = 2n^2 \times E_{ext}$$

Equation 3-29

The relationship between internal quantum efficiency and the measurements performed is shown in Equation 3-30.

$$E_{\text{int}} = \frac{2n^2 \pi e V_D}{R_F I_p \Omega hc} \int_0^\infty T(\lambda) d\lambda \left(\int_0^\infty \frac{T(\lambda) R_D(\lambda)}{\lambda} d\lambda \right)^{-1}$$

Equation 3-30

Both internal and external efficiencies are expressed as a ratio or as a percentage.

Power Efficiency

The power efficiency is commonly expressed as intensity (Lumens) of light emitted per watt of electrical power used by the light emitting diode as shown in Equation 3-31.

$$E_{pow} = \frac{Int(lm)}{I_P V_P}$$

Equation 3-31

V_P is the voltage across light emitting diode and *Int* is the light intensity in lumens.

RADIOMETRIC AND PHOTOMETRIC UNITS

Conversion of Measured Voltage to Watts

It is possible to convert the normalised emission spectrum, S(λ), to a spectrum with intensity in watts, P(λ) as shown in Equation 3-32. Hence the total number of watts detected by the photodiode, *P*, is the integral of P(λ).

$$P(\lambda) = S(\lambda) \times E(\lambda)$$

Equation 3-32

$$P = \int_0^\infty P(\lambda) d\lambda = \int_0^\infty S(\lambda) E(\lambda) d\lambda$$

Equation 3-33

Combining Equation 3-5,Equation 3-8, Equation 3-32 and Equation 3-33 produces Equation 3-34.

$$P(watts) = \frac{V_D}{R_F}\int_0^\infty \frac{T(\lambda)}{\lambda}d\lambda\left(\int_0^\infty \frac{T(\lambda)R_D(\lambda)}{\lambda}d\lambda\right)^{-1}$$

Equation 3-34

For emission at one wavelength, the conversion is much simpler.

$$P(watts) = \frac{I_D}{R_D} = \frac{V}{R_F R_D}$$

Equation 3-35

Conversion of Watts to Candela

The equation given by the National Institute for Science and Technology for the candela [6, 7] is given in Equation 3-36.

$$Int = K_m\int_0^\infty C(\lambda)L(\lambda)d\lambda\,,$$

Equation 3-36

where K_m is the CIE defined "maximum spectral luminous efficacy of radiation for photopic vision" and has a value of 683.002 lumens per watt. L(λ) is the emission spectrum of the source with intensity measured in Watts per (metre cubed steradian) (W m^{-3} sr^{-1}).

C(λ) is the *photopic relative luminous efficiency function* and it gives the ratio of the radiant flux at wavelength λ_m to that at wavelength λ, so that the two fluxes produce the same photopic luminous sensations under specified photometric conditions. The data were obtained from reference [8]. λ_m is chosen so that the maximum value of this ratio is unity. The variation of this function with wavelength is shown in Figure 3-23 as the solid line. The fit to this data is shown as the shaded triangles and can be approximated using two Gaussian functions with different parameters for wavelengths less than or greater than 555nm. The equation used is shown as Equation 3-37 and the parameters are shown in Table 3-1.

$$C(\lambda) = a \times \exp\left[-\frac{1}{2}\left(\frac{\lambda - b}{c}\right)^2\right]$$

Equation 3-37

Parameters	$\lambda \leq 555$ nm	$\lambda > 555$ nm
a	1.00	1.00
b	5.5163×10^{-7}	5.5880×10^{-7}
c	3.5761×10^{-8}	4.3678×10^{-8}

Table 3-1 *Parameters used in Equation 3-37 to produce approximation to CIE data*

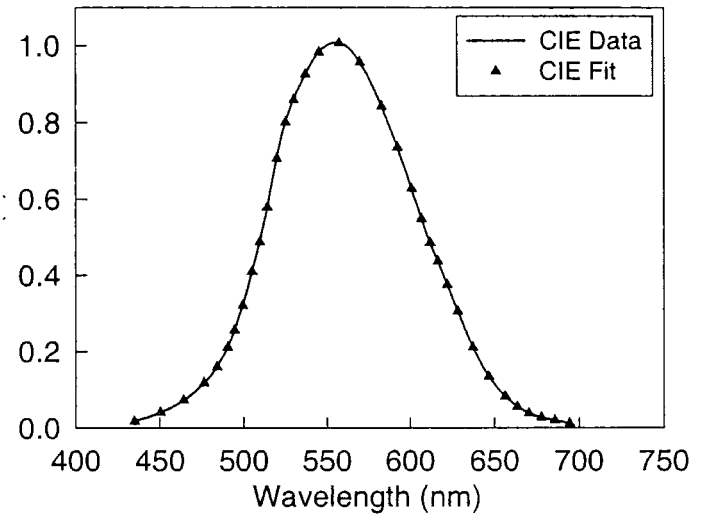

Figure 3-23 *CIE Photopic Response Curve*

The correction needed to convert from an emission spectrum with intensity measured in watts, P(λ), to a number of candela per square metre is shown in Equation 3-38. A_P is the area of the light emitting diode.

$$Int = \frac{K_m}{A_P \Omega} \int_0^\infty P(\lambda) C(\lambda) d\lambda$$

Equation 3-38

Using Equation 3-5,Equation 3-8, Equation 3-32 and Equation 3-38 gives Equation 3-39 and Equation 3-40 which show how the intensity in candela per square metre can be calculated from the measured data.

$$Int = \frac{K_m}{A_P \Omega} \int_0^\infty S(\lambda) E(\lambda) C(\lambda) d\lambda$$

Equation 3-39

$$Int = \frac{K_m V_D}{R_F A_P \Omega} \int_0^\infty \frac{T(\lambda) C(\lambda)}{\lambda} \left(\int_0^\infty \frac{T(\lambda) R_D(\lambda)}{\lambda} d\lambda \right)^{-1} d\lambda$$

Equation 3-40

The calculation of brightness and power efficiency is carried out by a Sigmaplot transform, candela.xfm, shown in Appendix 2.

Conversion of Candela to Lumens

D. A. Roberts, in The Photonics Design and Applications Handbook [9] describes the difference between the candela and the lumen. "The nuisance factor is π, which comes about because a Lambertian source with a luminance of 1cd/cm^2 has a luminous emittance of π lm/cm^2." Hence for conversion from candela per square metre to lumens, a factor πA_P must be used as shown in Equation 3-41.

$$Int(lm) = Int(cd / m^2) \times A_p \times \pi$$

Equation 3-41

CALIBRATION AND CROSS-CHECK

The photodiode and amplifier were calibrated and checked for linearity. The 514nm line from an argon ion laser was used in conjunction with a number of neutral density filters to vary the amount of light incident on the photodiode. A calibrated photodiode was used in an identical experimental set-up in order to calibrate the large area photodiode at a range of incident intensities. A full account of the calibration and linearity check can be found in Appendix 3. A calibration equation was obtained from this experiment and was used in each calculation, both for brightness and efficiency calculations.

A further cross-check was provided by a Minolta LS100 luminance meter. Several inorganic LEDs with a range of spectral outputs were used to cross-check the calculated brightness values (using the large area photodiode measurements in conjunction with spectral measurements of the LEDs) to those measured by the Minolta LS100. Several organic LEDs were also compared. The results are summarised for the inorganic LEDs and a ITO/PPV/Ca device in Figure 3-24. A detailed treatment of this cross-check can be found in Appendix 4.

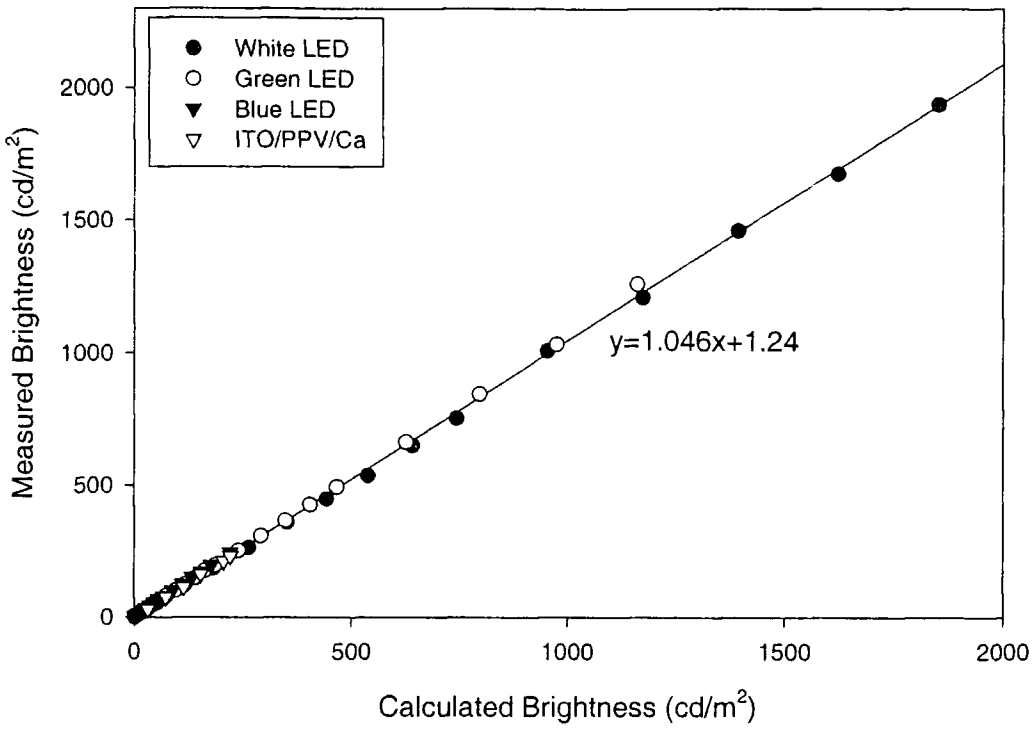

Figure 3-24 *Brightness of some LEDs measured by a luminance meter and calculated from intensity measurements by a photodiode. The line is a linear regression with coefficients shown.*

CHROMATICITY CO-ORDINATES

Three main definitions are required to understand the theory of colour co-ordinates. *Color Science* by Wyszecki and Stiles [8] contains definitions for colour, tristimulous values and chromaticity co-ordinates. "Color is that characteristic of a visible radiant energy by which an observer may distinguish differences between two structure-free fields of the same size and shape, such as may be caused by differences in the spectral composition of the radiant energy concerned in observation". Colour in this sense is *psychophysical colour* and is specified by the tristimulous values of the radiant energy entering the eye. "Tristimulous values of a color (or light) are the amounts of the three reference lights (matching stimuli, primary colors) required to give by additive mixture a match with the color (or light) considered". "The chromaticity co-ordinates of a color are the ratios of each tristimulous value of the color to their sum"[8].

Colour co-ordinates are useful as they allow a simple but accurate visual comparison of colours. Once the co-ordinates of a source are known, it is then possible to state accurately and compare its colour and calculate the co-ordinates of other coloured sources needed to produce various colours.

X, Y, Z Co-ordinates

A commonly used system of chromaticity co-ordinates is the 1931 CIE-(**X**,**Y**,**Z**) system of colour specification. This system uses three colour matching functions, $\bar{x}_\lambda, \bar{y}_\lambda$ and $\bar{z}_\lambda$ shown in Figure 3-25. The data were obtained from reference [8].

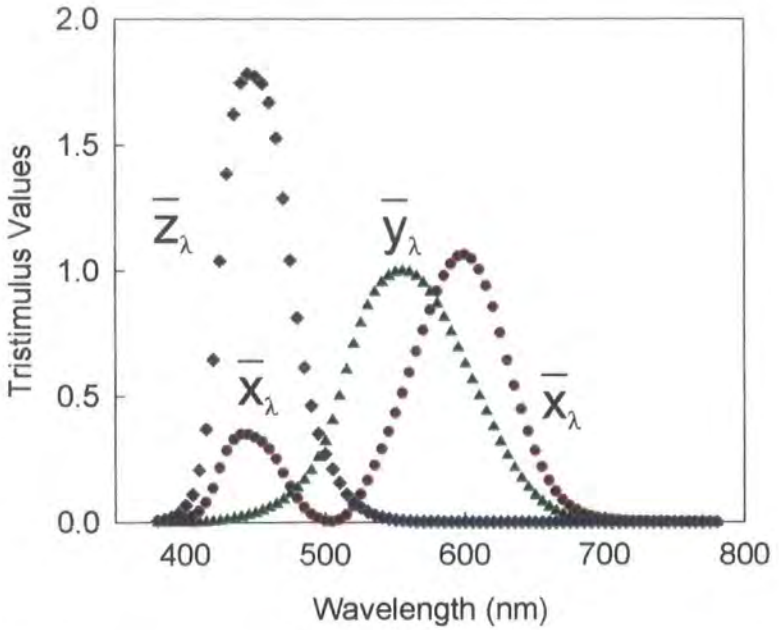

Figure 3-25 *CIE colour matching functions for x,y,z colour*

This scheme produces a 3-dimensional *x,y,z* colour space which is shown as Figure 3-26.

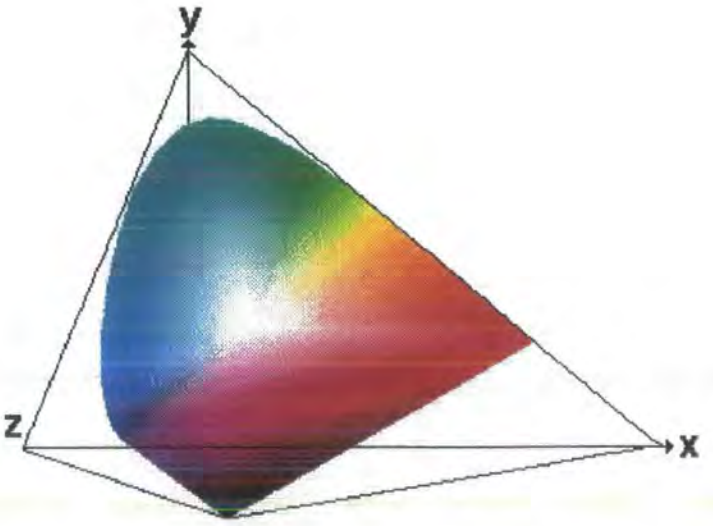

Figure 3-26 *3-dimensional x,y,z colour space (modified from reference [10])*

This 3-dimensional space can be mapped onto 2-dimensions without any loss of information through the relation $x+y+z=1$. This 2-dimensional scheme can be seen in Figure 3-27. It illustrates the relation between the co-ordinates and the colour they represent.

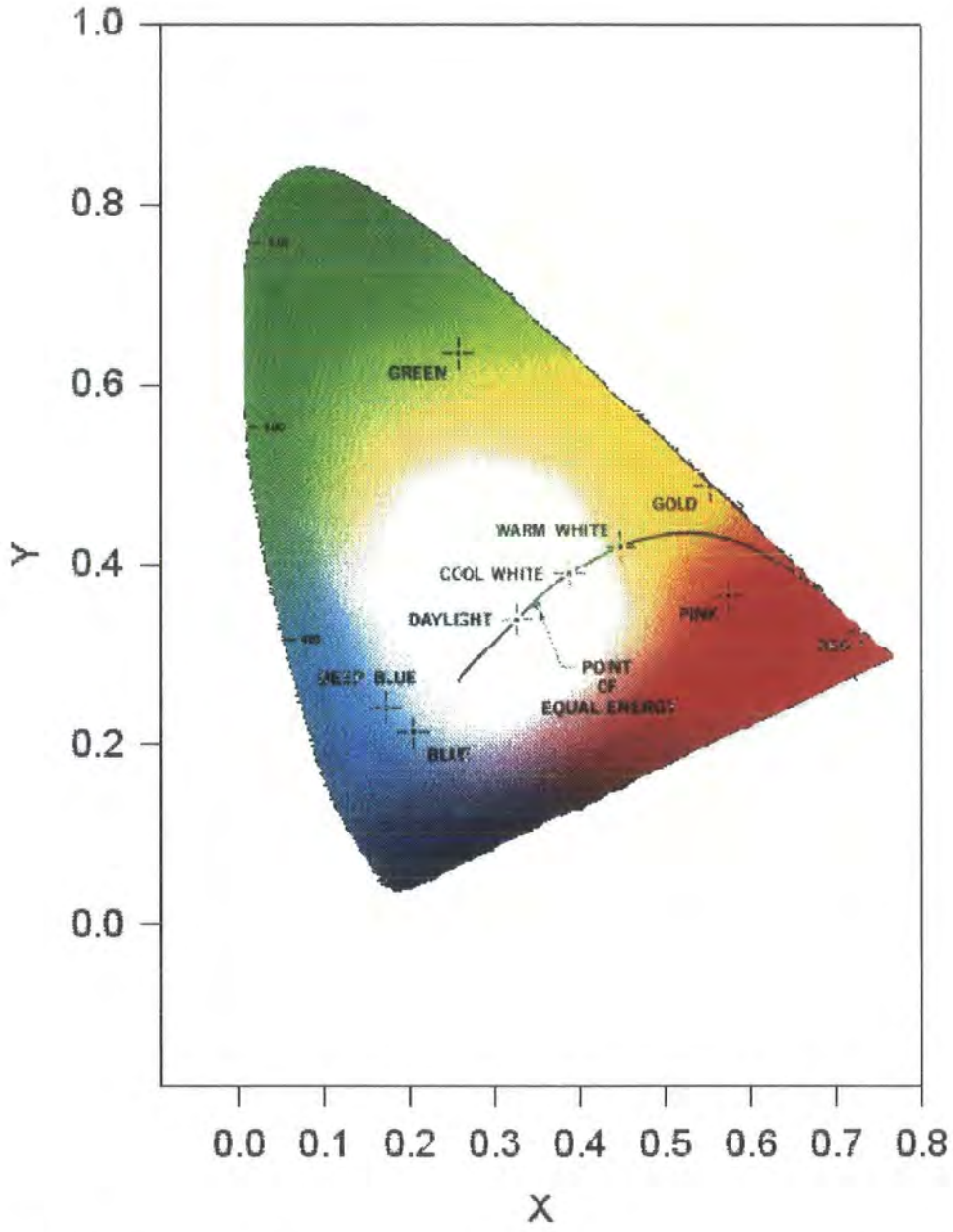

Figure 3-27 *2-dimensional representation of x,y colour space (from reference [10])*

The x,y,z values for a particular source can be calculated as follows. Firstly, the X,Y,Z primaries of the source can be calculated from Equations 3-42. $T'(\lambda)$ is the measured spectrum divided by lambda to produce intensity proportional to energy rather than number of photons. k is a constant and can be any value, although it is

commonly chosen so that the Y value will equal 100. If the measurement of $T'(\lambda)\Delta\lambda$ is absolute in watts then k can be set equal to K_m, and the value of Y gives the luminous flux of the source, measured in lumens [8].

$$X = k\sum_{\lambda} T'(\lambda)\bar{x}_{\lambda}\Delta\lambda \approx k\int_{\lambda} T'(\lambda)\bar{x}_{\lambda}d\lambda$$
$$Y = k\sum_{\lambda} T'(\lambda)\bar{y}_{\lambda}\Delta\lambda \approx k\int_{\lambda} T'(\lambda)\bar{y}_{\lambda}d\lambda$$
$$Z = k\sum_{\lambda} T'(\lambda)\bar{z}_{\lambda}\Delta\lambda \approx k\int_{\lambda} T'(\lambda)\bar{z}_{\lambda}d\lambda$$

Equations 3-42

The x,y,z values can then be calculated using Equations 3-43. They are expressed as (x,y,z), but the z value is often omitted and hence the values are quoted as (x,y).

$$x = \frac{X}{(X+Y+Z)}, y = \frac{Y}{(X+Y+Z)}, z = \frac{Z}{(X+Y+Z)}$$

Equations 3-43

The calculation of x,y,z colour co-ordinates is performed by a Sigmaplot transform, xyz.xfm, listed in Appendix 5.

R, G, B Co-ordinates

It is possible to define a colour in several colour schemes. Another of the major schemes is the 1931 CIE-(R,G,B) system. This scheme produces 3 perpendicular colour axes, the tristimulous values of each describe the amount of red, green and blue in a colour as illustrated in Figure 3-28 (note that the view angle is different in the two diagrams).

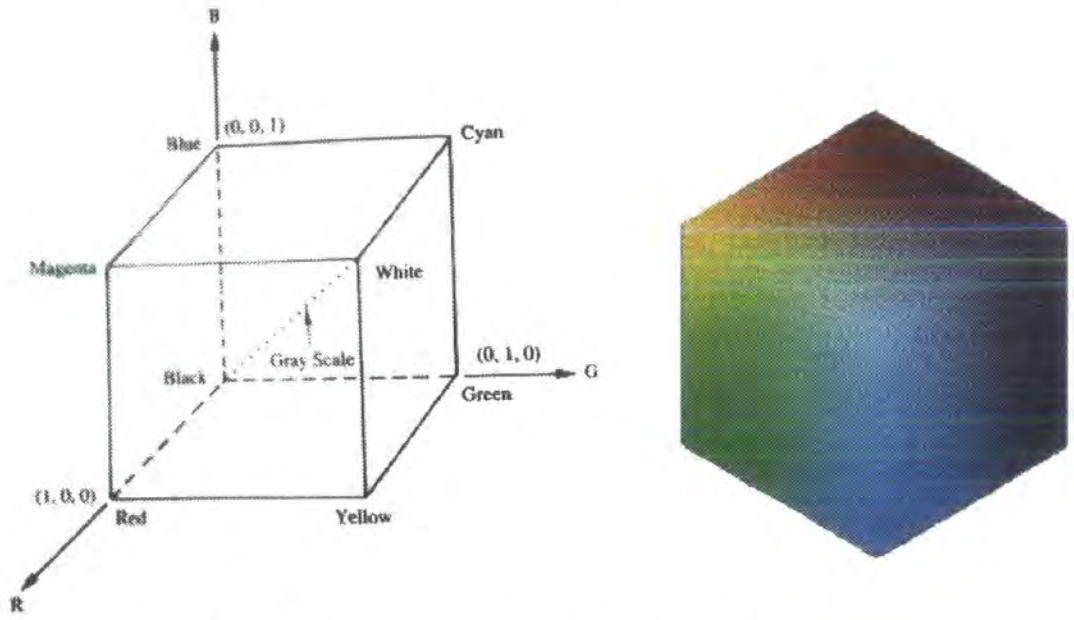

Figure 3-28 *CIE-(R,G,B) system (modified from reference [10])*

This system uses equations very similar to those shown for the CIE-(X,Y,Z), but the colour matching functions are different and are denoted $\bar{r}_\lambda, \bar{g}_\lambda$ and $\bar{b}_\lambda$. The corresponding chromaticity co-ordinates are (r,g,b), although due to the relation $r+g+b=1$, the b value is often omitted.

Conversion between Co-ordinate Systems

It is possible to convert between the colour systems using the projective transformations, shown as Equations 3-44 and Equations 3-45. This is useful as although the CIE (X,Y,Z) colour systems is widely used, RGB and other systems are also frequently used. The ability to convert between different colour systems is therefore useful not just for comparison, but also it is often easier to visualise colour changes from co-ordinate values in the RGB rather than the XYZ system.

$$r = \frac{2.36461x - 0.89654y - 0.46807z}{1.85464x + 0.51546y + 0.62989z},$$

$$g = \frac{-0.51517x + 1.42641y + 0.08876z}{1.85464x + 0.51546y + 0.62989z},$$

$$b = \frac{0.00520x - 0.01441y + 1.00920z}{1.85464x + 0.51546y + 0.62989z}.$$

Equations 3-44

$$x = \frac{0.49000r + 0.31000g + 0.20000b}{0.66697r + 1.13240g + 1.20063b},$$
$$y = \frac{0.17697r + 0.81240g + 0.01063b}{0.66697r + 1.13240g + 1.20063b},$$
$$z = \frac{0.00000r + 0.01000g + 0.99000b}{0.66697r + 1.13240g + 1.20063b}$$

Equations 3-45 *(from reference [8])*

It is possible to construct these equations from transformation data of the primaries of the system. For example if transforming to a new set of primaries (**J**, **K**, **L**) from (**R**, **G**, **B**), it is usually possible to find a matrix transformation as shown in Equation 3-46. If we call **A** the transformation matrix (a_{11}, a_{12} etc) then the corresponding transform for (**R**, **G**, **B**) from (**J**, **K**, **L**) will use the inverse of matrix **A**, which shall be denoted **B**, such that $\mathbf{A}^{-1}=\mathbf{B}$. It is then possible to construct a transform equation to calculate chromaticity co-ordinates as shown in Equations 3-47.

$$\begin{pmatrix} J \\ K \\ L \end{pmatrix} = \begin{pmatrix} a_{11} & a_{12} & a_{13} \\ a_{21} & a_{22} & a_{23} \\ a_{31} & a_{32} & a_{33} \end{pmatrix} \begin{pmatrix} R \\ G \\ B \end{pmatrix}$$

Equation 3-46

$$j = \frac{a_{11}r + a_{12}g + a_{13}b}{(a_{11} + a_{21} + a_{31})r + (a_{12} + a_{22} + a_{32})g + (a_{13} + a_{23} + a_{33})b},$$
$$k = \frac{a_{21}r + a_{22}g + a_{23}b}{(a_{11} + a_{21} + a_{31})r + (a_{12} + a_{22} + a_{32})g + (a_{13} + a_{23} + a_{33})b},$$
$$l = \frac{a_{31}r + a_{32}g + a_{33}b}{(a_{11} + a_{21} + a_{31})r + (a_{12} + a_{22} + a_{32})g + (a_{13} + a_{23} + a_{33})b}.$$

Equations 3-47

To produce the conversion from (j, k, l) to (r, g, b) requires the substitution of a_{xy} to b_{xy} where b_{xy} is a matrix element in the inverse matrix **B**.

CAPACITANCE VOLTAGE MEASUREMENTS

Capacitance-voltage measurements were carried out using a Keithley 595 Quasi Static CV meter. The device is held in a matrix of sprung gold pins, making electrical connections in the same manner as in the case of electroluminescence, above. The sample and holder are held inside a self-made, electrically shielded metal switching

box. The meter is controlled via IEEE, using a self-written computer program. This produces capacitance-voltage data in ASCII, comma delimited format. These measurements assume Schottky barrier formation and can provide valuable insight into the barrier depletion width and carrier concentration in polymer LEDs.

The capacitance per unit area, C_d, is related to the applied voltage, V, by the Mott-Schottky relation.

$$C_d^{-2} = \left(\frac{2}{q\varepsilon\varepsilon_0 N_A} \right) (V_{SO} - V)$$

Equation 3-48

N_A is the acceptor density, ε is the permittivity of the polymer and V_{SO} is the contact potential difference between the metal and the semiconductor. Hence the doping density of the device can be obtained by producing Mott-Schottky plots of C_d^{-2} versus applied voltage. The contact potential difference, V_{SO}, is obtained from the intercept of the tangent to the data with the abscissa. The acceptor density is then obtained from the Mott-Schottky relation (Equation 3-48), and the width of the depletion layer is calculated using Equation 3-49.

$$w = \sqrt{\frac{2\varepsilon\varepsilon_0 (V_{SO} - V)}{qN_A}}$$

Equation 3-49

A graphical representation of these terms can be seen in Figure 2-39.

REFERENCES

[1] T. Yamamoto, et al., J. Am. Chem. Soc., **116** , (1994), 4832-4845.

[2] N. C. Greenham, I. D. W. Samuel, G. R. Hayes, R. T. Phillips, Y. A. R. R. Kessener, S. C. Moratti, A. B. Holmes and R. H. Friend, Chem. Phys. Lett., **241** , (1995), 89-96.

[3] J. D. E. Beynon and D. R. Lamb, *Charge-coupled devices and their applications* (McGraw-Hill Book Company (UK) Limited, London, 1980).

[4] A. I. Burshteyn, *Semiconductor Thermoelectric devices*, 1st ed. (Temple Press Books Ltd., London, 1964).

[5] N. C. Greenham, R. H. Friend and D. D. C. Bradley, Adv. Mat., **6** , 6 (1994), 491-494.

[6] Y. Ohno and G. Sauter, J. Res. Natl. Stand. Technol., **100** , 3 (1995), 227-239.

[7] R. A. Nelson and L. Ruby, Metrologia, **30** , (1993), 55-60.

[8] G. Wyszecki and W. S. Stiles, *Color Science*, 1 ed. (John Wiley & Sons, Inc., 1967).

[9] D. A. Roberts, in *The Photonics Design and Applications Handbook 1993* (1993), p. H68-H71.

[10] Davis, from http://cs.fit.edu/courses/cse4255/cse5255/davis/text.html

Chapter 4 Optical Measurements of Single Polymer Layers

INTRODUCTION

This chapter presents results of optical measurements of the polymers used in polymer light-emitting diodes in subsequent chapters. Chapter 2 describes the link between photoluminescence and electroluminescence in conjugated polymer systems and hence these measurements are very important to the study of polymer light-emitting diodes.

In this chapter, the absorption and emission processes of polypyridine are investigated, and the differences in the optical spectra of PPY solution, film and powder samples are explored. The possibility of batch-to-batch variation of polypyridine is also investigated using optical, molecular weight, electron-spin resonance and chemical analysis. The effect of changing the chemical structure of polypyridine by the addition of side groups, the formation of copolymers and changing the bond configuration are also explored.

The conversion process of precursor route poly(*p*-phenylene vinylene) and poly(2-methoxy, 5-(2'ethyl-hexyloxy)-*p*-phenylene vinylene) is examined by optical spectroscopy. The conversion of these polymers on quartz substrates is compared to the conversion on indium tin oxide covered substrates, which is an essential part of light-emitting diode fabrication.

Measurement of photoluminescence spectra using a mercury arc lamp as the excitation source facilitated the excitation of the majority of samples in this study at the peak of their absorption. In addition to the standard photoluminescence spectrum, in the majority of cases, the excitation wavelength was varied over a considerable range of the absorption of the sample whilst a real time measurement of the spectrum was performed. This means that any spectral variation caused by absorption of different species should be identified.

POLYPYRIDINE

Polypyridine is more correctly referred to as poly(2,5-pyridinediyl). It is *para* linked, with the polymer linking through the 2 and 5 position on the ring. It can therefore be distinguished from the polymer linking through the 2 and 6 positions in the *meta* position or poly(2,6-pyridinediyl). In this work, the *para* linked polymer is referred to as polypyridine, PPY or P*p*PY. The meta linked polymer is referred to as poly(*m*-pyridine) or P*m*PY. The chemical structures of these polymers are shown in Figure 4-1.

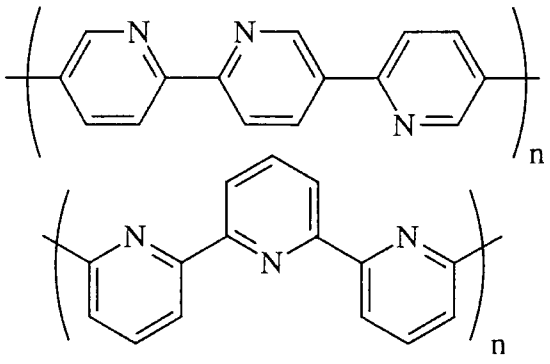

Figure 4-1 *Chemical structure of a) poly(p-pyridine) and b) poly(m-pyridine)*

Polypyridine (PPY) is a yellow powder readily soluble in formic acid and soluble to a lesser degree in hydrochloric and dichloroacetic acids. The solvent has an effect on the properties of the film, for example the photoluminescence of a film spun from a solution of dichloroacetic acid has a 4nm blue shift compared to the films cast from formic and hydrochloric acids (Figure 4-2). Films of polypyridine were mostly prepared from formic acid solution due to the superior film formation. Additionally, the solubility of PPY is considerably higher in formic acid than in hydrochloric acid.

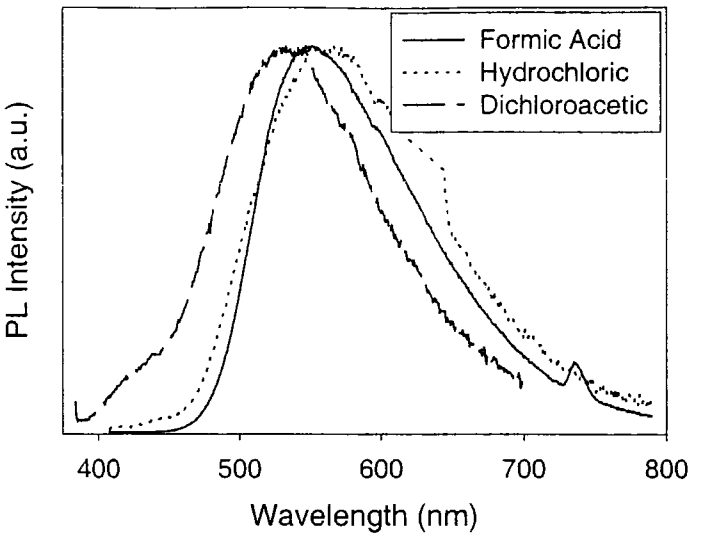

Figure 4-2 *Photoluminescence spectrum of polypyridine films cast from solutions of hydrochloric (dotted line), dichloroacetic (broken line) and formic (solid line) acids*

ABSORPTION AND EMISSION OF POLYPYRIDINE

Solution

The absorption and photoluminescence (PL) spectra of polypyridine (batch ER196) in formic acid solution are shown in Figure 4-3.

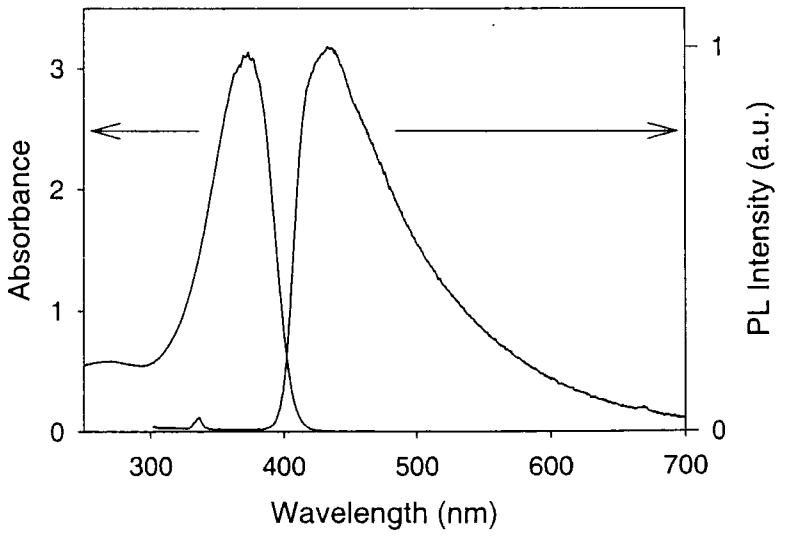

Figure 4-3 *Absorption and photoluminescence of polypyridine solution in formic acid (on a wavelength scale)*

The peak of absorption is at 374nm with a full width at half maximum (FWHM) of 55nm. The peak of photoluminescence in solution is 434nm, and the photoluminescence is quite broad, around 90nm FWHM. This emission is in the blue region of the spectrum. The mirror image relationship expected from absorption and luminescence spectra can be more readily identified using an energy scale. Above 5eV, the absorption of the formic acid masks the absorption of the polypyridine.

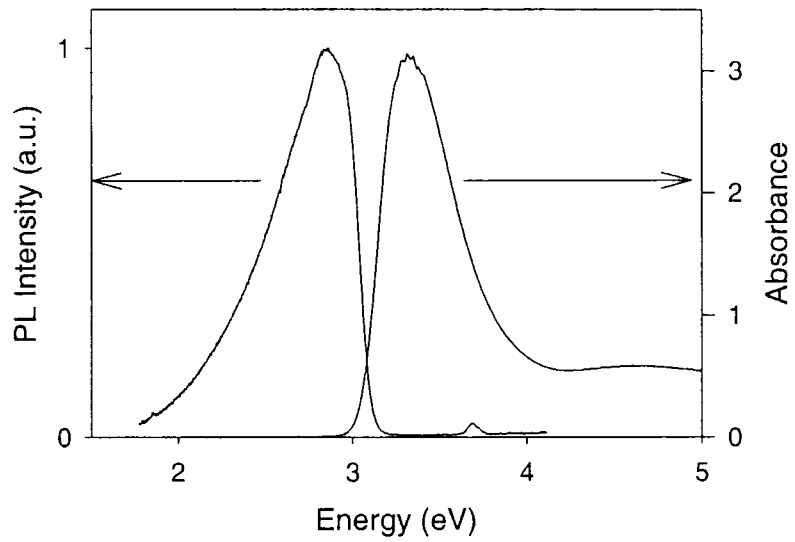

Figure 4-4 *Photoluminescence and absorption spectra of polypyridine in formic acid solution (on an energy scale)*

On an energy scale, the absorption and photoluminescence spectra look very similar, as expected. The peak of the absorption is at 3.32eV and the peak of the emission is at 2.86eV. There is an apparent Stokes shift, measured as the difference between the peak of the absorption and the peak of the luminescence, of 0.46eV (60nm). The FWHM of the peaks on the (linear) energy scale are similar, 0.58eV for absorption and 0.65eV for photoluminescence.

Film

The absorption and photoluminescence spectra of polypyridine film are shown in Figure 4-5.

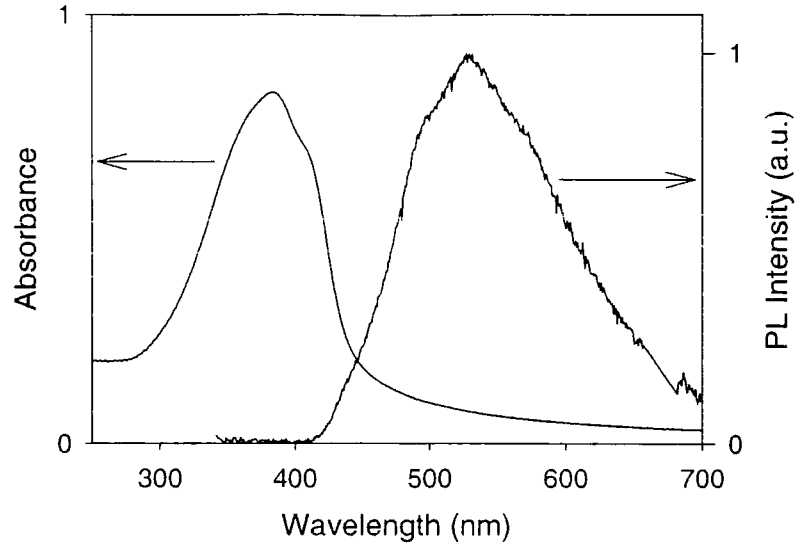

Figure 4-5 *Absorption and photoluminescence of polypyridine film (on a wavelength scale)*

The peak of absorption is at 384nm with a full width at half maximum of 102nm. The peak of the film photoluminescence is 527nm, and the emission is quite broad, around 135nm FWHM. This emission is in the green/yellow region of the spectrum. The mirror image relationship expected from absorption and luminescence spectra can again be observed more readily on an energy scale.

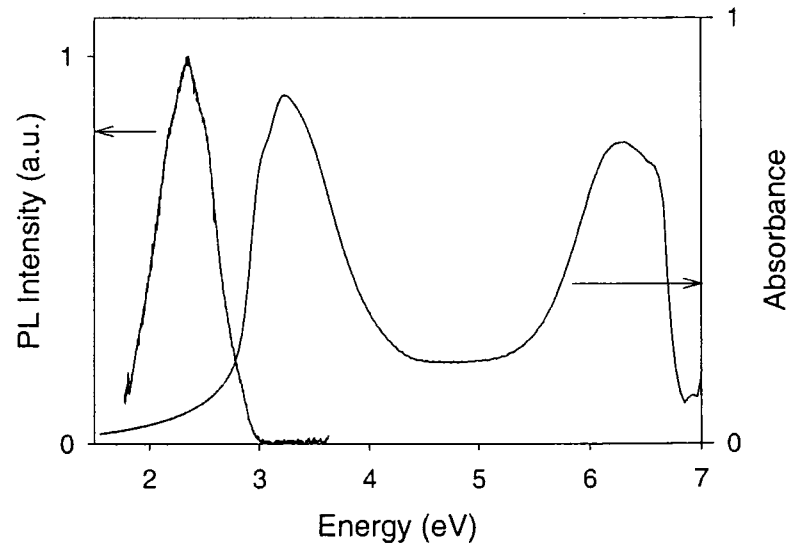

Figure 4-6 *Absorption and photoluminescence of polypyridine film (on an energy scale)*

The absorption and photoluminescence spectra again look very similar. The peak of the (lower energy) absorption is 3.23eV and the peak of the emission is 2.35eV. The apparent Stokes shift, is found to be 0.88eV (143nm). The FWHM of the

absorption is actually larger than that of the emission, 0.92eV FWHM for absorption and 0.58eV FWHM for emission. There is also evidence of vibronic structure on the absorption and emission curves. The absorption and PL of PPY batch 196 in solution and film is shown in Figure 4-7.

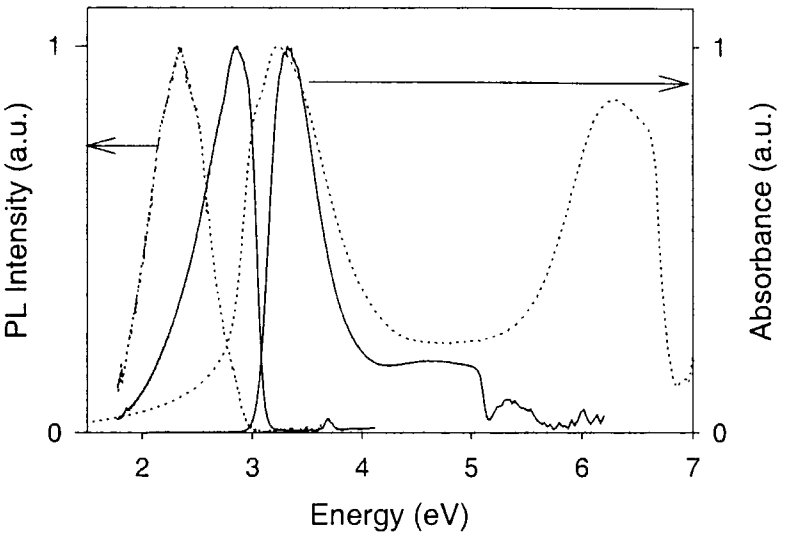

Figure 4-7 *Absorption and emission spectrum of PPY solution (solid line) and film (broken line)*

The 0.5eV difference in the energy of the emission in solution (2.86eV) and film (2.35eV) produces a large difference in the colour of the photoluminescence. This can be illustrated on a CIE-(x,y) colour co-ordinate diagram (Figure 4-8). The co-ordinates of the emission are (x,y,z) (0.19, 0.17, 0.63) for solution and (0.31, 0.46, 0.23) for film. The colour difference can be more readily identified using rgb co-ordinates. In the RGB system, the co-ordinates are (0.00, 0.24, 0.76) for solution and (0.24, 0.53, 0.24) for film. So it is clear from these values that there is a considerable drop in the relative blue content of the emission (0.76 to 0.24) and an increase in the relative green content (0.24 to 0.53).

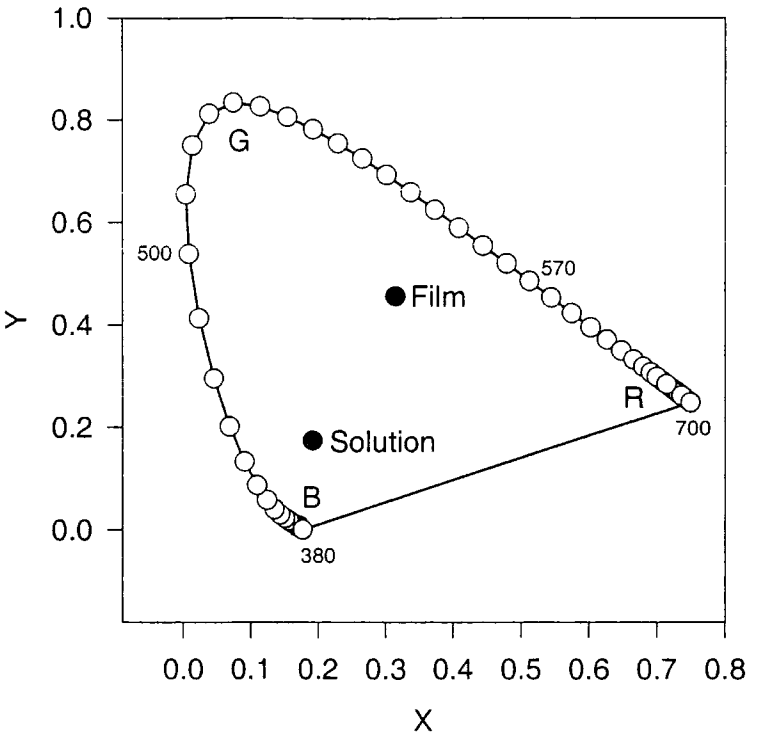

Figure 4-8 *Colour co-ordinate diagram for polypyridine photoluminescence in solution and film*

Gebler *et al* in reference [1] measure the peak of emission in PPY film as 2.35eV, identical to that measured above. The peak of the film absorption in their work is at 3.35eV, similar to the 3.23eV found in the present work. Blatchford *et al* [2] find the absorption and emission peaks of dilute solution arise at 3.35eV and 2.95eV, marginally higher than the 3.32eV and 2.86eV found in this work. Yamamoto *et al* [3] find a photoluminescence peak at 2.82eV in dilute solution, similar to the 2.86eV found in this work. The peak of the film emission is found to be 550nm (2.25eV) in a solution cast film, 0.1eV shifted from the film emission measured in this work.

Concentration Effects in PPY solution

The photoluminescence of PPY solution varies with solution concentration as shown in Figure 4-9. The spectra were measured in a transmission geometry.

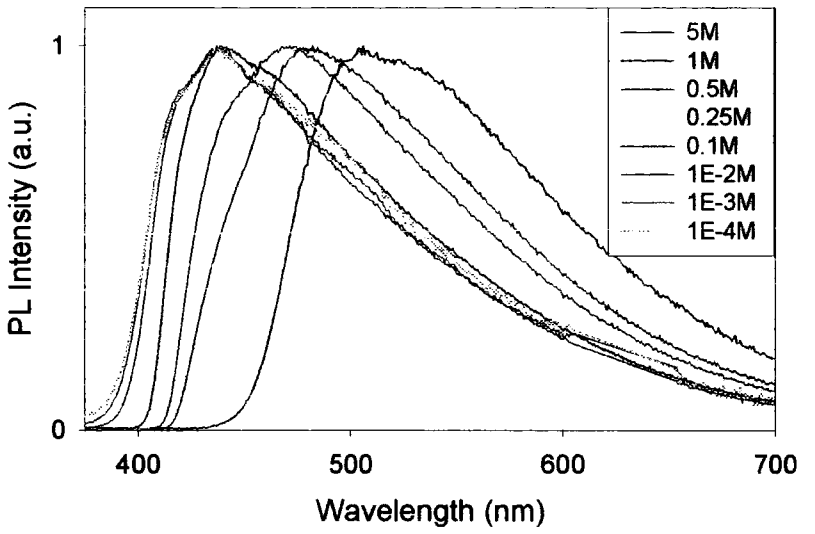

Figure 4-9 *Photoluminescence of PPY in formic acid solution as a function of solution concentration*

The concentration of the solution was varied from 5 molar to 0.0001 molar (moles of repeat units per litre). The highest concentration solution has a peak emission at 506nm (2.45eV). There is a red shift of emission with decreasing concentration, and the most dilute solution studied (1×10^{-4} M) has an emission peak at 438nm (2.83eV). The peak and FWHM of the emission as a function of concentration are shown in Figure 4-10.

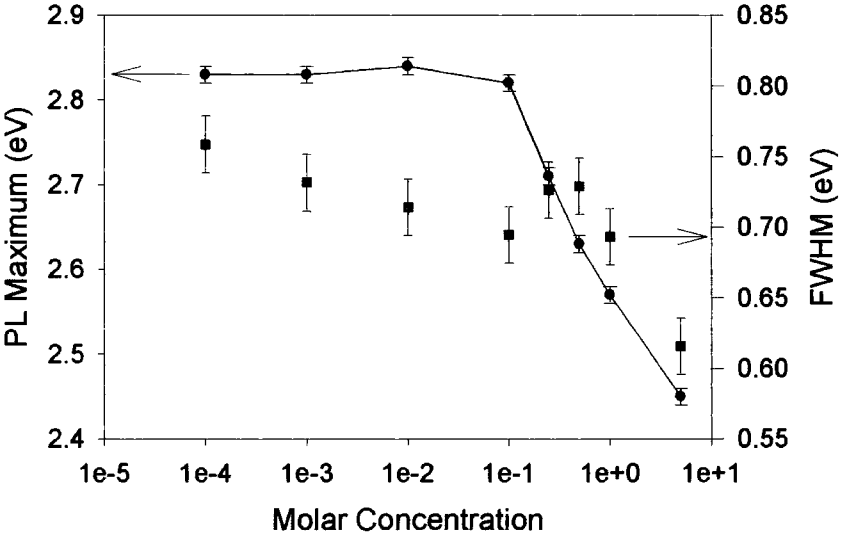

Figure 4-10 *Change in the peak of emission (circles and line) and FWHM (squares) as a function of solution concentration for PPY in formic acid*

The peak of emission shifts by 0.37eV in the concentration range 5M to 0.1M, then remains constant at approximately 2.83eV upon further dilution over 3 orders of magnitude. The FWHM of the emission generally increases with decreasing solution concentration. The absorption spectra of the higher concentration solutions is difficult to measure due to the high absorption and the very low concentration solutions have very little absorption. The absorption and luminescence spectra of the solutions are shown in Figure 4-11.

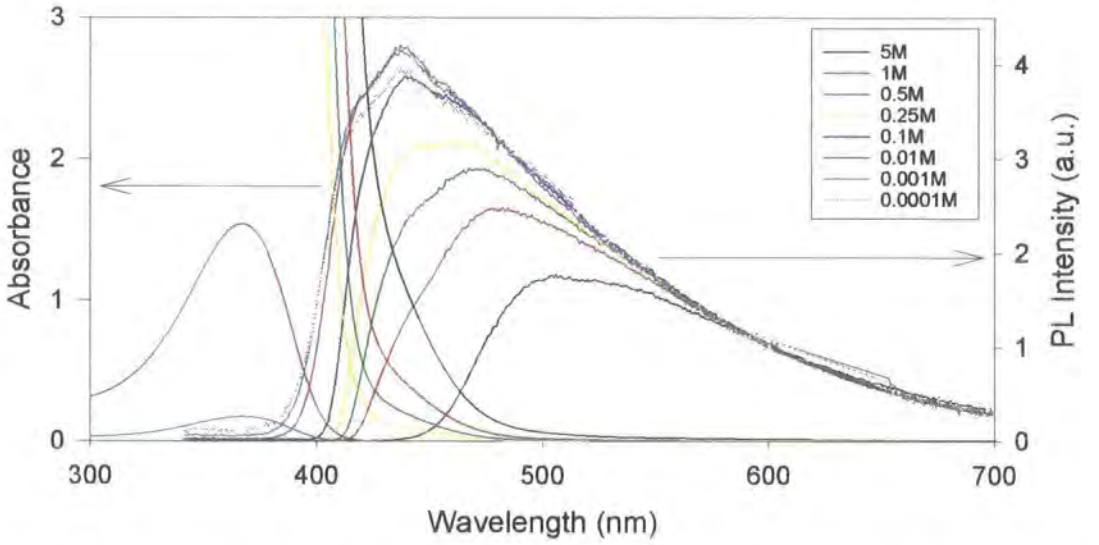

Figure 4-11 *Absorption and photoluminescence spectra with various concentrations of PPY solutions. The PL spectra are normalised so that the intensity equals 1 at 600nm*

The absorption spectrum changes with solution concentration. The magnitude of the absorption at various wavelengths is reduced, however, as the solution becomes less concentrated. The absorption spectrum data can be normalised to the concentration of the solution to investigate this phenomenon.

Figure 4-12 illustrates the similarity of the rescaled absorption spectra of the 5M to 0.25M solutions, suggesting that the differences in shape of the absorption spectra is the same across the concentration range in Figure 4-11.

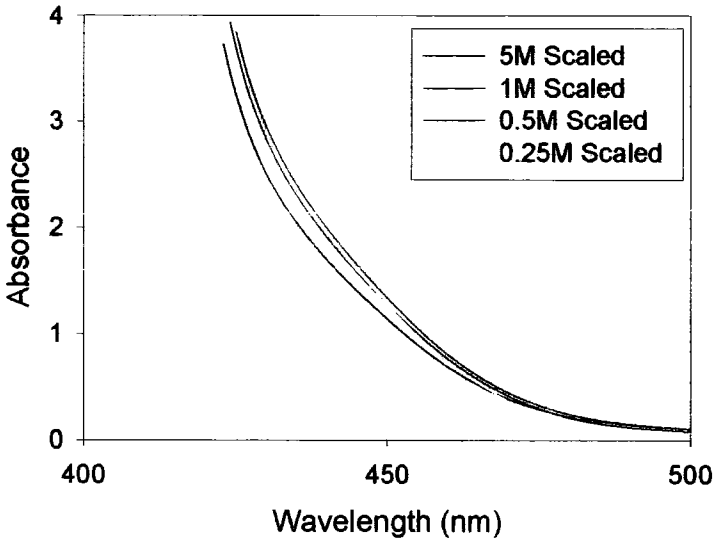

Figure 4-12 *Rescaled absorption spectra of PPY solutions of different concentrations*

The change in the photoluminescence spectra of the solutions appears to be due to self absorption. The increase in FWHM of emission with decreasing solution concentration, shown in Figure 4-10, would be found if the change in emission was due to self absorption. As the self absorption decreases, the emission from the high energy side would no longer be absorbed and hence the FWHM of the emission would increase. The geometry of the measurement of the photoluminescence spectrum aids the process of self absorption as the sample is excited on the opposite side to where the emitted light is collected (i.e. in transmission).

Yamamoto *et al* [3] show a similar change of PL spectrum with a more concentrated solution. There is a similar red-shift observed in that work, although there appears to be less self-absorption at the high energy side of the emission, and no absorption spectrum is shown in this work. The reduced self-absorption could be due to the geometry of the experiment. The data presented in reference [3] may be taken in reflection.

Powder

The photoluminescence of polypyridine in powder form can also be studied. A powder sample of PPY was prepared by compression of PPY with KBr to form a solid disc. The photoluminescence of the PPY powder disc was measured in the usual manner. The PL of the powder is compared to that of PPY in formic acid solution and a standard PPY film prepared by spin-coating from formic acid solution in Figure 4-13.

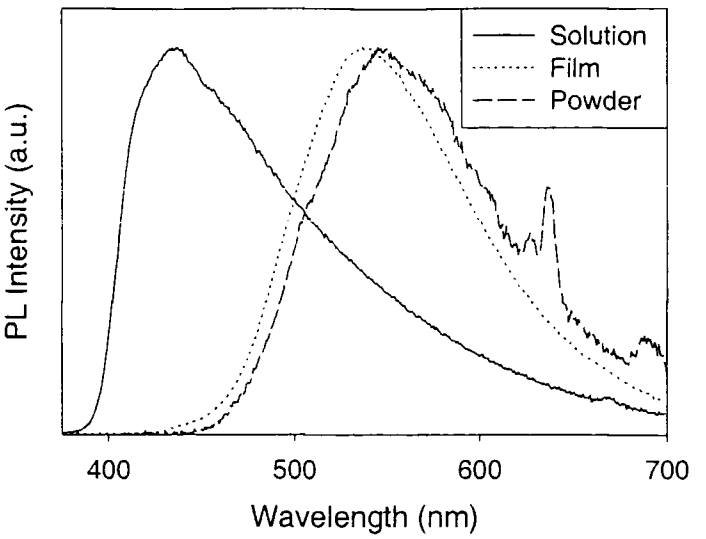

Figure 4-13 *Photoluminescence spectra of polypyridine film (dotted line), solution (solid line) and powder (broken line) samples*

The powder sample exhibits photoluminescence which is very similar to that of the film sample and dissimilar to that of solution. The peak of luminescence is at 545nm, a 10nm red shift from the peak of the film luminescence and 100nm from the peak of the solution luminescence at 435nm. The feature at approximately 630nm in the powder sample is due to the excitation source.

Discussion

The difference between solution and film emission could be produced in a variety of ways. However, excimer emission can be discounted. Emission from an excimer is relatively broad and featureless. The photoluminescence spectrum from the film is relatively narrow (certainly narrower than the absorption) and exhibits some vibronic structure.

Changes in the photoluminescence spectrum of PPY solutions with different concentrations seem to arise due to self-absorption of the emission at short wavelengths and not from a change of emission species, for example interchain aggregate emission. Figure 4-11 illustrates that any differences in the solution PL spectra appear only at shorter wavelengths, the longer wavelength emission is identical for each concentration. The changes in the absorption spectra seem to arise purely from the magnitude of absorption and no real change in shape seems to arise with increasing

concentration. This suggests that the emission in concentrated systems (i.e. film and highly concentrated solution) is not due to aggregate formation.

PPY films are found to be highly crystalline, as demonstrated by x-ray analysis of PPY film samples in references [4, 5]. This suggests a large degree of order within the polymer film. We suggest the changes in the optical properties between film and solution arise due to a change in conformation of the chain. In solution the chain is free to rotate, and some monomer units rotate out of the plane of the chain, limiting the conjugation length to the number of repeat units which lie between two consecutive ring twists. Theoretical studies have shown that isolated polypyridine chains will have monomer units out of the plane of the polymer [6-8]. The angle to which they rotate has been calculated as being between 20° [6] and 30° [8]. The reduced conjugation length will produce blue-shifted emission and absorption compared to those of the film. These twist are illustrated in Figure 4-14, where two ring twists produce a conjugation length limited to four repeat units.

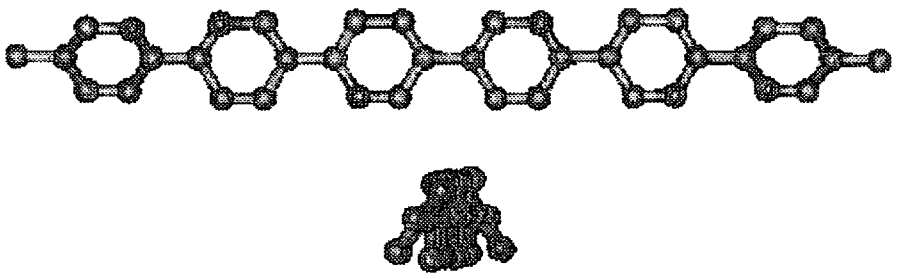

Figure 4-14 *Twists in PPY monomers in a PPY chain in solution*

In film, the pyridine chains are highly ordered which prevents the ring twisting out of plane. This will lead to an increase in the conjugation length and a red-shift of the emission and absorption. The red-shift will occur in chains where there is no other limit on the extent of conjugation along the chain i.e. there will be no change in chains which have defect sites limiting the extent of conjugation. Figure 4-15 illustrates the film conformation of a PPY chain. The lack of monomers twisted out of the plane of the chain produces a longer conjugation length than for chains in solution.

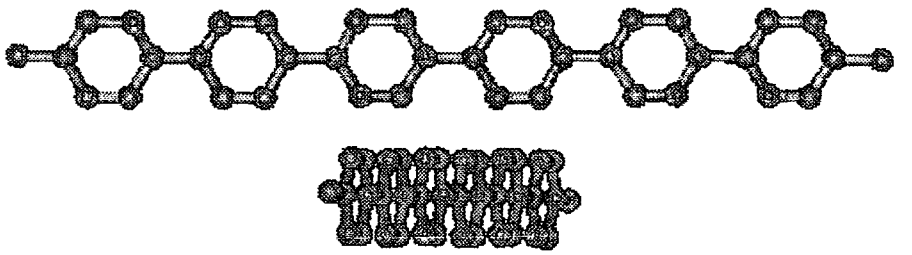

Figure 4-15 *Film conformation of a PPY chain*

This implies that a difference in the absorption spectrum between solution and film is expected: a large proportion of the absorption is caused by chain segments of the same conjugation length as in solution, but there will be a contribution to the absorption by longer conjugation length segments.

The similarity between the photoluminescence of the film and powder samples is in contrast to work published elsewhere [2]. This work suggested that emission in PPY arises due to the formation of aggregate states. The material under study is obviously different to our own in more than one respect. The PLQY of their polymer was found to be between 1% and 8%, considerably lower than the polymer in this study. The PL spectrum of their powder sample, prepared in a similar manner to our own (utilising KBr), more closely resembles that of the solution PL rather than resembling that of the film sample as found in this work. Also in reference [2], a strong dependence of the photoluminescence of film samples is found when the solvent is varied. Figure 4-2 illustrates that although a slight change in spectrum is observed with different solvents, the overall shape and approximate position of the emission is not significantly altered.

BLENDING OF POLYPYRIDINE

The effect of dilution of polypyridine in solid film can be investigated by the blending of PPY with another polymer. A suitable polymer for this task is poly(methyl methacrylate) (PMMA). PMMA is a readily available non-luminescent polymer, better known as Perspex, and it has been used in other blending work (see for example reference [9]). PMMA was obtained from Aldrich Chemicals and was used without further purification. The chemical structure of PMMA is shown in Figure 4-16.

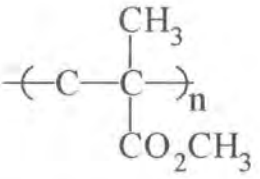

Figure 4-16 *Chemical structure of poly(methyl methacrylate)*

Solutions of a blend of PMMA and PPY were made by dissolving a known weight of each polymer in a common solvent (formic acid). The PPY:PMMA weight ratio of the mixture was varied between 1:0 (all polypyridine) to 1:100. Thin films of the blend were prepared by spin coating onto quartz substrates. As the solid state dilution of the polypyridine became larger (i.e. the PPY:PMMA ratio became smaller), fewer and fewer chromophores absorb the incident radiation, reducing the intensity of the absorption. The change in absorption with increasing dilution is shown in Figure 4-17.

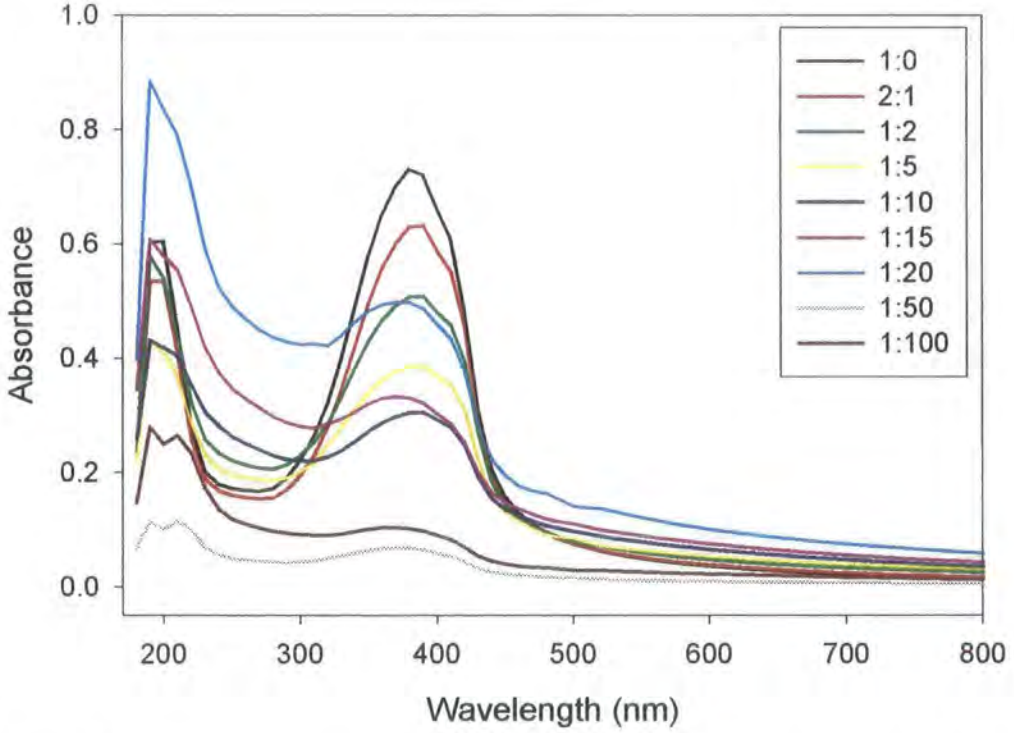

Figure 4-17 *Absorption spectra (absolute absorption) of PPY:PMMA blend films*

The effect of blending on the shape of the absorption is more obvious when the absorption spectra are normalised and offset (Figure 4-18). An increase in the scattering background can be observed.

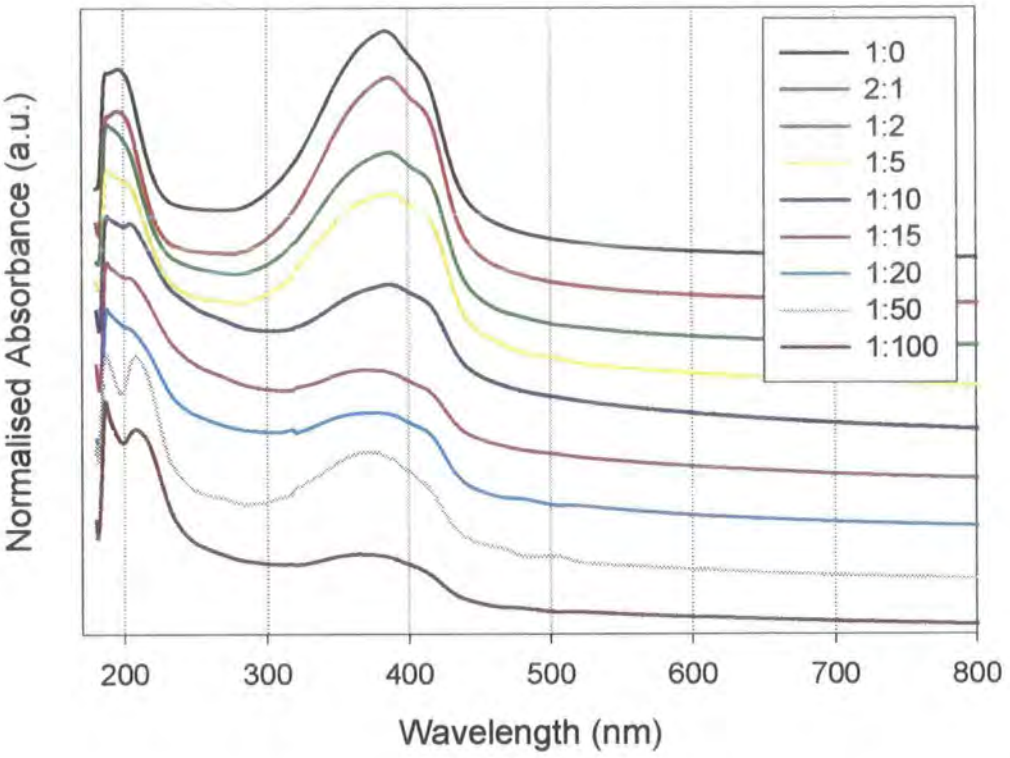

Figure 4-18 *Normalised and offset absorption spectra for PPY:PMMA blend films*

The change in the photoluminescence spectra with increasing blending is shown in Figure 4-19.

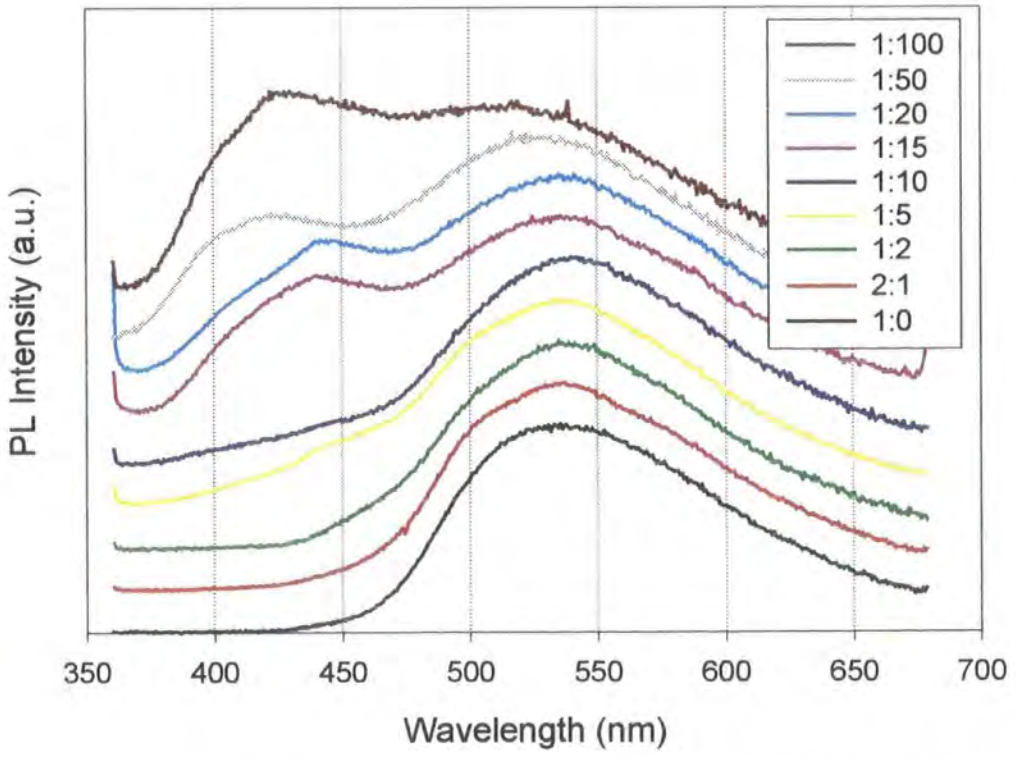

Figure 4-19 *Photoluminescence spectra of PPY:PMMA blend films*

The effect on the absorption spectrum of dilution in the solid state is to reduce the relative strength of the low energy absorption and increase the relative strength of the high energy absorption. There also appears to be evolution of a new absorption peak, splitting the absorption peak that appears at around 200nm, into two peaks at wavelengths higher and lower than 200nm. There is also an increase in the relative amount of absorption at wavelengths lower than 375nm and higher than 230nm.

In concentrated PPY films (low PMMA concentration), the photoluminescence spectrum is as expected and exhibits a single peak at around 530nm. As the concentration of PPY decreases (the concentration of PMMA increases), a second photoluminescence peak slowly evolves with subsequent dilutions, until finally in the 1:100 PPY:PMMA film, the peak at approximately 430nm is the more intense peak. The peak of the PPY solution photoluminescence is coincident at around 430nm. The excitation wavelength for each sample was 350nm (3.54eV) and no significant change in spectrum was observed with different excitation energies.

The colour change resulting from these spectral changes can be illustrated on a CIE (X,Y,Z) co-ordinate diagram (Figure 4-20).

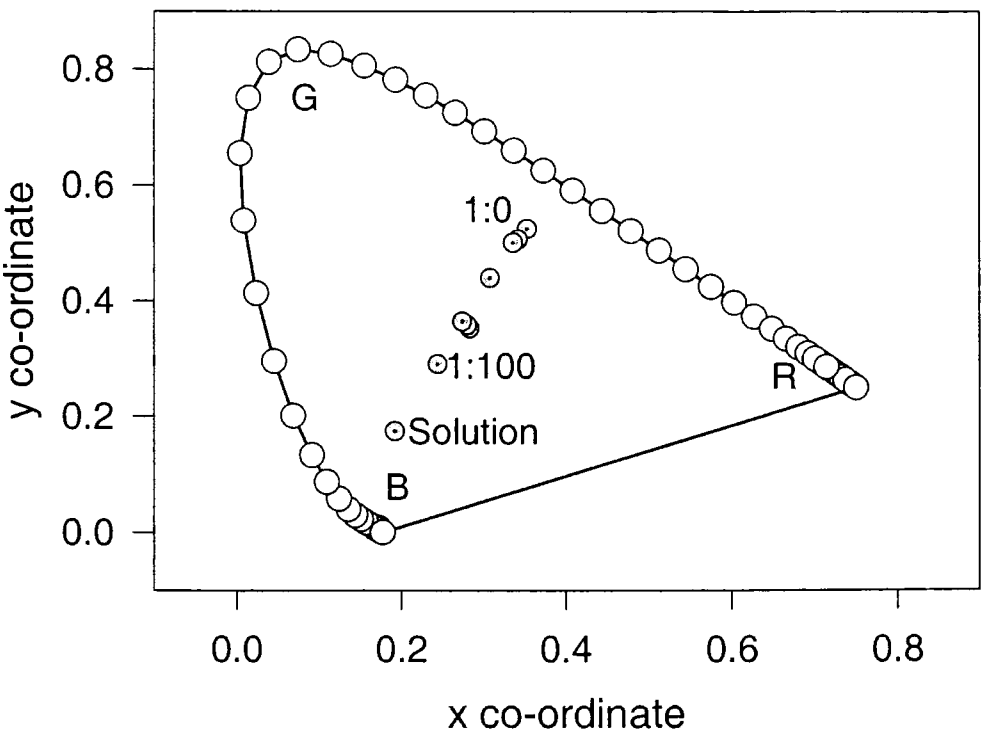

Figure 4-20 *CIE (X,Y,Z) colour co-ordinate diagram for PPY:PMMA blends*

The blending of PPY with increasing amounts of PMMA produces an increase in the amount of higher energy, solution like emission. Figure 4-20 illustrates the colour change of the photoluminescence as the relative concentration of the PPY is reduced. The emission of the unblended film in the CIE (X,Y,Z) system is described by the co-ordinates (0.35, 0.52) in Figure 4-20. The colour of the emission in this system is tuned through a considerable range towards the colour of the solution emission (0.19, 0.17). The co-ordinates of the most dilute blend studied are (0.24, 0.29). Hence through the use of blending, the colour of the emission can be tuned through a reasonable colour range. This is perhaps best illustrated in the CIE (R,G,B) colour system. The colour can be tuned from r,g,b co-ordinates of (0.31, 0.58, 0.12) for the undiluted PPY film, to (0.11, 0.37, 0.52) for the 1:100 PPY:PMMA blend film. Further blending is feasible and it is conceivable that this could give the solution emission colour of (0.00, 0.24, 0.76).

Discussion

The results obtained for the blending of PPY are consistent with the ring twist argument presented above. As in solution, the separation of the PPY chains reduces the amount of order present in the system. The reduction in order may reduce the packing of the chains, allowing the monomer units to twist out of the plane of the polymer chain. This will reduce the conjugation length as for the solution case. The decrease in the low energy absorption and emission would imply that there is a reduction in the amount of longer conjugation length segments capable of absorbing and emitting. Conversely, there is an increase of the relative strength of the higher energy absorption and photoluminescence as the blending of the PPY increases. This could be due to the increase in the number of shorter conjugation length segments as the number of ring twists increases.

A common problem with blends of polymers is phase segregation. Regions consisting of predominantly one polymer can form as the films dry. Noticeable segregation only occurs with PMMA/PPY when thick films are prepared on large substrates.

The blending of PPY illustrates one of the advantages of polymer luminescence. The colour of the emission can be tuned through a considerable range, from green to blue/green emission, by simple addition of a host polymer into a common solvent. The

chemistry of the systems has not been altered, yet considerable colour tuning and emission tailoring has been demonstrated.

BATCHES OF POLYPYRIDINE

Several different batches of polypyridine have been produced by Dr E. Rebourt and Dr L.E. Horsburgh. These batches have similar, though not identical characteristics. Batches manufactured by E. Rebourt have the prefix "ER" and those manufactured by L.E. Horsburgh have the prefix "L".

Absorption of Polypyridine Batches

The absorption of the solutions of some of the batches of polypyridine studied are shown below. The spectra are normalised to 1 and offset for clarity.

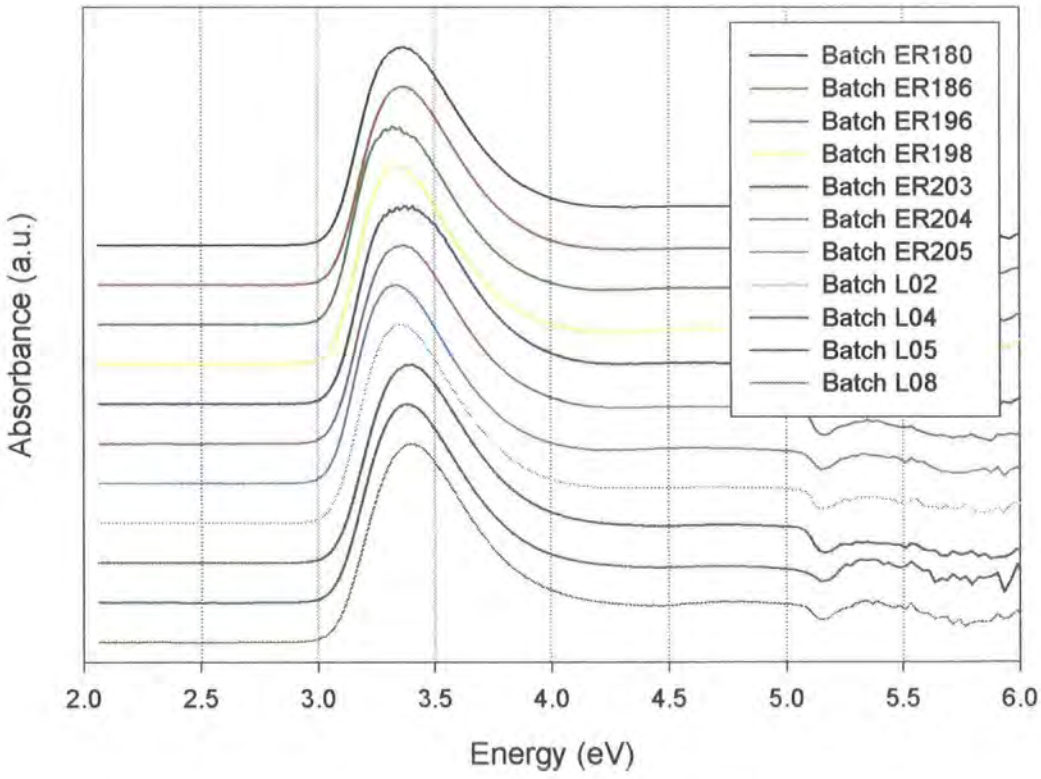

Figure 4-21 *Normalised and offset absorption spectra of some batches of PPY in formic acid solution*

Figure 4-21 illustrates the large degree of uniformity in the absorption spectra of solutions of various batches of polypyridine. All of the absorption spectra look very

similar and their absorption maxima are at around 3.3eV. All of the maxima lie in the range 3.31eV to 3.41eV. The absorption maxima of each of the batches in solution is summarised in Table 4-1.

The absorption spectra of films of the same batches of polypyridine on quartz substrates are shown below. For clarity, the absorption is normalised to 1 and the spectra of the batches are offset relative to one another.

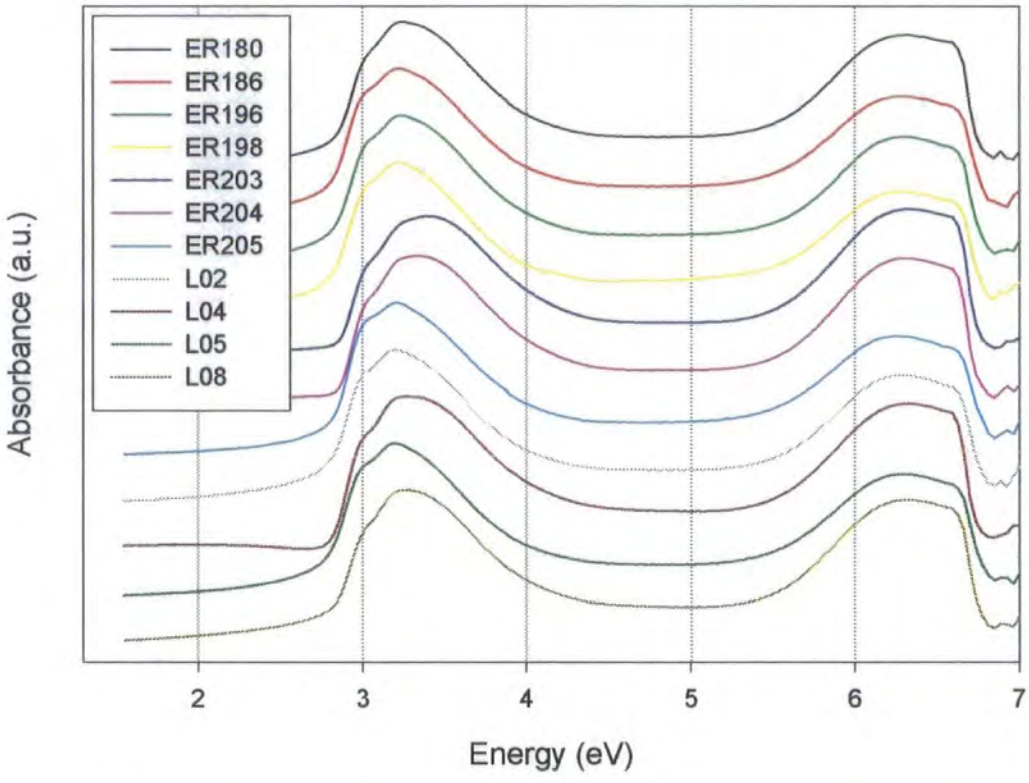

Figure 4-22 *Normalised and offset absorption spectra of some polypyridine batches in solid film on quartz substrates*

There is also a great deal of similarity between the various batches in the film absorption. The absorption maxima lie between 3.19eV and 3.39eV, and the spectra exhibit similar shapes. The absorption maxima of films of the batches of PPY are summarised in Table 4-2. All batches exhibit what appears to be a vibronic feature at around 3eV and display a higher energy absorption at around 6.5eV, which is similar in shape and position for each of the batches. This higher energy peak is not seen in solution absorption spectra due to the absorption of the formic acid. There is some variation, between the batches, in the relative intensity of the feature at 3eV. The feature only appears in the absorption spectrum of film samples and could be due to the absorption of longer conjugation length segments which arise due to the high ordering

of the polymer film. The variation of the relative intensity of the feature would therefore be due to a variation in the relative amount of longer conjugation length segments and hence a variation in the amount of ordering in the film. The larger variation of the position of the maximum of the absorption of the film samples compared to the samples in solution may also be a consequence of variation in film formation.

Photoluminescence of Polypyridine Batches

The photoluminescence of the various batches of polypyridine shows similar behaviour to that of the absorption. There is considerable similarity in both the position and shape of the luminescence, with only minor variations in each. The offset and normalised (to one) photoluminescence spectra of the batches of polypyridine in formic acid solution are shown below. The feature at approximately 3.7eV is excitation light.

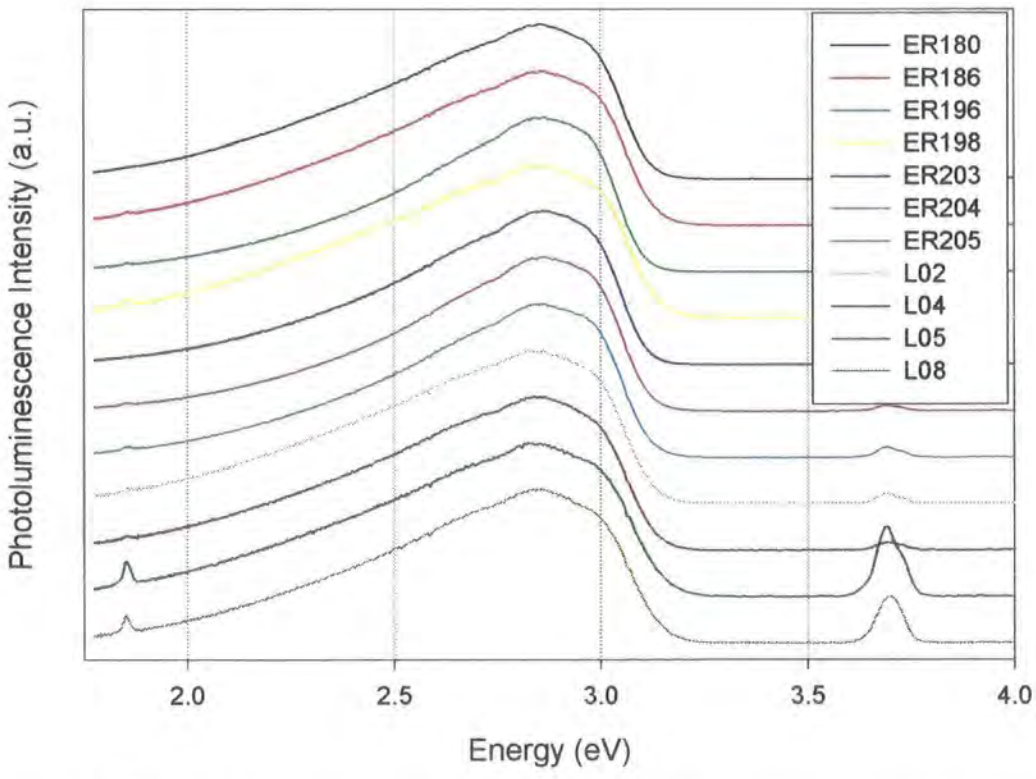

Figure 4-23 *Photoluminescence spectra of the batches of polypyridine in formic acid solution*

Figure 4-23 illustrates the similar photoluminescence spectra of solutions of the batches of polypyridine. The spectra have similar shape and all have a peak of

emission at an energy in the range 2.82eV to 2.86eV. There is a large low energy tail of emission and FWHM of between 0.55eV and 0.70eV. The apparent Stokes shift (measured as the difference in energy between the peak of absorption and luminescence) is between 0.46eV and 0.57eV.

The photoluminescence spectra of films of the batches of PPY are similar to one another, with similar peak positions and vibronic structure. The spectra are shown in Figure 4-24.

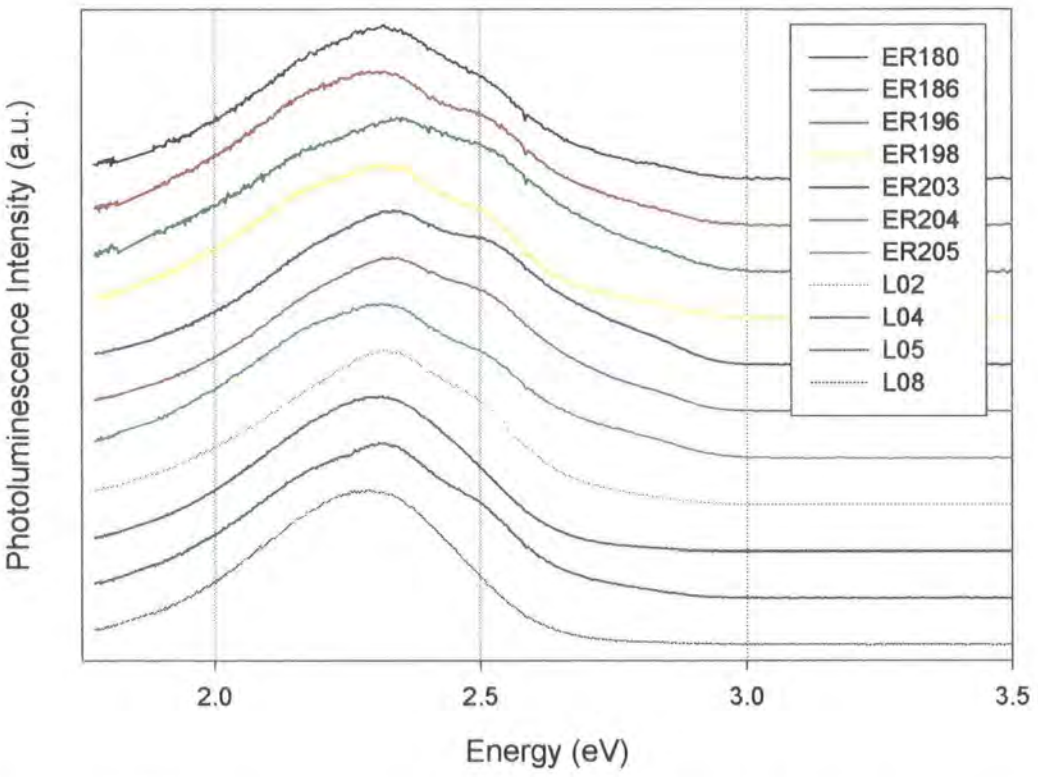

Figure 4-24 *Photoluminescence spectra of film samples of the batches of polypyridine*

The peak position of the photoluminescence varies between 2.29eV and 2.35eV for the batches. Most batches exhibit a feature at around 2.5eV. There are some differences in the relative intensity of the feature which may be a consequence of variations in the ordering of the films. The films were prepared using identical spin speed and time, although there was some variation in the concentration of the solutions from which the samples were prepared.

The data collected for the batches is summarised below. The excitation wavelength for all film and solution samples was 336nm (3.69eV).

Summary of Optical Measurements of PPY Solutions

The absorption and emission maxima were measured from the photoluminescence and absorption spectra of formic solutions of the batches of PPY. The full width at half maximum (FWHM) of the emission was measured from the photoluminescence spectra. The stokes shift was measured as the difference between the peak of the absorption and emission.

Batch Name	Absorption Maximum (eV)	Emission Maximum (eV)	FWHM Emission (eV)	Stokes Shift (eV)
ER180	3.37	2.86	0.65	0.51
ER186	3.36	2.85	0.65	0.51
ER196	3.32	2.86	0.55	0.46
ER198	3.34	2.83	0.69	0.51
ER203	3.41	2.86	0.57	0.55
ER204	3.36	2.86	0.56	0.50
ER205	3.33	2.85	0.58	0.48
L02	3.36	2.86	0.69	0.50
L04	3.41	2.84	0.66	0.57
L05	3.38	2.82	0.70	0.55
L08	3.40	2.84	0.66	0.56

Table 4-1 *Summary of data from optical measurements of PPY batches in formic acid solution*

The similarity of the optical behaviour of the various PPY batches in formic acid solution is illustrated in Table 4-1. The absorption maxima of each of the batches of PPY are very similar, lying within 0.05eV of the mean of the absorption maxima of 3.37eV. This distribution can solely be accounted for by the error in the measurement on the absorption spectrometer. Similarly, the emission maxima of the batches lie within 0.03eV of the mean of the emission maxima of 2.85eV, the approximate resolution of the measurement. The FWHM values lie within 0.08eV of the mean value of 0.63eV, suggesting no real physical significance. The deviation from the mean for the Stokes shift is also similar, all values lying within 0.06eV of the mean value of 0.52eV.

Summary of Optical Measurements of PPY Films

The absorption and emission maxima were measured from the photoluminescence and absorption spectra of PPY films. The full width at half maximum (FWHM) of the emission was measured from the photoluminescence spectra. The Stokes shift was measured as the difference between the peak of the absorption and emission. The photoluminescence quantum yield (PLQY) of the films was measured in an integrating sphere by M. Halim.

Batch Name	Absorption Maximum (eV)	Emission Maximum (eV)	FWHM Emission (eV)	Stokes Shift (eV)	PLQY (±2 %)
ER180	3.25	2.32	0.51	0.93	N/A
ER186	3.21	2.32	0.56	0.89	N/A
ER196	3.23	2.35	0.58	0.88	30
ER198	3.21	2.32	0.54	0.89	N/A
ER203	3.39	2.34	0.56	1.05	30
ER204	3.33	2.33	0.54	1.00	30
ER205	3.21	2.31	0.55	0.90	30
L02	3.20	2.32	0.48	0.88	7
L04	3.28	2.32	0.47	0.96	N/A
L05	3.20	2.31	0.50	0.89	30
L08	3.26	2.29	0.44	0.97	N/A

Table 4-2 *Summary of data from optical measurements of solid films of PPY batches*

The absorption maxima for films of batches of PPY have a greater variation than the corresponding data for solution. The absorption maxima lie within 0.14eV of the mean absorption maximum, the greater variation perhaps accounted for by a slight variation in film quality. The emission maxima lie within 0.03eV of the mean value. The FWHM of the samples lie within 0.08eV of the mean of 0.52eV, and Stokes shifts lie within 0.12 eV of the mean value of 0.93eV. Batch L02, which has a very low PL quantum yield compared to the other batches, exhibits no significant difference in its remaining optical properties.

Summary of Other Measurements made on PPY batches

Several other measurements were made on each of the PPY batches.

Molecular Weight

The molecular weight of the polymer batches was measured using a gel permeation chromatography column by Dr L.E. Horsburgh and Dr P.N. Adams. The time taken for a solution of PPY to pass through the column was measured and compared to standard samples of a known molecular weight. Comparison of these results allows calculation of the molecular weight of the PPY batch under test. The results are presented as the weight (atomic units) per chain. The weighted average molecular weight is shown in Table 4-3. The polydispersity of the molecular weight is also shown. This is a measure of the distribution of the molecular weights in the sample. The larger the polydispersity, the greater the spread of molecular weights in the sample. The results were confirmed by dynamic light scattering measurements.

Electron-Spin Resonance

Electron-spin resonance (ESR) measurements were taken by P. Devasagayam. The results presented are the integrals of the measured ESR spectra. The numbers represent the number of species with spin ½ in the powder samples. The higher the number, the higher the impurity (with spin ½) level.

Chemical Analysis

The batches were sent for chemical analysis. The results presented are the percentage composition (by weight) of carbon (C), nitrogen (N), hydrogen (H) and remainder (R).

Batch Name	Molecular Weight	Poly-dispersity	ESR Analysis	Chemical Analysis (% composition)			
				C	H	N	R
ER180	5600	1.77	1.621	73.67	3.88	16.7	5.74
ER186	5670	1.67	0.725	75.14	3.91	16.96	3.99
ER196	5960	1.73	2.684	N/A	N/A	N/A	N/A
ER198	6610	1.68	2.160	75.27	3.91	17.00	3.81
ER203	4340	1.64	N/A	N/A	N/A	N/A	N/A
ER204	5720	1.67	N/A	76.32	3.99	17.21	2.48
ER205	6566	1.73	N/A	75.65	3.93	16.88	3.54
L02	6220	1.64	N/A	76.23	3.89	17.07	2.81
L04	5390	1.72	N/A	N/A	N/A	N/A	N/A
L05	6720	1.74	N/A	N/A	N/A	N/A	N/A
L08	4970	1.70	N/A	N/A	N/A	N/A	N/A

Table 4-3 *Molecular weight, electron-spin resonance and chemical analysis of the PPY batches*

The PPY batches show a considerable range of molecular weights. The standard deviation of the molecular weight is approximately 13% of the mean value of 5796. The polydispersity of each batch is quite low, however, the batches having mean dispersity of 1.7. This illustrates that although there is a wide range of molecular weights between the batches, the range of molecular weights within the batches is limited. The chemical analysis of the batches shows limited differences, but there seems to be no correlation between the ESR analysis and the R value from the chemical analysis. A high value of the ESR data does not correspond to a relatively high value of R, nor does a low ESR value correspond to a low R value. This of course could be due to a number of impurities having paired electron spins.

Discussion

The reduction in the size of the average FHWM of the photoluminescence spectrum of film samples compared to that of solution samples can be understood in terms of excitation migration. In solution, the emission arises from a larger distribution of conjugation lengths as the emission occurs from the chain segment on which the excitation was created. In film, migration of the excitation to longer conjugation length segments is possible, which would produce a smaller distribution of emission energy.

Table 4-1 to Table 4-3 illustrate the limited effect that the molecular weight, polydispersity and impurity levels have on the spectral properties of the PPY batches.

Although it would be expected that these factors would have an effect on the emission of PPY, the value of the molecular weight means that an average chain has around 75 repeat units, far larger than the expected conjugation length. Hence a small impurity level and variation in the number of repeat units would not be expected to have a visible effect on the bulk optical properties of this material. Although optical spectroscopy is a powerful tool, it and the other tests summarised above, have proved to be of limited value in differentiating the various batches of PPY, and on the evidence presented above, the various batches of PPY should prove to be interchangeable.

POLY(*M*-PYRIDINE)

The polymer discussed above, polypyridine, is more correctly known as poly(*p*-pyridine) (P*p*PY). The linkage through the polymer chain is in the *para* rather than the *meta* position. Poly(*m*-pyridine) (P*m*PY) can be synthesised in a similar way to poly(*p*-pyridine) (P*p*PY), but starting with 2,6-dibromopyridine rather than 2,5-dibromopyridine. The chemical structures of P*p*PY and P*m*PY are shown in Figure 4-1.

The change in the chemical structure produces a change in the conjugation of the polymer. The meta linkage prevents overlap of the remaining p-orbitals, breaking the conjugation and limiting the conjugation length to two repeat units. This would be expected to produce blue shifted absorption and emission.

Absorption and Emission of P*m*PY

Figure 4-25 and Figure 4-26 show the absorption and photoluminescence respectively of P*m*PY solution and film spectra compared to P*p*PY (batch L05) solution and film spectra.

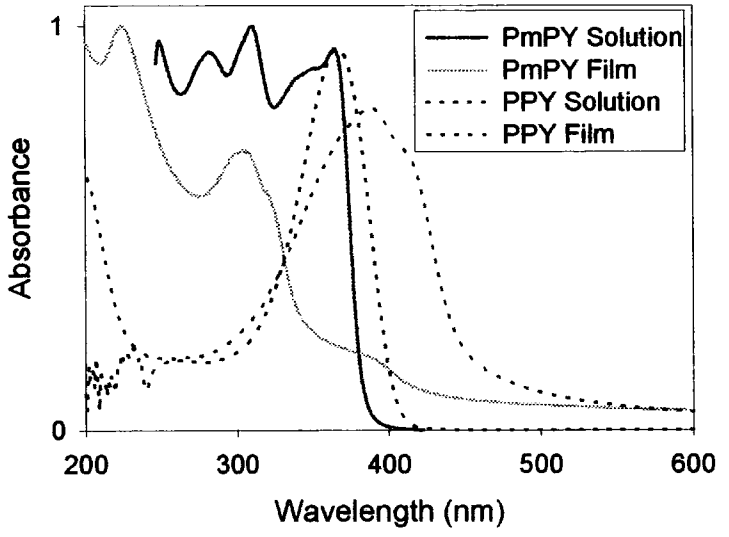

Figure 4-25 *Absorption of PmPY solution (brown line), PmPY film (yellow line), PpPY solution (dotted black line) and PpPY film (dotted red line)*

The absorption of P*m*PY solution and film shows a substantial blue shift from the comparable *para* linked polymer. The peak of the absorption of the P*m*PY solution

is at 311nm (3.99eV) and that of film at 224nm (5.54eV). The corresponding peaks for the *para* linked polymer are 367nm (3.38eV) for solution and 388nm (3.20eV) for film. The shapes of the absorption spectra also change dramatically. The solution absorption has several features between 390nm and 250nm, one of which seems to coincide with the peak of the P*p*PY solution absorption at 370nm, and another which appears to coincide with a strong feature of the P*m*PY film absorption spectrum at around 310nm. The four clearly resolved peaks are at 3.41eV, 4.01eV, 4.38eV and 4.98eV. The absorption spectrum of various P*m*PY solutions was measured several times by L.E Horsburgh, but the shape of the spectrum remained constant. The P*m*PY film absorption has two well resolved peaks at 304nm (4.08eV) and 225nm (5.51eV). There is also another peak at around 390nm (3.20eV), which appears to correspond with the P*p*PY film absorption maximum.

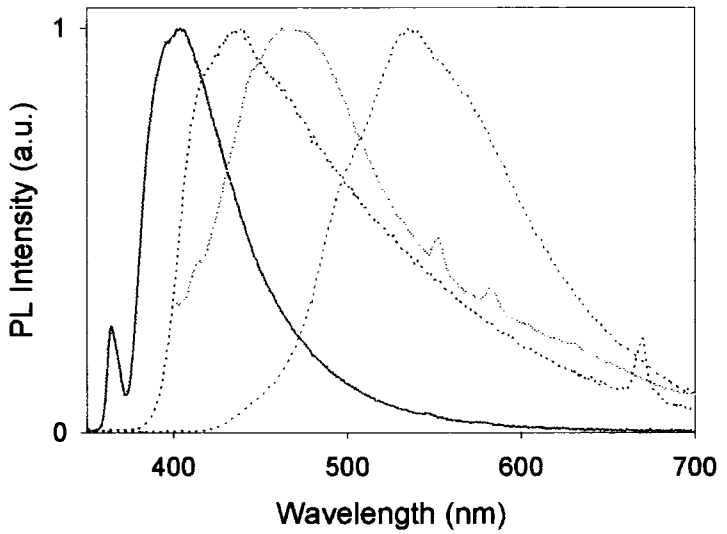

Figure 4-26 *Photoluminescence of PmPY solution (brown line), PmPY film (yellow line), PpPY solution (dotted black line) and PpPY film (dotted red line)*

P*m*PY solution exhibits a photoluminescence peak at 404nm (3.07eV) and the film has a peak at 463nm (2.68eV). The corresponding values for the para linked polymer are 439nm (2.82eV) for solution and 537nm (2.31eV). There is evidence for weak vibronic structure on the P*m*PY film spectrum, but none apparent on the solution spectrum. The *para* linked polymer exhibits structure on both the film and solution spectra.

Discussion

In Photoluminescence, the 0.39eV shift between film and solution PL probably arises through the same mechanism as the shift seen in P*p*PY, i.e. ring rotations which reduce the conjugation length of the polymer are prevented to some degree by the ordering of the film. A similar magnitude of shift is observed (0.51eV) in the case of P*p*PY.

The poly(*m*-pyridine) has an apparent Stokes shift of 0.61eV in solution and 0.88eV in film. This is comparable to similar values of 0.55eV and 0.89eV for P*p*PY in solution and film respectively.

Copolymers of Poly(*m*-pyridine) and Poly(*p*-pyridine)

A useful tool in investigating the luminescence of poly(*m*-pyridine) and poly(*p*-pyridine) is the synthesis of random copolymers of *para* and *meta* linked polypyridine. Copolymers were made by mixing known amounts of the starting material dibromopyridine. The amount of each of the *para* and *meta* linked polymer units was governed by adding different amounts of 2,5- and 2,6-dibromopyridine respectively. Several different compositions were made, starting the reaction with 3%, 18%, 25%, 35%, 42% and 50% 2,6-dibromopyridine. If the polymerisation occurred completely at random, this would produce *para* linked chain segments, between *meta* linked rings, with an average *para* length of 32.3, 4.6, 3.0, 1.86, 1.4 and 1 repeat units respectively. The chemical structure of a random copolymer of *meta* and *para* linked pyridine is shown below. The name of the copolymer is Poly(2,6-pyridine-co-2,5-pyridine) (P*m*PY-co-P*p*PY).

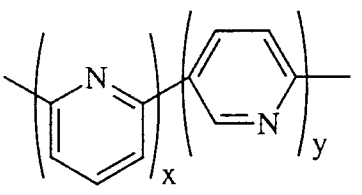

Figure 4-27 *Chemical structure of a random copolymer of meta and para linked polypyridine*

The purpose of this is two-fold. In addition to the colour tuning that can arise from these copolymers due to the change in conjugation length, the conjugation length

responsible for emission in normal P*p*PY can be probed as the *meta* linkage will disrupt the conjugation along the chain and provide insight in this area.

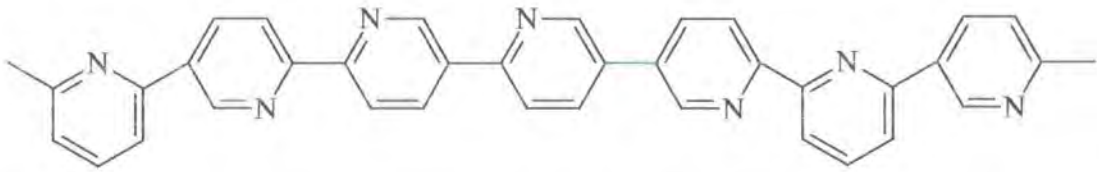

Figure 4-28 *Chemical structure of a section of PmPY-co-PpPY with a para length of 4 repeat units*

Emission from a copolymer with 4 *para* repeat units would be expected to be different from a copolymer with 2 *para* repeat units if the usual conjugation length of the emitting chain segment was longer than 2 repeat units.

The absorption spectra of different compositions of copolymers are shown below. The results are contrasted with the absorption spectra of pure *para* and *meta* linked polypyridine.

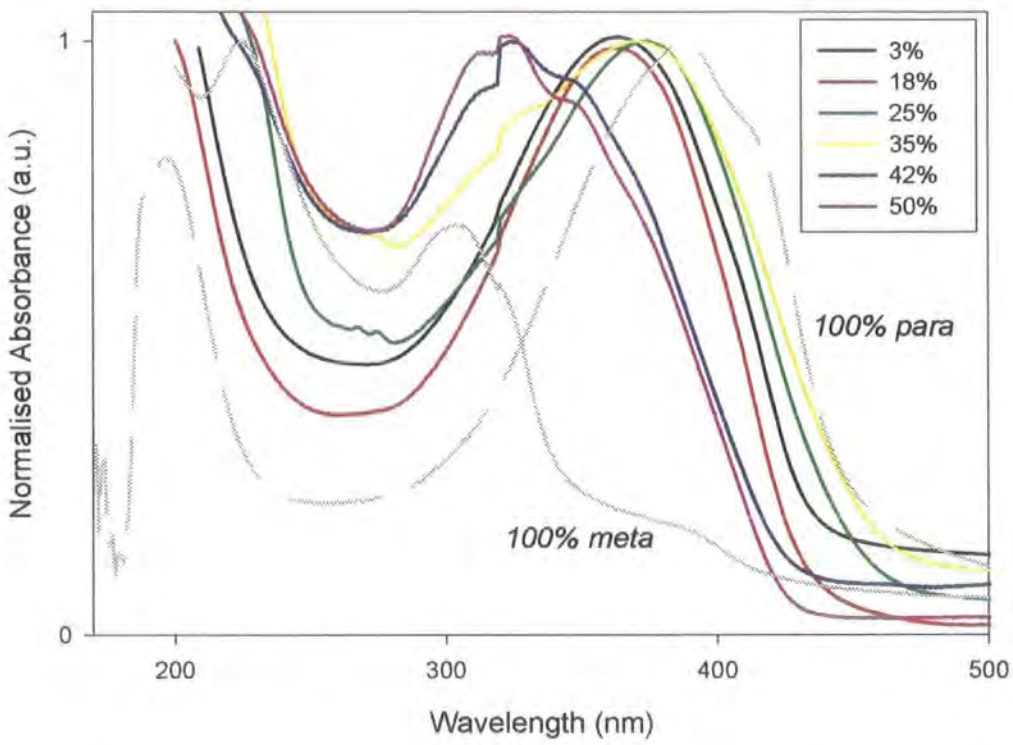

Figure 4-29 *Absorption spectra of copolymer films contrasted with absorption spectra of pure meta and para linked polymer films*

The absorption spectra show a gradual evolution of P*m*PY like behaviour with increasing amounts of *meta* linkage. The spectra of copolymers up to 25% *meta* linkage have a similar shape to the 100% *para*-linked polymer, but have up to a 25nm blue shift. The 50% copolymer has the highest degree of P*m*PY-like behaviour, with a shift in the low energy peak of the spectrum, and a substantial increase in the amount of high energy absorption (wavelengths lower than 300nm), although it does not exhibit purely 100% *meta* behaviour.

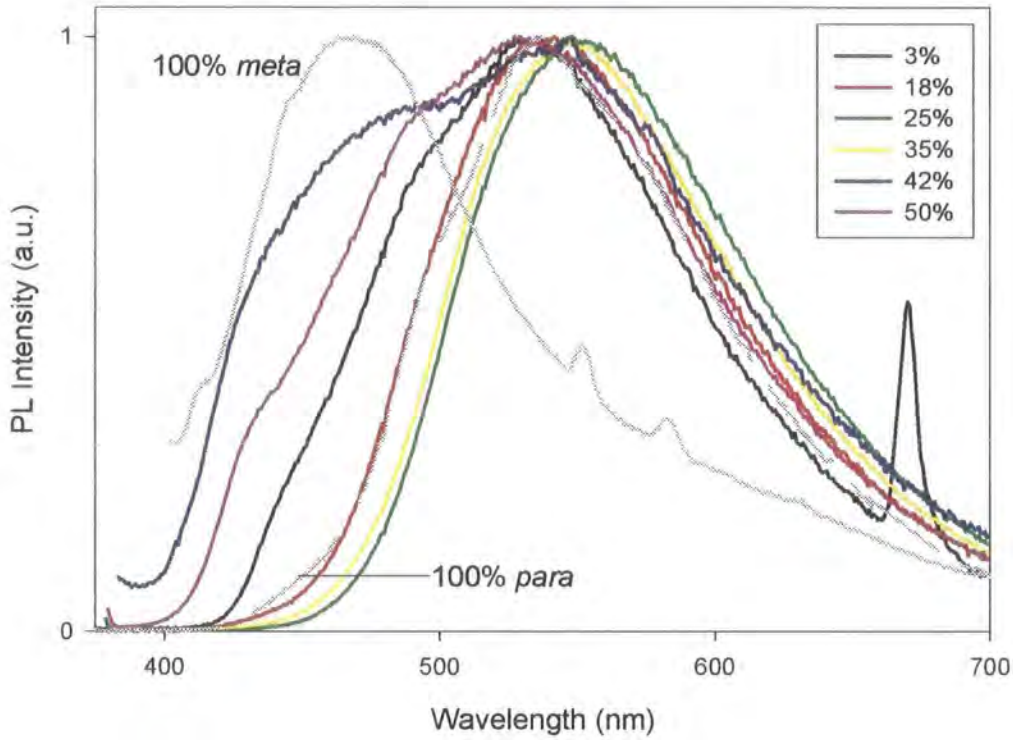

Figure 4-30 *Photoluminescence spectra of copolymer films contrasted with photoluminescence spectra of pure meta (100%meta) and para (100%para) linked polypyridine films*

The photoluminescence spectra of the copolymers shows no gradual evolution of 100% *meta*-linked polymer like behaviour. The photoluminescence spectra of most of the copolymers show no significant spectral change. The spectral shape of the emission of the 18%, 25% and 35% copolymers is very similar to that of the pure *para*-linked polymer, and the maximum of the emission is similar in these cases: 541nm for the 18%; 548nm for the 25% and 35% and 537nm for the pure *para*-linked polymer. The 3% copolymer has a similar peak position, but there is slightly more emission at higher energy. The 42% and 50% *meta*-linked copolymers, however, show significant

meta-like character, although the spectrum is not identical to that of the pure *meta*-linked polymer in either case.

The photoluminescence and absorption spectra of the solutions of the copolymers are very similar to one another, but dissimilar to the spectra for P*m*PY solution, as shown in Figure 4-31 and Figure 4-32 respectively. There is some similarity between the copolymer and P*p*PY solution absorption, however.

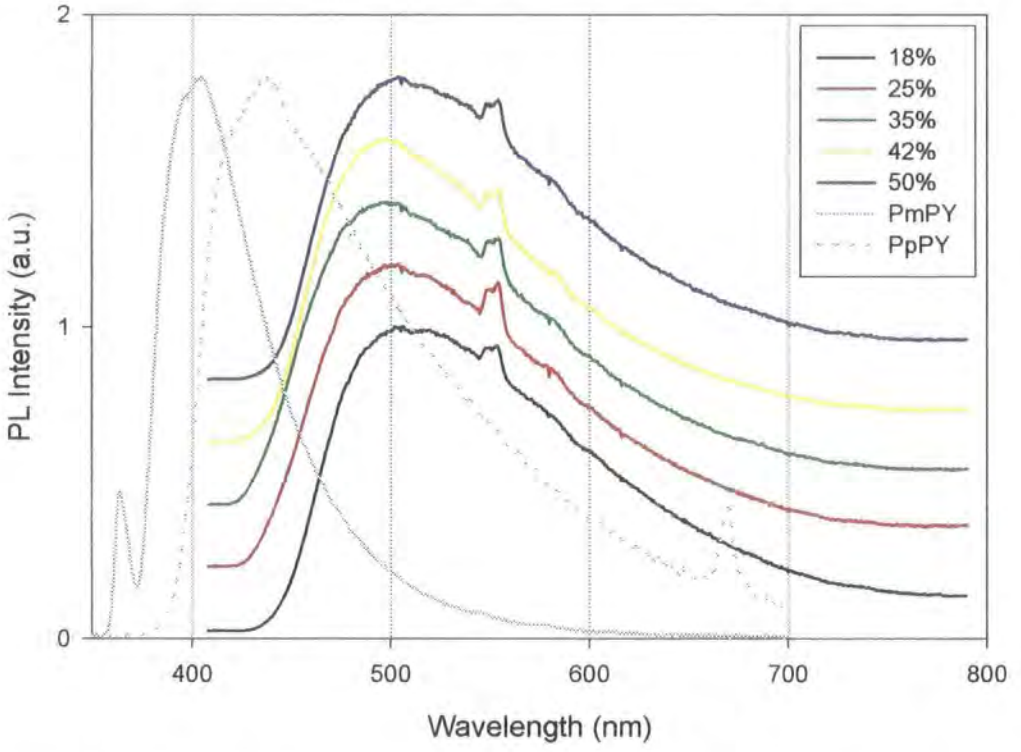

Figure 4-31 *Photoluminescence spectra of PmPY-co-PpPY solutions contrasted to those of PmPY and PpPY solutions*

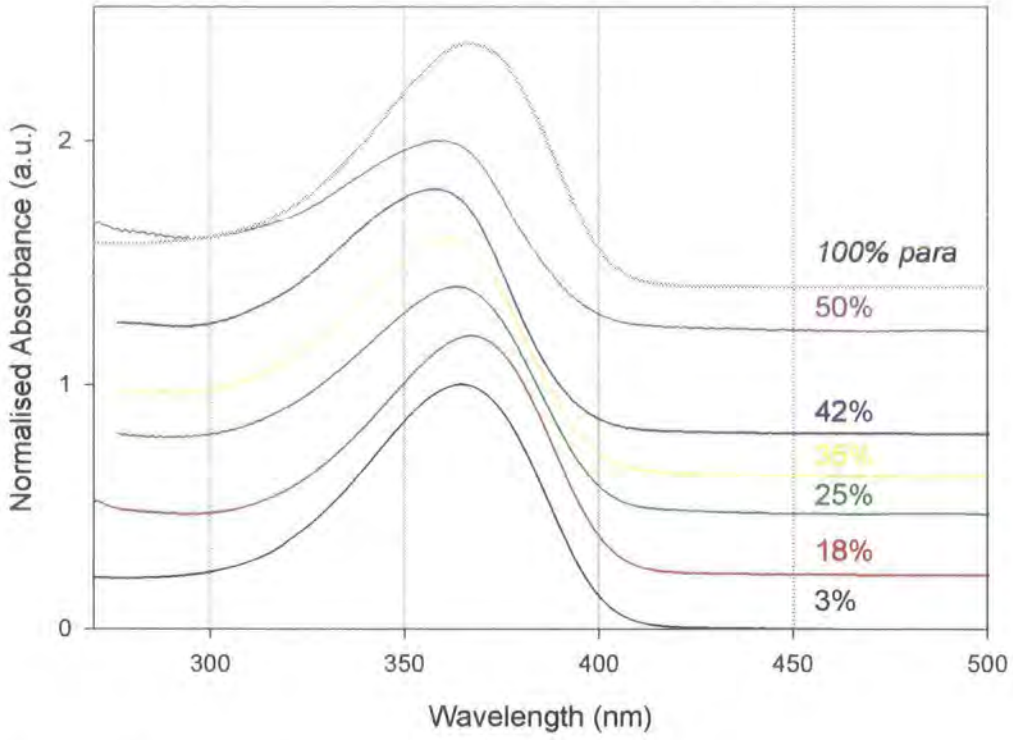

Figure 4-32 *Absorption spectra of PmPY-co-PpPY with varying meta content in formic acid solution*

The peak of the photoluminescence of solutions of the *meta* containing copolymers range from 498nm to 506nm (2.45 to 2.49eV), and exhibiting no significant shift. The shape of the luminescence is also very similar. The spectra are different in shape and position to the spectra of the pure *meta* and *para* linked polymers, which have peak positions at 404nm (3.07eV) and 439nm (2.82eV). The peak of the emission of the copolymers in solution is given in Table 4-4.

The peak of the film absorption is very similar and appears to be almost independent of the *meta* content of the copolymer. There does appear to be a broadening of the absorption spectrum and an increase in the amount of absorption at higher energy, however. The peak of the solution absorption for each copolymer is given in Table 4-4. The peak of absorption for P*p*PY in solution is around 367nm (3.38eV) and is similar in shape. P*m*PY in solution peaks at 311nm (3.99eV) and, although it does have a peak at around 370nm, is essentially dissimilar in shape.

Copolymer *meta* content	Absorption Max		Emission Max	
	nm	eV	nm	eV
3%	365	3.40	N/A	N/A
18%	367	3.38	506	2.45
25%	364	3.41	504	2.46
35%	361	3.43	498	2.49
42%	357	3.47	498	2.49
50%	360	3.44	504	2.46

Table 4-4 *Absorption and emission maxima for PmPY-co-PpPY copolymers, with various meta content, in formic acid solution*

Discussion of Copolymer Films

The variation in the peak of the absorption and the average energy of the emission (calculated as the energy at which half of the area under the curve lies) with percentage *meta* content is shown below. The range over which the calculation was carried out was the same in each case.

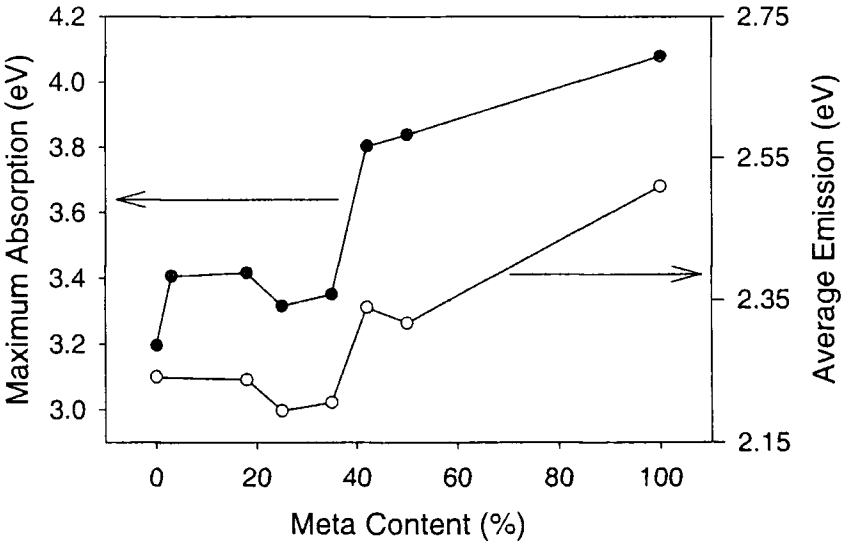

Figure 4-33 *Maximum absorption and average emission energy for polymers with varying meta-link composition*

In film samples, the behaviour expected of the copolymers is obtained. The absorption spectra of the copolymers (Figure 4-29) show the gradual evolution of meta-like absorption, to almost pure meta type absorption for the 42% and 50% *meta* linked polymer. There is also considerable *meta*-type character in the 35% copolymer, but considerable *para*-type character remains. The shape of the absorption spectra can be

understood by the action of the *meta* linkage in breaking the conjugation of the polymer. The P*m*PY absorption is due to absorption by short conjugation length segments, probably around 2 repeat units, possibly slightly longer due to the presence of *para* links as possible impurities. The copolymers will have a range of conjugation lengths due to the random nature of their formation, and the absorption spectrum will be the sum of the absorptions of the various conjugation length segments.

There is essentially little difference in the spectra of the 3%, 18% and 25% copolymer, although there is an increase in the amount of higher energy absorption. The copolymers with higher meta content, however, have substantially different spectra, and the point at which the spectra change appears to be around the 35% copolymer. This idea is reinforced by the change in the peak of the absorption increase shown in Figure 4-33. The peak absorption changes by 0.4eV between the 35% and 42% copolymer. This would suggest an average conjugation length of around 3 to 4 repeat units in film. This assumes a statistical distribution of the *para* linked units, producing an average *para* length of between 1.4 and 1.86 units (for the 35% and 42% copolymer), with the conjugation length increased by the presence of two *meta*-linked units at both sides of the *para*-linked section.

Estimation of the conjugation length from the photoluminescence spectra is complicated by the migration of excitations to lower energy chain segments before emission. Only the 42% and 50% copolymer (and the 3% which will be discussed later) show significant meta-like character. This is not surprising as the excitations would be expected to migrate to longer conjugation length segments. The distribution of *para* and *meta* links in the copolymers is unlikely to be completely random, implying that there may be several longer *para* lengths than statistics may suggest, in even the copolymers with the highest *meta*-link concentration. This means that any excitation has a reasonable chance to migrate to a nearby longer conjugation length segment to emit, hence little change in the photoluminescence spectrum would be expected until the probability of several nearby longer conjugation length segments is reduced. This would red-shift the emission, disguising the effect that the addition of the meta links to the polymer chain produces. To investigate the effect of reduced conjugation length on the emission spectrum, the energy at which half the area under the PL spectrum lies was calculated. This is presented as a function of meta content in Figure 4-33. The largest change observed is 0.15eV between the 35% and 42% meta containing copolymer, i.e. at the same point as that found for the peak of the

absorption. This suggests an average conjugation length in pyridine films of between 3 and 4 repeat units.

There is, however, another complication in the copolymer film photoluminescence. The chemical synthesis of the copolymer seems to have a significant effect on the properties of the polymer. Three batches of the 35% *meta*-linked copolymer were made and each displays different characteristics. The first batch was prepared at a temperature of 65°C whereas the second and third batches were prepared at 80°C. There may be a difference in the size of the kinetic barriers to polymerisation between the 2,5- and the 2,6-dibromopyridine and the change in temperature is an effort to reduce any effect that this may have. The photoluminescence spectrum from films of each of the batches are shown in Figure 4-34. The difference between the spectra of the 2nd and 3rd batch thought to arise from stray light in the measurement set-up (polymers containing *meta*-links have PL spectra which are more difficult to measure due to the weak PL that they exhibit).

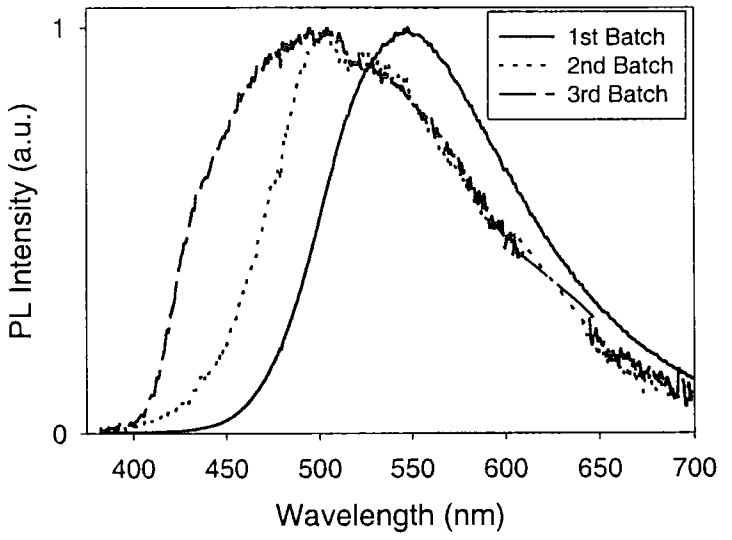

Figure 4-34 *Photoluminescence spectra of film samples of 3 batches of a 35% copolymer of para and meta linked polypyridine*

The temperature increase seems to have a considerable effect as a 3% copolymer synthesised at 80°C has optical properties which are inconsistent with the behaviour expected. As shown in Figure 4-29 and Figure 4-30, the 3% copolymer has an increase in the higher energy emission and absorption that should be only seen from the higher meta content copolymers. The action of the higher temperature may be to polymerise several *para* and *meta* links together, hence producing more *para* and *meta* character than a truly random copolymer would produce.

The use of a higher temperature in the reaction should provide a copolymer with different properties than synthesis at a lower temperature, if there is a difference in the kinetics of polymerisation of the 2,5- and 2,6-dibromopyridines. Figure 4-34 suggests that this is the case as there is considerably increased *meta*-type luminescence in the polymers prepared at a higher temperature. This is particularly evident in Figure 4-29 and Figure 4-30, where the 3% copolymer has more meta-type character than some of the higher meta content copolymers synthesised at a lower temperature.

The data also shows the haphazard colour tuning produced by the *meta*-linked copolymers. This is illustrated by a CIE(X,Y) colour co-ordinate diagram of the copolymers, shown in Figure 4-35.

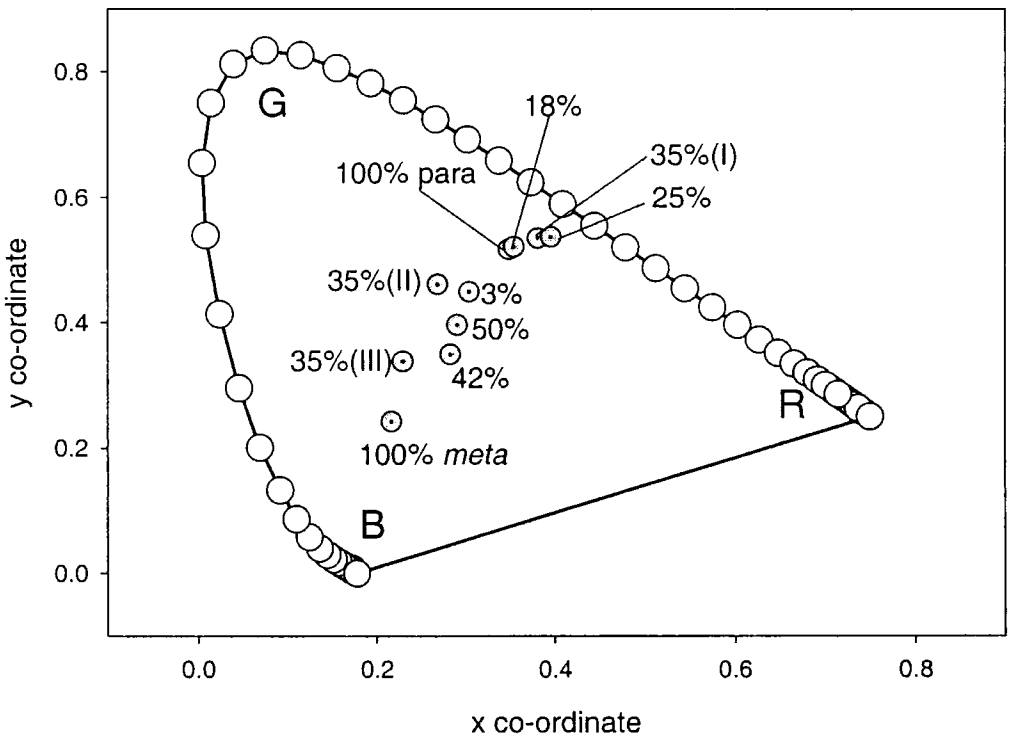

Figure 4-35 *CIE(X,Y) colour diagram showing the colour co-ordinates of para and meta linked copolymers*

The low percentage copolymers synthesised at 65°C show little colour change from the 100% *para*-linked polymer. Only the 50% *meta*-linked polymer shows a significant change in colour. The batches made at 80°C (35% (II and III) and 3%) show a considerable change in colour, but none approach the blue colour of the 100% *meta*-linked polymer. The 42% copolymer has the largest shift towards the 100% *meta* linked polymer.

Discussion of Copolymers in Solution

The absorption spectra of solutions of copolymers (Figure 4-32) suggest that the formation of ring rotations in polypyridine solution limits the conjugation length to around 3 repeat units. There is no significant change from the spectrum of 100% *para* linked PPY, even when the *meta* content is 50% (3 repeat units). It is not until there is only *meta* links (P*m*PY) that there is a significant change in the absorption spectrum (Figure 4-25). Even then, there is significant absorption coincident with the peak of the P*p*PY absorption, and absorption at higher energies suggesting conjugation lengths of 3 repeat units (an average *para* length of 1 unit and the conjugation length increased by the presence of two *meta*-linked units at both sides of the *para*-linked section) and smaller.

The photoluminescence spectra of solutions of the various copolymers (Figure 4-31) are also very similar, with each batch exhibiting a PL peak at between 2.45 and 2.49eV. In contrast to the absorption spectra, however, the PL spectra are dissimilar in shape and position to both the 100% *meta* and 100% *para* linked polymers. There is a 0.58eV and 0.33eV shift from the peak PL of P*m*PY and P*p*PY respectively. This may be a consequence of the change in the nature of the polymer chain. The pure *para* and *meta* linked polymers are rigid rod polymers, but the *meta* links in the copolymer allow the chain to be flexible and allow coiling of the chain. The coiling of PmPY-co-PpPY chains in solution is observed in light scattering measurements, performed by Hugh Burrows at Uppsala University, Sweden. Coiling of the polymer chain would facilitate the migration of excitations to longer conjugation length segments, resulting in a red shift of the photoluminescence spectrum.

POLY(6-HEXYL PYRIDINE)

A hexyl substituent on the pyridine ring can provide a polymer with improved solubility, i.e. a polymer soluble in a wide range of organic solvents. With a view to creating a more soluble derivative of PPY, a hexyl group was added to the monomer units before polymerisation took place. The hexyl group is in the 6 position on the ring, thus giving poly(6-hexyl pyridine) (PhexPY). Its chemical structure is shown below.

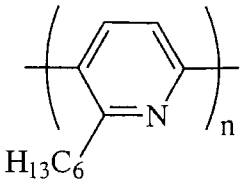

Figure 4-36 *Chemical structure of poly(6-hexyl pyridine)*

The absorption and photoluminescence of polyhexylpyridine in film and formic acid solution was measured and is shown as Figure 4-37.

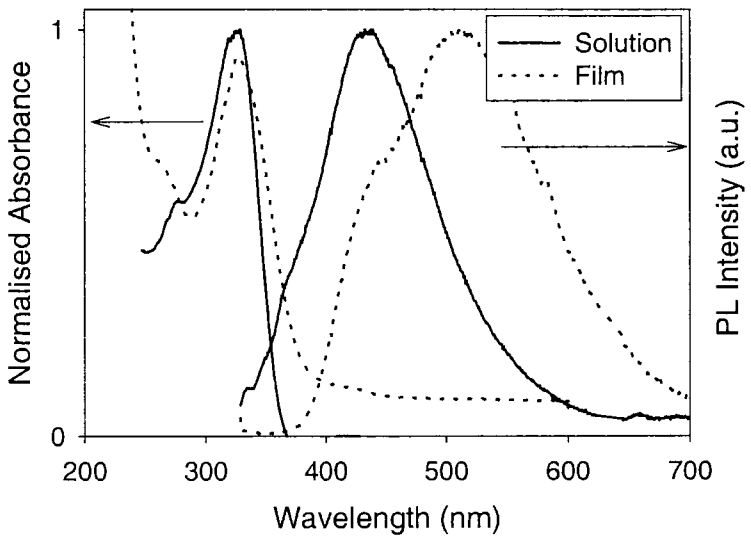

Figure 4-37 *Absorption and luminescence spectra of PhexPY solution (solid line) and film (dotted line)*

The absorption maxima of the solution and film have a similar peak position at 329nm (3.77eV) and 327nm (3.79eV) respectively. The peak of the luminescence is 439nm (2.82eV) for solution and 515nm (2.41eV) for film. The absorption of the PhexPY is blue shifted by 38nm (0.39eV) from that of PPY solution and by 61nm (0.59eV) from that of PPY film. The photoluminescence maximum in solution is coincident with that of PPY solution. The film PL of the PhexPY is blue shifted by 22nm (0.1eV). There is a secondary peak on the film PL spectrum which is coincident with the peak of the solution PL.

The range of solvents in which the polymer is soluble is increased. In addition to the acid solutions in which PPY is soluble, PhexPY is soluble in polar organic solvents such as THF, Acetone, DMF, chlorobenzene, chloroform and sparingly in toluene.

Discussion

The addition of the large hexyl group on the ring would be expected to increase the amount of ring twists due to the steric effects of the group. This is manifested in the absorption spectra which show a 0.39eV and 0.59eV blue shift in solution and film compared to unsubstituted PPY. Additional ring twists would be expected to limit the conjugation length, leading to a blue shifted absorption and emission. The photoluminescence in solution is similar to the unsubstituted PPY suggesting that in solution PPY has an already restricted conjugation length through normal rotation of the monomers out of plane. The film photoluminescence exhibits a very small blue shift compared to PPY film, suggesting that the hexyl group can reduce the close ordering evident in PPY films, hence preventing some of the reduction of the ring twists, hence limiting the conjugation length. This is further suggested by the secondary peak in the luminescence spectrum at the same wavelength as the peak of the solution emission. The intensity of the secondary peak appears to be relatively large suggesting that a large proportion of the emission arises from shorter conjugation length segments which must form a proportion of the distribution of conjugation lengths. This higher energy emission occurs even though there should be a reduction in the amount of excitations on higher energy segments due to excitation migration to longer chains. The relative intensities of the emission suggest that there may be a reduction in the excitation mobility and/or there are a considerable number of short chain segments suggesting most rings are twisted. The secondary peak in the film emission produces a broad spectrum and X,Y,Z colour co-ordinates close to those of the point of equal energy (a white light source), as shown in Figure 4-40. The values of (0.257, 0.344) are quite close to the (0.333, 0.333) required for a point of equal energy and hence the film emission looks relatively white. The solution photoluminescence produces X,Y,Z colour co-ordinates suggesting very blue emission (Figure 4-40).

Copolymers with 6-hexyl pyridine

A random copolymer of 6-hexyl pyridine and pyridine monomer units was also synthesised. 25% of the starting monomer was the hexyl substituted monomer, 75% was the standard 2,5-dibromopyridine monomer. This produces poly(6-hexyl pyridine-co-*p*-pyridine) (PhexPY-co-PPY).

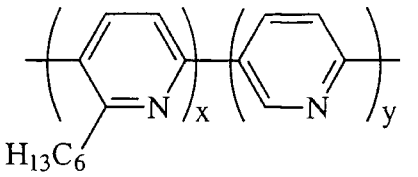

Figure 4-38 *Chemical structure of poly(6-hexyl pyridine-co-p-pyridine)*

The copolymer has different properties to the poly(6-hexyl pyridine), and is soluble in a smaller range of solvents, essentially the same range of solvents as unsubstituted polypyridine. The absorption and photoluminescence of the copolymer solution and film is shown in Figure 4-39.

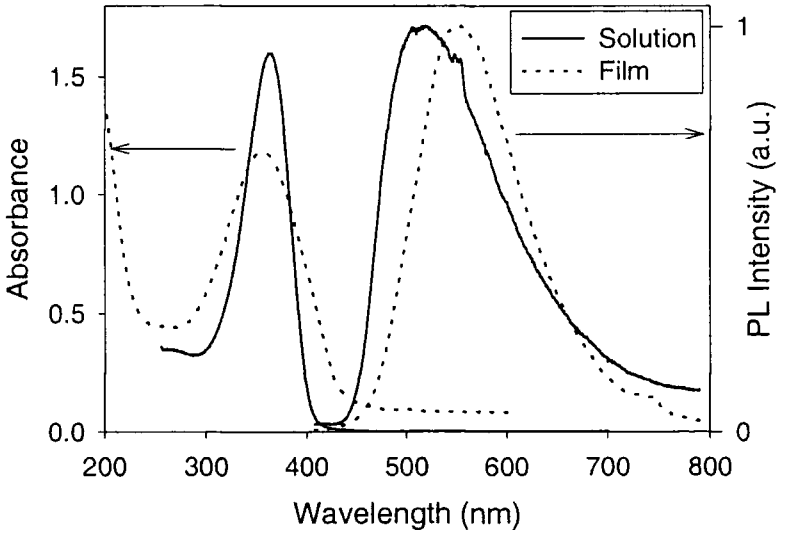

Figure 4-39 *Absorption and photoluminescence of PhexPY-co-PPY polymer solution (solid line) and film (dotted line)*

The peak of the absorption is at 363nm (3.42eV) in formic acid solution and 357nm (3.47eV) for film. The peak of the luminescence is at 519nm (2.39eV) in solution and 555nm (2.23eV) for film. The absorption is red-shifted from that of the PhexPY by 0.35eV for solution and 0.32eV for film. The photoluminescence is red-shifted from that of the PhexPY by 0.43eV in solution and 0.18eV in film. The absorption is blue-shifted from that of the PPY by 0.04eV (≈0) for solution and 0.27eV for film. The photoluminescence is red-shifted from that of PPY by 0.43eV in solution and 0.08eV (≈0) in film.

The CIE(X,Y) colour diagram contrasting the colour change between the photoluminescence of PhexPY, the PhexPY-co-PPY and unsubstituted PPY is shown in Figure 4-40.

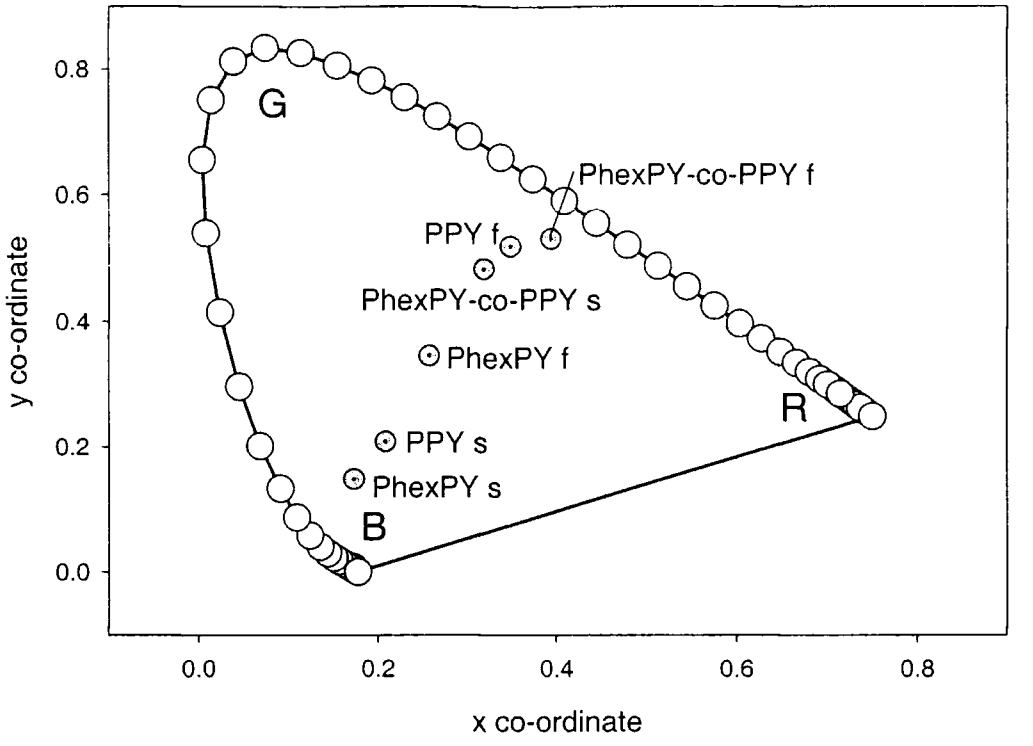

Figure 4-40 *CIE(X,Y) colour diagram for solution (s) and film (f) photoluminescence of PhexPY, PhexPY-co-PPY and unsubstituted PPY*

Discussion

The red-shifted absorption and emission of the copolymer from PhexPY in film and solution is expected as the unsubstituted pyridine rings will separate the hexyl substituted rings and limit the steric interaction of the hexyl groups. This would reduce the probability of steric induced ring twists found in PhexPY and hence increase the number of longer conjugation length segments, leading to a red-shift of the absorption and photoluminescence.

The similar peak position of the absorption and photoluminescence in solution and film suggests that the hexyl groups prevent the close packing and high ordering of the polymer chains. This prevents the reduction of the ring twists and produces similar energy absorption and emission in solution and film. The colour co-ordinates of the copolymer solution and film emission, shown in Figure 4-40, are far closer together than the corresponding co-ordinates of PPY or PhexPY.

The blue-shifted absorption relative to PPY would be expected as there are additional ring twists introduced by the steric effects of the hexyl groups. The red-shifted emission in solution may be a result of solvent interaction with the hexyl substituent.

REGULAR COPOLYMERS WITH 4-HEXYL PYRIDINE

Regular copolymers containing a hexyl derivative of pyridine have been prepared by Dr Chang-Sheng Wang in the Department of Chemistry, University of Durham. Regular copolymers have alternating monomer units rather than the statistical distribution of random copolymers. Two types of copolymer have been prepared, using 4-hexyl-2,5-pyridinediyl as one monomer unit and *p*-phenylene or 2,5-dimethoxy-1,4-phenylene as the other monomer unit. The copolymers are poly(4-hexyl-2,5-pyridine-co-*p*-phenylene) (CSW-6) and poly(4-hexyl-2,5-pyridine-co-2,5-dimethoxy-1,4-phenylene) (CSW-25). The chemical structure of these polymers is shown below.

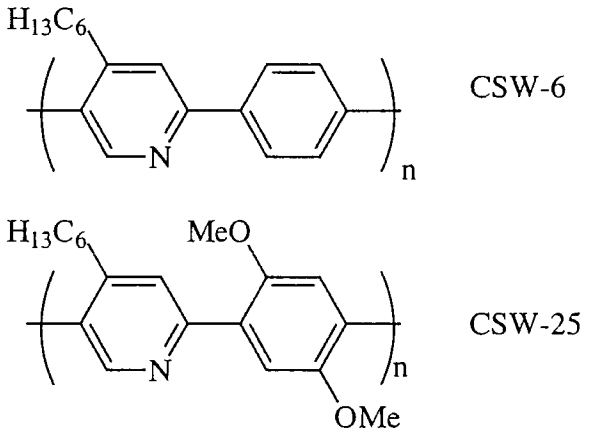

Figure 4-41 *Chemical structures of CSW-6 and CSW-25*

The absorption and photoluminescence spectra of CSW-6 solution and film is shown in Figure 4-42. The peak of the absorption of CSW-6 solution and the low energy peak of the film is at 332nm (3.73eV) and the peak of the emission is at 438nm (2.83eV) for solution and film.

The absorption and photoluminescence spectra of CSW-25 solution and film are shown in Figure 4-43. The peak of CSW-25 solution absorption is at 364nm (3.41eV) and the peak of the low energy absorption in the film sample is at 348nm (3.56eV). The peak of the photoluminescence is at 429nm (2.89eV) in solution and 438nm (2.83eV) in film.

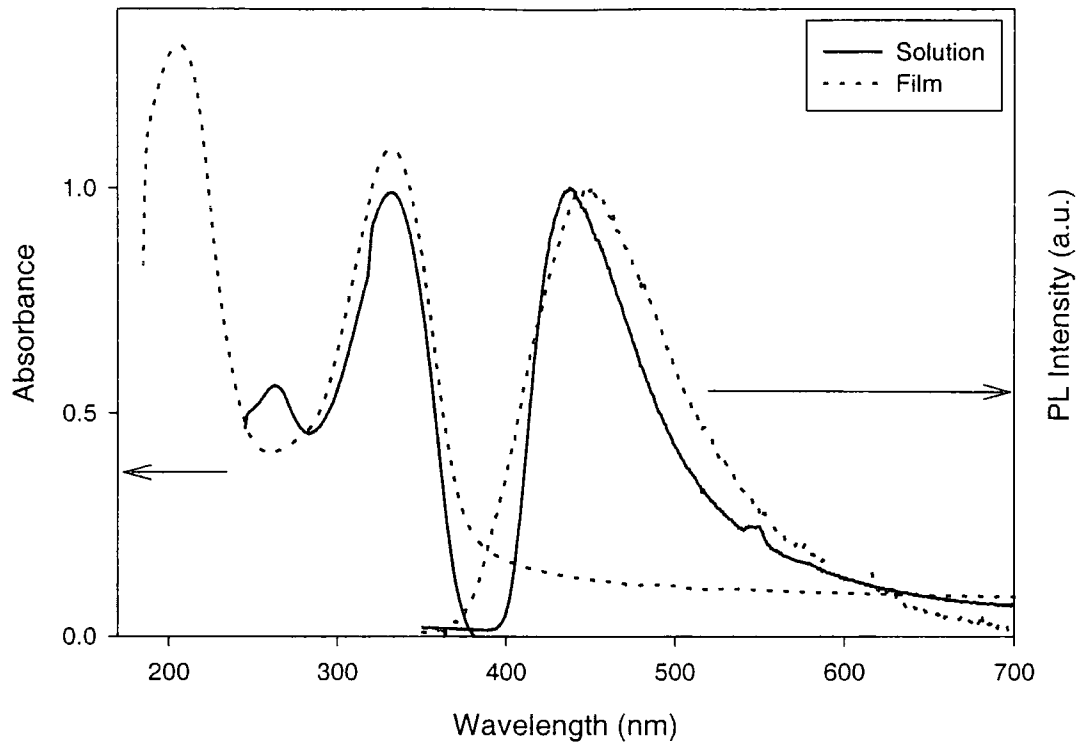

Figure 4-42 *Absorption and luminescence spectra of CSW-6 in formic acid solution (solid line) and film (dotted line)*

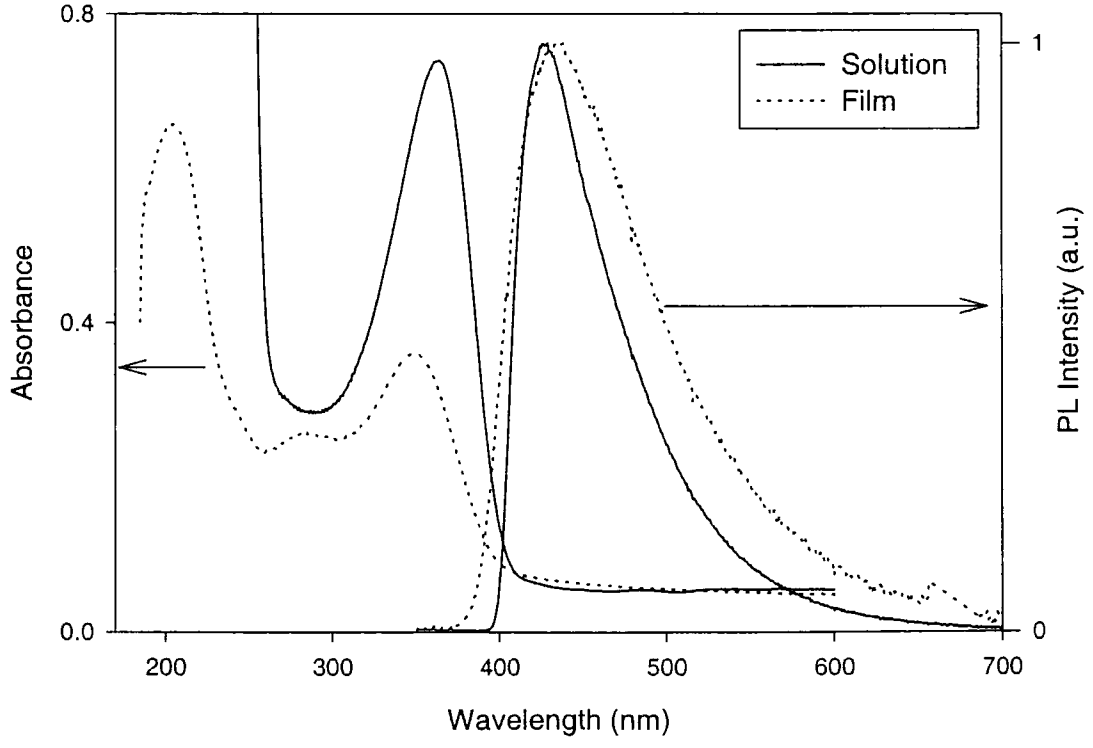

Figure 4-43 *Absorption and photoluminescence of CSW-25 solution (solid line) and film (dotted line)*

Further information of the effect that the methoxy substituted phenylene ring has on the optical properties of the polymer can be obtained from the comparison of the PL spectra of CSW-25 with CSW-29, a regular copolymer of 2,5-pyridinediyl and 2,5-dimethoxy-1,4-phenylene. The chemical structure of CSW-29 is shown in Figure 4-44.

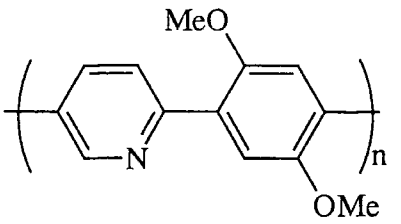

CSW-29

Figure 4-44 *Chemical structure of CSW-29*

The PL spectra of CSW-25, CSW29 and unsubstituted P*p*PY are shown below.

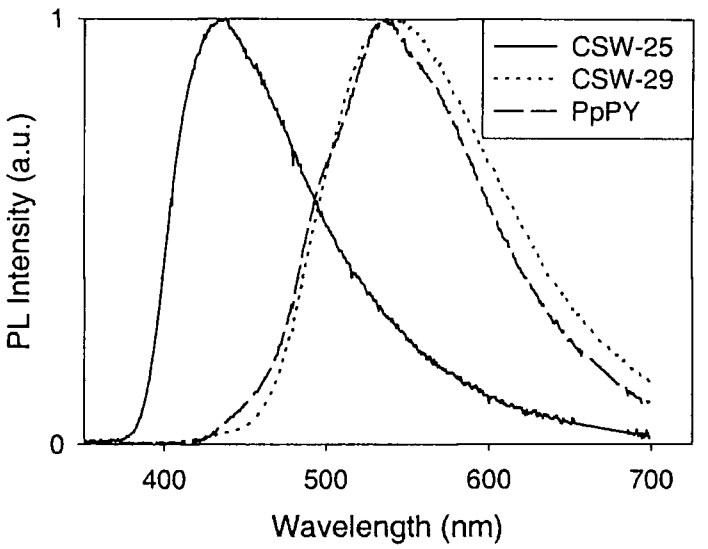

Figure 4-45 *Photoluminescence spectra of CSW-25, CSW-29 and PpPY films*

It can be seen from Figure 4-45, that the PL spectrum of CSW-29 closely resembles that of P*p*PY and not CSW-25. The peak of the luminescence is at 541nm (2.29eV), compared to the PL peak of 438nm in CSW-25 film and 537nm (2.31eV) for PPY. The colour co-ordinates of the films of the CSW polymers, compared to those of PPY, are shown below.

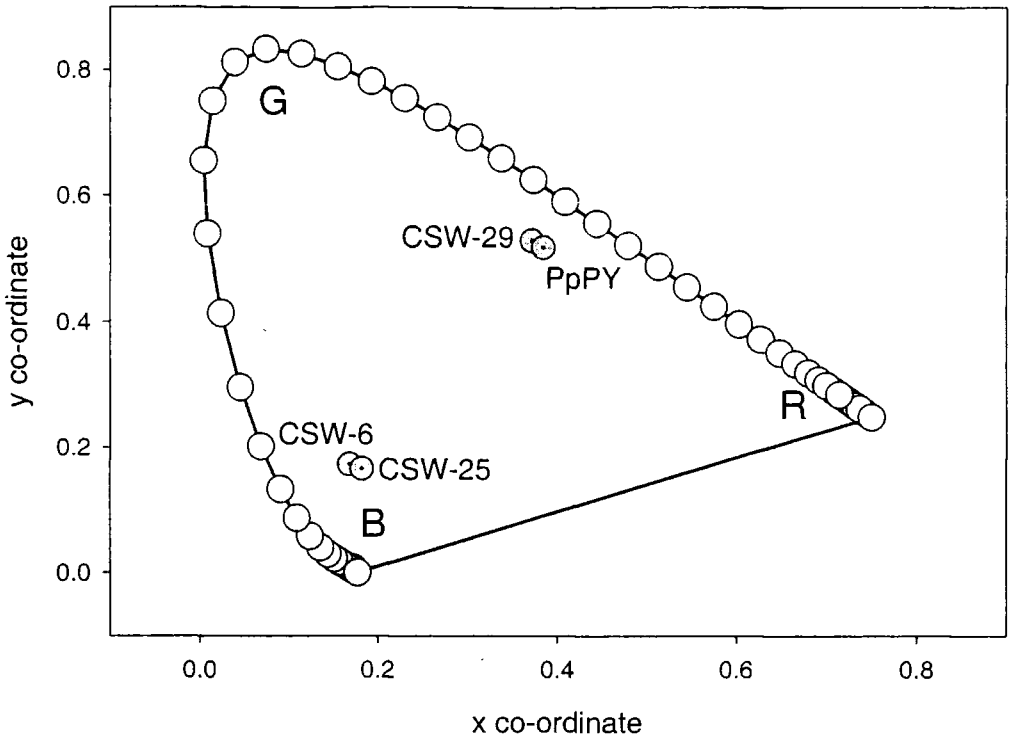

Figure 4-46 *Colour co-ordinates of CSW-6, CSW-25, CSW-29 and PPY film photoluminescence*

It can be seen from Figure 4-46 that the emission from CSW-6 and CSW-25 is in the blue region of the spectrum. The emission of CSW-29, however, is very similar in colour (green/yellow) to that of PPY.

Discussion

The regular copolymers with PhexPY monomers produce very blue emission, with a film emission peak position similar to that of PhexPY in solution. There is little difference in the optical spectra of CSW-6 and CSW-25, suggesting that the addition of the methoxy side groups to the phenylene monomer has little effect on the electronic states of the polymer. The inclusion of the dimethoxy substituted phenylene ring in the CSW-29 copolymer appears to produce a photoluminescence spectrum very similar to that of P*p*PY (Figure 4-45). The peak position of poly(*p*-phenylene) film emission is at 3.09eV, similar in position to the peak of the emission of CSW-6, CSW-25 and PhexPY solution, hence little noticeable modification may be expected. The small change in the spectrum of the CSW-29 polymer suggests that the phenylene ring has very little effect on the PL of the polymer, which is almost identical to that of P*p*PY. The addition of a hexyl group to the pyridine ring, however, produces a very large

effect. This means that the shifts observed for CSW-25 and CSW-6 must be brought about by the change in packing of the polymer chains.

POLY(*P*-PHENYLENE VINYLENE)

Poly(*p*-phenylene vinylene) is a commonly used luminescent polymer with well characterised properties. The polymer provides robust, high quality films which can be used in photoluminescence and electroluminescence experiments.

The absorption spectrum of a film of the precursor polymer and the fully converted poly(phenylene vinylene) (PPV) film is shown below. The film was converted on a quartz substrate, in vacuum, at 250°C for 10 hours.

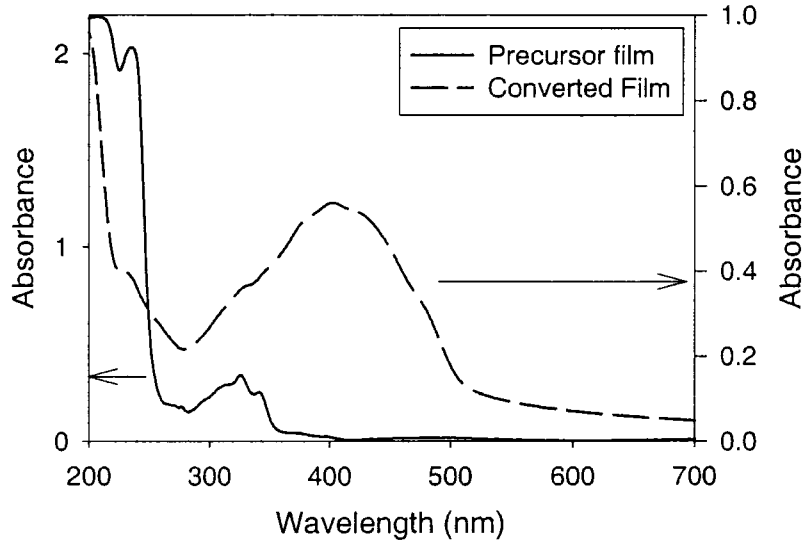

Figure 4-47 *Absorption spectra of PPV precursor film (solid line) and converted precursor film (broken line)*

The converted film has a large absorption peak at around 400nm (3.10eV), whereas the precursor has a small absorption peak at 330nm (3.76eV). Both have a strong absorption at around 200nm (6.20eV), with two peaks resolved. The lower energy peak is reduced in intensity compared to the higher energy after conversion. The results are similar to those shown by Herold *et al* [10], with similar behaviour of the absorption spectrum with increasing conversion. In this reference, the evolution of the peak at 400nm is better illustrated as the absorption spectrum is shown for several different amounts of conversion, not just the two shown above.

The absorption spectra of PPV converted on indium tin oxide (ITO) and on quartz are shown in Figure 4-48.

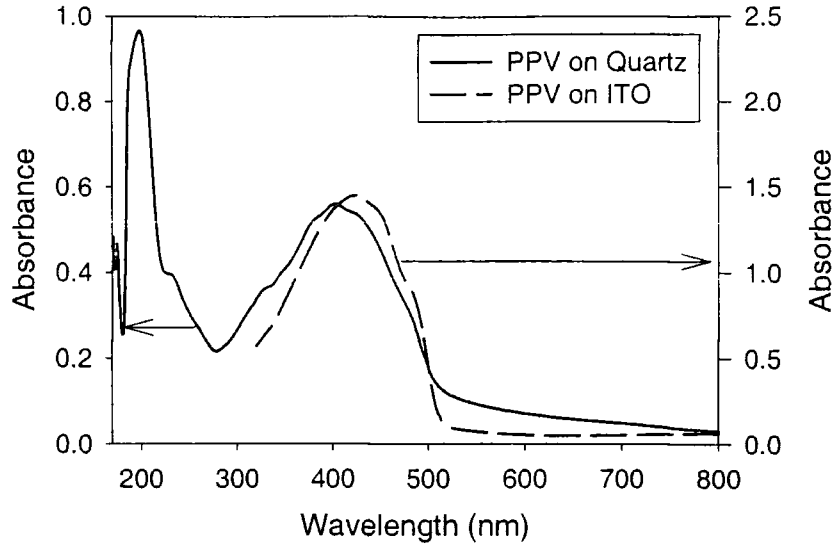

Figure 4-48 *Absorption spectra of PPV converted on quartz (solid line) and ITO (broken line)*

The absorption spectra of PPV converted on different substrates show little difference. Both have absorption peaks at around 400nm (3.10eV), with very little difference in the shape of the absorption. Absorption details at wavelengths less than 320nm are lost due to the absorption of the ITO in this region.

The absorption and photoluminescence spectra of PPV converted on quartz are shown below.

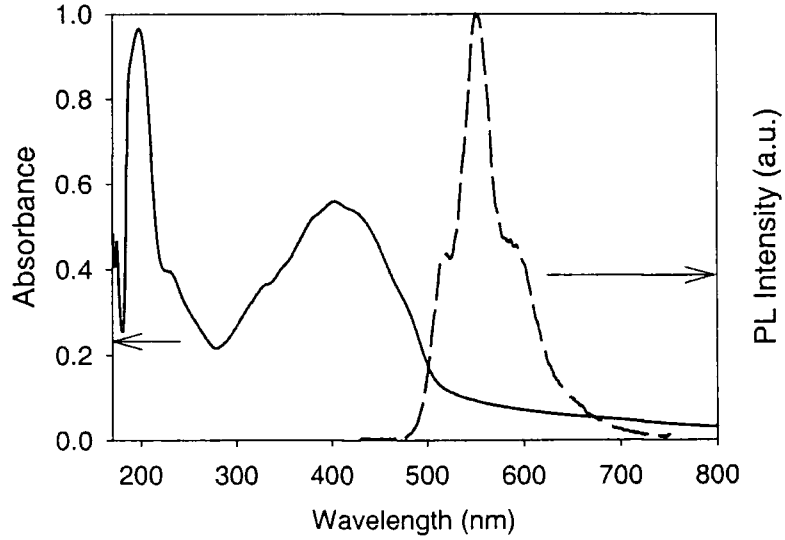

Figure 4-49 *Absorption and photoluminescence spectra of PPV converted on a quartz substrate*

The photoluminescence spectrum has a peak at 551nm (2.25eV). The are two strong vibronic shoulders at 518nm (2.39eV) and 590nm (2.10eV). The apparent

Stokes shift is 0.85eV. The FWHM of the emission is 0.18eV, though the vibronic peaks add to the width below the half-maximum point. The photoluminescence spectra of PPV converted on quartz and ITO substrates are shown in Figure 4-50.

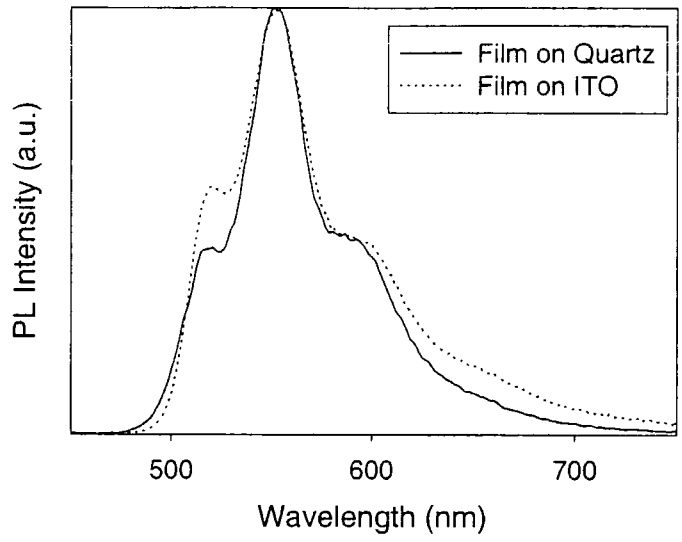

Figure 4-50 *Photoluminescence spectra of PPV converted on quartz (solid line) and ITO (dotted line) substrates*

The photoluminescence spectrum of PPV converted on ITO is changed slightly, with enhancement of the higher energy vibronic peak and slightly increased intensity from the low energy tail of emission.

The emission of PPV peaks at around 551nm, very close to the peak of the eye response at 555nm. The CIE X,Y,Z colour co-ordinates of PPV are (0.392, 0.582) and the emission is green/yellow.

Discussion

The changes in the photoluminescence spectrum due to conversion on ITO substrates could be a consequence of doping of the PPV by some contaminant from the ITO. The increased relative intensity of the first vibronic peak is also found, more pronounced, in reference [10]. In this reference, emission from PPV converted on ITO has a high energy vibronic peak with a higher relative intensity than the peak at 550nm. PPV converted on an ITO-less region (i.e. a region from which the ITO had been removed), however, shows a higher relative intensity from the peak at 550nm, compared to the high energy vibronic peak. This means that conversion of PPV on ITO has an effect on the polymer film which affects its optical properties. Another effect of conversion on ITO coated substrates is to significantly reduce the PLQY of

the polymer [10, 11]. Doping of PPV converted on ITO has been reported [12-15], and it has been suggested that the change in spectrum is due to doping of the polymer by $InCl_3$, which reduces the PL efficiency of the polymer and contributes to the eventual failure of an electroluminescent device [11, 12, 14]. This doping does reduce the turn-on voltage however (see for example references [11, 12]). In addition to the $InCl_3$ doping, oxygen on or in the ITO could play an important role. PPV is known to be particularly sensitive to oxygen, and the vinylene group is very vulnerable to oxidation, forming carbonyl groups and reducing the PLQY of the polymer [16, 17] and producing possible changes in the PL spectrum.

MEH-PPV

Poly(2-methoxy, 5-(2'ethyl-hexyloxy)-*p*-phenylene vinylene), or MEH-PPV, is a soluble derivative of PPV. The methoxy side chains improve the solubility of the polymer so that it is soluble in common organic solvents and also red-shift the emission from that of PPV. The polymer is available in powder form, which is soluble in chlorobenzene, chloroform, xylene and other organic solvents. It is also available in precursor form, as a precursor polymer requiring thermal treatment to produce the MEH-PPV via a chloride leaving group.

Soluble MEH-PPV

The results presented below are for solutions of MEH-PPV powder in chlorobenzene and films prepared by spin-coating from chlorobenzene solution. The absorption and photoluminescence spectra of MEH-PPV in chlorobenzene solution is shown in Figure 4-51. The peak of the solution absorption is 504nm (2.46eV) and that of film is 489nm (2.54eV). The peak of luminescence in solution is at 569nm (2.18eV) and the peak of PL in film is 628nm (1.97eV).

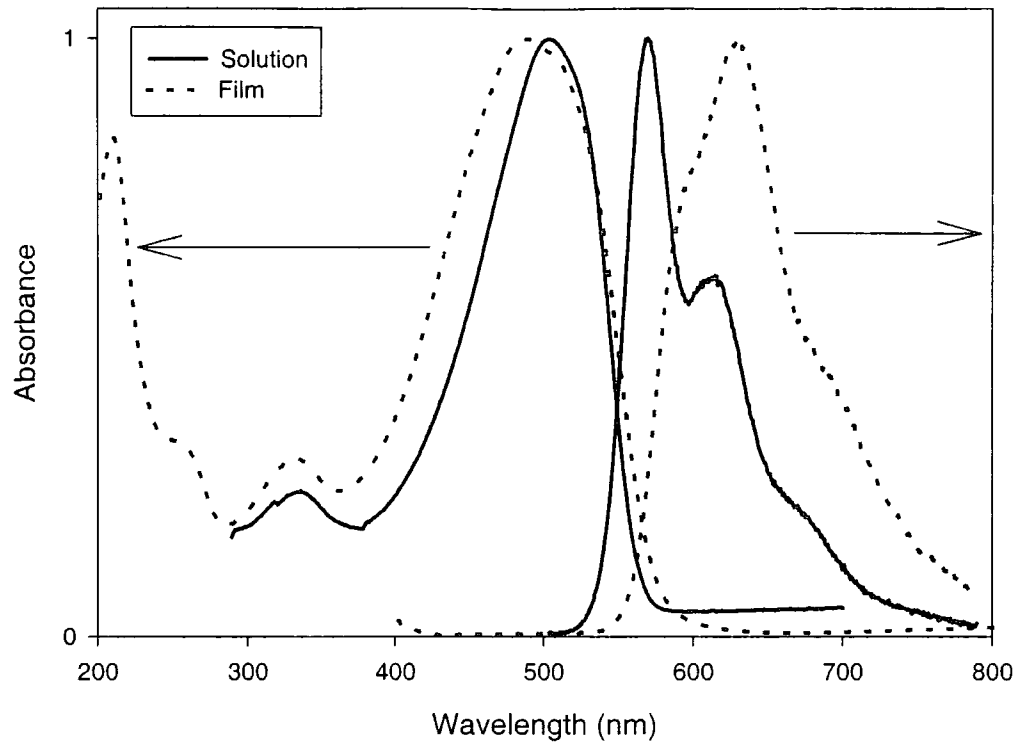

Figure 4-51 *Absorption and photoluminescence spectra of MEH-PPV solution and film*

The shape of the absorption is quite similar in both solution and film, although the photoluminescence spectra are different. This can be seen on an energy scale.

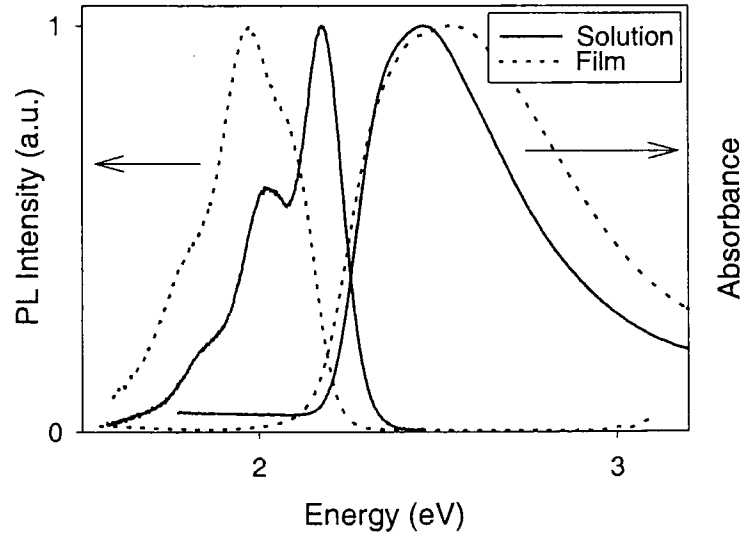

Figure 4-52 *Absorption and photoluminescence spectra of MEH-PPV solution and film on an energy scale*

Discussion

The high energy vibronic feature on the solution spectrum, the most intense vibronic peak, is reduced in intensity in the film spectrum, and the second highest vibronic peak is the most intense. This suggests a rearrangement of the molecule in film due to the packing of the polymer chains.

Precursor MEH-PPV

MEH-PPV films were prepared by spin-coating substrates with MEH-PPV precursor in THF solution. The polymer was made by thermal conversion at 160°C for 10 hours.

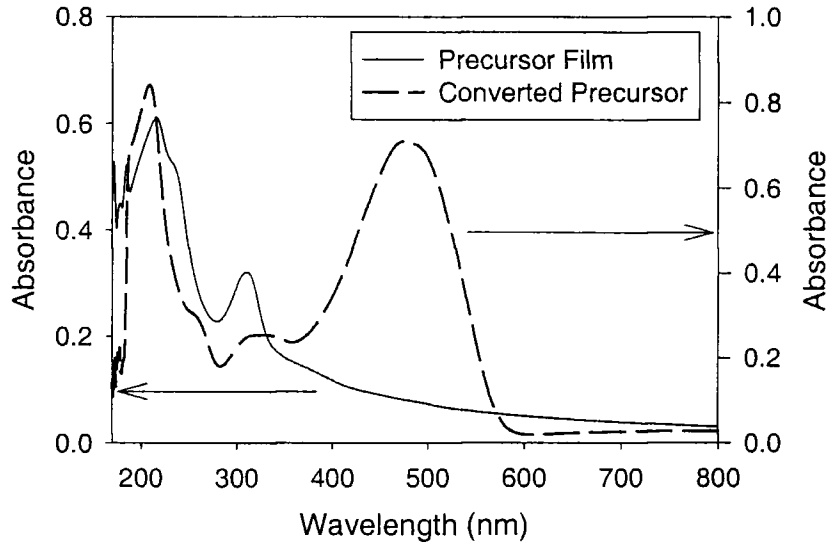

Figure 4-53 *Absorption spectra of MEH-PPV precursor before (solid line) and after thermal conversion (broken line) on a quartz substrate*

The absorption spectra of precursor and converted MEH-PPV shows the action of the conversion process. The large absorption peak at 490nm appears after thermal conversion has taken place and the absorption band at 300nm in the precursor disappears. The absorption spectra of the MEH-PPV prepared via the precursor route is different to that of the solution route MEH-PPV, as shown in Figure 4-54.

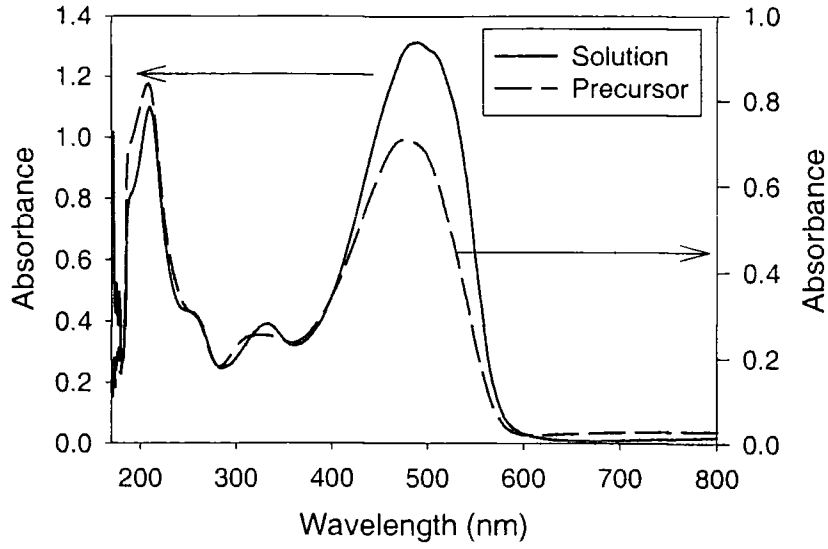

Figure 4-54 *Absorption spectra of solution (solid line) and precursor route (broken line) MEH-PPV films*

The photoluminescence spectra of the solution and precursor MEH-PPV are also similar, but not identical.

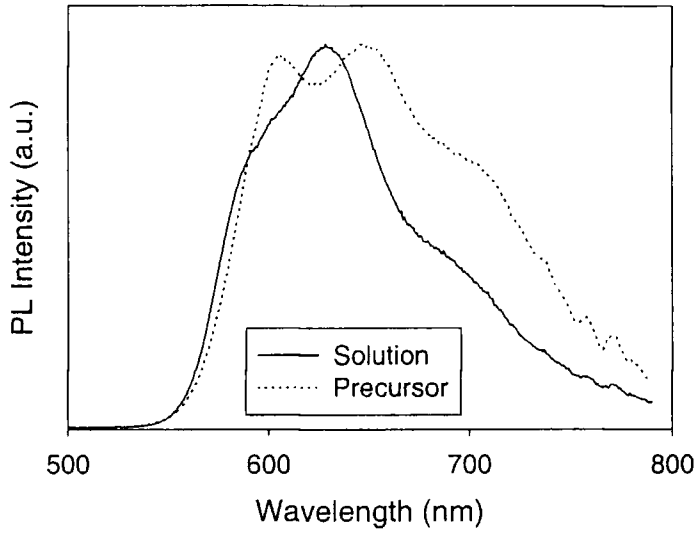

Figure 4-55 *Photoluminescence spectra of solution route (solid line) and precursor route (dotted line) MEH-PPV films*

The photoluminescence spectrum of the precursor route MEH-PPV shows a relatively larger intensity for the higher energy vibronic, and hence the two higher energy vibronic peaks show almost the same intensity. This is in contrast to the solution route MEH-PPV which has a higher relative intensity for the second vibronic peak rather than the first (highest energy peak). The change in the relative intensities changes the peak of the luminescence from 628nm (1.97eV) to 647nm (1.92eV).

There is a considerable difference in the absorption and photoluminescence of MEH-PPV precursor converted on different substrates. The PL spectra of the precursor MEH-PPV converted under identical conditions on a quartz and an ITO substrate are shown below.

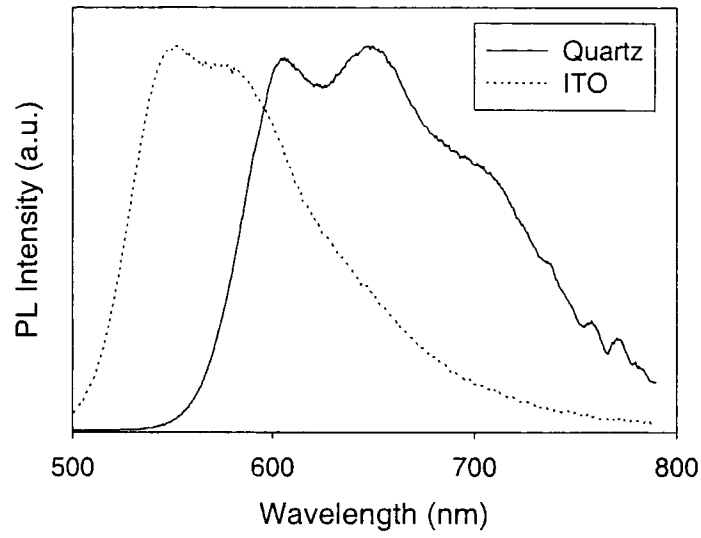

Figure 4-56 *Photoluminescence spectra of MEH-PPV precursor converted on quartz (solid line) and ITO (dotted line) substrates*

Figure 4-56 illustrates the large blue-shift and change in shape that is observed when MEH-PPV precursor is converted on ITO. The peak position is changed from 647nm for MEH-PPV precursor converted on quartz to 552nm (2.25eV) and this changes the colour substantially. The change in the emission is accompanied by a change in the absorption spectrum, shown in Figure 4-57.

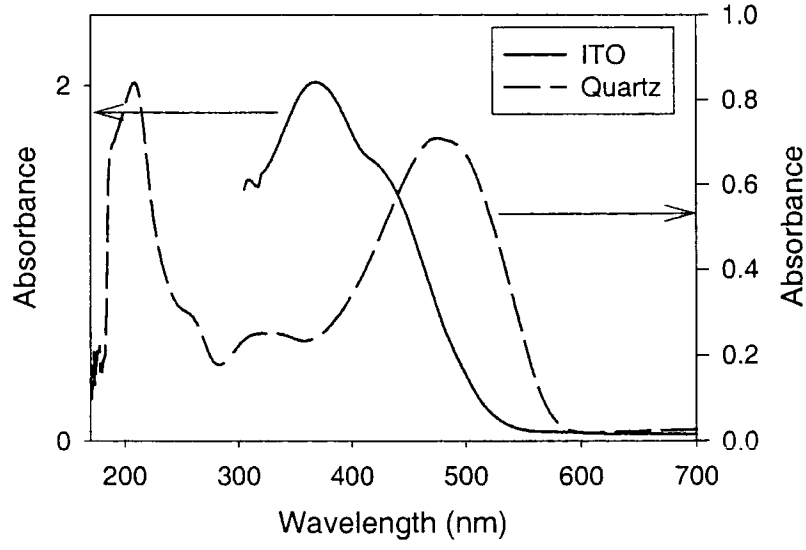

Figure 4-57 *Absorption spectra of MEH-PPV converted on ITO (solid line) and quartz (broken line)*

The peak of the absorption is shifted from 489nm (2.54eV) to 369nm (3.36eV). The ITO absorption masks any change at wavelengths shorter than 320nm. The shape of the absorption changes substantially when the precursor is converted on ITO, and a vibronic peak appears at around 425nm. There is very little absorption around 500nm.

Discussion

The change in the relative intensities of the vibronic peaks seen for MEH-PPV solution and film in Figure 4-52 could be partially due to self absorption effects, though the similarity of the film and solution absorption suggests that there is a difference in the molecular arrangement in solution and film. A similar change is also observed between films of a precursor MEH-PPV film converted on quartz and a film prepared by the solution route (Figure 4-55), which again, cannot be accounted for by self absorption due to the very similar absorption spectra (Figure 4-54). A change in the ordering of the polymer in the precursor prepared film is not entirely surprising, this is one of the major reasons for using a precursor polymer. The heat during the conversion process may be expected to yield a film with improved ordering.

The difference in the absorption spectra of the precursor prepared polymer and the solution prepared (Figure 4-54) is understandable. The absorption peak at around 500nm appears after conversion and is a product of the increased conjugation following the elimination of the chloride leaving group on the vinylene section of the polymer (Figure 4-53). The smaller relative intensity of the peak at 500nm compared to that at around 200nm in the precursor prepared polymer may be due to the reduced conjugation obtained via the precursor route. The solution route polymer is almost fully conjugated through the vinylene group when prepared, whereas the precursor must be converted and 100% conversion (i.e. 100% elimination of the chloride leaving group) would not be expected. The introduction of these conjugation defect sites (in this case accidentally through the use of a precursor polymer) can produce a polymer with a higher PLQY, by localising the excitation and preventing migration to quenching sites.

COLOUR OF EMISSION OF PPV DERIVATIVES

The CIE X, Y, Z colour co-ordinates of PPV and PPV derivatives are shown in Figure 4-58.

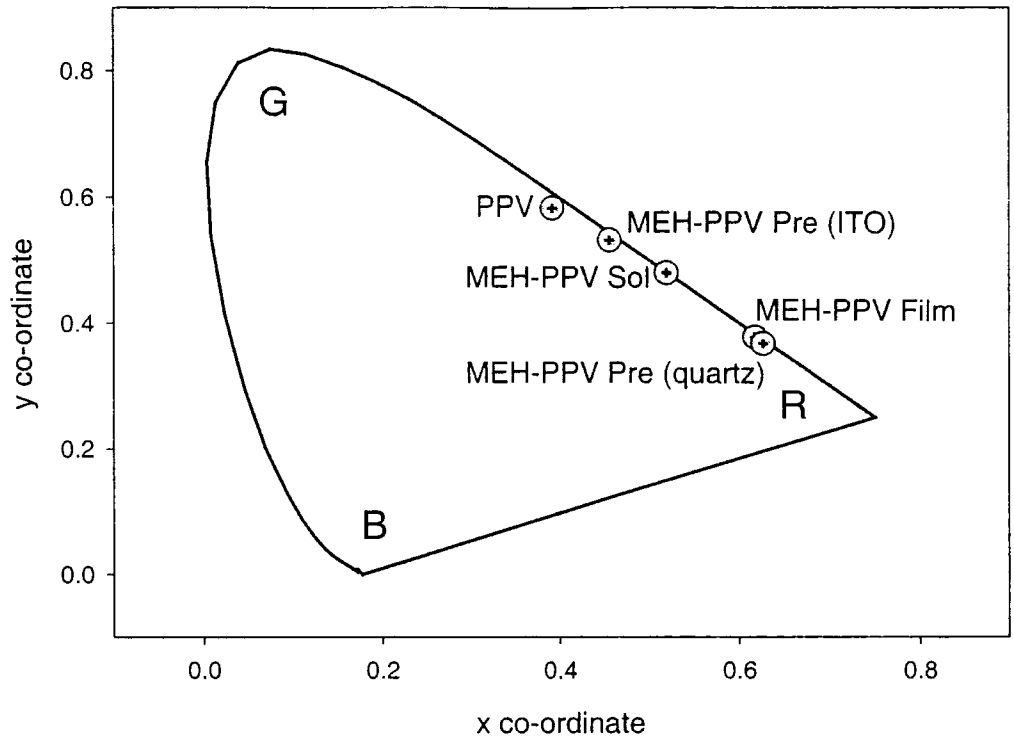

Figure 4-58 *Colour co-ordinates of PPV and MEH-PPV solution, film (from chlorobenzene solution) and MEH-PPV precursor converted on quartz and ITO substrates*

The difference in colour between the precursor polymer converted on ITO and quartz is considerable, as shown in Figure 4-58. The emission is closer to that of PPV than MEH-PPV, suggesting significant changes in the polymer film. The (r,g) co-ordinates of the precursor converted on quartz are (0.847, 0.149), whereas the precursor converted on ITO has the red value reduced and the green value increased to (0.529, 0.464), much closer to that of PPV (0.376, 0.604). Doping and/or chemical reaction of the film with a species from the ITO (possibly $InCl_3$ as for the PPV case [12]) during conversion is the most likely reason.

REFERENCES

[1] D. D. Gebler, Y. Z. Wang, J. W. Blatchford, S. W. Jessen, H.-L. Wang, T. M. Swager, A. G. MacDiarmid and A. J. Epstein, J. Appl. Phys., **78** , 6 (1995), 4264-4266.

[2] J. W. Blatchford, S. W. Jessen, L.-B. Lin, T. L. Gustafson, D.-K. Fu, H.-L. Wang, T. M. Swager, A. G. MacDiarmid and A. J. Epstein, Phys. Rev. B, **54** , 13 (1996), 9180-9189.

[3] T. Yamamoto, et al., J. Am. Chem. Soc., **116** , (1994), 4832-4845.

[4] A. P. Monkman, To be published, , (1998), .

[5] L. Patterson, To be published, , (1998), .

[6] J. W. Blatchford, T. L. Gustafson and A. J. Epstein, J. Chem. Phys., **105** , 20 (1996), 9214-9226.

[7] G. Greczynski, Master of Science Thesis, Linkoping, 1997.

[8] G. Greczynski, To be published, , (1998), .

[9] C. M. Heller, I. H. Campbell, B. K. Laurich, D. L. Smith, D. D. C. Bradley, P. L. Burn, J. P. Ferraris and K. Mullen, Phys. Rev. B, **54** , 8 (1996), 5516-5522.

[10] M. Herold, J. Gmeiner, W. Riess and M. Schwoerer, Synth. Met., **76** , 1-3 (1996), 109-112.

[11] M. Herold, J. Gmeiner, C. Drummer and M. Schwoerer, Journal Of Materials Science, **32** , 21 (1997), 5709-5715.

[12] M. Meier, S. Karg and W. Riess, J. Appl. Phys., **82** , 4 (1997), 1961-1966.

[13] S. Karg, M. Meier and W. Riess, J. Appl. Phys., **82** , 4 (1997), 1951-1960.

[14] W. Brutting, M. Meier, M. Herold, S. Karg and M. Schwoerer, Chemical Physics, **227** , 1-2 (1998), 243-252.

[15] W. Brutting, M. Meier, M. Herold, S. Karg and M. Schwoerer, Synth. Met., **91** , 1-3 (1997), 163-168.

[16] F. Papadimitrakopoulos, K. Konstadinidis, T. M. Miller, R. Opila, E. A. Chandross and M. E. Galvin, Chem. Mat., **6** , 9 (1994), 1563-1568.

[17] K. Z. Xing and N. Johansson, Adv. Mat., **9** , 13 (1997), 1027.

Chapter 5 Electroluminescence from Single Polymer Layer Structures

PPY

PPY single layer devices were fabricated by spin-coating PPY from formic acid solution onto ITO coated glass substrates. The device structure was completed by evaporation of metal electrodes.

Energy Levels of a PPY Device

The positions of the relevant energy levels in a PPY device are shown below. The positions assume the formation of a perfect device, with no doping or chemical interaction between the layers.

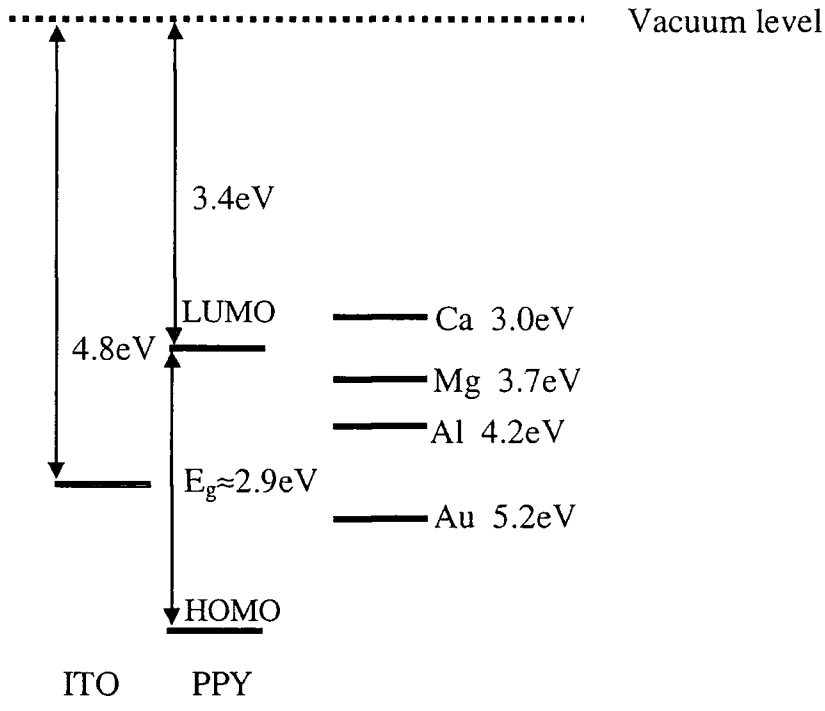

Figure 5-1 *Energy levels of an ideal PPY light-emitting diode*

In this idealised case, under forward bias, the ITO would present a 1.5eV barrier to hole injection into the HOMO of the polymer. Using calcium as the cathode would produce an ohmic contact as the energy level of the calcium is higher than that of the LUMO of the polymer, thus presenting no barrier to electron injection. Magnesium, aluminium and gold electrodes would present a barrier to electron injection with a magnitude of 0.3eV, 0.8eV and 1.8eV respectively. The calcium, magnesium and aluminium workfunctions were obtained from reference [1], the gold workfunction

from reference [2] and the ITO workfunction from reference [3]. The positions of the PPY energy levels were obtained from reference [4].

PPY Diodes with Aluminium Contacts

Single layer PPY devices with ITO and aluminium contacts have almost symmetric current-voltage (IV) characteristics in forward and reverse bias.

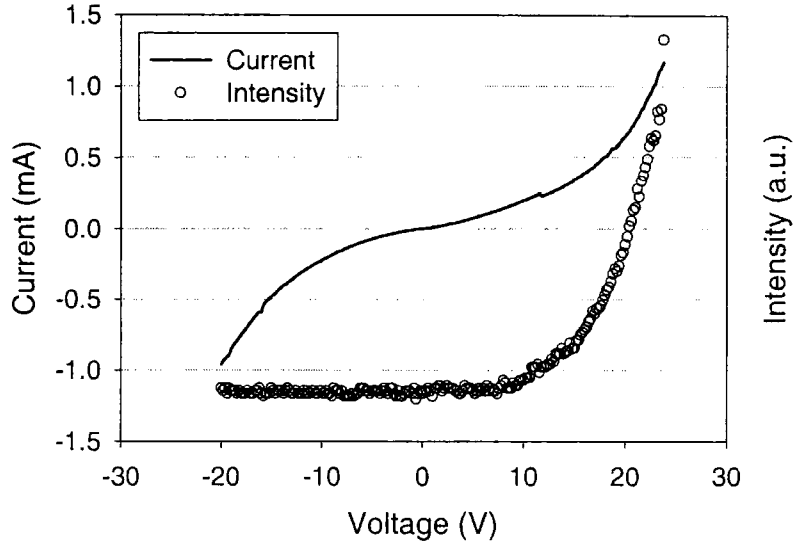

Figure 5-2 *Current-voltage and electroluminescence intensity-voltage behaviour of a single layer PPY device with aluminium contacts*

The current-voltage curve shows a diode-type shape in both forward and reverse bias, although there is no rectification. Electroluminescence is observed only in forward bias. Work published by other groups also shows stable EL only in forward bias [5]. The turn-on voltage for light emission (measured from the intercept of the tangent to the curve in the 15V to 25V range) is 13V. The polymer layer thickness is 52nm, hence the turn on field in this diode is 250MV/m. The approximately symmetric nature of the IV characteristics can be more readily observed when the magnitudes of the current and voltage are plotted (Figure 5-3). From Figure 5-3 it is possible to see that the IV characteristics of the diode are very similar in both forward and reverse bias, especially at lower voltages. At higher voltages, there is a higher current in reverse bias than in forward bias.

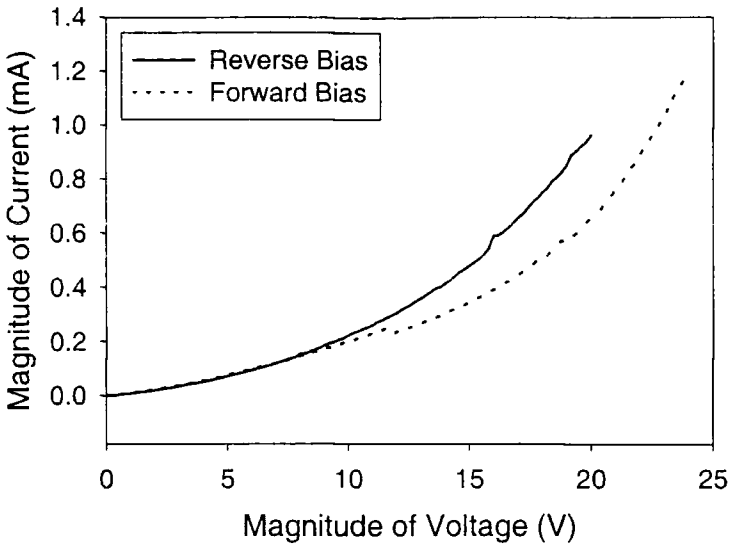

Figure 5-3 *Magnitude of current and voltage of a PPY diode in forward and reverse bias*

The electroluminescence (EL) and photoluminescence (PL) spectra of PPY are shown as Figure 5-4.

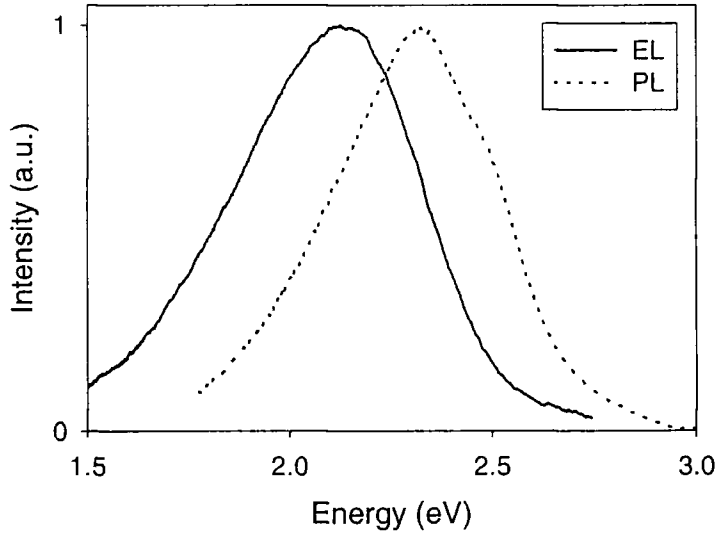

Figure 5-4 *Electroluminescence (solid line) and photoluminescence (dashed line) spectra of PPY*

There is a change in the peak position and shape of the electroluminescence spectrum compared to the photoluminescence spectrum. The peak of the EL is red-shifted by 0.2eV (50nm) from the PL peak, lying at 2.12eV (584nm) compared to the peak of the PL at 2.32eV (534nm). The full width at half maximum (FWHM) of the EL, 0.55eV (159nm), is slightly larger than that of the PL, 0.48eV (113.5nm). The weak vibronic feature found on the high energy side of the PL is not duplicated in the

EL. Although there are differences in the shape of the spectra due to the slightly larger FWHM and the loss of vibronic detail on the EL, a similarity in the overall shape of the spectra remains.

The quantum and power efficiencies of single layer PPY diodes can be calculated from the EL intensity and current-voltage information. The current density-intensity plot of a PPY single layer device can be seen in Figure 5-5.

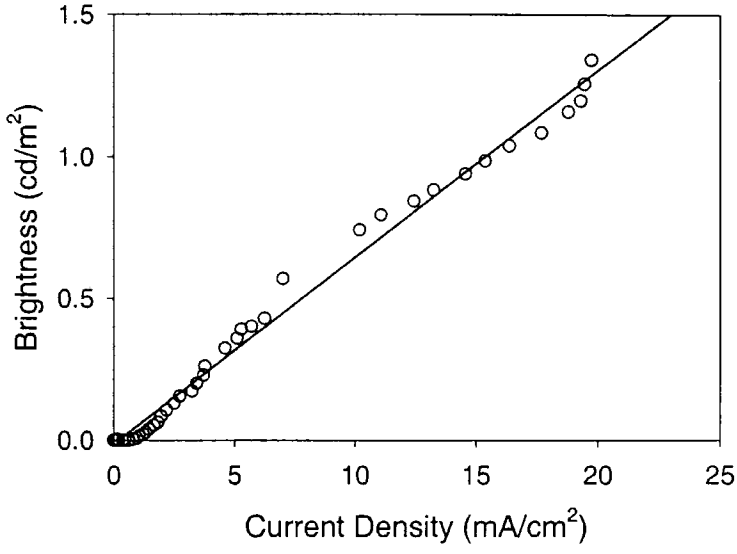

Figure 5-5 *Current density versus intensity plot for a single layer PPY device. The circles are data points and the solid line is a line of linear regression*

The peak efficiency of single layer PPY devices is 3.2×10^{-3}%. The peak brightness recorded for the device shown is 1.3 cd m^{-2}. The peak power efficiency is 1.2×10^{-3} lm/W (at 20.8V and 0.14mA).

PPY Diodes with Other Metal Contacts

To investigate the effect of changing the barrier to charge injection, the metal used for the top electrode was varied. Calcium (capped with aluminium), magnesium (capped with silver (Mg/Ag) and aluminium (Mg/Al)) and gold were used to vary the theoretical barrier to charge injection. The natural logarithm of the current density as a function of applied voltage is shown below for these metals. This allows the investigation of the characteristics in a Schottky framework. The circles represent data points and the solid lines are linear fits to the data.

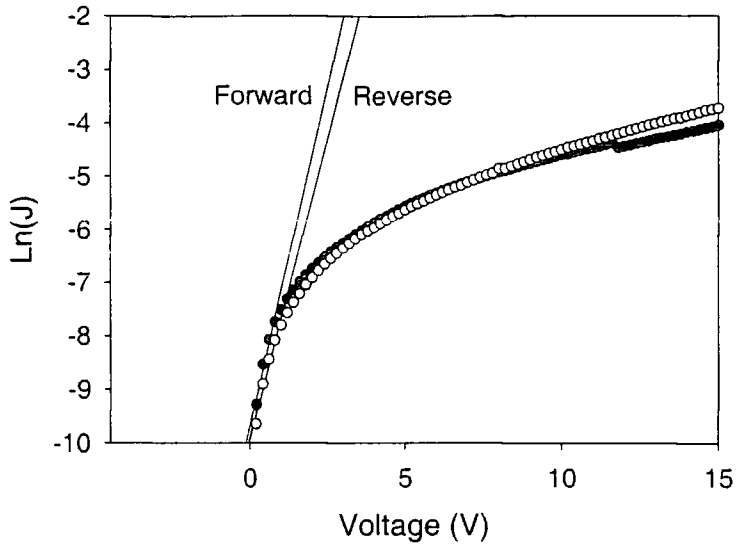

Figure 5-6 *Natural log of current density versus voltage curve (circles) and Schottky fit (lines) for an ITO/PPY/Al device in forward (filled circles) and reverse (open circles) bias*

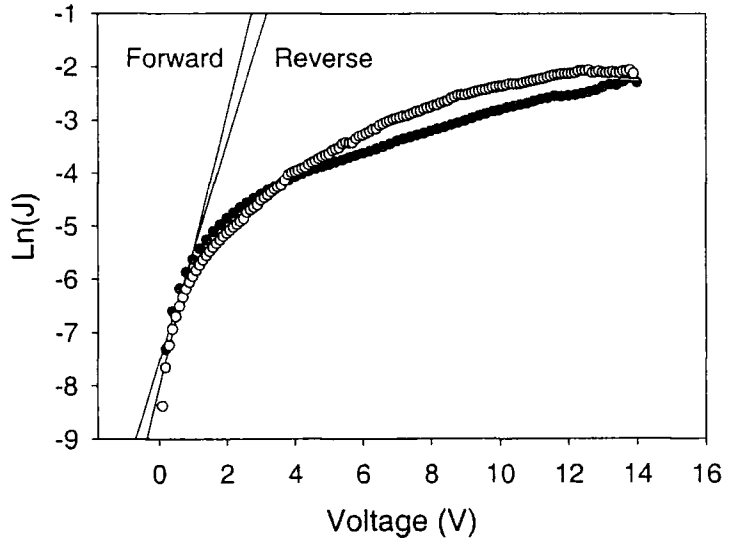

Figure 5-7 *Natural log of current density versus voltage curve (circles) and Schottky fit (lines) for an ITO/PPY/Ca/Al device in forward (filled circles) and reverse (open circles) bias*

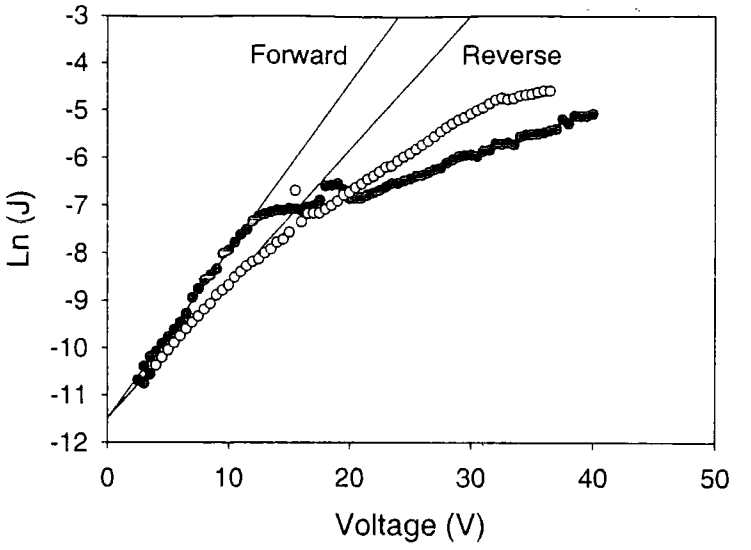

Figure 5-8 *Natural log of current density versus voltage curve (circles) and Schottky fit (lines) for an ITO/PPY/Au device in forward (filled circles) and reverse (open circles) bias*

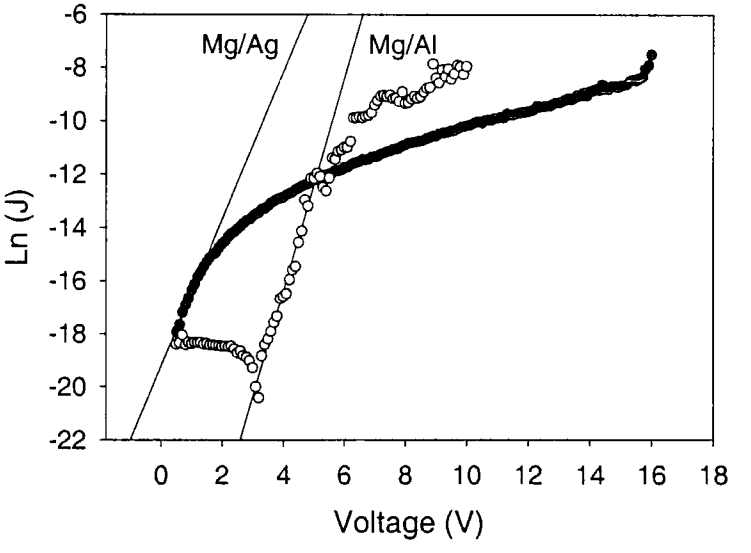

Figure 5-9 *Natural log of current density versus voltage curve (circles) and Schottky fit (lines) for ITO/PPY/Mg/Ag device (filled circles) and ITO/PPY/Mg/Al (open circles) devices*

The thicknesses of the devices shown are 52nm, 200nm, 200nm, 170nm and 154nm for the device with aluminium, calcium, gold, magnesium silver and magnesium aluminium electrodes respectively. With the thickness information, the current-field behaviour can be calculated. The current-field behaviour of the devices was calculated (not shown) and the field required to produce a certain current (in forward and reverse bias where applicable) was measured. This is shown as Figure 5-10.

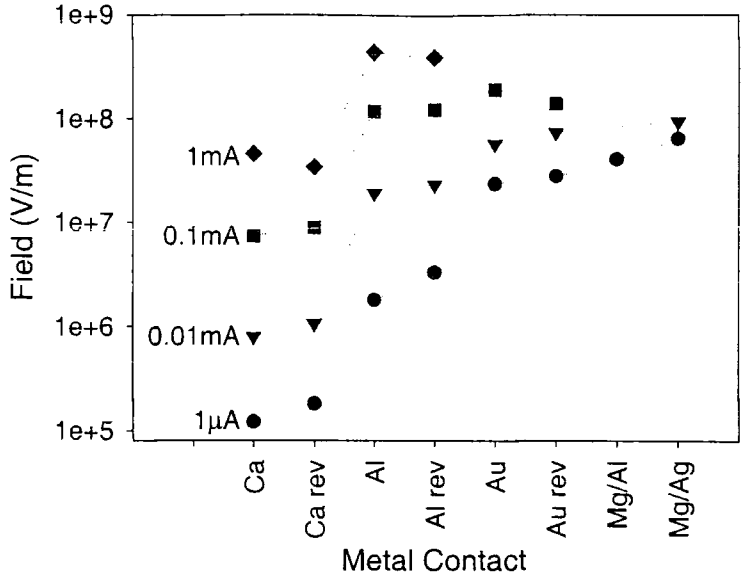

Figure 5-10 *Field required for various current levels in PPY diodes with different metal contacts*

It can be seen from Figure 5-10 that the field required for injection of a given current is lowest for calcium contacts and the field increases for aluminium, gold and magnesium aluminium, reaching a maximum for magnesium silver contacts. The field required in reverse bias (denoted by 'rev' following the metal contact symbol in Figure 5-10) is similar to the forward bias field for each metal contact. The field required is slightly higher at lower currents but is slightly lower for higher currents. Work elsewhere, using a PPY layer sandwiched between two insulating layers of the emeraldine base form of polyaniline, finds no significant difference in the IV characteristics of this device structure when metals with different work functions are used [5].

The height of the Schottky barrier, ϕ_b, and the diode ideality factor, n, can be calculated from the Schottky fits in Figure 5-6 to Figure 5-9. PPY is assumed to be a n-type semiconductor. Recalling that the height of the Schottky barrier is related to the barrier to hole injection by the relationship $\phi_h = E_g - \phi_b = E_g + \chi - \phi_m$, where E_g and χ are the band gap and electron affinity of the polymer, and ϕ_m is the workfunction of the metal, the barrier to hole injection can be calculated.

The results for each metal contact are summarised below. The external quantum efficiency of the devices in forward and reverse bias is also shown.

Metal	ϕ_b (±0.01 eV)	ϕ_h (±0.01 eV)	n	E_{ext} (%)
Al (for)	0.66	2.24	15	3×10^{-3}
Al (rev)	0.67	2.23	17	0
Ca (for)	0.61	2.29	18	5×10^{-5}
Ca (rev)	0.62	2.28	15	6×10^{-5}
Au (for)	0.71	2.19	111	1×10^{-4}
Au (rev)	0.71	2.19	137	1×10^{-4}
Mg/Ag	0.91	2.00	14	0
Mg/Al	1.25	1.65	9.8	0

Table 5-1 *Schottky barrier height (ϕ_b), barrier to hole injection (ϕ_h), diode ideality factor (n) and external quantum efficiency (E_{ext}) for various metal electrodes in PPY devices in forward (for) and reverse (rev) bias*

The Schottky barrier height calculated for the devices lies between 0.61eV and 1.25eV for the calcium and magnesium/aluminium electrodes respectively. The diode ideality factor varies from 9.8 to 137 for the magnesium/aluminium and gold (in reverse bias) electrodes respectively. The efficiency of the devices is highest using aluminium contacts, although there is little or no light output in reverse bias. The calcium devices have the lowest efficiency of the working devices, two orders of magnitude lower than the efficiency of the device utilising aluminium electrodes. The device with gold electrodes has an efficiency approximately one order of magnitude less than the device with aluminium electrodes. External quantum efficiencies of 0% indicate that no light was measured from the device.

The IV data of the ITO/PPY/Al device can be analysed in a Fowler-Nordheim (FN) and space charge limited current (SCLC) framework (see for example reference [6]). A FN plot of $ln(I/F^2)$ versus $1/F$ (where F is the applied field) should produce a straight line with a gradient proportional to $\varphi^{3/2}$ where φ is the (triangular) barrier height (see for example reference [2]). The FN plot is shown as Figure 5-11.

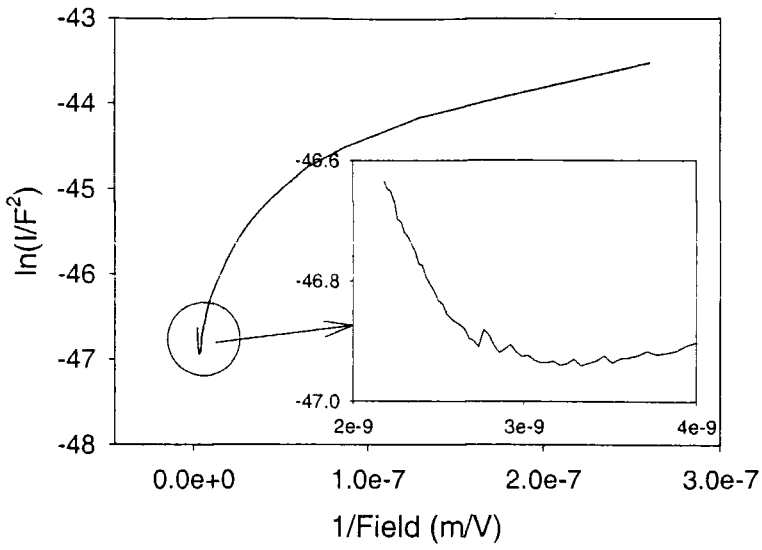

Figure 5-11 *Fowler-Nordheim plot of an ITO/PPY/Al device. Inset: rescaled view of the circled area*

The gradient of the straight line is positive over most of the range of the graph, and is only negative in part of the very small range (at high fields) circled and expanded (inset) in Figure 5-11. The calculation of a positive barrier requires a negative gradient and hence the FN treatment of the ITO/PPY/Al device appears to be inappropriate.

A SCLC fit to the data is shown in Figure 5-12.

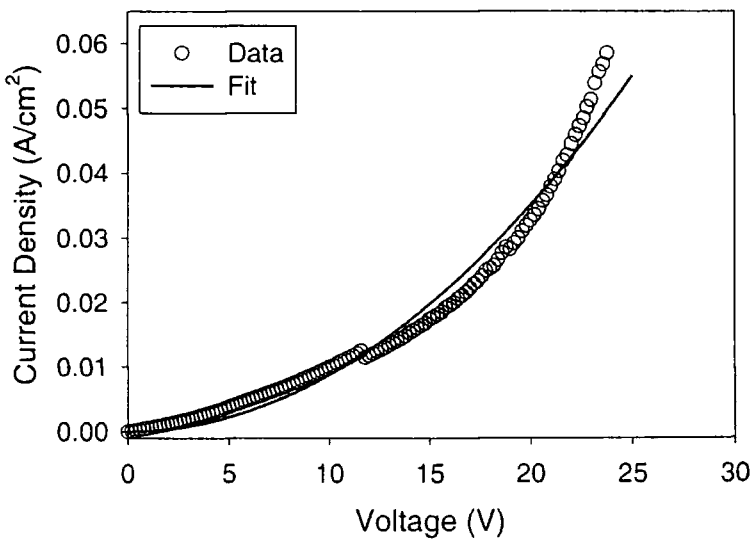

Figure 5-12 *Current density-voltage characteristics of an ITO/PPY/Al device (circles) and a SCLC fit to the data (solid line)*

The SCLC theory fit to the data shown in Figure 5-12 provides a method of measuring the charge mobility of PPY. The curve fit parameter, *a*, is related to the

current density by the equation of pure SCLC (Child's law), shown below. For an explanation of terms, see Chapter 2.

$$J = \frac{9\varepsilon_0 \varepsilon_r \mu V^2}{8d^3} = aV^2$$

Equation 5-1 *Child's law*

From the curve fit parameter and assuming a dielectric constant of ε_r=4 [5, 7], the charge mobility of the polymer can be calculated. It is more convenient to plot current density versus voltage squared, producing approximately linear plots, the gradients of which can be used to determine the charge mobility.

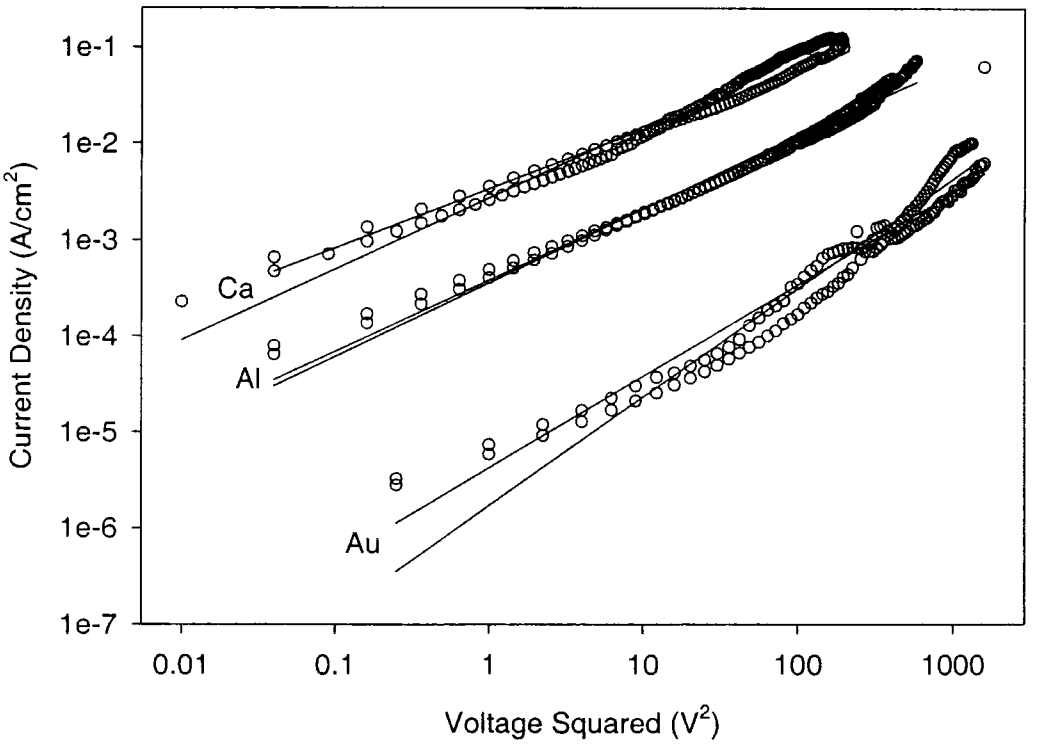

Figure 5-13 *Current density versus voltage squared data (circles) and linear regressions (solid lines) for PPY single layer diodes with various metal contacts in forward and reverse bias*

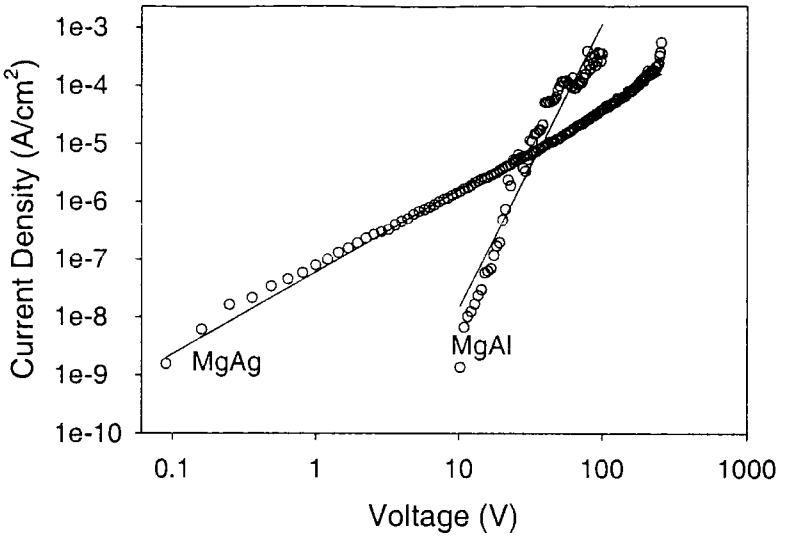

Figure 5-14 *Current density versus voltage squared data (circles) and linear regressions (solid lines) for PPY single layer diodes with magnesium/aluminium and magnesium/silver contacts*

The values of charge mobility and the coefficient of determination of the data (the r^2 value) can be calculated from lines of regression to the data in Figure 5-13 and Figure 5-14. The values are shown in Table 5-2.

Metal	μ ($cm^2 V^{-1}s^{-1}$)	r^2
Al (for)	$(4 \pm 2) \times 10^{-8}$	0.97
Al (rev)	$(4 \pm 2) \times 10^{-8}$	0.99
Ca (for)	$(1.0 \pm 0.2) \times 10^{-5}$	0.99
Ca (rev)	$(1.4 \pm 0.2) \times 10^{-5}$	0.96
Au (for)	$(7 \pm 1) \times 10^{-8}$	0.96
Au (rev)	$(1.6 \pm 0.3) \times 10^{-7}$	0.94
Mg/Ag	$(1.0 \pm 0.2) \times 10^{-8}$	0.75
Mg/Al	$(2.6 \pm 0.5) \times 10^{-8}$	0.80

Table 5-2 *Charge mobility (μ) and r^2 value of the linear regression line from the SCLC treatment of the current density-voltage data of the PPY devices*

The fits to the IV data in the SCLC framework for the devices with calcium, aluminium and gold electrodes are reasonable as suggested by the r^2 values, all of which are 0.94 and above. The fits for the device with magnesium electrodes have much reduced r^2 values suggesting a poorer linear fit. The fits shown in Figure 5-13 and Figure 5-14 are much improved at higher voltages, where there are far more data points and where the SCLC would be expected to commence (at lower voltages in

SCLC theory, the current is ohmic, i.e. $I \propto V$ rather than the $I \propto V^2$ behaviour of SCLC). SCLC is considered to be the dominant theory in other work on PPY single layer devices [5]. The values of the charge mobility obtained for PPY with magnesium, aluminium and gold electrodes are all approximately 10^{-7} to 10^{-8} cm^2 V^{-1} s^{-1}. This is an order of magnitude lower than values found for PPY (with a lower PLQY), assuming a similar value for ε_r, elsewhere [5], but lie within the range of mobilities found for charges in PPV (see for example reference [8]). The mobilities for devices with calcium electrodes are approximately three orders of magnitude higher than the values calculated for the other metals. Mobility values in forward and reverse bias, calculated for each metal, are approximately consistent with one another.

Discussion

Aluminium Electrodes

The symmetric nature of the IV characteristics of the ITO/PPY/Al diode in forward and reverse bias would not be expected from simple analysis of the energy levels (Figure 5-1). Theoretically, in forward bias, there is a 0.8eV barrier to electron injection (thought to be the majority charge carrier in PPY) from the aluminium to the LUMO of the polymer, and a 1.5eV barrier to hole injection from the ITO to the HOMO of the polymer. In reverse bias, the theoretical barrier to electron injection presented by the ITO is 1.4eV, and the barrier to hole injection from the aluminium is 2.1eV. This implies that in reverse bias there should be a reduced current flowing at a given voltage due to the increased barrier to electron injection. This is not the case however, except at very low currents (Figure 5-10) and hence very low fields. At higher fields, the reverse bias current is found to be higher than the forward bias current.

A reason for this behaviour could be the formation of an interfacial region between the metal and the polymer. The aluminium-polymer interface could be affected by the covalent bonding that would be expected in the first few Angstroms of the deposited metal. This may have an effect on the charge injection at that electrode, preventing efficient charge injection. The higher current (at high fields, in reverse bias) suggests that charge tunnelling plays a minor role in the injection process. In reverse bias, the charges do not have to tunnel through an interfacial region to get into the polymer and hence, once the barrier to tunnelling has been reduced by the applied bias, tunnelling can occur more easily, leading to higher current densities. The Fowler-

Nordheim treatment of the data suggests that tunnelling may play a minor role only at very high fields (Figure 5-11), although any effect it may have at low fields may be masked by the SCLC or Schottky type behaviour.

The absence of electroluminescence in reverse bias may be an indication of the difficulty in minority charge carrier injection (holes). The barrier to hole injection from the aluminium to the HOMO of the polymer is 0.6eV larger than the barrier of injection from ITO to the HOMO. There may be considerable current flow in reverse bias, but difficulty in injecting minority carriers (perhaps also due to an aluminium/polymer interfacial region) would prevent the formation and hence radiative decay of singlet excitons.

Other Metal Electrodes

PPY diodes provide a complex system for Schottky analysis. There is a significant probability that Schottky barriers are formed at the ITO/polymer and metal/polymer interfaces, making accurate Schottky analysis unlikely. This situation is not thought to arise in the case of PPV, for example, where the smaller difference in energy levels and doping of the polymer produce an ohmic-type contact at the ITO/polymer interface [9-11]. Further complications arise due to the probable formation of interfacial states between the electrodes and the polymer. The nature and effect of these regions has not yet been characterised. The possibility of doping of the polymer by either electrode would also add to the complexity.

Indications of deviation from an ideal system are the very large diode ideality factors and the lack of correlation between the calculated barriers to charge injection and the field required for a given current. If a Schottky barrier was formed only at the polymer/ITO interface then a constant barrier to charge injection would be expected (in the absence of doping caused by the metal electrode) when the metal workfunction was altered. This is not the case, and the calculated barriers to hole injection (Table 5-1) show an increase with decreasing workfunction of the metal used for the counter electrode. The results also show that the calculated barrier to hole injection increases as the field required for a given current (Figure 5-10) decreases.

The differences produced in the properties of devices with magnesium electrodes using various capping layers imply there are processes affecting the device performance other than those considered in this simple treatment. For example, one consequence of the use of silver as a capping layer is the production of a large degree

of inhomogeneity in the thickness of the polymer film, particularly in the region close to the metal contact. The field required for a given current and the barrier height data for the devices with magnesium electrodes do suggest that the capping layer has a considerable effect on the properties of the device. It also suggests that although low workfunction magnesium electrodes can be used to obtain a low barrier to charge injection, the efficiency of these devices is low, and less reactive metals with higher workfunctions can produce devices with higher efficiencies and lower fields required for a given current.

The similarities in performance in forward and reverse bias, with calcium electrodes in particular, are surprising. The theoretical barriers to electron and hole injection in reverse bias for a calcium device are 1.4eV and 3.3eV respectively. These are considerably larger than the barriers found in forward bias (≈0eV for electrons and 1.5eV for holes), yet the IV characteristics are almost symmetric. This implies that although the barriers to electron and hole injection are important (as suggested by Figure 5-10), a barrier independent current limiting process, for example SCLC, is also present. The fit to the IV data in a Schottky framework is reasonable only in a small voltage range, as observed elsewhere (see for example reference [12]), and fits in the SCLC framework, whilst not perfect, are reasonable across a large voltage range for all metal electrodes.

The calculated values of the charge mobility, similar for most of the metals studied, show a dramatic increase when calcium electrodes are used. This could be due to doping of the polymer, which would considerably affect the charge mobility. This doping would imply that there is a difference in the formation of calcium electrodes on PPY and PPV surfaces (see for example reference [13]) at relatively modest deposition vacuum pressures. Chemical interaction between the polymer or traces of residual acid[†] and reactive calcium and magnesium are conceivable. This may prevent the successful application of these metals as an electrode materials.

Schottky treatment cannot explain the symmetric nature of the IV curves in forward and reverse bias, and SCLC cannot explain the field dependence of the diodes, but a combination of the two can conceivably explain the IV properties of single layer PPY diodes.

[†] Although FTIR studies of solid PPY find no signature of residual formate to suggest any remainder of the volatile solvent, FTIR would be unlikely to detect very small amounts of residue, which could conceivably interact with reactive metals.

Quantum Efficiency

The electroluminescence quantum efficiency of the LEDs varies with electrode material and bias direction, as shown in Table 5-1. The efficient operation of an LED requires the balanced injection of electrons and holes. When there is a mismatch in the charge injection then there is a reduction in the efficiency of the device.

The data suggest that the device with aluminium electrodes has the most balanced electron and hole injection in forward bias. In reverse bias, even though a current flows (comparable in size to that in forward bias), there is no light observed. This may be due to the unfavourable injection of the minority charge carrier by the aluminium electrode. In the case of devices with gold electrodes, there is a comparable efficiency in forward and reverse bias, suggesting that hole injection from gold and ITO electrodes is of a similar efficiency. This would be expected from consideration of the similar positions of the energy levels of gold and ITO.

The calcium device efficiency is more perplexing, however. The low efficiency in forward bias can be explained by the mismatch of electron and hole injection. The electron injection from the calcium electrode would be expected to be much more favourable than the hole injection from the ITO, leading to a higher current and, with a similar number of injected holes to the aluminium electrode case, a reduced quantum efficiency. The reverse bias case is hard to understand. Efficient hole injection from a calcium electrode is hard to envisage, as is efficient electron injection from the ITO electrode. The efficiency of the calcium device in reverse bias may be a consequence of a more balanced electron and hole current, the increased charge mobility, the presence of an interfacial region, or the mismatch in energy levels may be alleviated somewhat by a change to more SCLC-type behaviour.

PPY:PMMA BLEND DIODES

Significant changes in the colour of emission of PPY can be achieved by producing blends of PPY and PMMA. The change in the colour of the photoluminescence of the blended films as a function of the solid state dilution is shown in Chapter 4. If blending produces a similar effect in electroluminescence then the application of blend films as the active layer in LEDs could provide a simple

method of producing a wide range of emission colours in a large number of discrete colour steps.

The current-field and electroluminescence-intensity characteristics of an ITO/PPY:PMMA/Al device with a PPY:PMMA ratio of 1:50 is shown below.

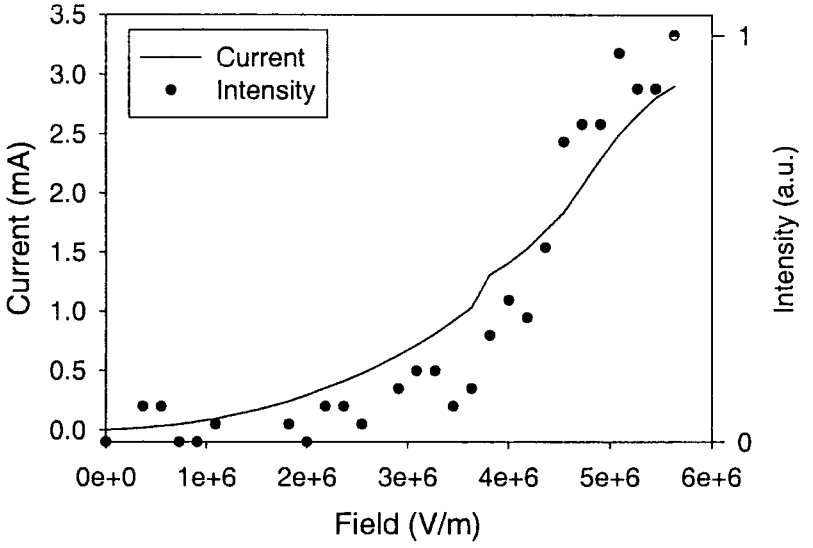

Figure 5-15 *Current-field (solid line) and EL intensity-field (circles) characteristics of an ITO/PPY:PMMA/Al blend device*

The efficiency of the device can be calculated by considering the EL intensity-current characteristics and the spectral output of the device. The intensity-current behaviour is shown in Figure 5-16 and the EL and PL spectra are shown in Figure 5-17.

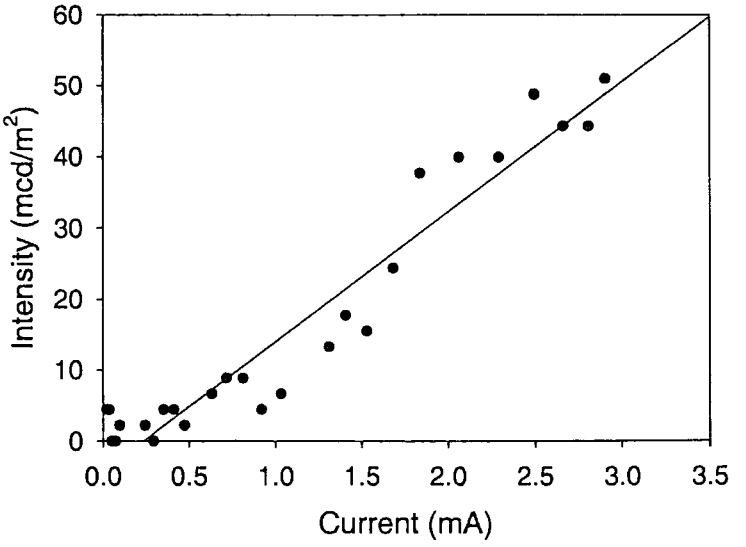

Figure 5-16 *Current-EL intensity characteristics of an ITO/PPY:PMMA/Al blend device*

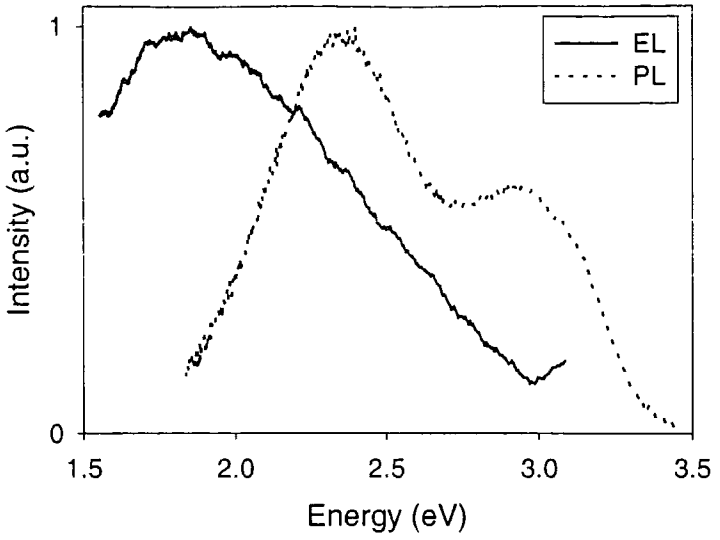

Figure 5-17 *Electroluminescence (solid line) and photoluminescence (dashed line) spectra of a 1:50 blend of PPY and PMMA*

The peak of the electroluminescence spectrum is at approximately 1.9eV (667nm), and the peak of the photoluminescence spectrum is at approximately 2.4eV (517nm). The EL spectrum exhibits a 0.5eV red-shift compared to the PL spectrum.

The peak brightness of approximately 50mcd/m^2 is very low and the external quantum efficiency is correspondingly low, 3×10^{-5}%. Schottky analysis of the current density-voltage data finds a barrier height of (0.62 ± 0.01) eV and a diode ideality factor of 9.8. SCLC analysis finds a charge mobility of (6.0 ± 0.8) $\times10^{-3}$ cm^2 V^{-1}s^{-1}.

Discussion

The quantum efficiency and brightness achieved by the blend LED are very low, and the EL spectrum is sufficiently different to the PL to suggest a change of emitting species. The EL spectrum is red-shifted by approximately 0.5eV from the PL spectrum. This is a larger red-shift than the 0.2eV observed between the EL and PL spectra of PPY (Figure 5-4). The difference in the shape of the blend spectra is more pronounced than the small change in spectral shape observed for pure PPY. Perhaps the most surprising result is the reduction in the field required for a given current in the device. The barrier to hole injection (calculated by Schottky analysis) in the blend device is 0.04eV higher than the barrier for a PPY device with aluminium electrodes. To achieve a current of 1mA, the blend device requires a field of approximately 3.5×10^6 V/m, whereas a PPY device with similar aluminium contacts requires a field of approximately 5×10^8 V/m. This is surprising as the chains of the higher conductivity

PPY are separated with essentially insulating PMMA. This would suggest that an increase in field and a decrease in mobility should arise, yet the opposite is observed. In addition, the PL spectrum of the blend film suggests a reduction in the conjugation length of the PPY chains, caused by additional ring twists, which would be expected to produce a further reduction in charge mobility. The value of the charge mobility is therefore far higher than would expected and hence the calculated value should be treated with some caution. The actual value of the charge mobility could be investigated more accurately using other methods, for example, by a time of flight measurement [14].

In summary, polymer light-emitting diodes utilising PPY:PMMA blends as the active layer exhibit low light levels, broad spectral output and short operating lifetimes. It is possible to achieve electroluminescence with solid state dilutions of PPY, but the spectral output is not similar to the photoluminescence of the blend and the efficiencies are very low.

DIODES WITH COPOLYMERS OF HEXYL-SUBSTITUTED PPY

Electroluminescence from single layer diodes with PhexPY-co-PPY has been observed. The IV-characteristics of an ITO/PhexPY-co-PPY/Al device are shown in Figure 5-18.

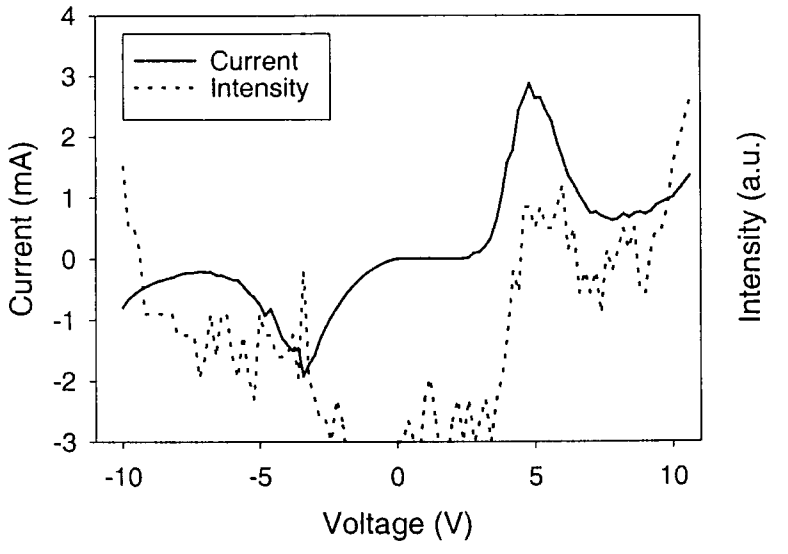

Figure 5-18 *Current-voltage and intensity-voltage behaviour of an ITO/PhexPY-co-PPY/Al device*

It can be seen from Figure 5-18 that the IV and intensity-voltage behaviour of an ITO/PhexPY-co-PPY/Al device are similar in shape in forward and reverse bias.

There are so called "current anomalies" in forward and reverse bias at around ±5V. These anomalies are observed as an increase in current with increasing voltage, followed by a decreasing current with increasing voltage (and hence a negative differential resistance). Beyond this point, the diode-type shape of the IV curve is restored. Similar anomalies have been observed in other systems [3, 15, 16], but there have been very few rigorous investigations and few publications. It has been suggested that the anomalies arise due to short-circuits at local weak spots [3], but these tend to be temporary, whereas the anomalies observed in this study are reproducible over several device runs. The EL intensity follows the increasing current in these regions and emission is observed in the current anomaly region both in forward and reverse bias. The EL intensity at voltages higher than the current anomaly, is higher for a smaller current and hence the EL is more efficient in these regions.

The external quantum efficiency (calculated using a PL spectrum of the copolymer) for the device is approximately 5×10^{-5} % in forward and reverse bias. The Schottky barrier, calculated using data in the region of the current anomaly, is (0.78 ± 0.01) eV and (0.57 ± 0.01) eV in forward and reverse bias respectively. The diode ideality factors are very high, 18 and 30 respectively, suggesting Schottky treatment should be treated with caution. The charge mobility varies from $(1.0 \pm 0.3) \times10^{-5}$ cm^2 V^{-1} s^{-1} in forward bias, around the current anomaly to $(8 \pm 2) \times10^{-7}$ cm^2 V^{-1} s^{-1} before the anomaly in reverse bias, and after the current anomaly (in both forward and reverse bias).

Discussion

The hexyl copolymer diode has barrier heights and charge mobilities similar in magnitude to the unsubstituted PPY diode with aluminium electrodes. The efficiency of the device is very low, preventing the collection of an EL spectrum. The use of the PL spectrum may not be valid, but should not affect the efficiency calculation to a significant degree.

Current anomalies are found in devices with a range of active layers, predominantly in devices which are tested in vacuum (see for example references [3, 15, 16]) and an all encompassing theory of the origin of the anomalies has yet to be published.

DIODES WITH COPOLYMERS OF META-LINKED PPY

Single polymer layer diodes using P*m*PY-co-P*p*PY as the active layer were fabricated with three different P*m*PY to P*p*PY ratios. Active layers with a P*m*PY content of 18%, 35% and 50% were used to investigate the effect that reduced conjugation length would have on the charge transport and EL properties of a device. The current-field characteristics of the three devices are shown below.

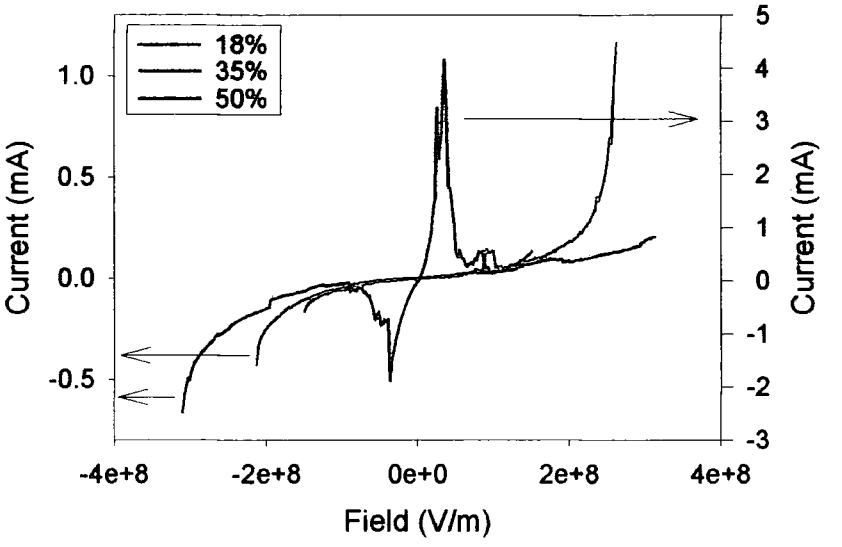

Figure 5-19 *Current-field characteristics of an ITO/PmPY-co-PpPY/Al device with an active layer with 18%, 35% and 50% meta content*

The current-field characteristics show that as the amount of *meta*-links in the polymer increases, the field required for a given current is reduced. Current anomalies appear strongly only in the 50% *meta*-linked copolymer characteristics, although they appear weakly in the 35% *meta*-linked copolymer. No EL from any device was detected. The charge mobility of the polymers can be calculated from the gradients of current density-voltage squared plots, shown in Figure 5-20.

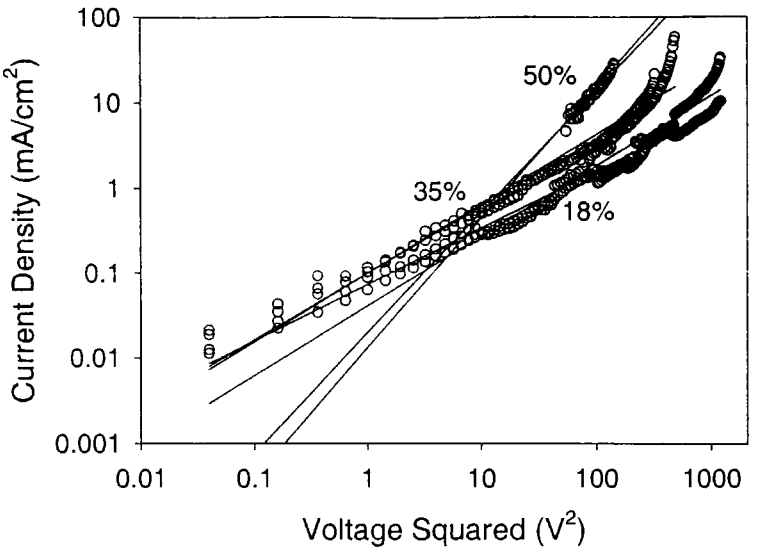

Figure 5-20 *Current density-voltage squared curves of ITO/PmPY-co-PpPY/Al devices with 18%, 35% and 50% meta copolymer composition (circles). The lines are linear regression lines to the data*

The Schottky barrier heights and diode ideality factors were found for the copolymer diodes from the gradients and intercepts of Figure 5-21 to Figure 5-23.

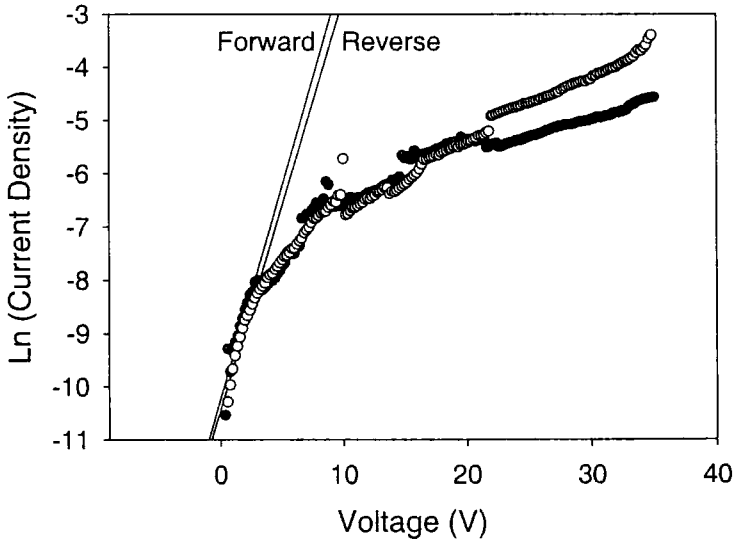

Figure 5-21 *Natural log of current density versus voltage curve (circles) and Schottky fit (lines) for an 18% PmPY ITO/PmPY-co-PpPY/Al device in forward (filled circles) and reverse (open circles) bias*

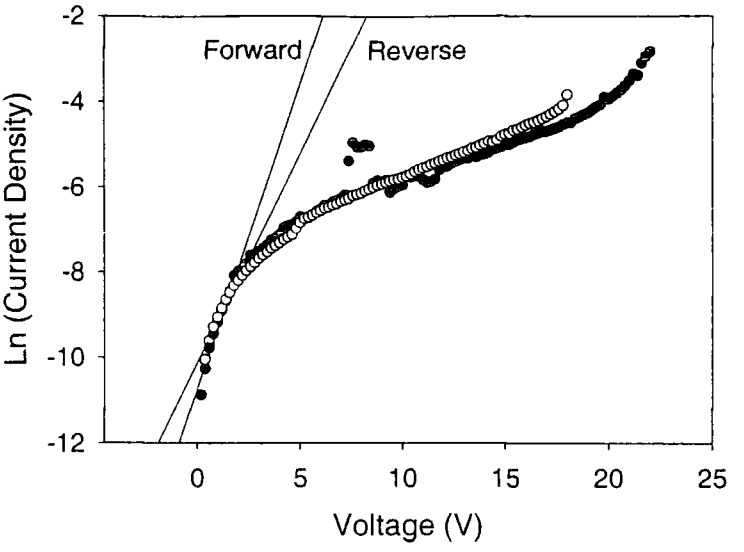

Figure 5-22 *Natural log of current density versus voltage curve (circles) and Schottky fit (lines) for a 35% PmPY ITO/PmPY-co-PpPY/Al device in forward (filled circles) and reverse (open circles) bias*

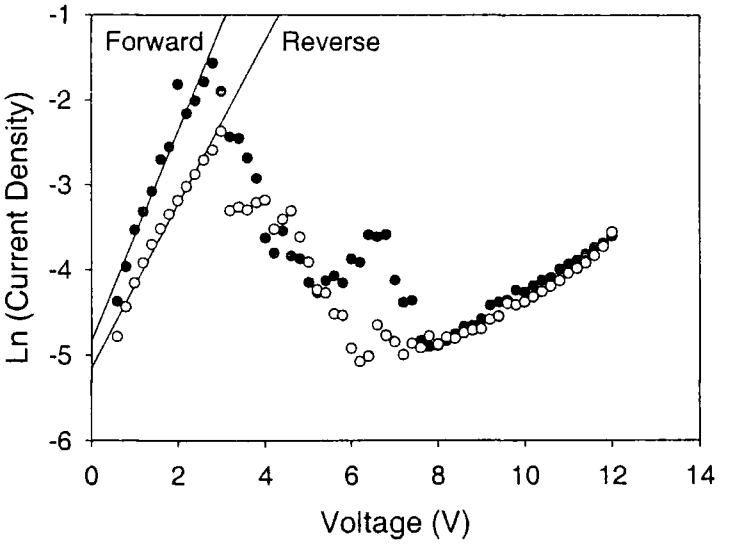

Figure 5-23 *Natural log of current density versus voltage curve (circles) and Schottky fit (lines) for a 50% PmPY ITO/PmPY-co-PpPY/Al device in forward (filled circles) and reverse (open circles) bias*

A summary of the charge mobilities, Schottky barrier heights and diode ideality factors, calculated for the copolymer diodes, can be found in Table 5-3. The values of barrier height and charge mobility calculated for the 50% copolymer are calculated from data around and after the current anomaly respectively.

%meta	ϕ_b (±0.01 eV)	n	μ ($cm^2\ V^{-1}s^{-1}$)	r^2
18 (for)	0.68	49	$(2.6 \pm 0.9) \times 10^{-8}$	0.96
18 (rev)	0.68	51	$(7 \pm 2) \times 10^{-8}$	0.93
35 (for)	0.69	26	$(8 \pm 2) \times 10^{-8}$	0.70
35 (rev)	0.67	48	$(6 \pm 2) \times 10^{-8}$	0.93
50 (for)	0.55	25	$(3 \pm 1) \times 10^{-7}$	0.98
50 (rev)	0.56	33	$(3.2 \pm 0.9) \times 10^{-7}$	0.92

Table 5-3 *Calculated barrier height (ϕ_b), diode ideality factor (n), charge mobility (μ) and r^2 coefficient for the linear regression in for ITO/PmPY-co-PpPY/Al devices with 18%, 35% and 50% meta copolymer composition*

Discussion

The charge mobility values for the 18% and 35% *meta*-linked copolymers, shown in Table 5-3, are very similar to the values calculated for the pure *para*-linked polymer shown in Table 5-2. The inclusion of *meta*-links does not appear to have a significant effect until the *meta*-linked content is 50%. The charge mobility then increases to approximately 3×10^{-7} $cm^2\ V^{-1}s^{-1}$ for the 50% *meta*-linked copolymer, an increase from approximately 6×10^{-8} $cm^2\ V^{-1}s^{-1}$ for the other copolymers. It would be expected that a reduction in the conjugation length would lead to a reduction in charge mobility, but this increase may be linked to the current anomaly observed in the IV-characteristics of the 50% *meta*-linked copolymer, or in a change in the conformation of the chain brought about by the *meta*-linked sections.

The origin of the current anomalies may be linked to the decrease in conjugation length of the polymer used in the device. An increase in the size of the current anomaly is observed with increasing *meta* links and hence a decreasing conjugation length. Optical measurements of *meta*-linked copolymer films begin to show significant changes when the *meta* content reaches 35%. A small current anomaly is observed in the IV characteristics of the 35% copolymer device, although the anomalies observed in the 50% copolymer device are larger. Large current anomalies are observed in devices using PhexPY-co-PPY. A conjugation length smaller than that of PPY would be expected in this copolymer and hence the appearance of current anomalies in PhexPY-co-PPY devices may be expected. The

reason for the increased anomalous behaviour with decreased conjugation length is unclear, although it may be a consequence of an increased number of charge traps in the polymer layer.

The Schottky barrier heights calculated for the 18% and 35% *meta*-linked copolymers are consistent with the 0.66eV calculated for the pure *para*-linked polymer diode with aluminium contacts. The 50% copolymer has a slightly smaller Schottky barrier height and hence a larger barrier to hole injection, consistent with the widening of the band gap. The differences are small, and the very large diode ideality factors imply that in-depth analysis of these differences would not be particularly useful.

The lack of measurable EL from the copolymer diodes could be due to a mismatch of injected charge carriers, and/or the reduced PLQY qualitatively observed for the increasingly *meta*-linked copolymers could play a vital role.

DIODES WITH REGULAR COPOLYMERS

Diodes using poly(4-hexyl-2,5-pyridine-co-*p*-phenylene) (CSW-6) and poly(4-hexyl-2,5-pyridine-co-2,5-dimethoxy-1,4-phenylene) (CSW-25) as the active layer have also been fabricated and tested. Aluminium electrodes were used to complete the ITO/CSW/Al structures. The IV and intensity-voltage characteristics of a device with CSW-6 as the active layer are shown below.

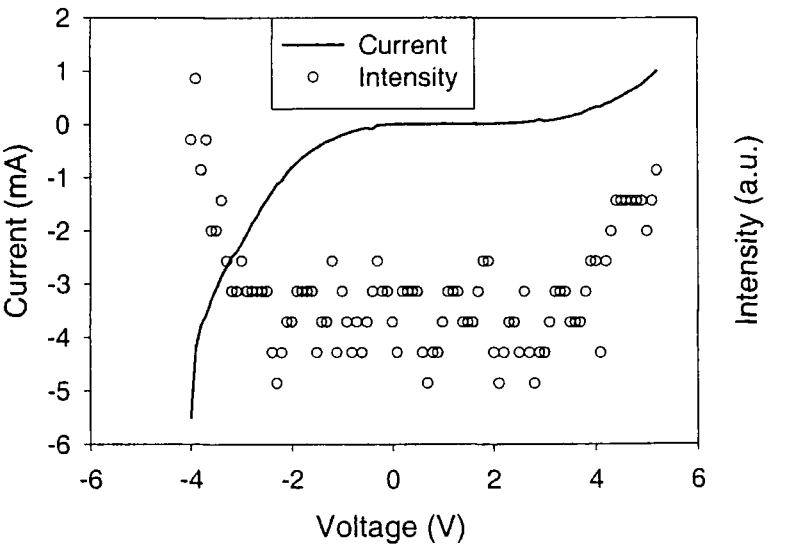

Figure 5-24 *IV and intensity-voltage characteristics of an ITO/CSW-6/Al device*

No EL was observed from, and no significant current was able to pass through the device based on CSW-25, possibly due to its large thickness (430nm). The EL

spectrum of the CSW-6 device is compared to the photoluminescence spectrum in Figure 5-25.

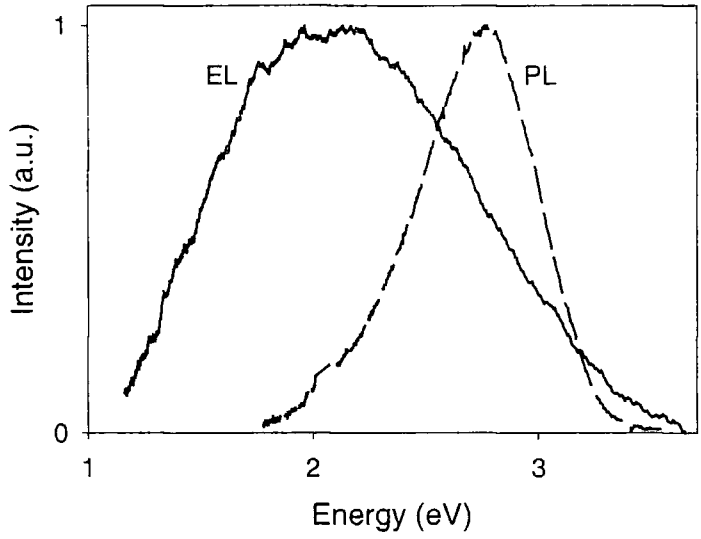

Figure 5-25 *Electroluminescence (solid line) and photoluminescence (broken line) of CSW-6*

The peak of the EL spectrum is at 2.13eV (582nm), a 0.64eV (134nm) red-shift from the peak of the PL spectrum. The EL spectrum is broader than the PL spectrum, with a FWHM of 1.35eV (400nm) compared to the width of the PL spectrum of 0.98eV (104nm).

The efficiency of the device is 1.6×10^{-5} % in forward bias and 6×10^{-6} % in reverse bias. Schottky fits to the data in forward and reverse bias yield Schottky barrier heights of (0.68 ± 0.01) eV and (0.58 ± 0.01) eV and diode ideality factors of 23 and 24 respectively. These high values again indicate the deviation of PPY related polymer devices from theoretically expected Schottky-type behaviour. SCLC analysis yields charge mobilities of $(1.1 \pm 0.2) \times10^{-5}$ cm^2 $V^{-1}s^{-1}$ and $(1.0 \pm 0.2) \times10^{-4}$ cm^2 $V^{-1}s^{-1}$ for forward and reverse bias.

Discussion

The EL and PL spectrum of CSW-6 are different in shape and peak position. The EL is significantly red-shifted and broader than the PL suggesting a change in emitting species or possibly a field effect. Barrier heights and diode ideality factors are similar in size to those found for the copolymers and PPY devices. Charge mobilities in these polymers are significantly higher than the mobilities found for the other copolymers and for PPY with calcium electrodes. The EL quantum efficiency of the

device is very low, and approximately the same as the efficiency of the other copolymer in this study. This suggests that there is considerable imbalance of charge injection and transport, perhaps due to a considerable difference in the mobility of positive and negative charge carriers.

SUMMARY AND CONCLUSIONS

The colour co-ordinates of the PPY and derivatives electroluminescence spectra are compared to the PL spectra in Figure 5-26.

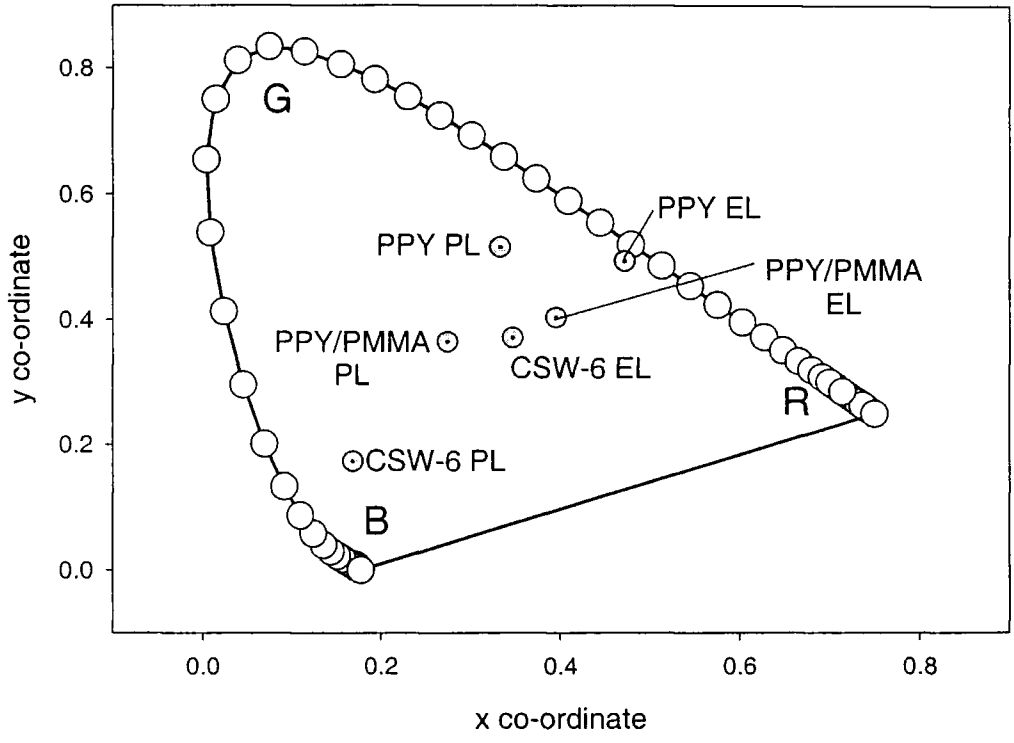

Figure 5-26 *Colour co-ordinates of the EL and PL of PPY and derivatives*

The electroluminescence from PPY and its derivatives tends to be inefficient in a single layer configuration with aluminium electrodes. The peak efficiency of these devices is around 3×10^{-3}%, approximately the same as a single layer PPV diode with aluminium contacts. The efficiency of PPV devices can be improved through the use of low workfunction metals (see for example references [17, 18]). The use of low workfunction metals with PPY appears to have little effect on the barriers to charge injection, and clearly has a detrimental effect on the efficiency of the devices (see Table 5-1). This could be due to interfacial states or some interaction with the polymer (for example the charge mobility results, in Table 5-2, for PPY/Ca devices suggest doping of the polymer).

Devices using PPY and PPY related materials as the active layer are unconventional in several ways. Firstly, the reverse bias IV characteristics of the devices tend to be symmetric and exhibit symmetric barriers to charge injection. This is not what is expected from the treatment of the theoretical energy levels of the polymer and electrode materials used. This does allow some novel device structures to be fabricated, however [19-22]. Light is observed, in some systems, in both forward and reverse bias allowing the use of PPY in device structures which facilitate AC operation [5]. This symmetry leads to the lack of a single model which can adequately describe the behaviour of PPY LEDs. The data shown above demonstrate that Schottky and SCLC in conjunction can be used to explain some of the behaviour, but the values obtained for the diode ideality factor, for example, indicate that this approach is far from perfect, although it does allow some comparison of PPY and its derivatives.

Secondly, the EL spectrum differs from the PL spectrum quite significantly. A difference in EL and PL spectra has been observed in diodes with a wide range of materials, including PPY elsewhere, (see for example references [23-26]) and also in light-emitting electrochemical cells, particularly after ageing [27]. This difference suggests that the widely held view (see for example reference [28]) that a common species is responsible for both EL and PL may be incorrect or there could be some electrochemical interaction under the effect of an applied field. This is an inconvenient feature of PPY and particularly its derivatives. Polymers, such as CSW-6, which exhibit PL in the violet/blue region of the spectrum may have EL which is almost white. Obviously, for design and development purposes, this is far from ideal.

Finally, PPY exhibits strong resistance to photo-oxidation [29] and electro-chemical oxidation [30], unlike PPV [29, 31]. It does, however, display a puzzling PLQY decrease under illumination in both nitrogen and vacuum [29] which may be due to an excited state interaction with oxygen.

In summary, although PPY and its derivatives exhibit a range of colours from blue to green/yellow and (approximately) white in PL, a change of emission species, possible electrochemistry or field effects limit the range of colours of the EL. Single layer diodes using these polymers exhibit relatively low efficiencies and operating stability. The strengths of these materials lie in the utilisation of their novel charge transport properties, their lack of sensitivity to energy level mismatch and their resistance to oxidation. Hence the true application of PPY and derivatives should be found in their application in novel multilayer device structures.

PPV

Single layer devices using poly(*p*-phenylene vinylene) as the active layer were prepared and characterised. PPV films were prepared by thermal conversion of the precursor polymer on ITO coated glass substrates. The device structure was completed by evaporation of metal electrodes. The energy levels of an ideal PPV device with various metal contacts is shown in Figure 5-27.

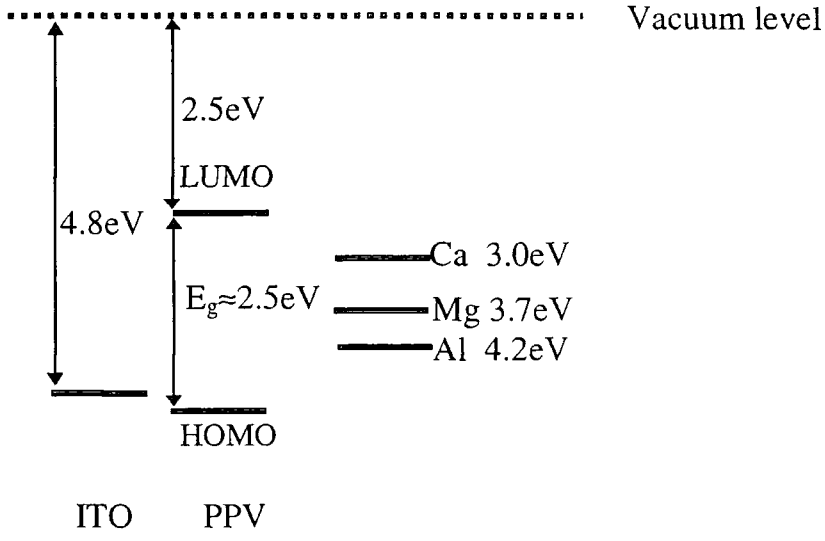

Figure 5-27 *Energy levels of an ideal PPV light-emitting diode*

Metal workfunctions are from the references listed for Figure 5-1. PPV energy levels were obtained from reference [32]. In forward bias, ITO presents a barrier of approximately 0.2eV to hole injection into the HOMO of the polymer. Calcium, magnesium and aluminium present a barrier to electron injection of 0.5eV, 1.2eV and 1.7eV respectively.

PPV single layer diodes show a small reverse bias current and a large forward bias current, and hence are significantly different to devices using PPY as the active layer.

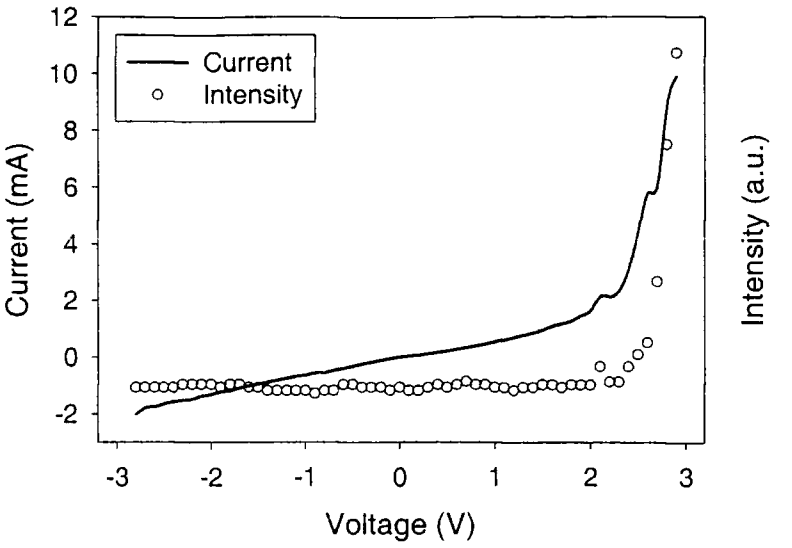

Figure 5-28 *Current-voltage (line) and intensity-voltage (circles) characteristics of an ITO/PPV/Al device*

For ITO/PPV/Al devices, a large current flows in forward bias, leading to electroluminescence only in the forward bias direction. A small leakage current is observed in reverse bias, but no light is observed. The electroluminescence spectrum of a typical diode is compared to the photoluminescence spectrum of PPV converted on an ITO substrate in Figure 5-29.

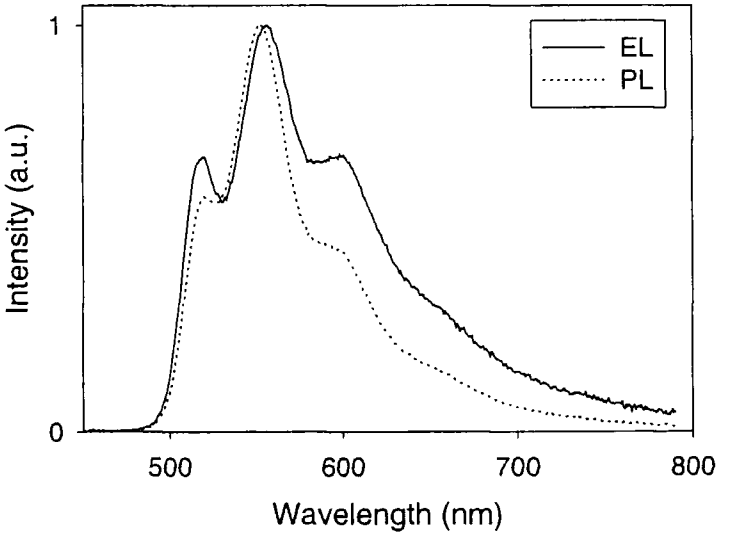

Figure 5-29 *Electroluminescence (solid line) and photoluminescence (dashed line) spectra of PPV*

The similarity in the shape and peak position of the electroluminescence and photoluminescence spectra of PPV is shown in Figure 5-29. The EL spectrum has a

peak at 556nm (2.23eV), and the PL spectrum has a peak at 552nm (2.25eV). The spectra are very similar to those published elsewhere [1, 33].

CALCIUM AND ALUMINIUM ELECTRODES FOR PPV DIODES

Magnesium, aluminium and calcium were used to vary the barrier heights to electron injection in PPV diodes. The current-field characteristics of diodes with an ITO/PPV/metal structure are shown in Figure 5-30.

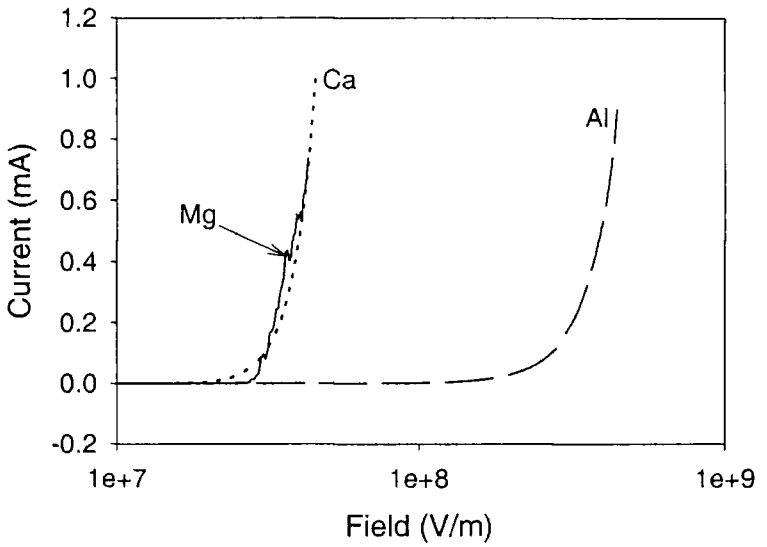

Figure 5-30 *Current-field characteristics of ITO/PPV/metal diodes, with magnesium (solid line), aluminium (broken line) and calcium (dotted line) electrodes*

The field required for significant current flow is highest for diodes with aluminium electrodes, and lowest in diodes with calcium electrodes. Diodes with magnesium contacts require similar fields for a given current to calcium devices. Changing the metal used for the electrode also has an effect on the quantum efficiency of the diode. The current-intensity behaviour of devices with aluminium, magnesium and calcium contacts is shown in Figure 5-31.

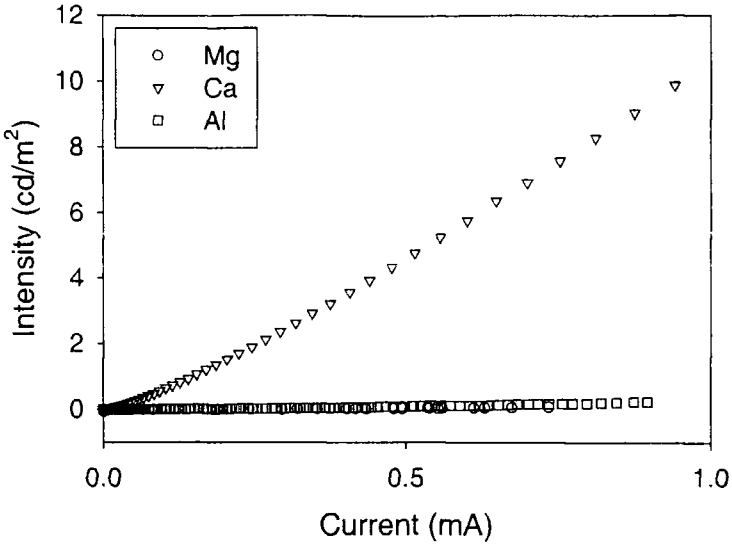

Figure 5-31 *Current-intensity characteristics of single layer PPV diodes with various metal contacts*

The current-intensity curves suggest that devices with calcium electrodes are more efficient than diodes with magnesium or aluminium electrodes. This is confirmed by the calculation of external quantum efficiencies of the devices. There is often a range of quantum efficiency values for devices with the same structure and often very small differences in fabrication. The external quantum efficiency values given in Table 5-4 are for the devices shown above, and also a range of values is given for other devices of the same structure.

Structure	E_{ext} (shown)	E_{ext} (min)	E_{ext} (max)
ITO/PPV/Ca	9×10^{-3}	4×10^{-4}	4×10^{-2}
ITO/PPV/Mg	7×10^{-5}	5×10^{-5}	1×10^{-4}
ITO/PPV/Al	2×10^{-4}	1×10^{-4}	5×10^{-3}

Table 5-4 *External quantum efficiencies for single layer PPV diodes with various metal electrodes*

Karg *et al* [11] find external quantum efficiencies of 0.005% to 0.05% for PPV diodes using calcium electrodes and 0.0001% to 0.02% using aluminium electrodes, similar values to those listed in Table 5-4. Holmes *et al* [1] quote internal quantum efficiencies, but assuming a polymer refractive index of approximately 2.5, the external quantum efficiencies can be calculated as 0.01%, 0.005% and 0.0002% for single layer PPV diodes with calcium, magnesium and aluminium electrodes respectively.

Schottky fits to the data can be obtained from the natural log of current density versus voltage plots in small ranges of the J-V characteristics. These fits are shown below.

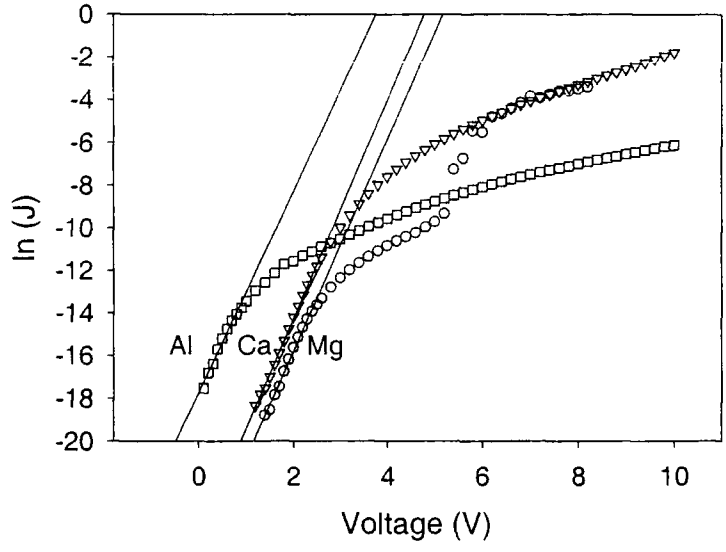

Figure 5-32 *Natural log of current density versus voltage plots (symbols) and lines of regression to the data for single layer PPV diodes with various metal electrodes*

Analysis of the slope and intercept of the regression lines allows the calculation of the diode ideality factor and the Schottky barrier height. These values are summarised in Table 5-5.

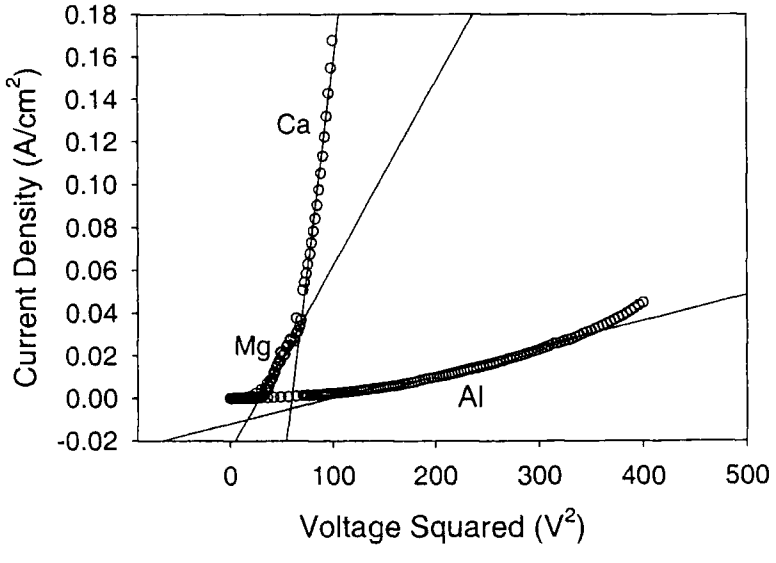

Figure 5-33 *Current density-voltage squared curves for single layer PPV diodes with various metal electrodes*

Metal	ϕ_b (±0.01 eV)	N	μ ($cm^2 V^{-1}s^{-1}$)	r^2
Mg	1.07	7.8	$(8 \pm 1) \times 10^{-6}$	0.80
Ca	1.05	7.6	$(1.7 \pm 0.3) \times 10^{-5}$	0.77
Al	0.87	8.3	$(2.0 \pm 0.9) \times 10^{-8}$	0.70

Table 5-5 *Calculated barrier height (ϕ_b), diode ideality factor (n), charge mobility (μ) and r^2 coefficient for the linear regression in the SCLC framework for ITO/PPV/metal devices with magnesium, calcium and aluminium electrodes*

Assuming PPV is a p-type semiconductor and using the relationship between the height of the Schottky barrier and the barrier to electron injection ($\varphi_e = E_g - \phi_b = \phi_m - \chi$), the barrier to electron injection can be calculated. The barriers to electron injection are 1.45eV, 1.43eV and 1.63eV for calcium, magnesium and aluminium electrodes respectively. The theoretical barriers to electron injection are 0.5eV, 1.2eV and 1.7eV respectively.

Karg *et al* [11] find Schottky barrier heights of 1.4eV and 1.6eV for PPV diodes with aluminium and calcium electrodes respectively. They ascribe the small difference in barrier heights, and hence the small difference in barriers to electron injection, to the role that interfaces play in charge injection in polymer LEDs. They note that there should be a 1.5eV difference in the Schottky barrier heights between calcium and aluminium, based on the theoretical positions of the energy levels, but only a 0.2eV difference is observed. The 0.2eV difference between aluminium and calcium electrodes is observed in this study. Karg *et al*, in their more systematic study, find diode ideality factors of 2.0 and 2.2 for calcium and aluminium electrodes, far better than the values obtained in this study.

Marks *et al* [34] find charge mobilities of around 10^{-9} to 10^{-10} cm^2 V^{-1} s^{-1} for PPV, approximately 4 orders of magnitude smaller than those listed in Table 5-5. They do, however, acknowledge that their values are low and suggest this may be due to the presence of local shorts. They calculate a charge mobility an order of magnitude smaller for PPV diodes with aluminium electrodes compared to those with calcium and magnesium electrodes. Karg *et al* find charge mobilities in the range 10^{-5} to 10^{-6} cm^2 V^{-1} s^{-1} for PPV diodes with both calcium and aluminium electrodes.

The current-voltage data can be analysed in the Fowler-Nordheim framework, and a Fowler-Nordheim plot for ITO/PPV/Metal diodes is shown as Figure 5-34.

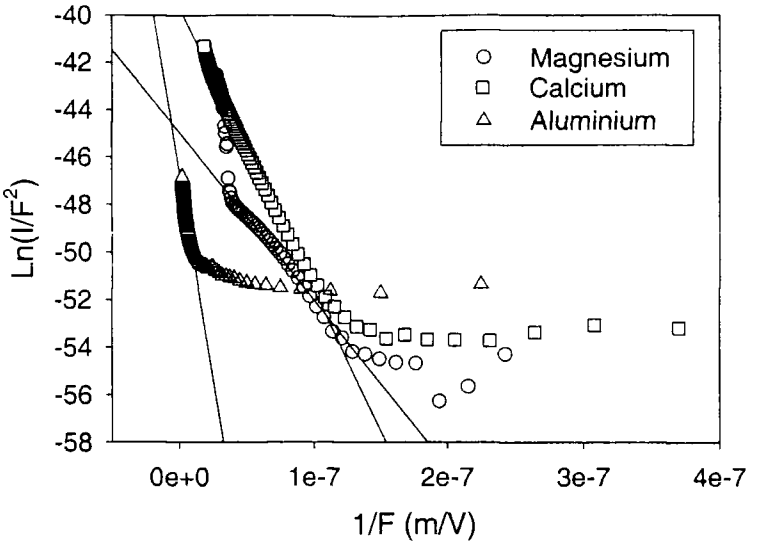

Figure 5-34 *Fowler-Nordheim plot for ITO/PPV/Metal diodes with magnesium, calcium and aluminium electrodes*

The barrier heights calculated for the data above, assuming triangular barriers, are shown in Table 5-6.

Metal	ϕ_b (eV)
Mg	0.05 ± 0.02
Ca	0.07 ± 0.02
Al	0.14 ± 0.07

Table 5-6 *Barrier heights of ITO/PPV/Metal diodes calculated from Fowler-Nordheim treatment of the data*

Marks *et al* [34] find barriers of 0.17eV, 0.24eV and 0.18eV from Fowler-Nordheim analysis of PPV diodes with magnesium, calcium and aluminium electrodes. The values listed in Table 5-6, are therefore lower than the values published elsewhere.

SUMMARY AND DISCUSSION

The colour co-ordinates of PPV PL and EL are shown in Figure 5-43, and illustrate the similarity between the processes.

External quantum efficiencies calculated for single layer PPV diodes in this study are similar to values published in the literature. The quantum efficiency for a single layer device with magnesium contacts is lower than the value published in reference [1], and this could be a consequence of evaporation of the magnesium contacts used in this study.

Schottky and Fowler-Nordheim barriers calculated in this study are slightly lower than those found elsewhere [11, 34], and this could be a consequence of differences in fabrication procedures and conversion conditions.

In summary, diodes with PPV as the active layer tend to exhibit more diode-like behaviour than PPY based diodes. Their characteristics can be investigated in a SCLC, Schottky and Fowler-Nordheim framework, and each theory provides a reasonable fit to the data over a limited range. None of the three frameworks provides a perfect fit over all the data, and the calculated barrier heights do not correspond to what is expected theoretically, although the Schottky fit provides reasonable agreement with the barriers to electron injection for aluminium and magnesium electrodes. The data do suggest that interface formation plays a large role in polymer diode performance, as suggested elsewhere (see for example reference [35]).

Single layer diodes with MEH-PPV as the active layer were fabricated and characterised. MEH-PPV was spin-coated from solution onto ITO coated substrates and aluminium electrodes were evaporated to complete the device structure. The energy levels of the device are shown in Figure 5-35.

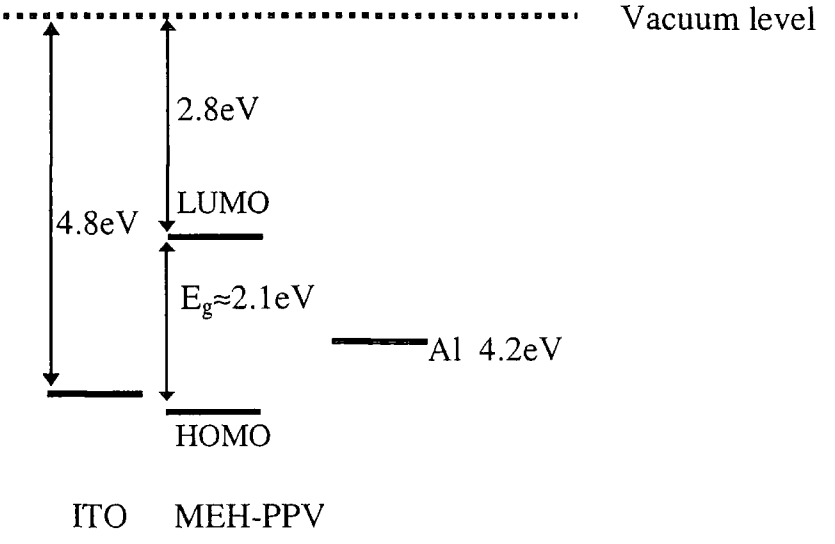

Figure 5-35 *Energy levels of an ideal MEH-PPV light-emitting diode*

In forward bias, the theoretical barrier to hole injection from ITO is 0.1eV and the barrier to electron injection from the aluminium is 1.4eV. The positions of the MEH-PPV energy levels were obtained from reference [2].

The IV and intensity-voltage characteristics of an ITO/MEH-PPV/Al diode are shown in Figure 5-36.

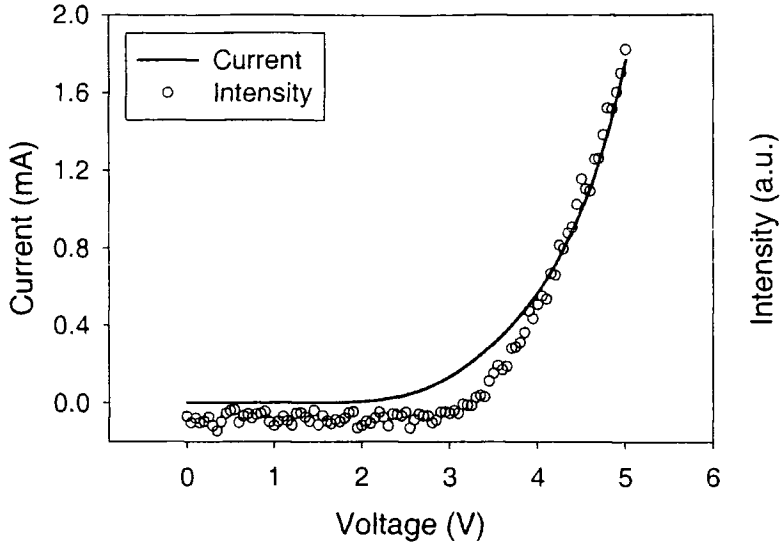

Figure 5-36 *Current-voltage and intensity-voltage characteristics of an ITO/MEH-PPV/Al device*

The EL quantum efficiency can be calculated from the current-intensity characteristics and the EL spectrum. The current-intensity characteristics can be seen in Figure 5-37 and the EL spectrum is compared to the PL spectrum in Figure 5-38.

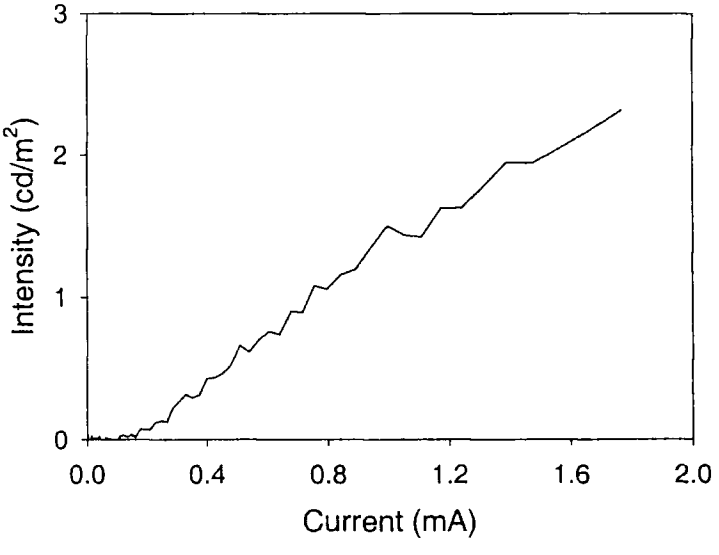

Figure 5-37 *Current-EL intensity characteristics of an ITO/MEH-PPV/Al device*

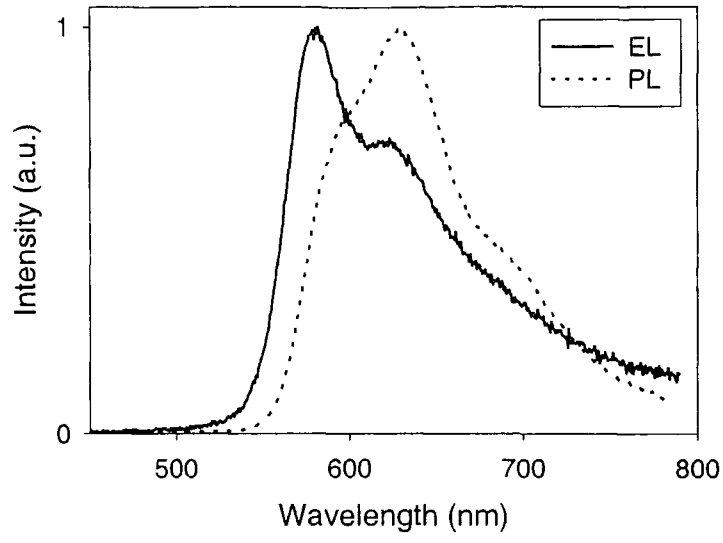

Figure 5-38 *Electroluminescence (EL) and photoluminescence (PL) spectra of MEH-PPV*

The peak of the EL is at 582nm (2.13eV) and the peak of the PL is at 628nm (1.97eV). The spectra are similar in shape, though not identical. The source of the shift in the peak of the luminescence appears to be the change in the relevant intensities of the vibronic features of the spectrum. The EL spectrum is similar in shape another published elsewhere [36]. The external quantum efficiency of the device shown is 1.3×10^{-3} %, although typical devices with aluminium contacts have efficiencies ranging from 0.001% for devices made with the batch of MEH-PPV shown to 0.009% for devices made with a different batch of MEH-PPV. These values are significantly higher than the 0.0001% reported elsewhere [2, 36].

The IV characteristics of MEH-PPV devices can be studied in a Schottky, SCLC and Fowler-Nordheim framework. The natural log of current density versus voltage plot, used for Schottky analysis, is shown in Figure 5-39.

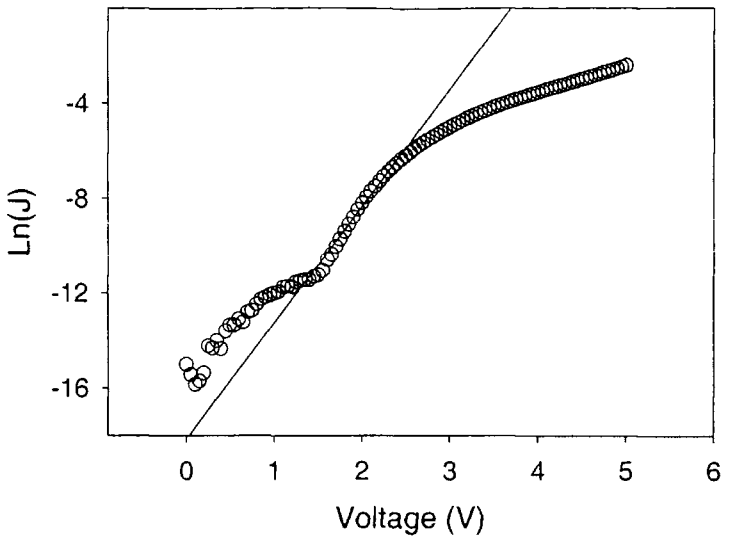

Figure 5-39 *Natural log of current density versus voltage plots (circles) and lines of regression to the data for an ITO/MEH-PPV/Al diode*

Analysis of the slope and gradient of the regression produces a value of the Schottky barrier of (0.88 ± 0.01) eV and a diode ideality factor of 7.9. The barrier to electron injection calculated from the Schottky barrier height is 1.2eV, close to the theoretically expected value of 1.4eV. Campbell et al [37] find a Schottky barrier height of 1.1eV for ITO/MEH-PPV/Al diodes, slightly larger than the value in this study. A current density versus voltage squared plot, for SCLC analysis, is shown in Figure 5-40.

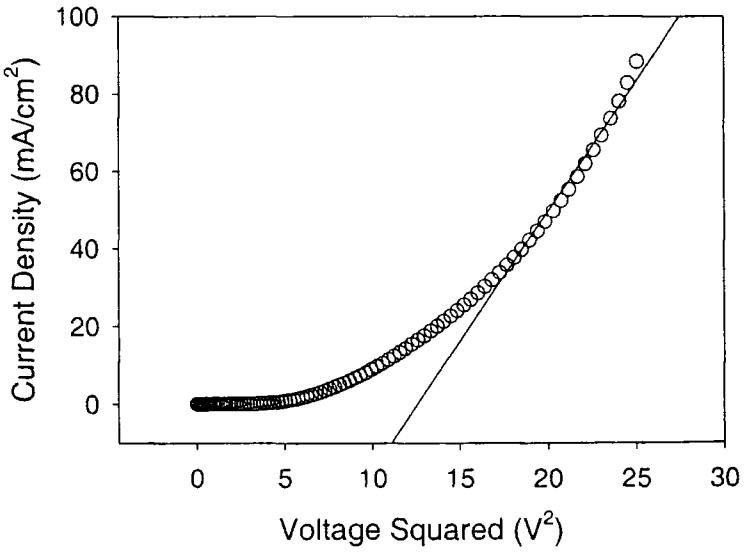

Figure 5-40 *Current density-voltage squared characteristics (circles) and linear regression (line) for an ITO/MEH-PPV/Al diode*

Analysis of the gradient of the linear regression to the data in Figure 5-40 yields a charge mobility of $(1.7 \pm 0.4) \times 10^{-5}$ cm^2 V^{-1} s^{-1} and an r^2 value of 0.98 over a limited range. Campbell *et al* [37] find a highly field dependent charge mobility which would have a value of approximately 2.6×10^{-5} cm^2 V^{-1} s^{-1} at comparable field to that considered above.

A Fowler-Nordheim plot of the IV characteristics is shown in Figure 5-41.

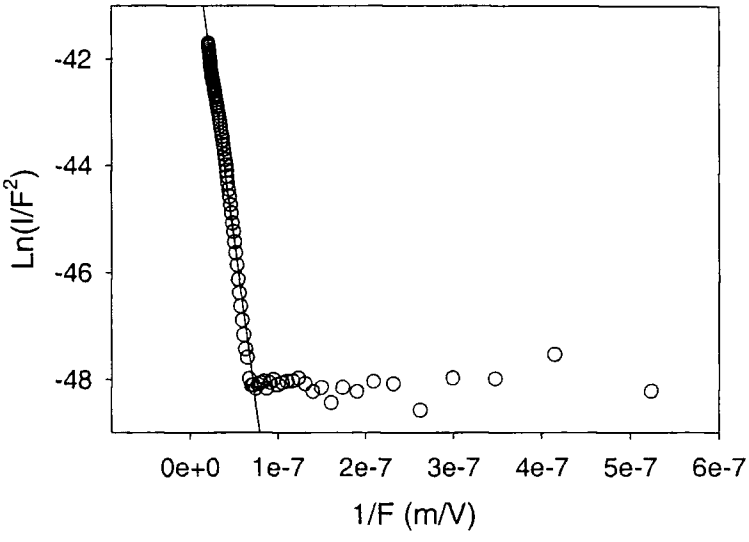

Figure 5-41 *Fowler-Nordheim plot for an ITO/MEH-PPV/Al diode*

Fowler-Nordheim analysis, assuming the formation of a triangular barrier, yields a barrier height of (0.07 ± 0.03) eV. Parker [2] finds a barrier height of 0.22eV from similar analysis of ITO/MEH-PPV/Al diodes.

MEH-PPV PRECURSOR

The EL spectrum of devices using precursor processed MEH-PPV as the active layer is different to the EL of devices using solution processed MEH-PPV, as shown in Figure 5-42.

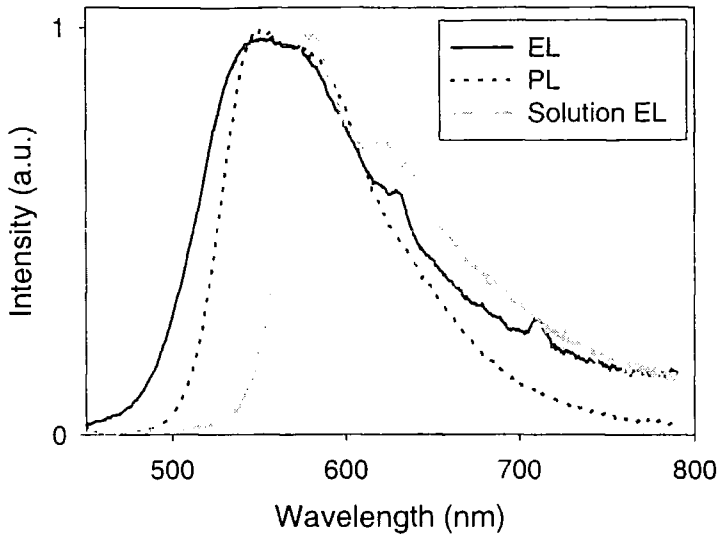

Figure 5-42 *Photoluminescence (PL) and electroluminescence (EL) spectra of MEH-PPV precursor and EL from solution processed MEH-PPV (Solution EL)*

The EL spectrum of MEH-PPV precursor converted on ITO is similar its PL spectrum, as would be expected. Both spectra are dissimilar to the EL (and PL) spectra of MEH-PPV films prepared via the solution route. This is consistent with absorption and photoluminescence measurements, which suggest a substantial interaction between the MEH-PPV precursor and ITO, when the precursor is thermally converted on ITO.

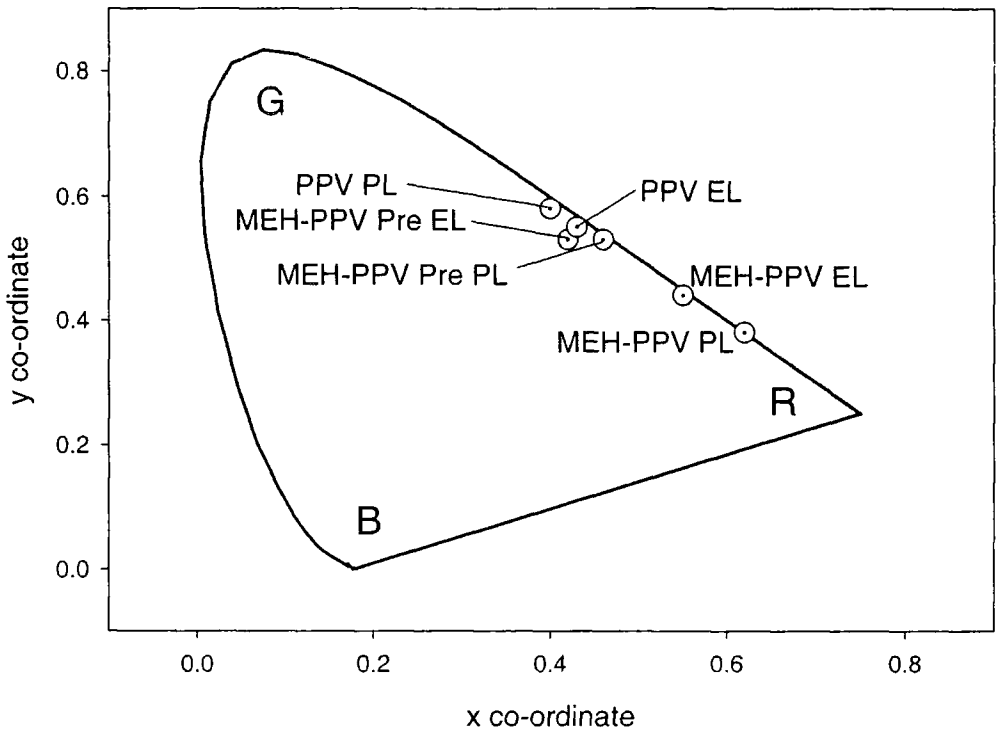

Figure 5-43 *Colour co-ordinate diagram of electroluminescence (EL) and photoluminescence (PL) for PPV, solution processed MEH-PPV and MEH-PPV prepared via the precursor route (MEH-PPV Pre)*

The x,y co-ordinates of (0.62, 0.38), calculated for MEH-PPV PL, agree with those calculated by Karg *et al* [38]. The colour of the EL of the MEH-PPV device prepared via the precursor route more closely resembles the EL of PPV than the EL of solution processed MEH-PPV.

The barriers calculated for MEH-PPV devices are smaller than those reported elsewhere [2, 37], although this is not surprising as the polymer is from a different source to that used above. The barrier to electron injection calculated from the Schottky treatment of the data is close to what is theoretically expected. The SCLC, Schottky and Fowler-Nordheim fits to the data all provide reasonable agreement, although again, only over a limited data range.

Quasi-static capacitance-voltage (CV) measurements were carried out using a Keithley 595 quasi-static CV meter. The bias sweep rate has an effect on quasi-static measurements (see for example reference [39]) and hence the step rate was varied between 0.5 mV/s and 40 mV/s. Mott-Schottky results are presented for step rates of 1mV/s to 2 mV/s. Recalling that the capacitance per unit area, C_d, is related to the applied voltage, V, by the Mott-Schottky relation

$$C_d^{-2} = \left(\frac{2}{q\varepsilon\varepsilon_0 N_A} \right) (V_{SO} - V),$$

Equation 5-2

where N_A is the acceptor density, ε is the permittivity of the polymer and V_{SO} is the contact potential difference between the metal and the semiconductor. Hence the doping density of the device can be obtained by producing Mott-Schottky plots of C_d^{-2} versus applied voltage. The width of the depletion layer can then be calculated from Equation 5-3.

$$w = \sqrt{\frac{2\varepsilon\varepsilon_0 (V_{SO} - V)}{qN_A}}$$

Equation 5-3

Capacitance values were corrected for the effect of leakage currents using Equation 5-4.

$$C_{corrected} = C_{measured} - \frac{(Q/t)(\tau_{delay})}{V_{step}}$$

Equation 5-4

The equation is obtained from the Keithley 595 instruction manual. The value Q/t is measured by the instrument at the same time as the capacitance, τ_{delay} is the time delay between each voltage increment and V_{step} is the size of each voltage increment.

PPY DIODES

The capacitance-voltage characteristics of an ITO/PPY/Al diode are shown in Figure 5-44.

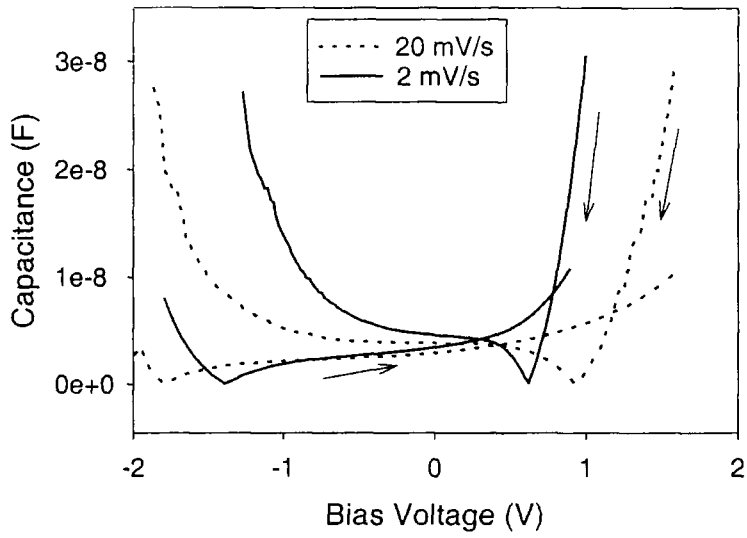

Figure 5-44 *Capacitance-voltage characteristics of an ITO/PPY/Al device at step rates of 2mV/s and 20mV/s*

A Mott-Schottky plot of the data with a step voltage of 2mV/s is shown in Figure 5-45.

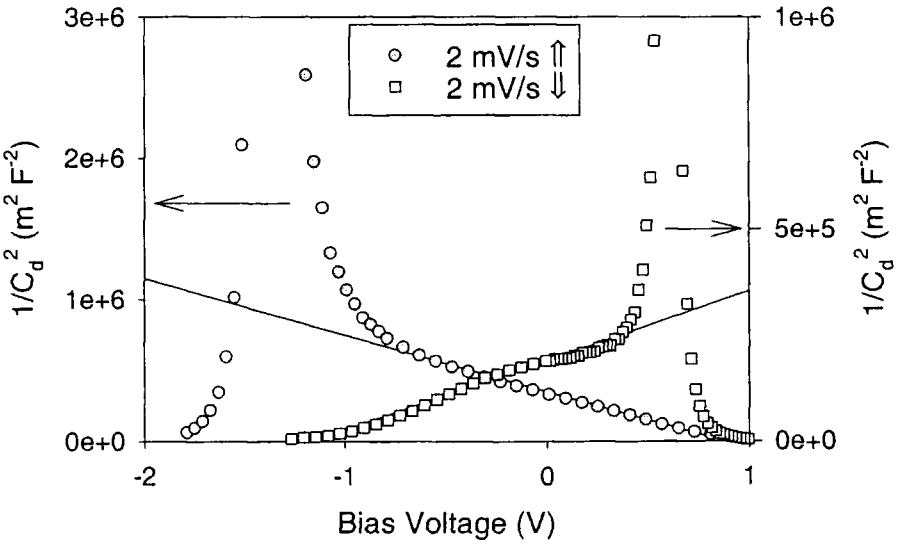

Figure 5-45 *Mott-Schottky plot for an ITO/PPY/Al device*

Mott-Schottky plots should produce a straight line fit only in reverse bias. Due to the symmetric nature of the IV characteristics and Schottky barriers of PPY based devices, the Mott-Schottky plots are very similar, though not identical, and exhibit

linear characteristics in both forward and reverse bias. From the slope and intercept of the Mott-Schottky plot it is possible to calculate the donor density and the built-in voltage (contact potential difference). The width of the depletion region was calculated from these values. The results for PPY with increasing voltage (forward bias) and decreasing voltage (reverse bias) are shown in Table 5-7.

V_{step}	V_{SO} (V)	N_D (m^{-3})	W (nm)
+ve	0.9 ± 0.2	$(9 \pm 2) \times 10^{23}$	21 ± 1
-ve	1.2 ± 0.2	$(2.1 \pm 0.4) \times 10^{24}$	15 ± 1

Table 5-7 *Built in voltage (V_{SO}), donor density (N_D) and depletion region width (w) for an ITO/PPY/Al device with a positive and negative step voltage*

The calculated values of the built-in voltage are slightly larger than the calculated Schottky barrier heights in forward and reverse bias. This may be due to an additional series resistance (due to the depletion layer), in addition to the resistance of the bulk polymer. This means that all of the applied bias does not appear across the depletion region and hence values of V_{SO} are higher than expected [16]. The values of the built-in voltage suggest that there is increased band bending in reverse bias, and although the Schottky barriers are similar in forward and reverse bias, they are not identical. The values of the donor density are similar in magnitude with those reported for polypyrrole [40] and thiophene oligomer [41] diodes. The depletion widths are smaller than the device thickness of 40nm, so the devices are not fully depleted.

PPV DIODES

The capacitance-voltage characteristics of an ITO/PPV/Al diode are shown in Figure 5-46.

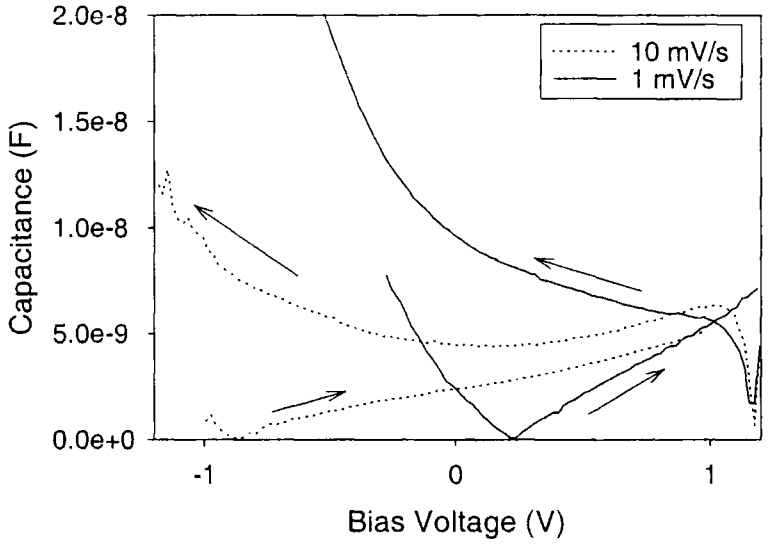

Figure 5-46 *Capacitance-voltage characteristics of an ITO/PPV/Al device at step rates of 1mV/s and 10mV/s*

The capacitance-voltage behaviour of the ITO/PPV/Al device in forward and reverse bias is significantly different, and the symmetry observed in the case of the PPY device is not found. The difference between forward and reverse bias is also observed in the Mott-Schottky plot (Figure 5-47).

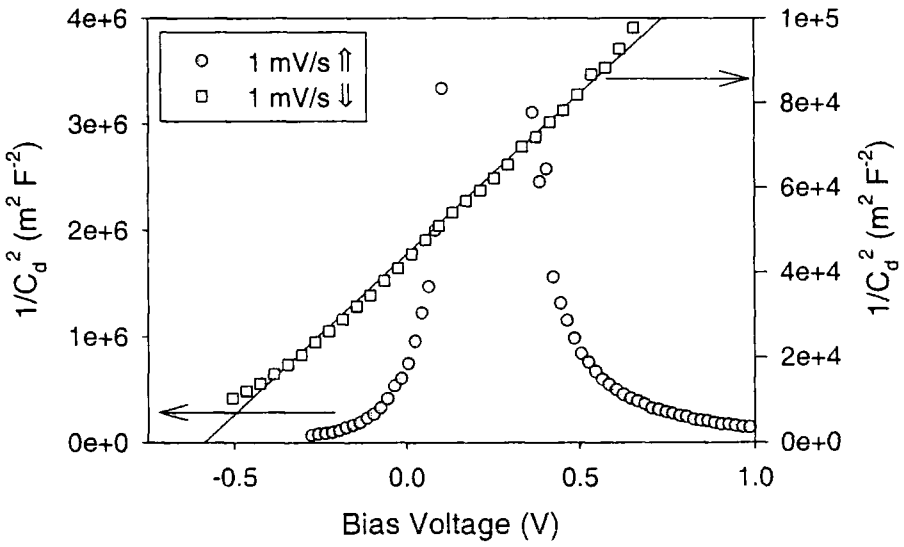

Figure 5-47 *Mott-Schottky plot for an ITO/PPV/Al device*

In the Mott-Schottky plot for the PPV device, there is clearly only a linear relationship in reverse bias (open squares in Figure 5-47), and a more complex relationship in forward bias. Analysis of the data allows calculation of the acceptor density, built-in voltage (contact potential difference) and the width of the depletion region. These values are shown in Table 5-8.

V_{SO} (V)	N_A (m^{-3})	w (nm)
0.6 ± 0.1	$(4.7 \pm 0.9) \times 10^{24}$	7.5 ± 0.4

Table 5-8 *Built in voltage (V_{SO}), acceptor density (N_A) and depletion region width (w) for an ITO/PPV/Al device*

The calculated value for the acceptor density is consistent with values found in the literature [7, 11]. The depletion width is lower than the value of 50nm quoted in the literature. The built-in voltage is similar to the Schottky barrier height of 0.87eV found for an ITO/PPV/Al device.

MEH-PPV DIODES

The capacitance-voltage characteristics of an ITO/MEH-PPV/Al diode, using a MEH-PPV film prepared via the solution route, are shown in Figure 5-48.

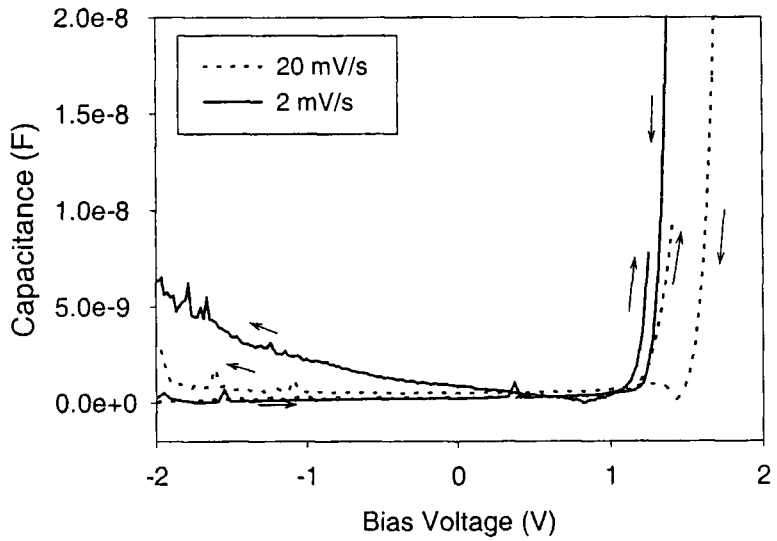

Figure 5-48 *Capacitance-voltage characteristics of an ITO/MEH-PPV/Al device at step rates of 2mV/s and 20mV/s*

The capacitance-voltage characteristics of the MEH-PPV device are different to both the PPY and PPV based devices. A significant change in capacitance is only

observed at high positive voltages, and very little capacitance change is observed at negative voltages. The Mott-Schottky plot of these data is shown in Figure 5-49.

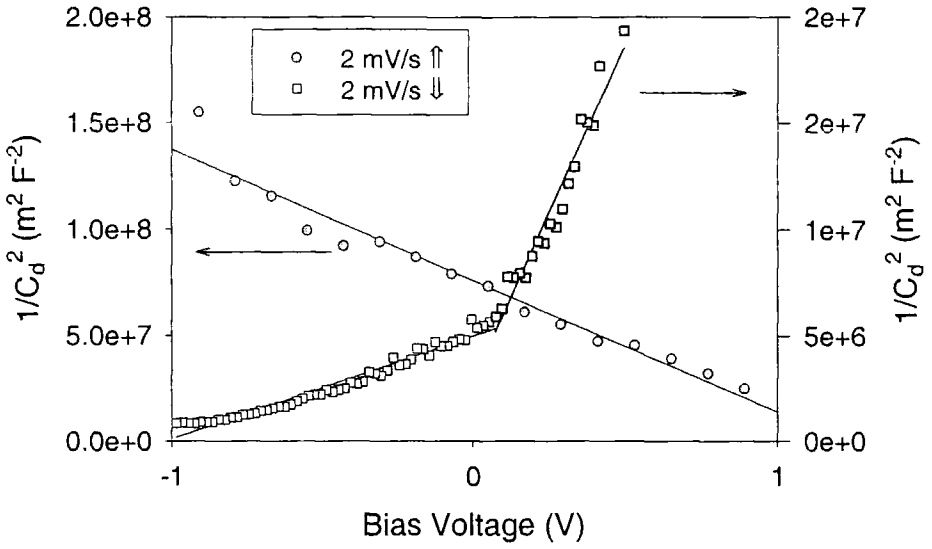

Figure 5-49 *Mott-Schottky plot for an ITO/MEH-PPV/Al device*

The Mott-Schottky plot of an ITO/MEH-PPV/Al device shows a simple linear relationship only in forward bias (filled circles in Figure 5-49), i.e. in the opposite sense to that found for the PPV based device. Similar, but slightly more complex behaviour is found for MEH-PPV diodes using MEH-PPV prepared via the precursor route, as shown by the Mott-Schottky plot in Figure 5-50.

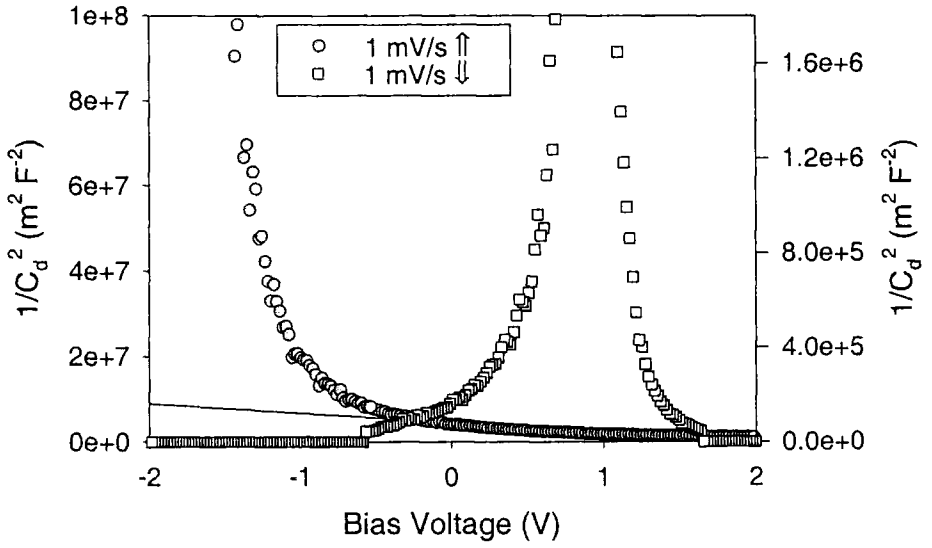

Figure 5-50 *Mott-Schottky plot for an ITO/MEH-PPV/Al device using MEH-PPV prepared via the precursor route*

The Mott-Schottky plot for the device using MEH-PPV prepared via the solution route shows linear behaviour over a reasonable range in forward bias, as in the

case for the solution prepared case, but at high negative voltages exhibits highly non-linear behaviour. The reverse bias behaviour is similar in both cases, though not identical.

The acceptor density, built-in voltage and the width of the depletion region were calculated from these plots and the values are shown in Table 5-9.

Route	V_{SO} (V)	N_A (m^{-3})	w (nm)
Solution	1.2 ± 0.2	$(6 \pm 1) \times 10^{21}$	300 ± 20
Precursor	2.0 ± 0.4	$(1.6 \pm 0.3) \times 10^{24}$	53 ± 3

Table 5-9 *Built in voltage (V_{SO}), acceptor density (N_A) and depletion region width (w) for an ITO/MEH-PPV/Al device prepared via solution and precursor routes*

The acceptor density of the MEH-PPV diode prepared via the precursor route is similar to the value of 10^{22} m^{-3} quoted by Campbell *et al* [37]. The depletion width is larger than the thickness of the device, indicating that the device is fully depleted, as found elsewhere [2]. The comparison between MEH-PPV prepared via the solution and precursor routes is interesting. The acceptor density for solution prepared MEH-PPV is approximately 3 orders of magnitude less than that of PPV, which is consistent with the concept of the polymer doping during conversion on ITO substrates (see for example reference [7]). The MEH-PPV prepared via the precursor route and hence via thermal conversion on ITO has an acceptor density 3 orders of magnitude higher, comparable to that of PPV. In addition, the width of the depletion layer at zero bias is no longer thicker than the device thickness (105nm). There is an increase in the built-in voltage, suggesting that there is some modification to the energy levels of the polymer, consistent with the optical measurements presented in the previous chapter.

SUMMARY AND CONCLUSIONS

Electroluminescent devices using a single polymer layer have been fabricated and characterised. Devices using PPV and MEH-PPV exhibit diode-like characteristics and exhibit different behaviour when operated under forward and reverse bias. In contrast, single layer devices using PPY and PPY derivatives exhibit almost symmetrical current-voltage behaviour. PPV and PPY based devices generally exhibit a reduction in the field required for a given current when lower workfunction metals are used as the material for the cathode. PPY based devices with low workfunction metals require a similar field for a given current in forward and reverse bias, even though the theoretical barrier to charge injection is far higher in reverse bias. This is a departure from the simple model of device operation.

The EL efficiency of devices with aluminium electrodes using PPY, PPV or MEH-PPV as the active layer is of the order of 10^{-3}%. The efficiency of PPV based devices can be improved through the use of low workfunction calcium electrodes. The use of metals other than aluminium with PPY has a detrimental effect on the efficiency of the devices.

Successful colour tuning of electroluminescent devices by blending of PPY with PMMA is unlikely due to the significant differences between the PL and EL spectra of blend films and poor operating characteristics of such devices. Similar spectral differences and poor operating characteristics are observed for devices using a regular PPY copolymer. Devices using random copolymers of PPY have anomalous current-voltage characteristics which become more apparent as the conjugation length of the polymer is decreased. No electroluminescence is observed from copolymers containing *meta*-linked monomer units.

Schottky, SCLC and Fowler-Nordheim analysis of the device characteristics provides some insight into the device operation but cannot provide a robust model of device operation, particularly for devices using PPY. Schottky analysis of the data in this study provides diode ideality factors which are very high. The range over which the data fit the model is also limited, and can be very limited in some cases. The data tend to fit over a voltage range at which no light is observed. This also applies to the capacitance-voltage analysis which assumes the formation of a Schottky barrier. Fowler-Nordheim and SCLC analysis provide models which fit at higher fields and currents and hence in regions where light emission occurs. The fits to the data can be

somewhat inaccurate, however, and Fowler-Nordheim analysis of PPY devices, for example, is completely inappropriate. Modified versions of all three simple models do exist, but they tend to be far more complex, highly material dependent and the validity of the modifications has yet to be fully explored.

The devices in this study were fabricated primarily as light-emitting diodes. ITO plays an important role in the behaviour of polymer LEDs and idealised device structures should be fabricated for any systematic investigation of device models. This should also improve the accuracy and validity of values derived from the treatment of current-voltage data within the various models.

Quasi-static capacitance-voltage analysis is not widely used to investigate polymer LEDs. Idealised samples without ITO should produce more consistent results and the analysis of the data requires the assumption of the formation of a Schottky barrier. It has been shown in this chapter that Schottky analysis of polymer LEDs is often difficult and the range over which the Schottky assumption is valid can be very small. This is compounded by the high capacitance, which is often found for polymer LEDs and the small range of some commercial CV meters. CV analysis can provide some useful information, however. It shows that PPV and PPY diodes have a similar doping density, even though PPV films are considered to be doped during the conversion process. The symmetry of the current-voltage characteristics of devices using PPY in forward and reverse bias is also observed in the capacitance-voltage measurements. CV analysis shows that MEH-PPV films prepared via solution processing have an acceptor density 3 orders of magnitude lower than PPV and preparation of MEH-PPV via a precursor route and thermal conversion on ITO coated substrates produces an acceptor density similar to that of PPV. This suggests significant doping of the polymer during the thermal conversion. This provides insight into possible reasons for the substantial changes observed in optical characteristics of MEH-PPV films prepared via the precursor route.

REFERENCES

[1] A. B. Holmes, et al., Synth. Met., **55-57** , (1993), 4031-4040.

[2] I. D. Parker, J. Appl. Phys., **75** , 3 (1994), 1656-1666.

[3] F. Garten, J. Vrijmoeth, A. R. Schlatmann, R. E. Gill, T. M. Klapwijk and G. Hadziioannou, Synth. Met., **76** , 1-3 (1996), 85-89.

[4] T. Miyamae, D. Yoshimura, H. Ishii, Y. Ouchi, K. Saki, T. Miyazaki, T. Koike and T. Yamamoto, J. Chem. Phys., **103** , 7 (1995), 2738-2744.

[5] A. J. Epstein, et al., Synth. Met., **78** , (1996), 253-261.

[6] A. J. Campbell, D. D. C. Bradley and D. G. Lidzey, J. Appl. Phys., **82** , 12 (1997), 6326-6342.

[7] M. Meier, S. Karg and W. Riess, J. Appl. Phys., **82** , 4 (1997), 1961-1966.

[8] P. W. M. Blom, M. J. M. deJong and M. G. vanMunster, Phys. Rev. B., **55** , 2 (1997), R656-R659.

[9] W. Brutting, M. Meier, M. Herold, S. Karg and M. Schwoerer, Synth. Met., **91** , 1-3 (1997), 163-168.

[10] W. Brutting, M. Meier, M. Herold, S. Karg and M. Schwoerer, Chemical Physics, **227** , 1-2 (1998), 243-252.

[11] S. Karg, M. Meier and W. Riess, J. Appl. Phys., **82** , 4 (1997), 1951-1960.

[12] S. S. Pandey, M. K. Ram, V. K. Srivastava and B. D. Malhotra, Journal Of Applied Polymer Science, **65** , 13 (1997), 2745-2748.

[13] J. Birgerson, M. Fahlman, P. Broms and W. R. Salaneck, Synth. Met., **80** , 2 (1996), 125-130.

[14] B. J. Chen and S. Y. Liu, Synth. Met., **91** , 1-3 (1997), 169-171.

[15] V. Cimrova and D. Neher, Synth. Met., **76** , 1-3 (1996), 125-128.

[16] D. M. Taylor and H. L. Gomes, J. Phys. D.-Appl. Phys., **28** , 12 (1995), 2554-2568.

[17] D. Braun and A. J. Heeger, Thin Solid Films, **216** , 1 (1992), 96-98.

[18] A. R. Brown, N. C. Greenham, R. W. Gymer, K. Pichler, D. D. C. Bradley, R. H. Friend, P. L. Burn, A. Kraft and A. B. Holmes, Proceedings of Nato ARW, , .

[19] H. L. Wang, F. Huang, A. G. MacDiarmid, Y. Z. Wang, D. D. Gebler and A. J. Epstein, Synth. Met., **80** , (1996), 97-104.

[20] Y. Z. Wang, D. D. Gebler, D. J. Spry, D. K. Fu, T. M. Swager, A. G. MacDiarmid and A. J. Epstein, IEEE Trans. Elect. Dev., **44** , 8 (1997), 1263-1268.

[21] T. Yamamoto, H. Suganuma, Y. Saitoh, T. Maruyama and T. Inoue, Jpn. J. Appl. Phys. Part 2, **35** , 9A (1996), 1142-1144.

[22] S. Dailey, M. Halim, E. Rebourt, L. E. Horsburgh, I. D. W. Samuel and A. P. Monkman, J. Phys: Cond. Matt., **10** , (1998), 5171-5178.

[23] D. D. Gebler, Y. Z. Wang, J. W. Blatchford, S. W. Jessen, H.-L. Wang, T. M. Swager, A. G. MacDiarmid and A. J. Epstein, J. Appl. Phys., **78** , 6 (1995), 4264-4266.

[24] H. N. Cho, D. Y. Kim, Y. C. Kim, J. Y. Lee and C. Y. Kim, Adv. Mat., **9** , 4 (1997), 326.

[25] M. Remmers, D. Neher, J. Gruner, R. H. Friend, G. H. Gelinck, J. M. Warman, C. Quattrocchi, D. A. Dossantos and J. L. Bredas, Macromolecules, **29** , 23 (1996), 7432-7445.

[26] M. Onoda, Y. Ohmori, T. Kawai and K. Yoshino, Synth. Met., **71** , 1-3 (1995), 2181-2182.

[27] Y. Yang and Q. B. Pei, J. Appl. Phys., **81** , 7 (1997), 3294-3298.

[28] R. H. Friend, D. D. C. Bradley and A. B. Holmes, Physics World, **November 1992** , (1992), 42-46.

[29] M. Halim, I. D. W. Samuel, E. Rebourt and A. P. Monkman, Synth. Met., **84** , 1-3 (1997), 951-952.

[30] T. Yamamoto, et al., J. Am. Chem. Soc., **116** , (1994), 4832-4845.

[31] K. Z. Xing and N. Johansson, Adv. Mat., **9** , 13 (1997), 1027.

[32] F. Cacialli, R. H. Friend, N. Haylett, R. Daik, W. J. Feast, D. A. Dossantos and J. L. Bredas, Appl. Phys. Lett., **69** , 25 (1996), 3794-3796.

[33] W. Riess, S. Karg, V. Dyakonov, M. Meier and M. Schwoerer, Journal Of Luminescence, **60** , 1 (1994), 906-911.

[34] R. N. Marks, D. D. C. Bradley, R. W. Jackson, P. L. Burn and A. B. Holmes, Synth. Met., **57** , 1 (1993), 4128-4133.

[35] W. Brutting, E. Buchwald, G. Egerer, M. Meier, K. Zuleeg and M. Schwoerer, Synth. Met., **84** , 1-3 (1997), 677-678.

[36] D. Braun and A. J. Heeger, Appl. Phys. Lett., **58** , 18 (1991), 1982-1984.

[37] I. H. Campbell, P. S. Davids, D. L. Smith, N. N. Barashkov and J. P. Ferraris, Appl. Phys. Lett., **72** , 15 (1998), 1863-1865.

[38] S. Karg, J. C. Scott, J. R. Salem and M. Angelopoulos, Synth. Met., **80** , 2 (1996), 111-117.

[39] J. R. Hauser, IEEE Trans. Elect. Dev., **44** , 6 (1997), 1009-1012.

[40] R. Singh and A. K. Narula, Appl. Phys. Lett., **71** , 19 (1997), 2845-2847.

[41] D. M. deLeeuw and E. J. Lous, Synth. Met., **65** , 1 (1994), 45-53.

Chapter 6 Electroluminescence from Multiple Polymer Layer Structures

POLY(VINYL CARBAZOLE)

Poly(vinyl carbazole), or PVK, has been used as a hole-transporting layer by several groups, for example references [1-6]. It has also been used as a hole-transporting host polymer in blends with a range of polymers [7-11] and in novel diode structures, not necessarily solely as a hole transporting polymer [12, 13]. In this study PVK will be used as a polymer hole-transporting layer.

Optical Characterisation

The chemical structure of PVK is shown below. It is soluble in a range of solvents, but films of PVK in this study were prepared by spin-coating from solutions of chlorobenzene. The PVK was obtained from Aldrich Chemicals and used without further purification.

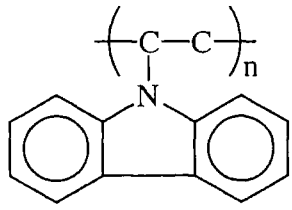

Figure 6-1 *Chemical structure of PVK*

Films of PVK were prepared on quartz substrates. The absorption and photoluminescence spectrum of a PVK film is shown in Figure 6-2. The photoluminescence of PVK is qualitatively weak compared to PPY and PPV for example. The peak of the absorption is at 231nm (5.37eV) and the peak of the luminescence is at 417nm (2.97eV). The peak position of the luminescence spectrum is similar to that found by Gebler *et al* [4].

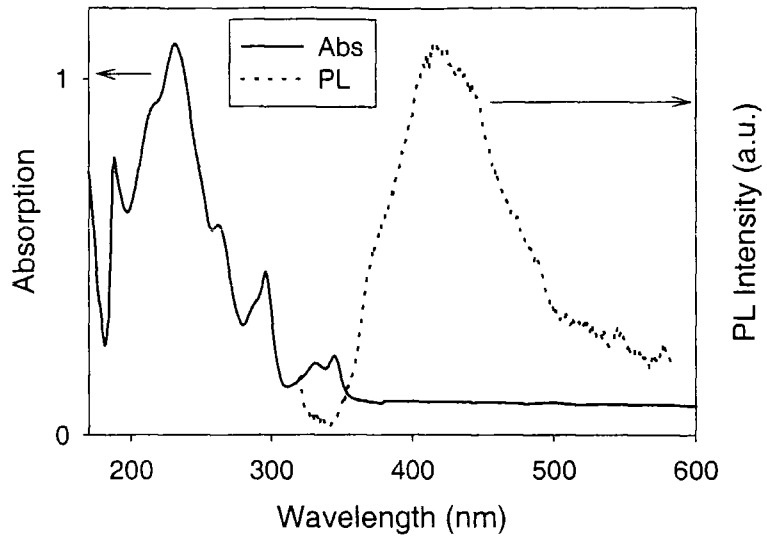

Figure 6-2 *Absorption (solid line) and photoluminescence (dotted line) of PVK*

Another very important feature of PVK is its high optical transmission across the visible region of the spectrum, as shown in Figure 6-3.

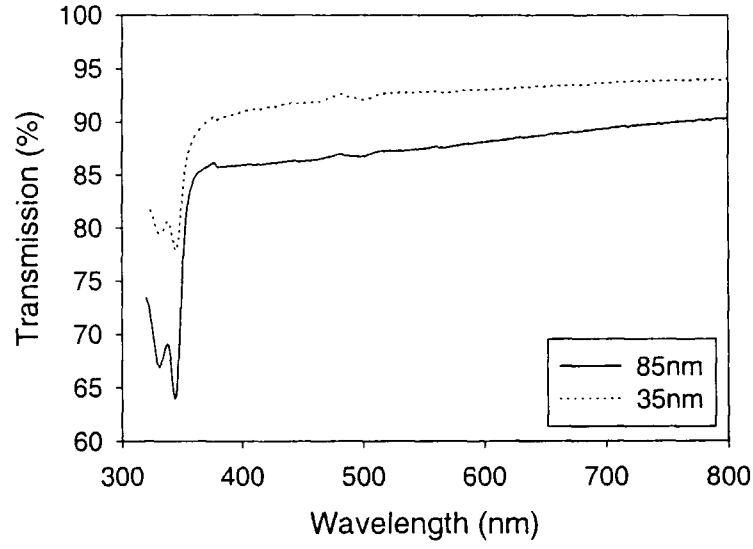

Figure 6-3 *Transmission of PVK films with thicknesses of 85nm and 35nm*

The low absorption of PVK in the visible region means that the transmission is higher than 90% and 85% for a 35nm and a 85nm thick PVK film respectively, over the full range of the electroluminescence of PPY, for example. This means that a thin PVK layer can be used as a hole-transporting layer with little reduction in intensity.

Devices Utilising PVK

In the present study, PVK is used as a hole-transporting layer in polymer LEDs with two polymer layers. The PVK is spin-coated onto the ITO coated glass substrate from a solution of chlorobenzene. PPY is spin-coated onto the PVK from formic acid solution (PVK is insoluble in formic acid) before the device structure is completed by the evaporation of aluminium contacts. The device structure is shown in Figure 6-4.

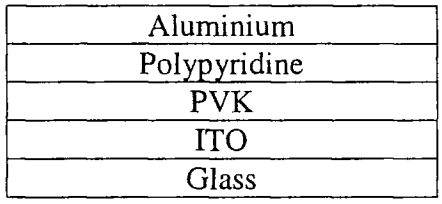

Figure 6-4 *Device structure of a bilayer PVK/PPY device*

The energy levels of this device are shown in Figure 6-5. The position of the energy levels of PVK are from references [1, 12].

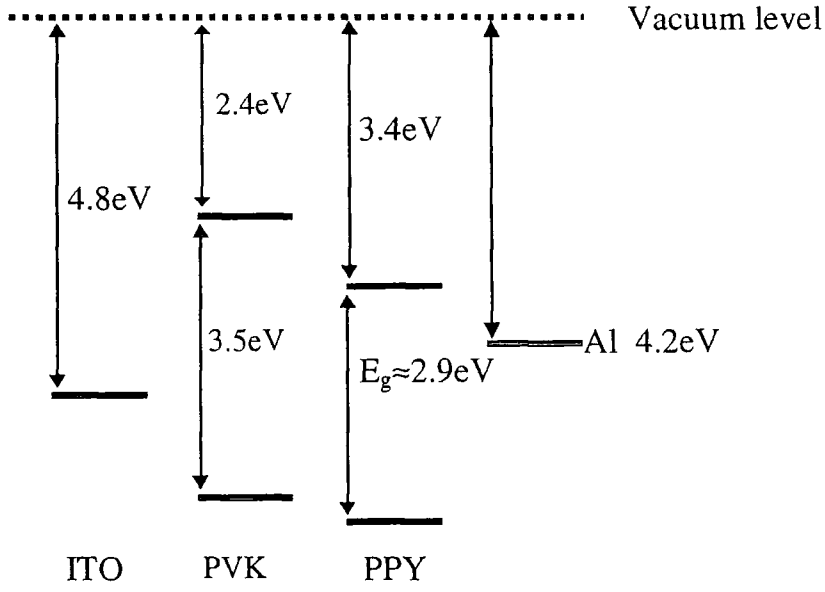

Figure 6-5 *Energy levels of an ITO/PVK/PPY/Al device*

The theoretical barrier to hole injection from the ITO into the PVK layer is 0.4eV smaller than the barrier to hole injection from ITO into PPY. A barrier to hole injection is expected at the PVK/PPY interface, but charge transport across this interface should be assisted by interaction between the polymer layers. PVK exhibits

reasonable hole transporting properties, and a high transmission across the visible region of the spectrum, as shown in Figure 6-3. This makes PVK very suitable for hole-transport, on the transparent side of the device structure, shown in Figure 6-4.

The current-voltage (IV) and intensity-voltage behaviour of an ITO/PVK/PPY/Al device with a 85nm PVK layer and a 40nm PPY layer are shown in Figure 6-6. The intensity-current characteristics are inset.

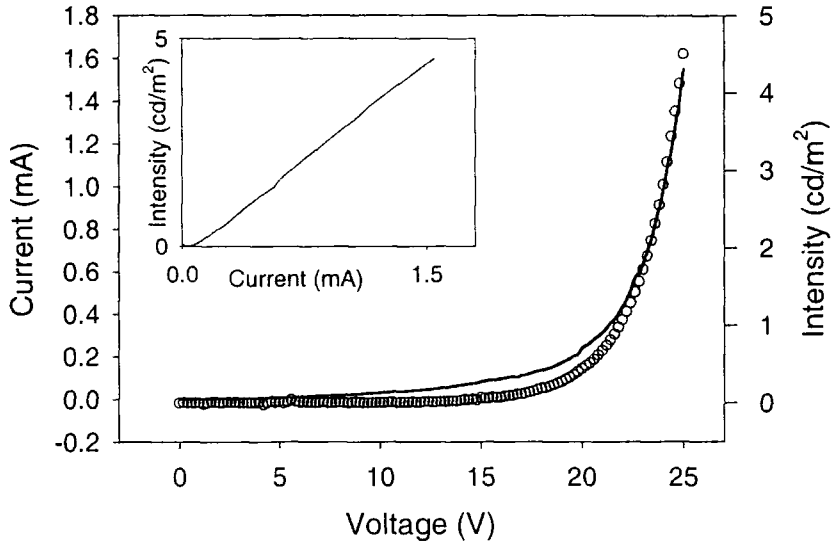

Figure 6-6 *IV (line) and intensity-voltage (circles) characteristics of an ITO/PVK/PPY/Al device. Inset: Intensity-current characteristics*

The external quantum efficiency of the device shown was calculated to be 2.8×10^{-3}%, although the devices of this configuration show a range of efficiencies up to 4.6×10^{-3}%. The efficiency was calculated using a single layer PPY EL spectrum, which should provide reasonable accuracy. There have been reports of exciplex emission in the EL and PL from bilayers of PVK and derivatives of PPY, but no suggestion of the formation of exciplexes between PPY and PVK [3-6]. The efficiency of single layer PPY devices, without the PVK layer are up to 3×10^{-3}%, so devices with a PVK layer show a modest improvement in efficiency. Schottky and SCLC analysis of the IV characteristics of the bilayer device find a Schottky barrier height of (0.70 ± 0.01) eV, a diode ideality factor of 48 and a charge mobility of $(9 \pm 2) \times10^{-8}$ $cm^2 V^{-1}s^{-1}$.

Perhaps the most interesting results come from the variation of the thickness of the PVK and PPY layers. Two other bilayer device configurations were investigated and compared to a single layer PPY device (labelled 'PPY'). A summary of the

structures of these devices can be seen in Table 6-1. The characteristics presented above are for device 'A'.

Device	PVK Thickness (nm)	PPY Thickness (nm)
A	85	40
B	50	70
C	85	145
PPY	--	45

Table 6-1 *Thickness of PVK and PPY layers in the bilayer devices studied*

Changing the thickness of the layers in the device has a detrimental effect on the quantum efficiency. No electroluminescence was detected from Devices 'B' and 'C'. The behaviour of the bilayer PVK/PPY devices is compared to that of a single layer device in Figure 6-7.

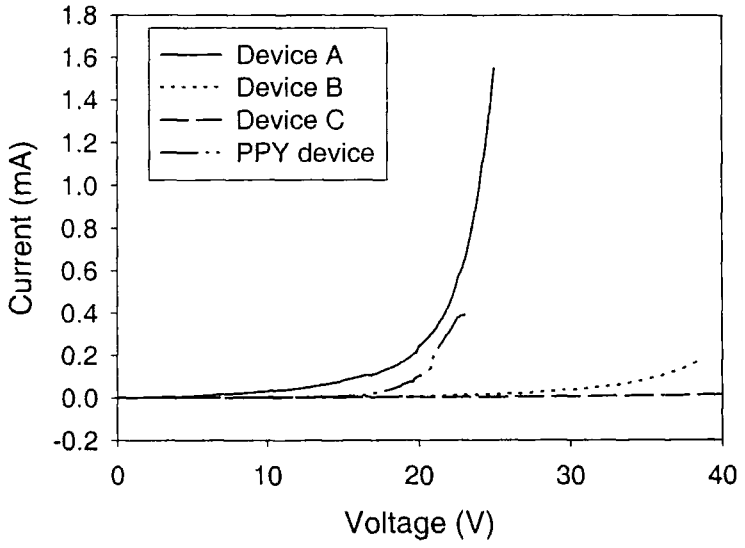

Figure 6-7 *Current-voltage characteristics of PVK/PPY bilayer devices and a single layer PPY device*

The voltage required for a given current for device 'A' is slightly lower than that of the single layer PPY device, despite device 'A' being approximately a factor three thicker. The voltage required for a given current is higher for device 'B' and higher still for device 'C'. Device 'B' has a similar overall thickness to device 'A', but Figure 6-7 clearly shows the considerable difference between the two devices. Device 'C' is thicker than the other devices, although it has a similar PVK thickness to device A.

Summary and Discussion

Optical measurements of PVK films have shown high transmission across the visible region of the spectrum, which is important for a hole-transporting layer in the device structure shown in Figure 6-4. Devices fabricated with a PVK hole-transporting layer and a thin layer of PPY (Device 'A') demonstrate electroluminescence with a modest increase in efficiency and a reduced voltage required for a given current, compared to single layer PPY diodes. The Schottky barrier height and charge mobility of device 'A' are slightly higher than the corresponding values of a single layer PPY device (0.66 ± 0.01eV, and $(4 \pm 2) \times 10^{-8}$ cm^2 $V^{-1}s^{-1}$), suggesting a reduction in the barrier to charge injection and a minor improvement in charge transport through the device.

The thickness of the PPY layer appears to be the crucial factor in determining the current-voltage behaviour of the PVK/PPY devices. The presence of a thick PPY layer reduces the current at a given voltage and the electroluminescence quantum efficiency of the device. The contrasting behaviour of devices 'A' and 'B' clearly show the effect that a thick PPY layer has on the performance of a bilayer device and hence thick PPY layers should be avoided in these bilayer LEDs.

In summary, there is a reduction in the voltage required for a given current and a small enhancement in the external quantum efficiency of PPY diodes when a PVK hole-transporting layer is used. This enhancement is lost when a thick PPY layer is used.

POLY(ANILINE)

Two forms of polyaniline (PANi) are currently used in polymer LEDs. An insulating form (the emeraldine base form) has been used in symmetrically configured devices, with a layer of PANi either side of an emitting layer, producing devices which can operate under an alternating current [14-19]. The conducting form of PANi (the doped emeraldine salt form) has been applied as the hole-transporting layer in polymer LEDs with a variety of luminescent polymers [20-24]. Thin films of the conducting form of polyaniline were prepared and used in this study.

Preparation and Characterisation

High molecular weight ($M_W \approx 2\times10^5$ g mol^{-1}) polyaniline was prepared by Dr P.N. Adams. The conducting form of polyaniline was prepared by the acid doping of PANi with 2-acrylamido-2-methyl-1-propanesulfonic acid (AMPSA). AMPSA was obtained from Aldrich Chemicals. Further details on the synthesis, doping process and the conductivity of PANi films prepared in this way can be found in reference [25] and references therein.

The chemical structure of PANi (emeraldine salt form) and AMPSA is shown in Figure 6-8.

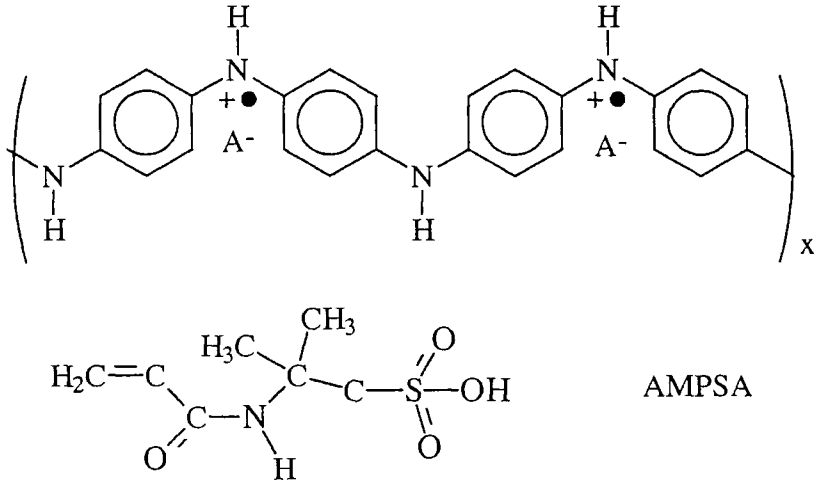

Figure 6-8 *Chemical structure of PANi (emeraldine salt) and AMPSA (after references [26] and [25] respectively)*

A solution of 60% acid doped polyaniline was prepared by mixing polyaniline and AMPSA in the weight ratio of 1:1.37 PANi:AMPSA. The mixture was dissolved in a mixture of 15% dichloroacetic acid and 85% formic acid, to form a 1% by weight solution. The mixture was homogenised for 20 minutes, before being placed in a centrifuge for an hour at approximately 3500rpm. The solution was then filtered through a 0.45μm filter. Thin films of acid doped polyaniline were prepared by spin-coating from this solution at 3200rpm or 1600rpm, producing films with a thickness of approximately 30nm and 60nm respectively. The transmission spectrum of a 30nm PANi film is shown in Figure 6-9.

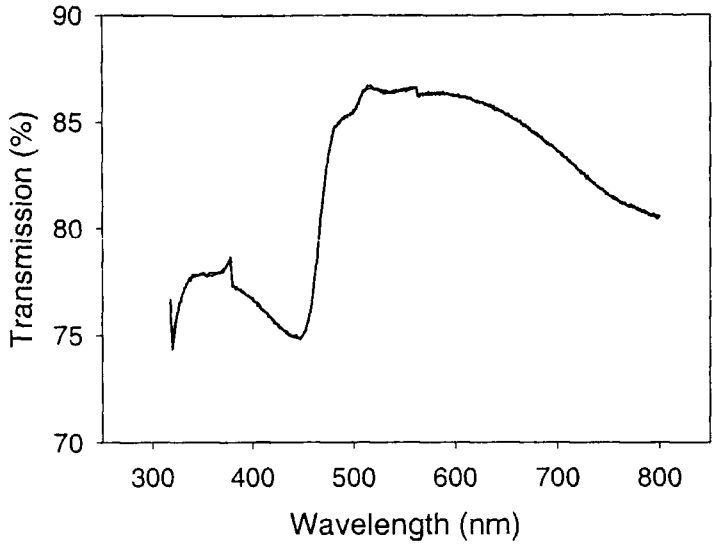

Figure 6-9 *Transmission spectrum of a 30nm PANi film*

The PANi film has transmission higher than 80% over most of the visible region of the spectrum. Bilayer devices with MEH-PPV or PPY as the active layer, and PANi as a hole-transporting layer were fabricated by sequential spin-coating of the polymer layers onto ITO coated substrates. The device structure was completed by evaporation of aluminium electrodes. The mixture of dichloroacetic and formic acids is quite volatile and hence is a good spinning solvent. The spinning time for required for the PANi layer is approximately 90 seconds, with 10 minutes drying time required in ambient conditions. This route therefore has significant advantages over PANi films prepared via spin-coating from water, for example.

Bilayer Devices with PANi and MEH-PPV

The current-voltage and intensity-voltage characteristics of a bilayer ITO/PANi/MEH-PPV/Al device with a PANi thickness of 50nm and a MEH-PPV thickness of 50nm are shown in Figure 6-10.

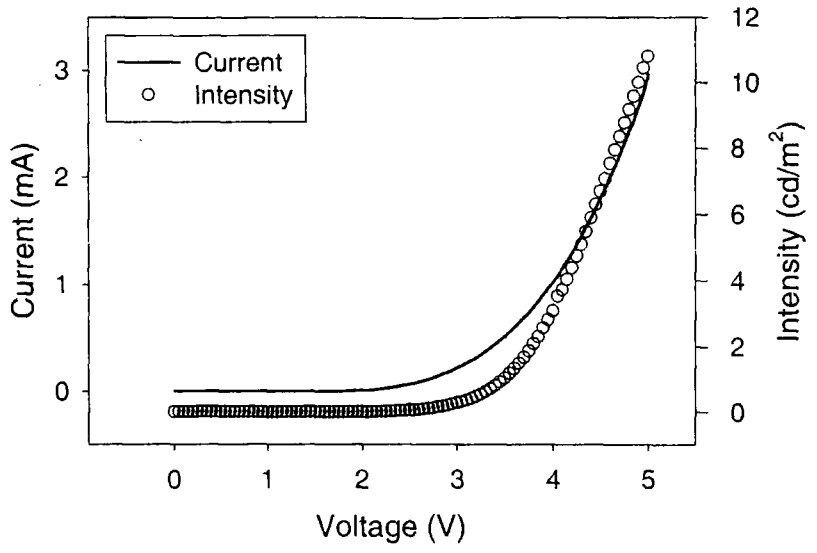

Figure 6-10 *Current-voltage and intensity-voltage characteristics of an ITO/PANi/MEH-PPV/Al device*

The current-voltage characteristics of the device with a PANi hole-transporting layer are compared to those of a single layer MEH-PPV device without a PANi hole-transporting layer in Figure 6-11.

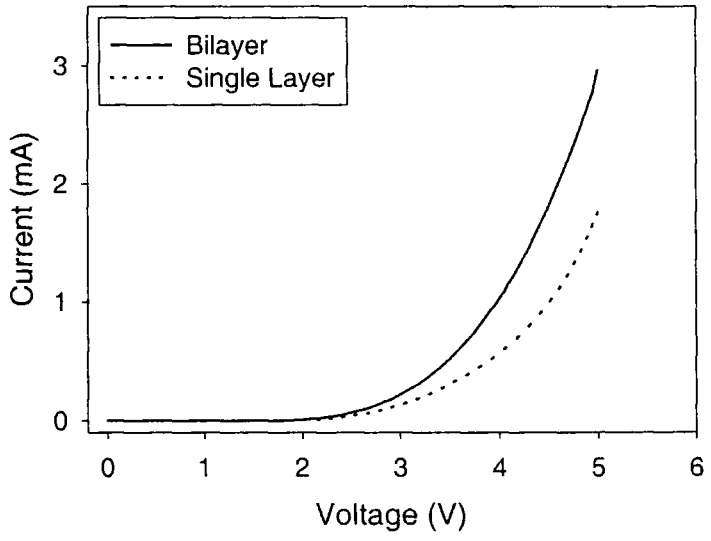

Figure 6-11 *Current-voltage characteristics of a MEH-PPV device with (bilayer) and without (single layer) a PANi hole-transporting layer*

The single and bilayer device have a similar thickness (105 nm for the single layer and 100 nm for the bilayer) and hence there is a reduced field required for a given current in the bilayer device, suggesting a reduced barrier to charge injection. The bilayer device has an higher external quantum efficiency than the single layer device, as illustrated by the larger gradient of the intensity-current characteristics (Figure 6-12).

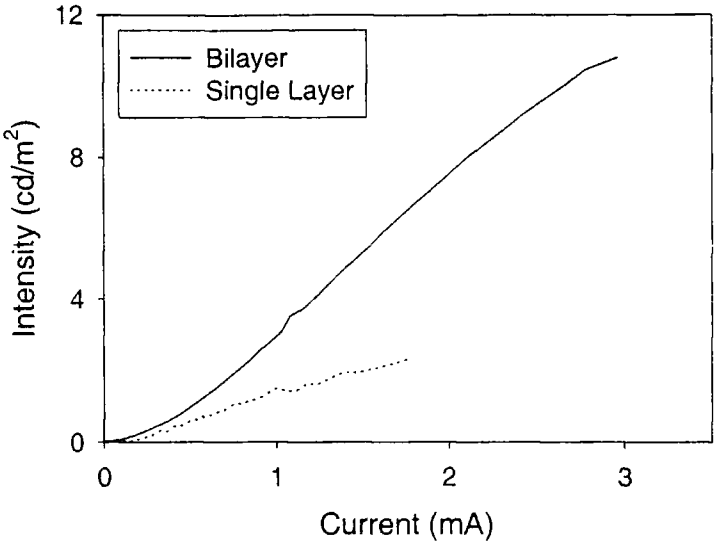

Figure 6-12 *Intensity-current characteristics of a MEH-PPV device with (bilayer) and without (single layer) a PANi hole-transporting layer*

The electroluminescence spectra of the devices with and without the PANi layer are similar, with an identical peak position, as illustrated in Figure 6-13.

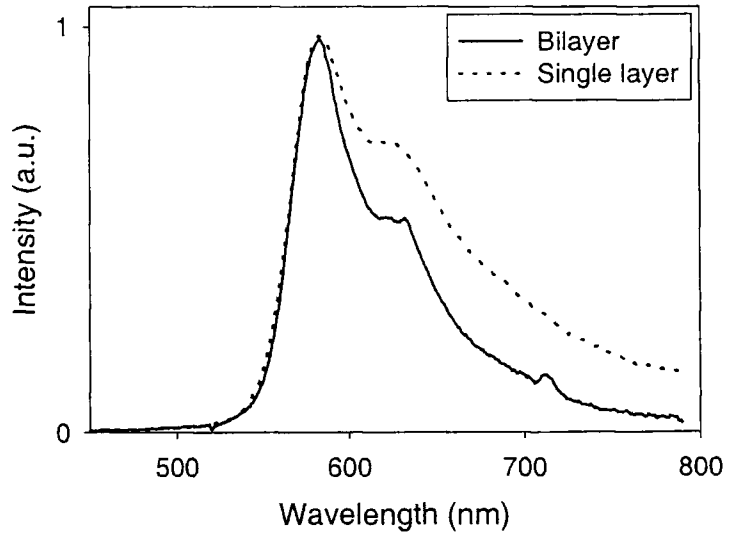

Figure 6-13 *Electroluminescence spectra of MEH-PPV devices with (bilayer) and without (single layer) a PANi hole-transporting layer*

The minor differences in the EL spectra do not produce a difference in the colour co-ordinates of the emission of the bilayer device. The CIE-(x,y) co-ordinates are (0.55, 0.44), identical to those of the single layer device.

The external quantum efficiency of the bilayer device is higher than that of the single layer device, as suggested by Figure 6-12. The bilayer device has an external quantum efficiency of 3.1×10^{-3}%, compared to the efficiency of the single layer device

of 1.3×10^{-3}%. Due to the reduction in voltage required for a given current, and the higher quantum efficiency, the power efficiency of the bilayer device is higher than the single layer. The bilayer device has an efficiency of 5.2×10^{-3} lm/W, and the single layer device has an efficiency of 2.0×10^{-3} lm/W.

Schottky, SCLC and Fowler-Nordheim fits to the data yield a Schottky barrier height of (1.38 ± 0.01) eV, a diode ideality factor of 2.5, a charge mobility of (2.5 ± 0.6) $\times10^{-5}$ $cm^2V^{-1}s^{-1}$ and a barrier height of (0.07 ± 0.03) eV.

Summary and Discussion

The use of a conducting PANi hole-transporting layer improves the quantum efficiency of over that of a device without the PANi layer. The reduction in the field for a given current produced by the PANi layer means that the power efficiency of the device shows a greater improvement than the quantum efficiency. The quantum and power efficiency improvements in this study are a factor 2.4 and 2.6 respectively. The charge mobility calculated for this device is similar to the mobility found for single layer MEH-PPV device (1.68×10^{-5} cm^2 V^{-1} s^{-1}). The Schottky barrier height in the bilayer device is 0.5eV higher than in the single layer device, suggesting a reduction in the barrier to charge injection.

Similar studies elsewhere use calcium rather than aluminium electrodes, and hence the quantum efficiencies reported are higher than those found in this study. The efficiency improvements can be compared, however. Karg *et al* [23] show that the inclusion of a PANi layer produces a quantum efficiency improvement of a factor 2.2 and a power efficiency improvement of a factor 1.9 over a single layer MEH-PPV device with calcium electrodes. Yang *et al* [24] show an efficiency improvement of a factor 1.3 when using a PANi hole-transporting layer and find a barrier height of 0.08-0.12eV from Fowler-Nordheim analysis. Carter *et al* [20] demonstrate improved lifetime from devices using a PANi hole-transporting layer, but the efficiency improvements over a device without the PANi layer are unclear.

In summary, the quantum and power efficiency of MEH-PPV devices have been increased by more than a factor of 2 by the inclusion of a PANi hole-transporting layer, similar to efficiency improvements reported elsewhere. The electroluminescence spectrum was not significantly altered by absorption by the PANi layer, producing a device with identical colour co-ordinates.

Bilayer Devices with PANi and PPY

The current-voltage and intensity-voltage characteristics of a bilayer ITO/PANi/PPY/Al device with a PANi thickness of 40nm and a PPY thickness of 95nm are shown in Figure 6-14.

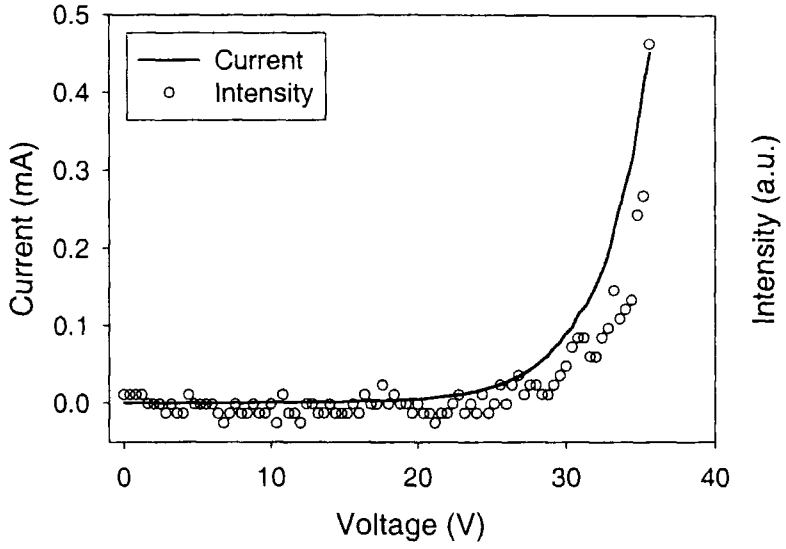

Figure 6-14 *Current-voltage and intensity-voltage characteristics of an ITO/PANi/PPY/Al device*

The use of a PANi hole-transporting layer produces a device with a lower field required for a given current, as illustrated in Figure 6-15.

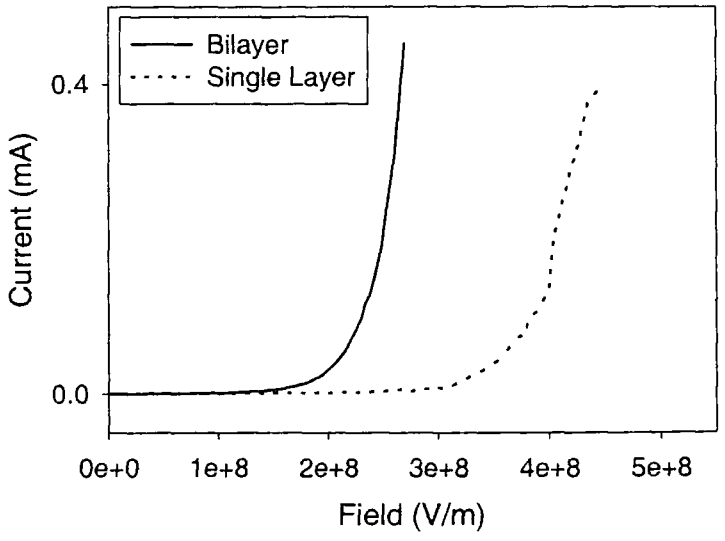

Figure 6-15 *Current-voltage characteristics of a PPY device with (bilayer) and without (single layer) a PANi hole-transporting layer*

The quantum efficiency is lower in the bilayer device than in the single layer device. This is illustrated by the intensity-current characteristics (Figure 6-16).

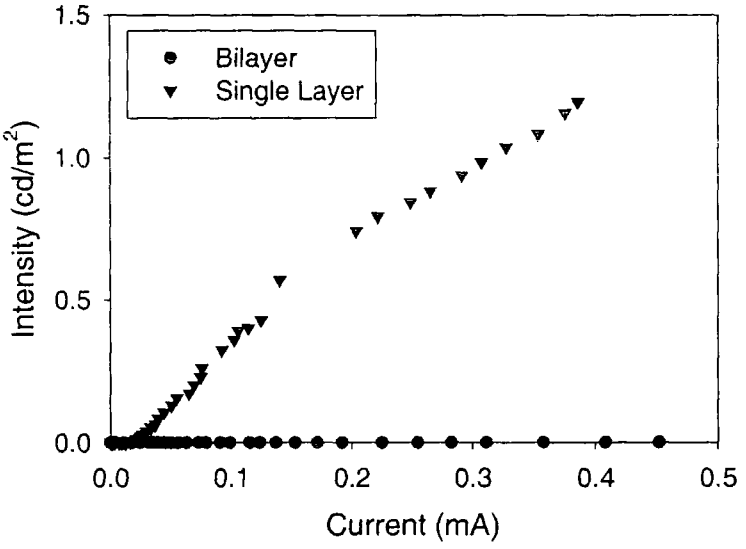

Figure 6-16 *Intensity-current characteristics of a PPY device with (bilayer) and without (single layer) a PANi hole-transporting layer*

The low efficiency of the bilayer device prevented the measurement of a EL spectrum. Using the single layer EL spectrum, the external quantum efficiency of the bilayer device was found to be 2.8×10^{-4}%, approximately an order of magnitude lower than the efficiency of a single layer device. Due to the reduced quantum efficiency, the peak power efficiency of the bilayer device is lower than that of the single layer device.

Schottky and SCLC analysis of the current-voltage characteristics yields a Schottky barrier height of (0.75 ± 0.01) eV, a diode ideality factor of 152 and a charge mobility of $(3.4 \pm 0.7) \times10^{-7}$ cm^2 V^{-1} s^{-1}.

Summary and Discussion

The addition of a PANi hole-transporting layer reduces the field required for a given current for a PPY device, but has a detrimental effect on the quantum efficiency of the electroluminescence. This could be a consequence of contamination of the PPY layer by the PANi. PPY is spin-coated from formic acid, in which polyaniline is soluble to some degree. Luminescence quenching by the PANi contaminants in the film is a possible reason for the low quantum efficiency.

The Schottky barrier height is 0.1eV higher in the bilayer device than in the single layer device, and the charge mobility is an order of magnitude higher, suggesting a reduction in the barrier to charge injection and an improvement in charge transport.

BILAYER DEVICES WITH PPV AND PPY

The novel charge-transporting properties of polypyridine, discussed in the previous chapter, led to the successful application of PPY as an electron-transporting polymer in bilayer LEDs. The bilayer devices were fabricated by preparing PPV films on ITO coated substrates by thermal conversion via the precursor route. PPY films were then spin-coated onto the PPV layer (PPV is insoluble in formic acid, like most other luminescent polymers) and device structures were completed by the evaporation of metal electrodes. A schematic representation of this structure is shown below.

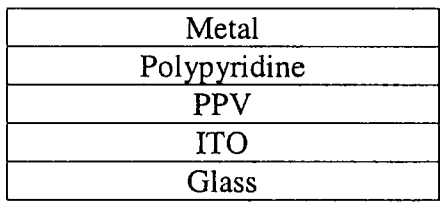

Figure 6-17 *Schematic representation of the structure of bilayer PPV/PPY devices*

Energy Levels of a Bilayer PPV/PPY Device

The energy levels of a device with the structure ITO/PPV/PPY/Metal are shown in Figure 6-18. In forward bias, this structure should exhibit a barrier to electron injection similar to that found for single layer PPY devices, and a barrier to hole injection similar to that found in single layer PPV devices.

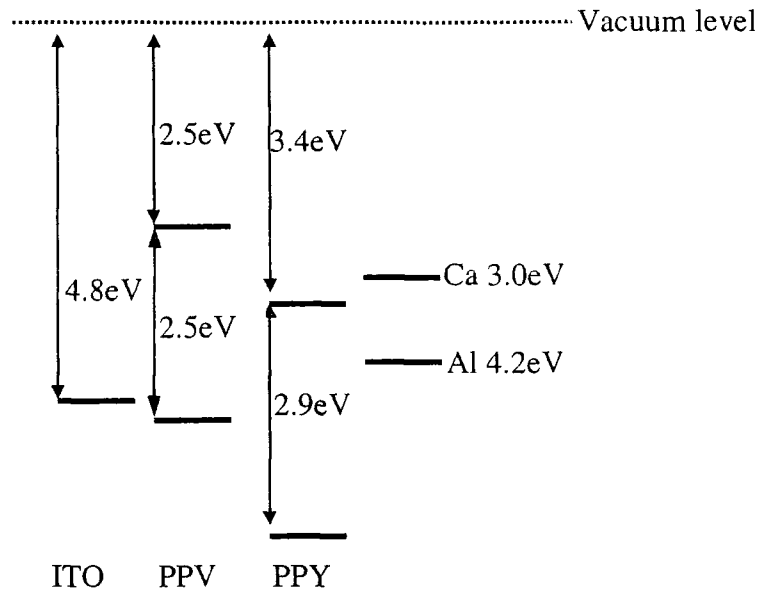

Figure 6-18 *Energy levels of an ITO/PPV/PPY/Metal device*

Device Performance

The IV and intensity-voltage characteristics of an ITO/PPV/PPY/Al device are shown in Figure 6-19. The PPV thickness is 85nm and the PPY thickness is 50nm. The PPY is from batch ER180 and the importance of this will be made clear later in this chapter.

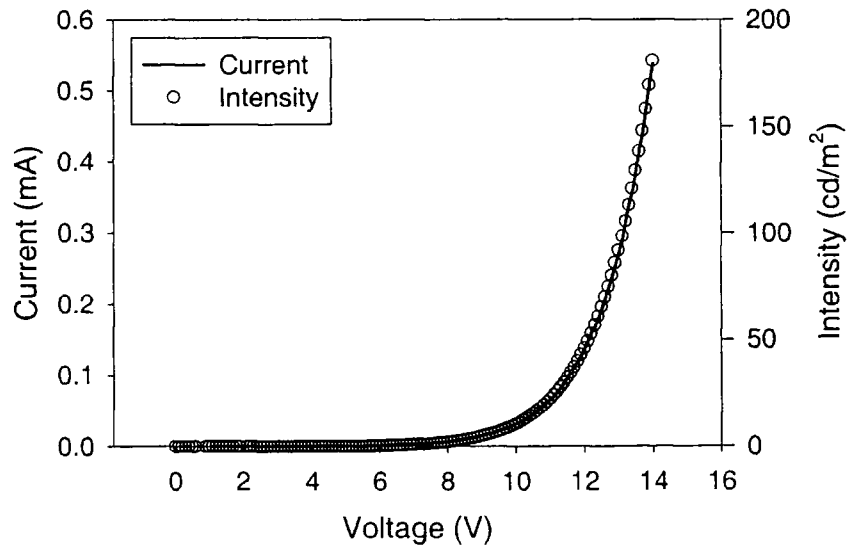

Figure 6-19 *Current-voltage and intensity-voltage characteristics of an ITO/PPV/PPY/Al device*

The characteristics show diode-type behaviour and the emission closely follows the current. The current-intensity characteristics of the device are shown in Figure 6-20.

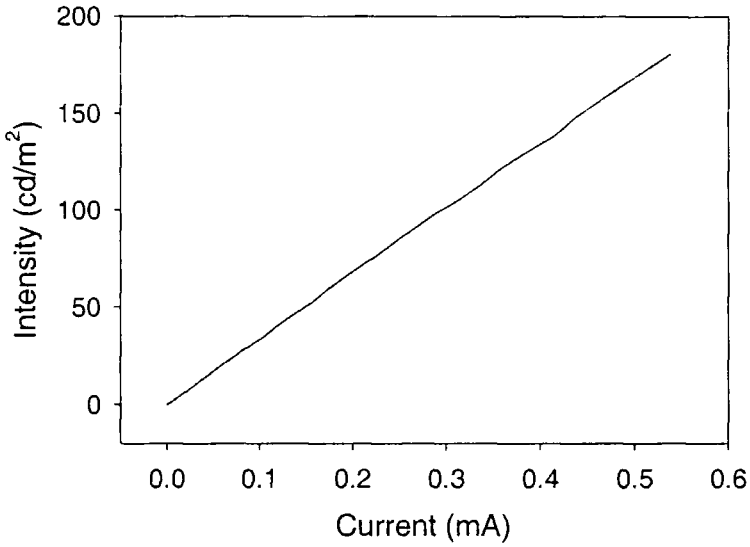

Figure 6-20 *Current-intensity characteristics of an ITO/PPV/PPY/Al device*

The electroluminescence spectrum of the device is shown in Figure 6-21.

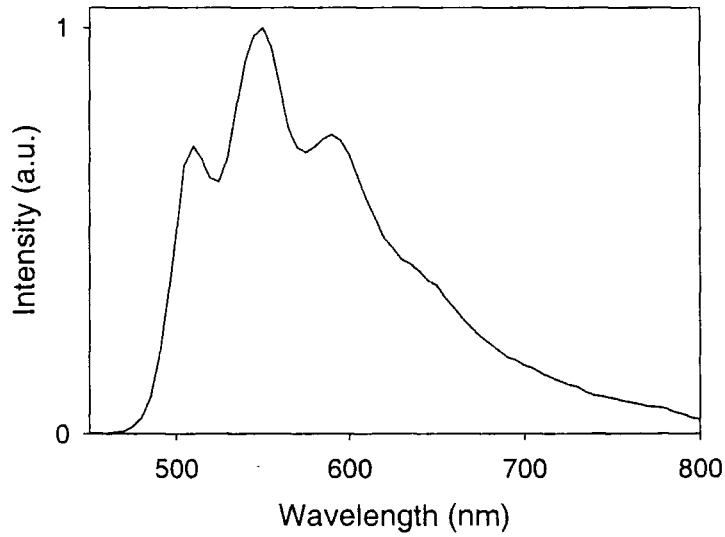

Figure 6-21 *Electroluminescence spectrum of a bilayer ITO/PPV/PPY/Al device*

The external quantum efficiency of the device shown above was calculated to be 0.25%. This is considerably higher than the efficiency of single layer devices with PPV or PPY as the active layer. The efficiency is approximately a factor sixty higher than the efficiency of a single layer PPV device with aluminium contacts. The bilayer device is a factor twenty higher in efficiency than a single layer PPV device with more reactive calcium contacts. There is also an efficiency improvement of more than a

factor 80 over a single layer PPY device. The efficiency improvements are illustrated in Figure 6-22.

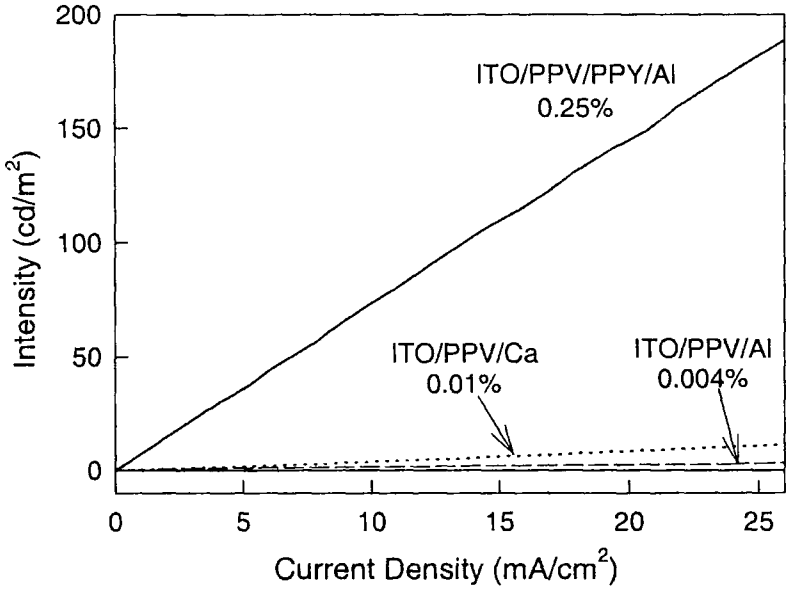

Figure 6-22 *Intensity-current characteristics of a bilayer PPV/PPY device compared to single layer PPV devices with aluminium and calcium contacts*

The electroluminescence spectrum of the bilayer device is compared to the electroluminescence spectra of PPV and PPY single layer devices in Figure 6-23.

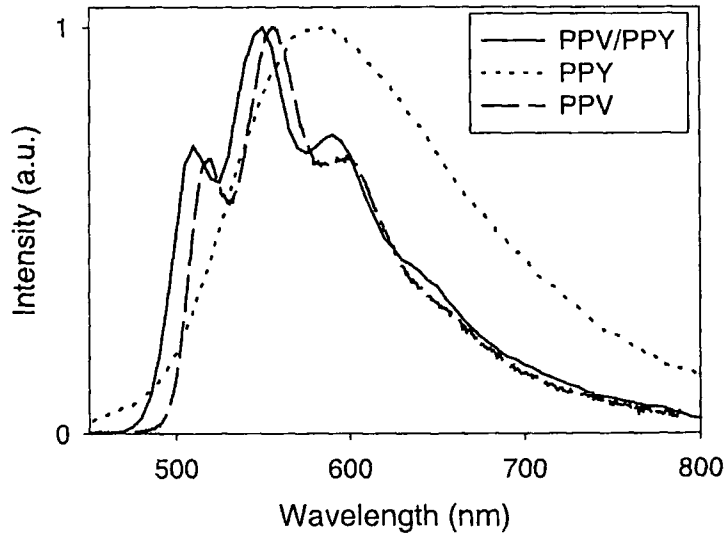

Figure 6-23 *Electroluminescence spectrum of a bilayer PPV/PPY device compared to the spectra of single layer PPV and PPY devices*

The bilayer electroluminescence spectrum is very similar to that of a single layer PPV device. It must be noted that the bilayer device spectrum was measured on a diode array and spectrograph, whereas the single layer spectra were measured on a

CCD and spectrograph, and minor changes between the PPV single layer and bilayer spectra may be solely due to the change in the measurement method. Pure emission from PPY followed by absorption and remission from the PPV layer is unlikely due to the low absorption of the PPV layer at the energies at which the PPY emission occurs. The absorption spectra of PPV and PPY films are compared to the electroluminescence spectra in Figure 6-24.

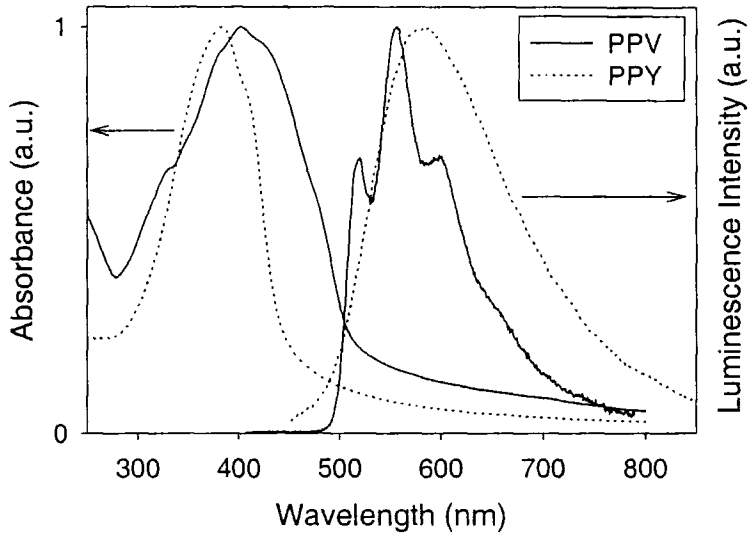

Figure 6-24 *Absorption and electroluminescence spectra of PPV and PPY*

The current-field behaviour of single layer PPV devices with calcium and aluminium electrodes are compared to the current-field characteristics of the bilayer device in Figure 6-25.

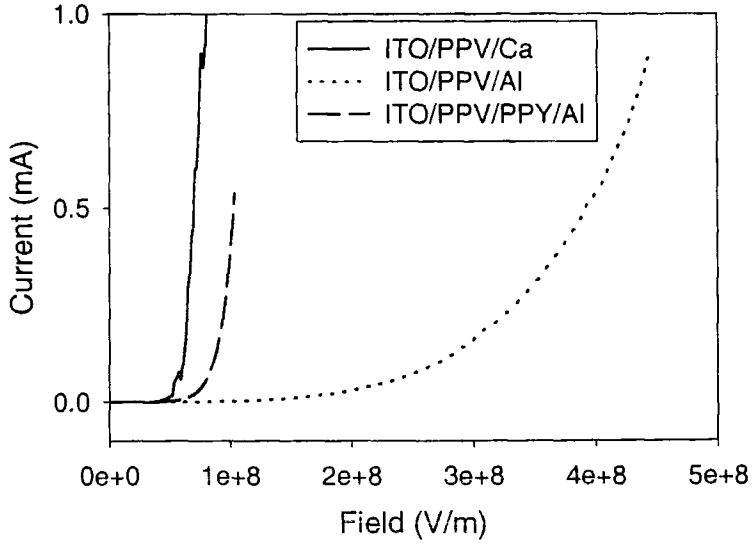

Figure 6-25 *Current-field characteristics of a bilayer PPV/PPY device compared to single layer devices with calcium or aluminium electrodes*

The inclusion of a PPY layer between the aluminium electrode and the PPV layer produces a device which requires a lower field for a given current. The field required for a given current is slightly higher in the bilayer device than in the single layer PPV device with calcium contacts.

The current-voltage characteristics of the bilayer device can be analysed in a Schottky (Figure 6-26), space charge limited current (Figure 6-27) and Fowler-Nordheim (Figure 6-28) framework.

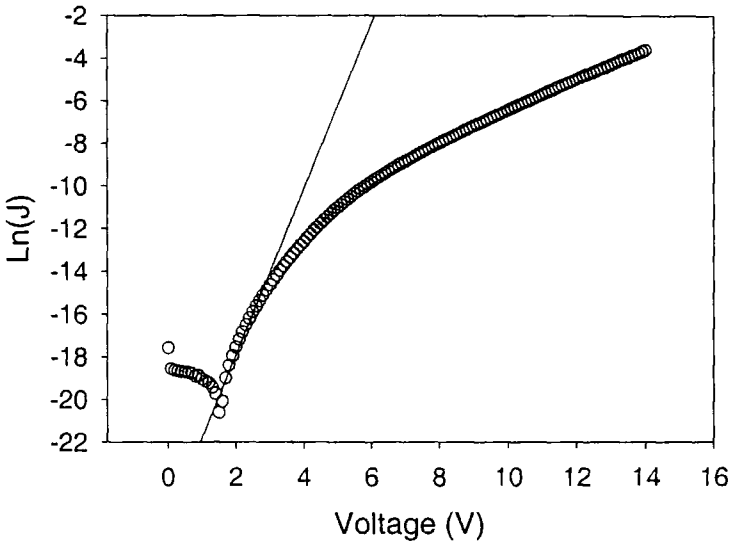

Figure 6-26 *Schottky analysis of a PPV/PPY bilayer device*

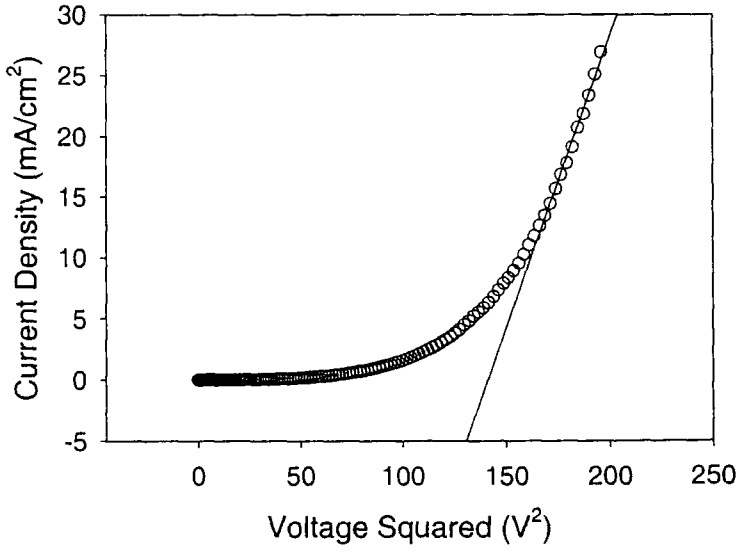

Figure 6-27 *Space charge limited current analysis of a PPV/PPY bilayer device*

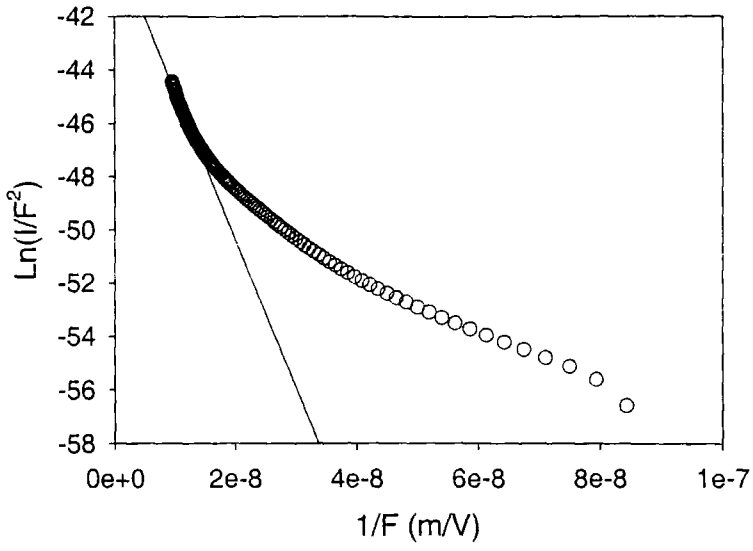

Figure 6-28 *Fowler-Nordheim analysis of a PPV/PPY bilayer device*

The Schottky barrier height, charge mobility and Fowler-Nordheim barrier height calculated for the bilayer PPV/PPY device are compared to single layer PPV and PPY devices in Table 6-2.

Device Structure	Schottky Barrier Height (± 0.01 eV)	Charge Mobility ($cm^2 V^{-1} s^{-1}$)	F-N Barrier Height (eV)
ITO/PPV/PPY/Al	1.01	$(3 \pm 1) \times 10^{-6}$	0.18 ± 0.07
ITO/PPV/Al	0.87	$(2.0 \pm 0.9) \times 10^{-8}$	0.14 ± 0.07
ITO/PPV/Ca/Al	1.05	$(1.7 \pm 0.3) \times 10^{-5}$	0.07 ± 0.02
ITO/PPY/Al	0.66	$(4 \pm 2) \times 10^{-8}$	N/A
ITO/PPY/Ca/Al	0.61	$(1.0 \pm 0.2) \times 10^{-5}$	N/A

Table 6-2 *Schottky barrier height, charge mobility and Fowler-Nordheim (F-N) barrier height of various device structures*

The Schottky barrier height calculated for the bilayer PPV/PPY device is close to the value calculated for a single layer PPV device with calcium electrodes. This implies that the barrier to electron injection is similar in both cases, and the barrier to electron injection in the bilayer device is lower than that found for a single layer device with aluminium electrodes. These data are in agreement with the current-field characteristics shown in Figure 6-25. The diode ideality factor calculated for the device shown above is 13.5, a larger value than those found for single layer PPV devices, and similar to those found for PPY devices. The charge mobility found for the

bilayer device is larger and smaller than the values found for single layer devices with aluminium and calcium contacts respectively. The barrier height, determined by Fowler-Nordheim treatment of the data, is higher than those found for single layer PPV devices with aluminium or calcium electrodes.

Efficiency Characterisation of Bilayer Devices

The Effect of Thickness Ratio

The efficiency of PPV/PPY bilayer devices varies with the relative thickness of the PPV and PPY layers. The ratio of the thickness of the PPV layer to the thickness of the PPY layer can be varied to investigate this effect. The variation in diode external quantum efficiency with PPV:PPY thickness ratio (r) is shown in Figure 6-29.

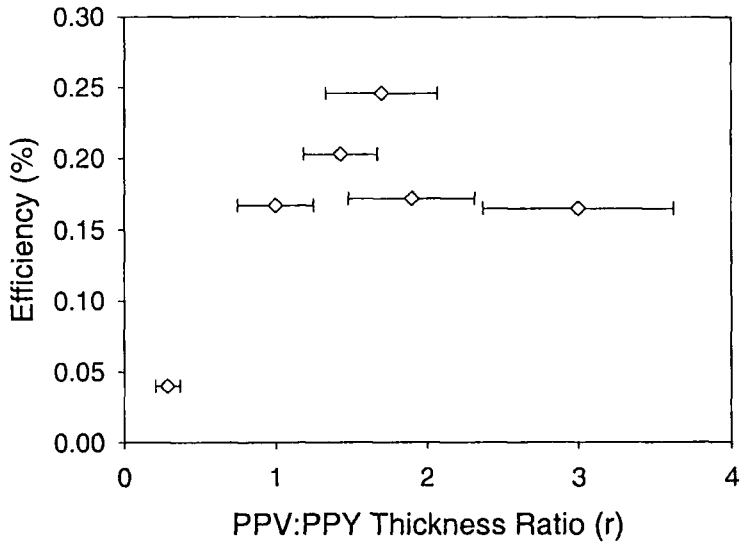

Figure 6-29 *External quantum efficiency as a function of PPV:PPY layer thickness ratio*

The peak efficiency is for the device with a PPV:PPY thickness ratio of 1.7. The characteristics of this device are shown above. For layer thickness ratios greater or less than 1.7, there is a decrease in device efficiency. Schottky, SCLC and Fowler-Nordheim analysis of the devices shown in Figure 6-29, find values of Schottky barrier height, charge mobility and Fowler-Nordheim barrier height which are shown in Table 6-3.

PPV:PPY Thickness Ratio (r)	Total Thickness (nm)	Peak EQE (%)	Schottky Barrier Height (±0.01 eV)	Charge Mobility ($cm^2 V^{-1} s^{-1}$)	F-N Barrier Height (eV)
0.29 ± 0.08	180	0.04	1.05	$(6 \pm 1) \times 10^{-9}$	0.19 ± 0.02
1.0 ± 0.3	120	0.17	0.93	$(8 \pm 2) \times 10^{-6}$	0.30 ± 0.03
1.4 ± 0.2	170	0.20	1.09	$(4.4 \pm 0.8) \times 10^{-6}$	0.20 ± 0.02
1.7 ± 0.3	135	0.25	1.01	$(3.0 \pm 0.6) \times 10^{-6}$	0.18 ± 0.02
1.8 ± 0.4	125	0.17	1.07	$(4.1 \pm 0.9) \times 10^{-6}$	0.23 ± 0.03
3.0 ± 0.6	160	0.16	1.02	$(3.3 \pm 0.6) \times 10^{-6}$	0.23 ± 0.02

Table 6-3 *Peak external quantum efficiency (EQE), Schottky barrier height, charge mobility and Fowler-Nordheim barrier height of PPV/PPY bilayer devices with various PPV:PPY thickness ratios*

The calculated Schottky barrier heights and charge mobilities for the bilayer devices are similar for each thickness ratio. The one exception is for the device with a thickness ratio of r=0.29, which exhibits a charge mobility approximately 3 orders of magnitude lower than the other devices. The inclusion of this device in the comparison of the effect of thickness ratio is complicated by a further important manufacturing step. The device with thickness ratio 0.29 was fabricated by evaporation of the aluminium electrode approximately 2 hours after the final PPY layer was spin-coated, during which time it was held under vacuum in an evaporator. The remaining devices had the aluminium evaporated after being held in vacuum for approximately 14 hours. This was carried out at a pressure of approximately 10^{-6} mbar in an evaporator, and the vacuum was not interrupted before evaporation of the metal. This key step produces devices with a significantly higher efficiency and hence the inclusion of the device with the thickness ratio of 0.29 in this comparison is not ideal. This device is important, however, as there were no other devices with a similar thickness ratio fabricated with the same batch of PPY (ER180) and PPV. The importance of the batch of PPY and PPV will be explored later.

The Effect of Vacuum Treatment

The effect on holding devices in vacuum for approximately 14 hours on device efficiency can be illustrated by considering devices with a similar structure and

PPV:PPY thickness ratio. Two examples of increased device efficiency following vacuum treatment are shown in Table 6-4.

Thickness Ratio	Hours in Vacuum	EQE
1.7 ± 0.3	2	0.19
1.7 ± 0.3	14	0.25
1.3 ± 0.3	2	0.08
1.4 ± 0.2	14	0.20

Table 6-4 *External quantum efficiency of PPV/PPY bilayer devices with varying exposure to vacuum*

This comparison is not ideal and variations in fabrication between the devices (fabricated at different times) could produce a variation in device efficiency. A study of three devices fabricated in an identical manner was undertaken. One device had contacts evaporated immediately, one device was held in vacuum for 14 hours and the final device was heated at 60°C for 2 hours in vacuum ($\approx 10^{-3}$ mbar). The thickness ratio, external quantum efficiency, Schottky barrier height and charge mobility of the three devices are shown in Table 6-5.

PPV:PPY Thickness Ratio (r)	Treatment	Peak EQE (%)	Schottky Barrier Height (±0.01 eV)	Charge Mobility ($cm^2 V^{-1} s^{-1}$)
1.5 ± 0.3	13 hours in Vacuum	0.14	0.86	$(1.1 \pm 0.2) \times 10^{-5}$
1.6 ± 0.3	None	0.075	0.97	$(2.0 \pm 0.4) \times 10^{-6}$
1.8 ± 0.4	2 hours at 60°C	0.083	0.81	$(8 \pm 2) \times 10^{-6}$

Table 6-5 *Variation of external quantum efficiency (EQE), Schottky barrier height and charge mobility with treatment of polymer layers*

It can be seen that the efficiency of the device held for 14 hours in vacuum is the highest of the three and the device heated for 2 hours at 60°C has a slightly higher efficiency than the device which was untreated. The change in the Schottky barrier height of the devices may be significant, although it should be noted that the reduction in value of the Schottky barrier represents an increase in the barrier to electron injection in the (more efficient) treated devices. The purpose of the heat treatment of the final

device is to investigate the possibility of trace amounts of formic acid remaining in the PPY film. This possibility has been mentioned in Chapter 5, and certainly any small trace of formic acid would be expected to be extracted from a thin polymer film after 14 hours in a good vacuum. However, it would be expected that heating for 2 hours at 60°C would also remove any possible trace of formic acid, and the differences in device values between the vacuum and heat treated devices, illustrated in Table 6-5, suggest that the presence of trace amounts of formic acid may not be the main factor in the improvement of device efficiency. There is some enhancement of the charge mobility and quantum efficiency of the heat treated device compared to the untreated device and this could be due to the removal of trace amounts of formic acid, although it could also be due to a change in morphology of the polymer chains.

It is also important to note that the more efficient devices exhibit a higher charge mobility. It would appear that the treatment of the polymer layers prior to evaporation of the metal electrode leads to an increased charge mobility. The treatment of the polymers may be expected to reduce the amount of adsorbed oxygen on the surface of the PPY film. If this occurs and calcium electrodes were utilised, then an increase in charge mobility would be expected, and the increase would be brought about by doping of the polymer by the calcium ions. However, aluminium is used in this study and this tends to form covalent bonds with polymers, leading to a decrease in charge mobility (see Chapter 2), although the exact nature of the interaction of aluminium with PPY is unknown. The increase in charge mobility may be brought about by the reduction in the amount of adsorbed oxygen on the surface leading to less aluminium oxide formation on the surface, producing improved injection and transport of charges from the electrode. The heating and/or vacuum treatment may also increase the crystallinity of the PPY, leading to a higher charge mobility.

The Effect of Aged PPV

The devices shown above are manufactured with "aged" PPV. PPV precursor is usually stored at low temperatures, i.e. in a freezer. The PPV used in the devices above was accidentally aged due to an interruption in the power to the freezer, resulting in the precursor solution being held at room temperature for several days. This would be expected to produce some conversion of the PPV precursor before the deliberate conversion process is carried out. The qualitative effects, observed in the precursor solution, were a change of colour from colourless to a slight yellow tinge and an

increase in the viscosity of the solution. This solution is called "aged" PPV in this study. Comparison between bilayer devices using the aged PPV and PPV prepared from a fresh batch of PPV precursor is shown in Table 6-6. The first two devices are a simple comparison and the latter two devices were prepared keeping the fabrication steps as similar as possible.

PPV:PPY Thickness Ratio (r)	PPV	Peak EQE (%)	Schottky Barrier Height (±0.01 eV)	Charge Mobility ($cm^2 V^{-1} s^{-1}$)	F-N Barrier Height (eV)
1.1 ± 0.2	Aged	0.019	0.98	$(7 \pm 1) \times 10^{-7}$	0.34 ± 0.02
1.1 ± 0.2	Fresh	0.011	1.03	$(9 \pm 2) \times 10^{-6}$	0.23 ± 0.02
1.5 ± 0.3	Aged	0.031	0.92	$(3.3 \pm 0.6) \times 10^{-6}$	0.19 ± 0.02
1.1 ± 0.2	Fresh	0.031	0.95	$(3.2 \pm 0.7) \times 10^{-6}$	0.22 ± 0.02

Table 6-6 *Comparison of bilayer PPV/PPY devices using aged and fresh PPV*

The results from this study are inconclusive. The use of aged PPV appears to reduce the height of the Schottky barrier. There is the possibility of an increase in efficiency, although this may be due to differences in the fabrication of the first two devices, which is suggested by the difference in charge mobility between the two devices. Attempts to produce efficiency improvements using deliberately aged PPV precursor proved fruitless.

The photoluminescence quantum yield of the aged PPV may be expected to be higher than that of the fresh PPV. It is widely known that partially converted PPV can not be subsequently converted as fully as fresh PPV and that partially converted PPV has a higher PLQY [27]. Measurements of the PLQY of aged and fresh PPV in this study find values which are identical at 24±2%, however.

Bilayer Devices using Calcium Electrodes

A comparison was made between two bilayer devices, one utilising aluminium contacts and another using calcium contacts. The current-voltage results from these devices are shown in Figure 6-30.

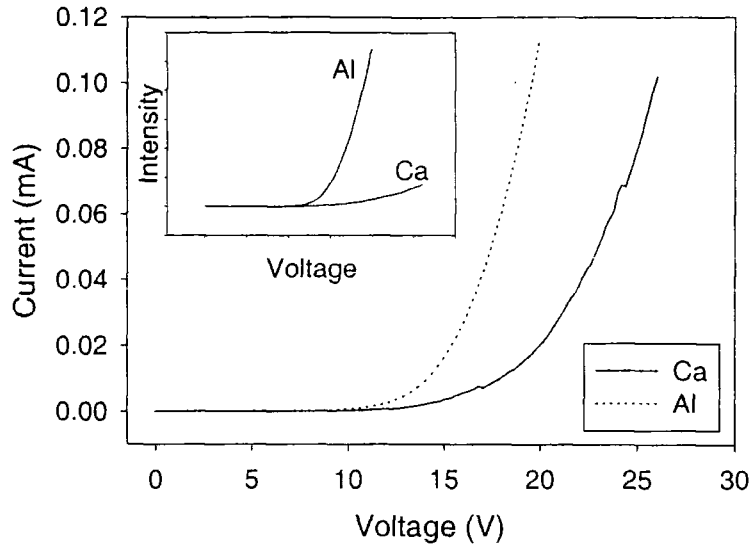

Figure 6-30 *Current-voltage characteristics of bilayer PPV/PPY devices with calcium or aluminium electrodes. Inset: Intensity-voltage characteristics of the devices*

The intensity-current characteristics of the devices are shown below.

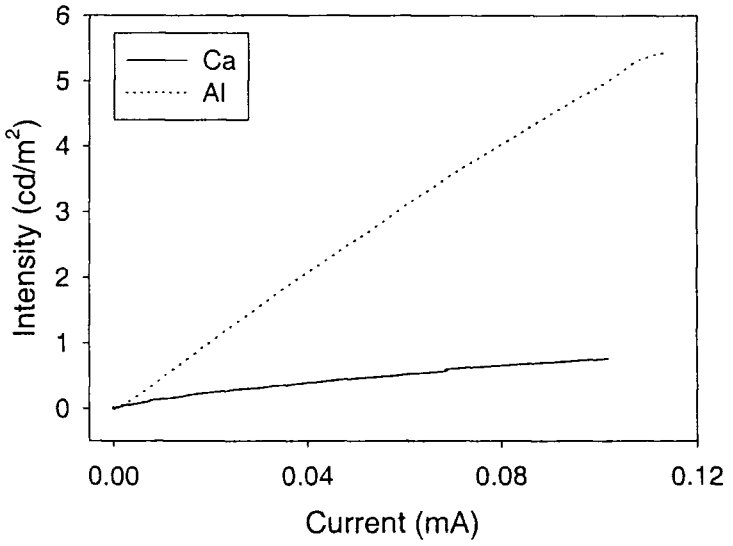

Figure 6-31 *Intensity-current characteristics of bilayer PPV/PPY devices with calcium or aluminium electrodes*

The behaviour of the bilayer devices with aluminium or calcium electrodes is somewhat surprising. The two devices have the same measured thickness, yet there is a reduction in the voltage required for a given current for the aluminium device, as illustrated in Figure 6-30. The voltage required for light emission is also lower in the device using aluminium electrodes. Figure 6-31 shows a higher gradient for the intensity-current curve of the device with aluminium electrodes, suggesting a higher external quantum efficiency. This is confirmed by calculation of the external quantum

efficiencies listed in Table 6-7. The Schottky barrier height, charge mobility and Fowler-Nordheim barrier height are also listed.

PPV:PPY Thickness Ratio (r)	Metal Electrode	Peak EQE (%)	Schottky Barrier Height (±0.01 eV)	Charge Mobility ($cm^2 V^{-1} s^{-1}$)	F-N Barrier Height (eV)
2.3 ± 0.5	Al	0.048	1.06	$(1.6 \pm 0.3) \times 10^{-7}$	0.20 ± 0.03
2.3 ± 0.5	Ca	0.008	0.97	$(9 \pm 2) \times 10^{-8}$	0.22 ± 0.03

Table 6-7 *External quantum efficiency, Schottky barrier height, charge mobility and Fowler-Nordheim barrier height of bilayer PPV/PPY devices with calcium or aluminium electrodes*

The results found for the bilayer devices are surprising as they do not correspond to the behaviour which is expected from the theoretical analysis of the energy levels (Figure 6-18). A smaller barrier to electron injection would be expected from the calcium electrode yet the Schottky barrier is lower (and hence the barrier to electron injection is higher) than the device with aluminium electrodes. Similarly, Fowler-Nordheim analysis of the device also shows a larger barrier in the device with calcium electrodes. There is a decrease in efficiency of device operation when calcium electrodes are used, although it is not as large as the decrease in PPY single layer devices with similar electrodes. The difference in charge mobility calculated for these devices is in the opposite sense to the variation observed in the single layer devices. Calcium electrodes in single layer devices were found to increase the charge mobility, whereas the charge mobility in this case is lower with calcium electrodes.

It is interesting to note that the behaviour of bilayer devices with calcium and aluminium electrodes is the opposite to that found for single layer PPV diodes. There is an increase in the field required for a given current and a decrease in device efficiency when calcium is used as an electrode material in bilayer devices. This fact, coupled with the study of the behaviour of single layer PPY devices with calcium electrodes, led to the termination of further study of the use of calcium electrodes with bilayer PPV/PPY devices.

Studies of oxadiazole based electron-transporting polymer layers elsewhere find both increased [28] and decreased [29] efficiency when calcium electrodes are used, and the effect appears to be highly material dependent.

The Effect of Different PPY Batches

The devices examined above predominantly used PPY batch ER180. Optical, molecular weight and impurity measurements on PPY batches (presented in Chapter 4) suggest that the PPY batches should be interchangeable. This is not the case however. The dramatic efficiency improvement observed when using batch ER180 as an electron-transporting polymer is not found for other batches. Although a substantial increase in efficiency is found for bilayer devices with other batches of PPY, the efficiency improvement is not as large as that found when using batch ER180. Bilayer devices were fabricated using PPY batches ER180, ER196, ER198, ER203, ER204, L02, L04, L05 and L08. For each batch, the thickness ratio was varied to cover a range of values in an attempt to find the ratio with highest efficiency. The peak efficiency and the thickness ratio which provides the peak efficiency of the series of devices for each batch is listed in Table 6-8. The Schottky barrier height and charge mobility of the device with the highest efficiency are also listed. The comments column indicates which devices were made with aged PPV and which were fabricated with fresh PPV. The comment "Del-Aged PPV" indicates the use of deliberately aged PPV (PPV precursor solution left at ambient temperatures, in the dark, for 166 hours).

PPY Batch	PPV:PPY Thickness Ratio (r)	Peak EQE (%)	Schottky Barrier Height (± 0.01 eV)	Charge Mobility ($cm^2 V^{-1} s^{-1}$)	Comments
ER180	1.7 ± 0.3	0.250	1.01	$(3.0 \pm 0.6) \times 10^{-6}$	Aged PPV
ER196	2.6 ± 0.7	0.050	0.87	$(9 \pm 2) \times 10^{-6}$	Aged PPV
ER198	2.0 ± 0.4	0.066	0.79	$(6 \pm 1) \times 10^{-6}$	Aged PPV
ER203	0.9 ± 0.1	0.067	1.12	$(9 \pm 2) \times 10^{-6}$	Fresh PPV
ER204	1.3 ± 0.2	0.011	1.02	$(1.9 \pm 0.4) \times 10^{-6}$	Fresh PPV
L02	2.3 ± 0.5	0.045	1.06	$(1.6 \pm 0.3) \times 10^{-6}$	Fresh PPV
L04	4.0 ± 0.8	0.041	1.02	$(8 \pm 2) \times 10^{-7}$	Fresh PPV
L05	2.2 ± 0.3	0.068	1.03	$(6 \pm 1) \times 10^{-6}$	Fresh PPV
L08	0.8 ± 0.2	0.005	1.11	$(3.1 \pm 0.7) \times 10^{-6}$	Del-Aged PPV

Table 6-8 *Peak efficiency, Schottky barrier height and charge mobility for the most efficient thickness ratio for bilayer PPV/PPY devices fabricated with different PPY batches*

There appear to be some trends, although some results do not agree with the trends. There seems to be a general increase in efficiency with increasing charge

mobility, although the results for batches L02 and L04 contradict this trend. Also the very high efficiency of the device using batch ER180 does not have an abnormally high charge mobility. There is a general increase in the thickness ratio which produces the maximum efficiency with decreasing charge mobility. There appears to be a reduction in Schottky barrier height in the devices using aged PPV, but again, this trend may not be valid. The values of the Schottky barrier height shown in Table 6-8 do show that the Schottky barrier height and hence the barrier to electron injection in these devices is similar to values found for single layer PPV diodes with calcium electrodes (1.05eV), confirming what is observed in Figure 6-25.

Three batches of PPY, batch ER196, L04 and L05 were used in further investigations of the efficiency variation of PPV/PPY bilayer devices with various PPV:PPY thickness ratios.

Bilayer Devices with PPY Batch ER196

The efficiency variation of bilayer devices, using PPY batch ER196, as a function of layer thickness ratio is shown in Figure 6-32.

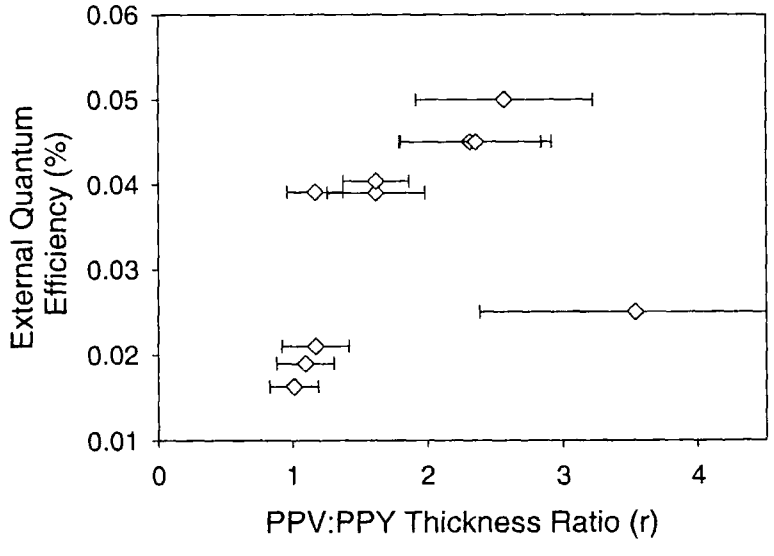

Figure 6-32 *Variation of external quantum efficiency with PPV:PPY thickness ratio for bilayer devices using PPY batch ER196*

A variation in the efficiency of the devices with PPV:PPY thickness ratio is observed, with a maximum efficiency of 0.05% for the device with r=2.6. The efficiency is lower for devices with thickness ratios greater or smaller than this value.

Bilayer Devices with PPY Batch L04

The efficiency variation of bilayer devices, using PPY batch L04, as a function of layer thickness ratio is shown in Figure 6-33.

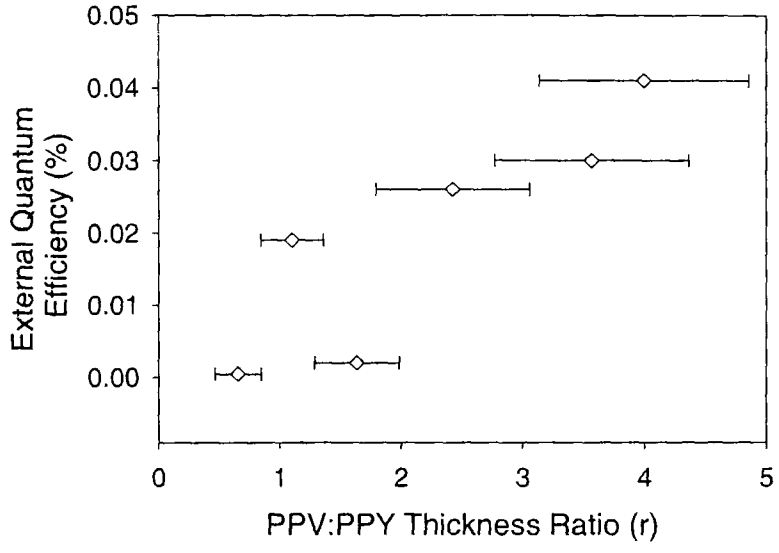

Figure 6-33 *Variation of external quantum efficiency with PPV:PPY thickness ratio for bilayer devices using PPY batch L04*

Devices made with PPY batch L04 show a variation of efficiency similar to that found for devices made with batch ER180. A low efficiency is observed for low PPV:PPY layer thickness ratios, and there is a layer thickness ratio which produces a peak efficiency. The maximum of the efficiency is for the device with a PPV:PPY thickness ratio of r=4.0, rather than the r=1.7 found in the case of PPY batch ER180, however. It is evident from Figure 6-33 that the range of PPV:PPY ratios should be extended to ensure that the maximum efficiency was truly observed at r=4, but time and material constraints prevented this.

Bilayer Devices with PPY Batch L05

The efficiency variation of bilayer devices using PPY batch L05 as a function of layer thickness ratio is shown in Figure 6-34.

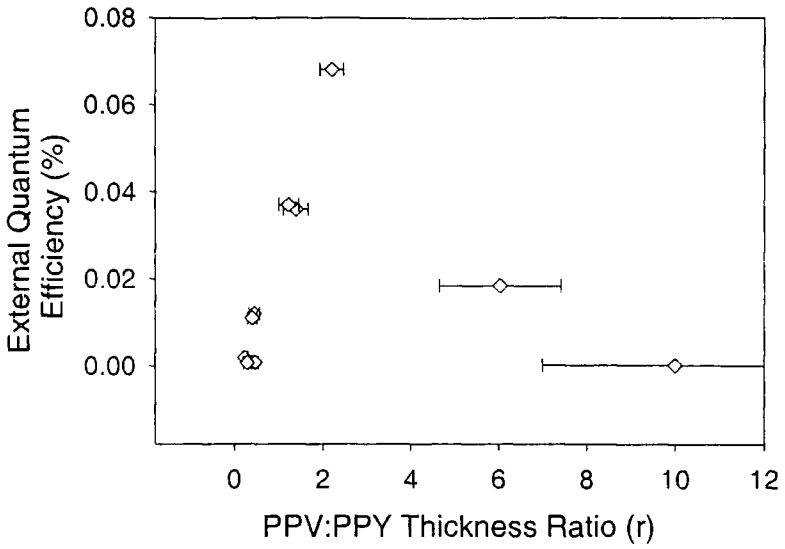

Figure 6-34 *Variation of external quantum efficiency with PPV:PPY thickness ratio for bilayer devices using PPY batch L05*

Bilayer devices with PPY batch L05 show a variation in efficiency with thickness similar to that found for other batches. The data for 11 devices are shown in Figure 6-34, but due to the inexact nature of preparing the devices by spin-coating, some thickness ratios are over represented. These devices do vary in their overall thickness and the similar nature of their efficiencies is a good indication that the variation in efficiency is predominantly due to the effect of the PPV:PPY thickness ratio. The structure and efficiencies of the devices are listed in Table 6-9.

PPV:PPY Thickness Ratio (r)	Total Thickness (nm)	PPV Thickness (nm)	PPY Thickness (nm)	Peak Efficiency (%)
0.24 ± 0.06	210	40	170	0.002
0.30 ± 0.09	175	40	135	7.180e-4
0.4 ± 0.1	160	45	115	0.011
0.4 ± 0.1	150	45	105	0.012
0.47 ± 0.07	250	80	170	7.820e-4
1.2 ± 0.2	165	90	75	0.037
1.4 ± 0.3	145	85	60	0.036
2.1 ± 0.3	250	170	80	0.068
4.2 ± 0.6	260	210	50	3.740e-4
6 ± 1	205	175	30	0.018
10 ± 3	220	200	20	2.420e-4

Table 6-9 *Structures and efficiencies for bilayer devices using PPY batch L05*

The device with the highest efficiency has a thickness ratio of r=2.1, and the efficiency of devices with different thickness ratios is lower.

Spectral Characterisation of Bilayer Devices

The use of the CCD and spectrograph facilitated easier and more rapid spectral measurement. Bilayer PPV/PPY devices were fabricated with PPY batches L04 and L05 with a range of PPV:PPY thickness ratios to investigate what effect this would have on the spectral output of the devices.

Devices with Batch L04

The electroluminescence spectra of bilayer devices with various PPV:PPY thickness ratios is shown in Figure 6-35. The thickness ratio for each spectrum is shown on the left-hand side of the graph.

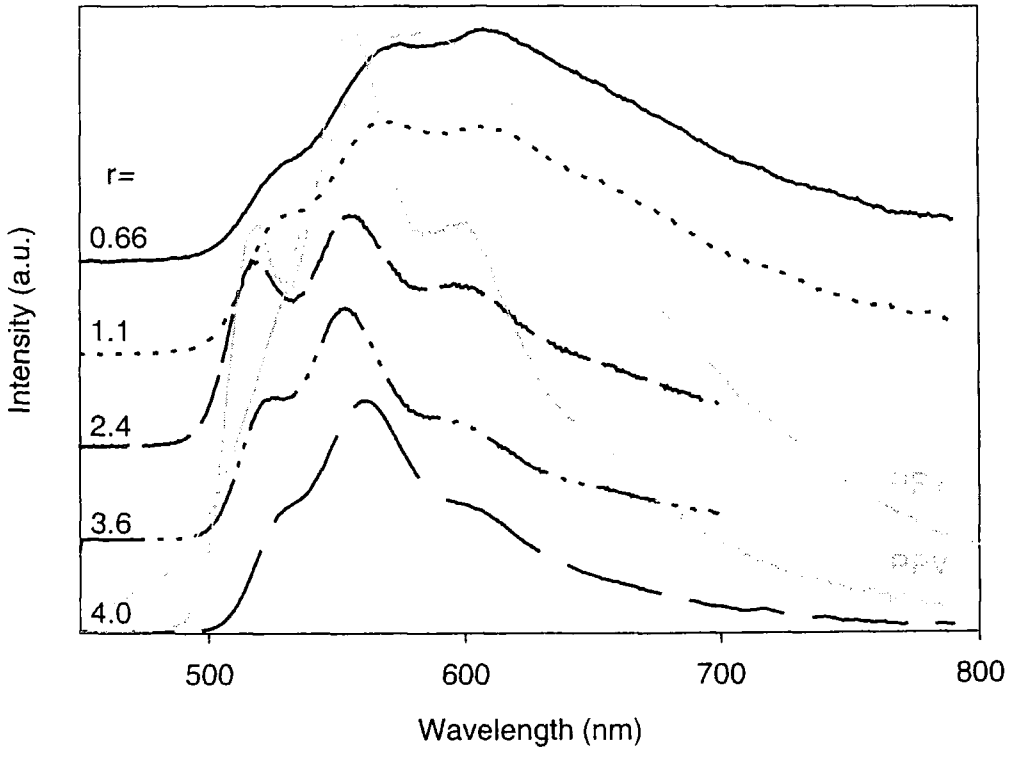

Figure 6-35 *Electroluminescence spectra of PPV/PPY bilayer devices as a function of PPV:PPY layer thickness ratio. The EL spectra of single layer PPV and PPY devices are shown in grey*

The EL spectra shown in Figure 6-35 have an increasing PPY character with decreasing PPV:PPY thickness ratio. This is manifested as higher intensity in the low energy "tail" of the emission spectra which leads to an apparent increase in the relative intensity of the third PPV vibronic peak. The effect that the layer thickness ratio has on the colour of emission of the devices can be seen in Figure 6-36. As expected by consideration of the spectra in Figure 6-35, the bilayer devices with low PPV:PPY thickness ratios have emission colours closer to that of single layer PPY devices and those with high ratios have emission colours closer to that of single layer PPV devices.

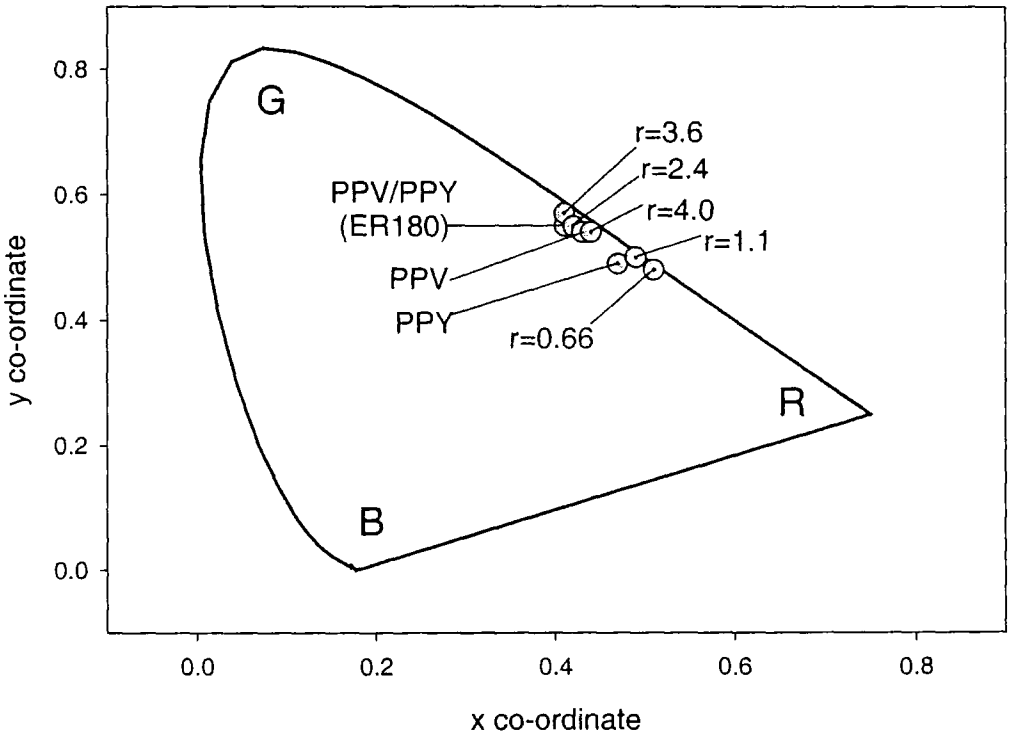

Figure 6-36 *Colour co-ordinate diagram for bilayer devices with various PPV:PPY thickness ratios (r). The colour of emission of single layer PPV and PPY devices and the bilayer device using PPY batch ER180 are also shown.*

A complication that may arise in the study of electroluminescence spectra from such devices is the effect that the applied field may have on the spectra. For example, colour variation with different applied bias has been observed in bilayer LEDs with PPV and an electron transport layer [30]. To investigate this, the spectra of one of the devices was measured as a function of applied voltage. The spectra are shown in Figure 6-37.

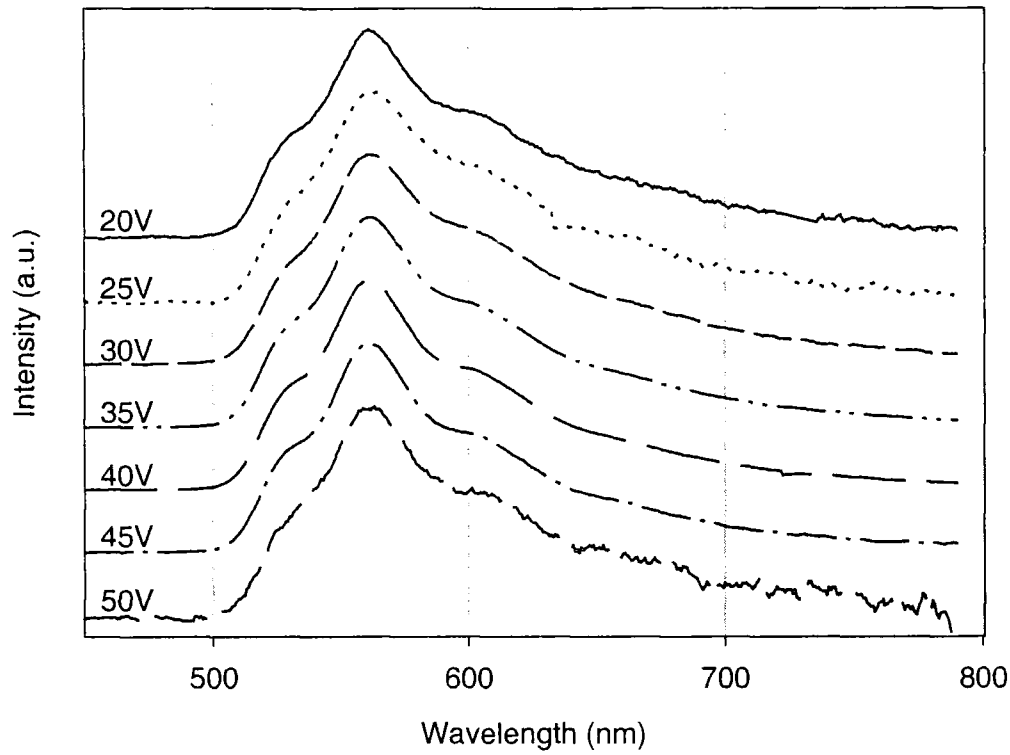

Figure 6-37 *Electroluminescence spectra of a bilayer device (r=4) as a function of applied voltage*

It can be seen from Figure 6-37 that the magnitude of the applied voltage has no significant effect on the electroluminescence spectrum of the device studied.

Devices with Batch L05

The range of PPV:PPY thickness ratios was extended using PPY batch L05. The electroluminescence spectra found in this study illustrate more complex behaviour than that found for the devices using batch L04.

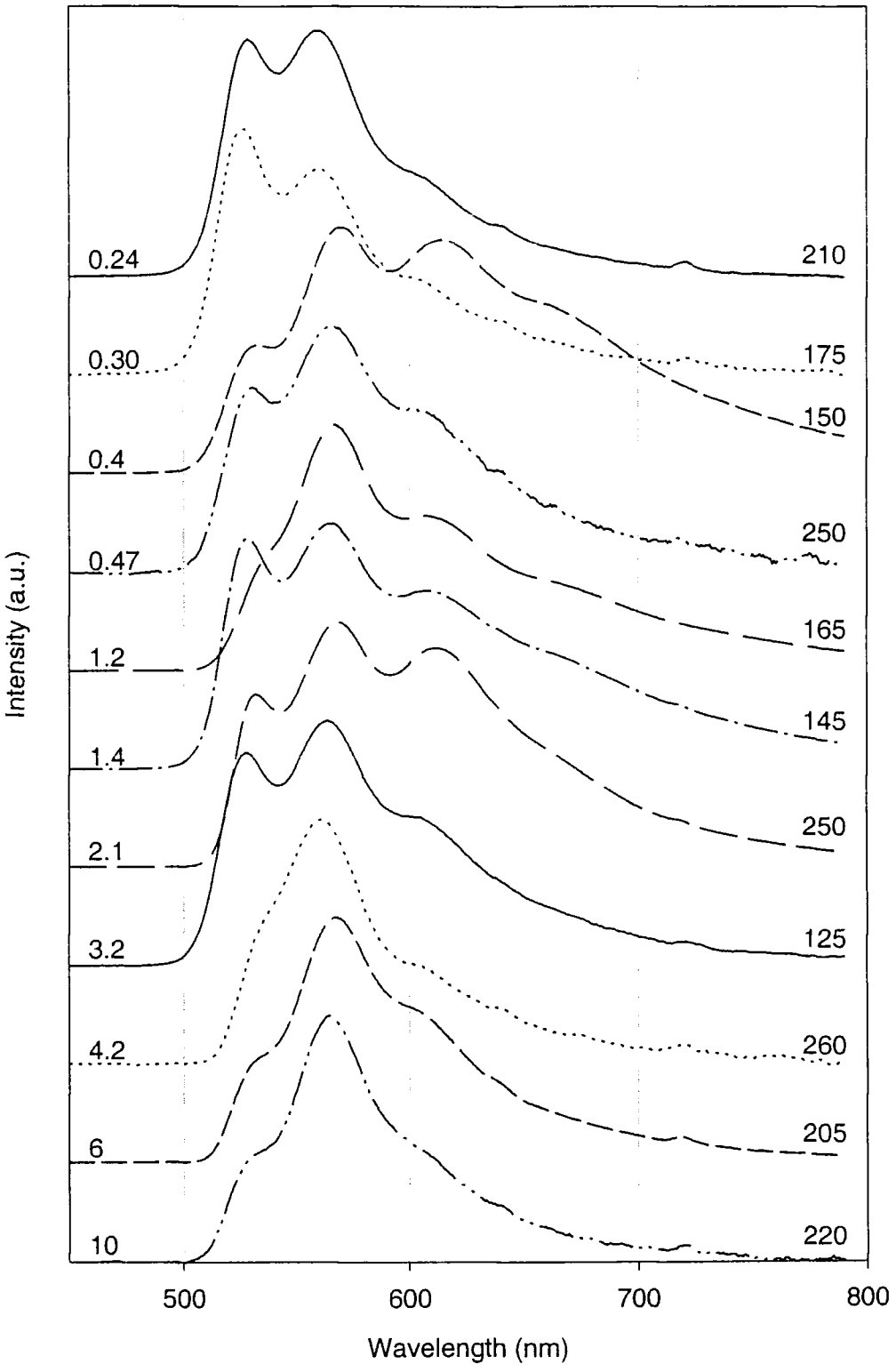

Figure 6-38 *Electroluminescence spectra of bilayer devices using PPY batch L05. The PPV:PPY thickness ratio is listed on the left and the total thickness of the device (in nm) is listed on the right*

It can be seen from Figure 6-38 that the simple relationship between thickness ratio and spectrum observed for bilayer devices in Figure 6-35 no longer remains.

There appears to be a relative enhancement of some parts of the spectra in Figure 6-38 which appears to be dependent on more than the thickness ratio of the device. It is also apparent that the spectral trends do not appear to follow the trends in overall thickness. Clearly there is a complex relationship between device structure and spectra which cannot be explained by a simple layer thickness argument.

Capacitance-Voltage Characterisation

The capacitance-voltage characteristics of an ITO/PPV/PPY/Al diode are shown in Figure 6-39. The device has a thickness ratio of 1.5 ± 0.3 and uses PPY batch L04.

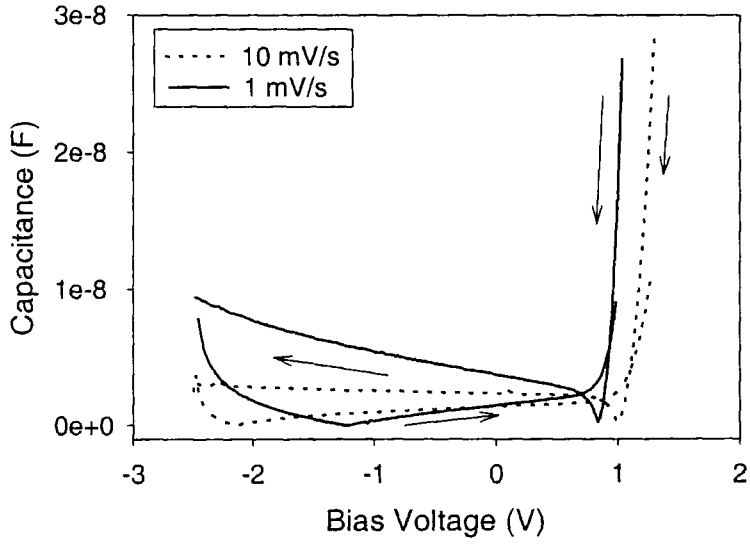

Figure 6-39 *Capacitance-voltage characteristics of an ITO/PPV/PPY/Al device at step rates of 1mV/s and 10mV/s*

The capacitance-voltage behaviour of the ITO/PPV/PPY/Al device in forward and reverse bias is significantly different to the behaviour found for the single layer PPV device. A Mott-Schottky plot of the data with a step voltage of 1mV/s is shown in Figure 6-40.

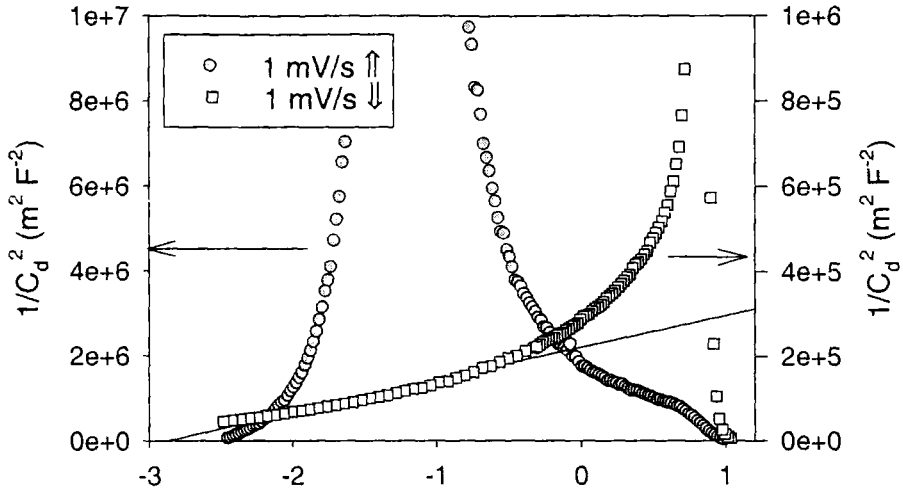

Figure 6-40 *Mott-Schottky plot for an ITO/PPV/PPY/Al device*

The Mott-Schottky plot of the bilayer device has some similarity in shape with that of the single layer PPV device. There is clearly only a linear relationship in reverse bias (open squares in Figure 6-40), and a more complex relationship in forward bias. Analysis of the data allows calculation of the acceptor density, built-in voltage (contact potential difference) and the width of the depletion region. These values are shown in Table 6-10.

V_{SO} (V)	N_A (m^{-3})	w (nm)
2.87	4.60×10^{24}	17

Table 6-10 *Built in voltage (V_{SO}), acceptor density (N_A) and depletion region width (w) for an ITO/PPV/PPY/Al device*

The value of N_A is very similar to that found for the single layer PPV and PPY diodes (see Chapter 5). The width of the depletion region is slightly larger than that found for the single layer PPV device, but similar to that found for the PPY device. The contact potential difference is far larger than that found for either single layer device. This high value may be a consequence of the difference in energy levels between the PPY and aluminium and also there could be some contribution from the mismatch of energy levels at the polymer heterojunction.

Summary and Discussion of PPV/PPY Bilayer Devices

Device Operation

The efficiency improvement observed for PPV diodes, upon addition of a PPY layer, is very encouraging. The most efficient bilayer device (with PPY batch ER180) has an efficiency 60 times higher than a single layer PPV device with aluminium contacts and 20 times higher than a single layer PPV device with calcium contacts. This increase in efficiency may be due to several factors. Possibly the most important factor is the balancing of positive and negative charge carriers in the device. Efficient operation of polymer light-emitting diodes requires balanced electron and hole injection and transport.

Charges migrating through a device will only contribute to the quantum efficiency of a device if they meet with an oppositely charged polaron to form a polaron-exciton which can then (if singlet) radiatively decay. If the charge simply migrates through the device, it adds to the current and reduces the quantum efficiency of the device. It is therefore important to have a similar number of opposite charges migrating through a device so that the charges can meet. Bilayer PPV/PPY devices may improve the balance of charge injection and transport so that the numbers of positive and negative charges in the device are more closely matched. The requirement of efficient devices having balanced charge injection provides an explanation of the variation in efficiency observed when the PPV:PPY thickness ratio is varied (Figure 6-29 and Figure 6-32 to Figure 6-34). Changing the thickness ratio, r, moves the region where positive and negative charges meet in the device, and the amount of trapping of charge that occurs. In a single-layer device the position of the region of light-emission will be defined by the relative mobilities of positive and negative polarons in a single material, but in bilayer devices the situation is complicated by the presence of the polymer heterojunction. There is a large barrier to hole injection from PPV to PPY, and a smaller barrier to electron injection from PPY to PPV as shown in Figure 6-18. This explains why light-emission retains a large amount of PPV-like character, even at low thickness ratios (Figure 6-35). The negative polarons migrate through the PPY layer to meet with oppositely charged polarons which are migrating through the PPV layer. The configuration of the polymer energy levels means that hole injection into the PPY layer is less likely than electron injection into the PPV layer and hence radiative recombination would preferentially occur in the PPV layer. It is

obvious from Figure 6-35, however, that some emission does come from the PPY layer. This is to be expected. As the PPY layer gets thicker compared to the PPV layer then there is a larger probability of opposite charges combining in the PPY layer, essentially because the charges have to travel further and hence will be in the PPY layer for a longer length of time. Efficiency variation with thickness ratio in bilayer devices using an electron-transporting polymer have been observed elsewhere [30].

An additional way in which the efficient electron-transporting layer may benefit LED performance is by moving the emissive region away from the metal contact. As discussed in Chapter 2, the metal electrode can quench luminescence either directly or by interference effects, and the displacement of the emissive region into the bulk of the polymer should increase the efficiency.

Comparison with other Electron-transporting Polymers

Although PPY has been studied previously as the emissive layer in polymer LEDs [21, 31] and has also given intriguing a.c. operation (see for example reference [14]), the efficiency of these devices is very low. This work differs from the previous work as PPY is used as an electron-transporting layer and not as an emissive layer [21, 31] and also the high photoluminescence quantum yield shown by our PPY suggests that refinements which have been made to the synthesis have resulted in a polymer with higher purity. The efficiency of LEDs made from small organic molecules has been improved by incorporating electron-transporting/hole-blocking layers (see for example references [32-36]). This has stimulated a search for efficient electron-transporting polymers which could be incorporated into multilayer devices [29, 31, 37-39]. The comparison in this report will be limited to polymer electron-transporting layers in polymer LEDs. Several approaches to electron-transporting polymers have been taken including oxadiazoles [28, 29, 40-42], poly(quinoline)s [30], poly(quinoxaline)s and related materials [37, 38, 40, 43-45], cyano-substituted PPVs [46, 47], and pyridine containing copolymers [38]. A summary of the performance of these electron-transporting polymers is listed below. The general type of the material is listed, the factor by which the efficiency is improved over a comparable single layer device, the efficiency of the best bilayer device and any comments which have relevance. Aluminium electrodes are used for all devices, unless stated otherwise. It should be noted that Table 6-11 is not a complete listing of all electron-transporting polymers.

Electron Transporting Polymer	Hole Transporting Polymer	f	QE (%)	Comments	Refer-ence
Oxadiazole	PPV	6	0.6	Internal QE	[42]
Oxadiazole	MEH-PPV	40	0.08		[29]
Oxadiazole	PPV	10	0.01		[28]
CN-PPV	PPV	N/A	4	Internal QE CN-PPV is emissive layer	[46]
Quinoxaline	PDAOPV	10	0.35	Integrating sphere efficiency	[37]
Quinoxaline	PPV	2	0.04	Mg:Ag electrode	[44]
Quinoxaline	PPV	10-40	0.13		[30]

Table 6-11 *Comparison of the effect of some types of electron-transporting polymers in polymer LEDs. The type of material used as the electron-transporting material, the hole-transporting and emissive material, the efficiency improvement factor over a single layer device with the same electrode material (f) and the quantum efficiency (QE) of the bilayer device are listed*

Table 6-11 illustrates that the efficiency improvement and overall efficiency of devices fabricated using a PPY electron-transporting polymer are comparable to the largest improvements found in the references listed above. The efficiency of devices using PPY batches other than ER180 still exhibit a much improved efficiency (approximately a factor 20 higher than single layer devices with aluminium electrodes), and a reasonable external quantum efficiency.

Efficiency Variation with PPY Batch

A large number of bilayer devices with various batches of PPY were fabricated in an effort to repeat the considerable improvements in efficiency obtained using PPY batch ER180 (a factor 3.8 better than the other batches). This was found to be impossible and the reason for this is unclear. Optical measurements of the PPY batches, shown in Chapter 4, show no significant difference between the PPY batches in either solution or film. The molecular weight of batch ER180 is unremarkable, but the polydispersity (i.e. the number of different molecular weights) is the highest of the batches. It is unlikely that this is the cause of the efficiency increase. The impurity level of batch ER180 in the CHNR analysis is the highest of any batch, although the ESR results for this batch are unremarkable. The analysis finds a impurity content of

5.74% by weight, higher than the next highest value of 3.99% for batch ER186. There may be some correlation between this impurity level and the efficiency of devices made with the particular batch of PPY, although the reason for this is not immediately obvious. Comparison of the peak efficiency of bilayer devices shown in Table 6-8 and the impurity level in Table 4-3 does show an increasing efficiency with increasing impurity level. This provides a possible reason for the enhanced operation with batch ER180. The increased impurity level may lead to n-doping the polymer, producing a very small light-emitting electrochemical cell (LEC) type effect. LECs exhibit lower operating voltages, high efficiency and facilitate the use of air stable metals as electrode materials [48, 49]. Other factors vary in this study, however, and drawing strong conclusions from this may be unwise.

Another possible reason for the increased efficiency may be the crystallinity of the PPY. PPY films are highly ordered [50, 51] and the high efficiency may be due to a large degree of ordering assisting in the efficient transport of charges through the PPY layer.

The variation in the thickness ratio of the most efficient device with a particular batch of PPY (Table 6-8) can be understood by considering the mobility of the PPY used. The mobility of the PPV would not be expected to alter significantly (the exception is the aged PPV compared to the fresh PPV) and hence the calculated charge mobility for the bilayer devices should provide a reasonable measure of the relative mobility of the PPY. If the PPY has a low mobility then a relatively thin layer would be expected to produce balanced charge transport and hence an efficient device. If the PPY has a high mobility then a thicker layer would be required to provide balanced charge transport. It is therefore expected that the most efficient device using PPY with a low charge mobility will have a high PPV:PPY thickness ratio and the most efficient device using PPY with a high charge mobility will have a lower PPV:PPY thickness ratio. This is observed only for some of the batches presented in Table 6-8, but the effect may be masked by the exact peak of the thickness ratio not being found or by other factors such as variation in the fabrication process.

Spectral Variation of Bilayer Devices

The variation in spectrum with PPV:PPY thickness ratio, shown in Figure 6-35, has been explained above by simple consideration of the probability emission occurring from a particular polymer layer, producing an EL spectrum which is simply a mixture

of PPV and PPY emission. This explanation does not require the formation of an excimer/exciplex type state which is considered to be responsible for emission in some bilayer devices using PPY and PPY derivatives [3, 31]. A study (elsewhere) of PPV bilayer devices using polyquinolines and related materials, finds no exciplex/excimer emission in optical measurements [30]. A spectral variation with different polymer layer thicknesses is found in reference [30], and is similar to what is found in this study.

The variation of EL spectra, shown in Figure 6-38, is far more complex than that shown in Figure 6-35. Some of the spectra appear to be affected by microcavity type effects. Deliberately fabricated microcavities can be used to alter the emission properties of LEDs (see for example references [52, 53]), and effects similar to those reported for microcavity devices appear to be found in this study. This can be understood by realising that the device structure of the devices studied may provide some microcavity modification. The aluminium electrode is approximately 100% reflecting, and the ITO electrode will be approximately 10% reflecting across a range of wavelengths. This would produce a cavity with a low quality factor and hence little enhancement would be expected. The situation is further complicated by the wide wavelength range of the emission and by the existence and position of the polymer heterojunction. The heterojunction may provide a refractive index mismatch and the position of the heterojunction, from which the majority of the light emission is thought to originate, will vary with thickness ratio. This means that the main emission zone may coincide with a node or anti-node of one of the modes of the cavity, entirely by chance. These considerations prevented detailed analysis of the spectra.

BILAYER DEVICES WITH MEH-PPV AND PPY

Energy Levels

It is also possible to fabricate bilayer devices using a PPY electron-transporting layer and MEH-PPV in place of PPV. The energy level positions of a bilayer ITO/MEH-PPV/PPY/Al device are shown below.

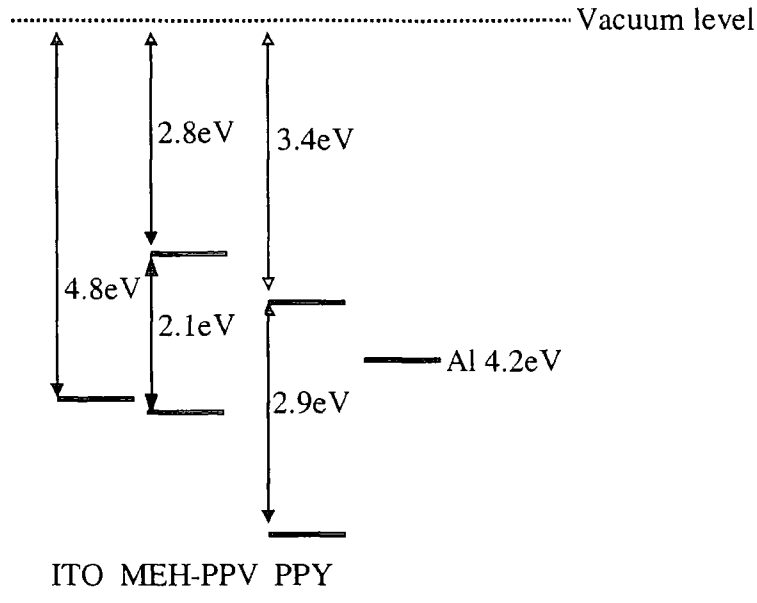

Figure 6-41 *Positions of the energy levels in a bilayer ITO/MEH-PPV/PPY/Al device*

The energy level positions of a bilayer device using MEH-PPV indicate that the theoretical barrier to electron injection from the PPY to the MEH-PPV layer is smaller than the corresponding barrier for bilayer devices using PPV. The barrier to hole injection from the PPY to MEH-PPV is slightly larger, however.

Device Performance of a Bilayer MEH-PPV/PPY Device

The current-voltage and intensity-voltage characteristics of a bilayer device using MEH-PPV are shown below. The devices were fabricated with PPY batch 196.

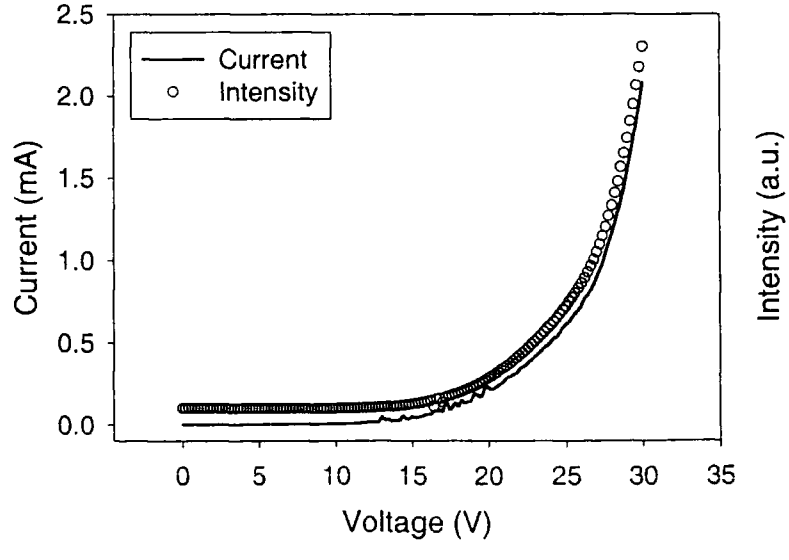

Figure 6-42 *Current-voltage and intensity-voltage characteristics of a bilayer MEH-PPV/PPY device*

The bilayer device has diode-like characteristics, similar to those found for most devices. The intensity-current characteristics of the device are shown in Figure 6-43.

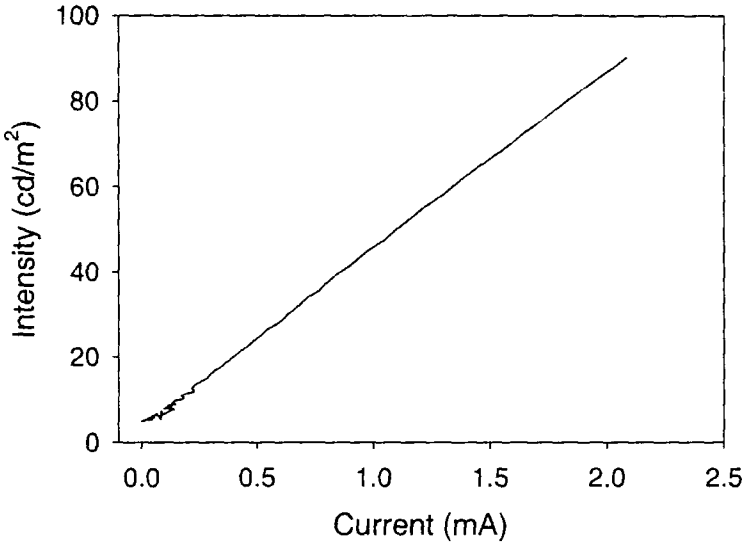

Figure 6-43 *Intensity-current characteristics of a bilayer MEH-PPV/PPY device*

The electroluminescence spectrum of the bilayer MEH-PPV/PPY device is compared to the EL spectra of single layer PPY and MEH-PPV devices in Figure 6-44.

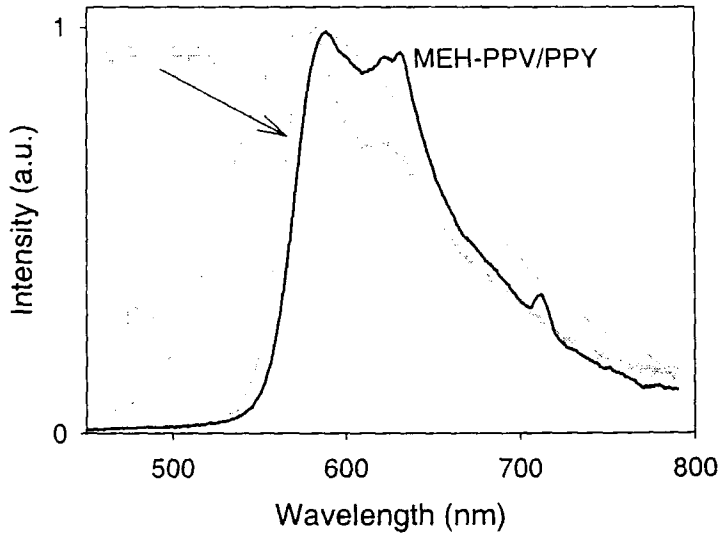

Figure 6-44 *Electroluminescence spectra of MEH-PPV/PPY bilayer, PPY and PPV single layer devices*

The EL spectrum of the bilayer device is very similar to the EL spectrum of single layer MEH-PPV devices and is dissimilar to the EL from PPY. The similarity is reflected in the colour co-ordinates of the emission. The bilayer device has CIE (X,Y) values of (0.58, 0.41), close to the single device values of (0.55, 0.44).

The external quantum efficiency of the device shown is 0.036%. This represents an efficiency increase of factor 4 over a single layer MEH-PPV device. This can be illustrated by comparison of the intensity-current characteristics of single and bilayer MEH-PPV devices (Figure 6-45).

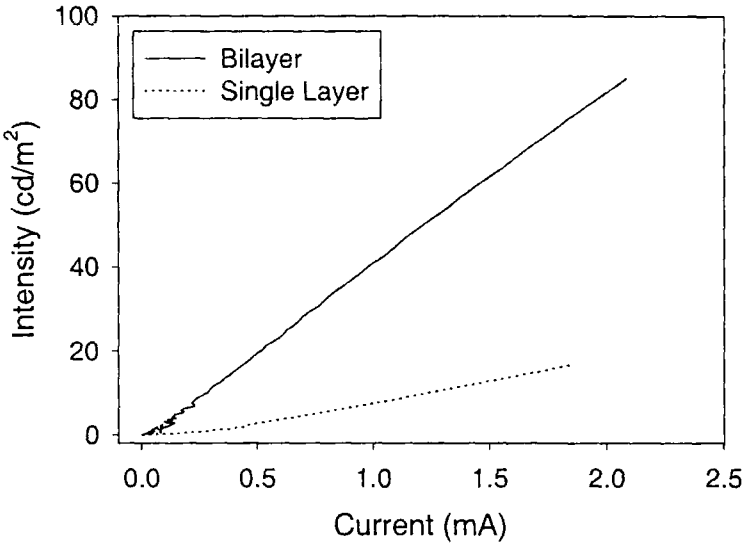

Figure 6-45 *Intensity-current characteristics of single and bilayer MEH-PPV devices*

The field required for a given current is higher in the bilayer device than in the single layer device (both with aluminium contacts). This is the opposite to what is found for the bilayer device using PPV as the active and hole-transporting layer. The current-field characteristics of both devices are compared in Figure 6-46.

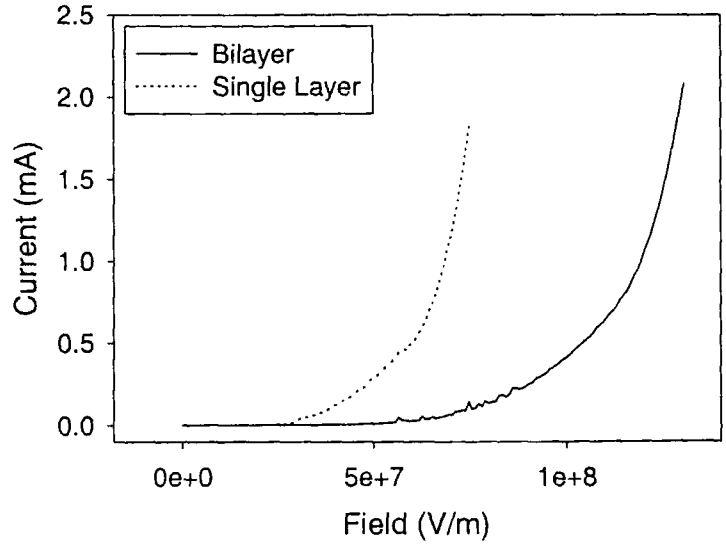

Figure 6-46 *Current-field characteristics of single and bilayer MEH-PPV devices*

The Schottky barrier height, charge mobility and Fowler-Nordheim barrier height of the bilayer device can be calculated from Schottky, SCLC and Fowler-Nordheim analysis of the current-voltage data.

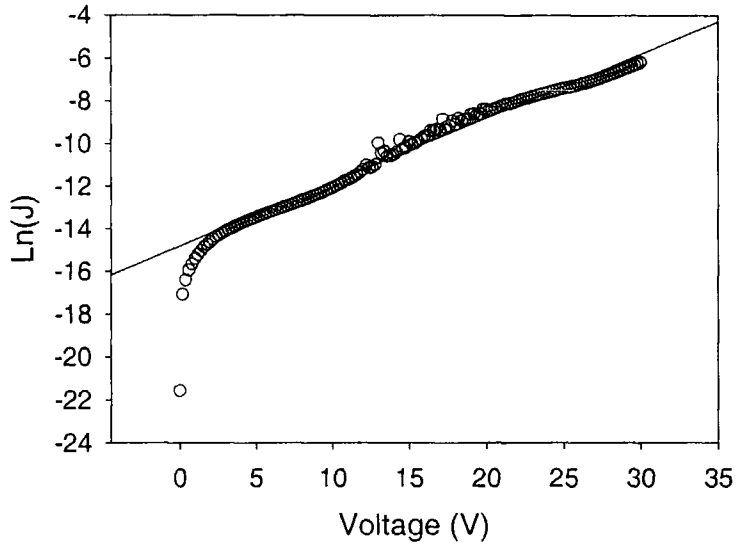

Figure 6-47 *Schottky analysis of a bilayer MEH-PPV/PPY device*

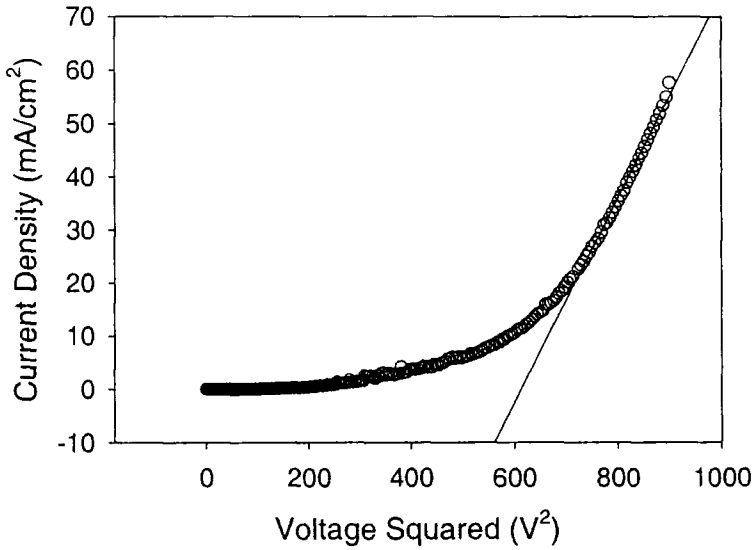

Figure 6-48 *SCLC analysis of a bilayer MEH-PPV/PPY device*

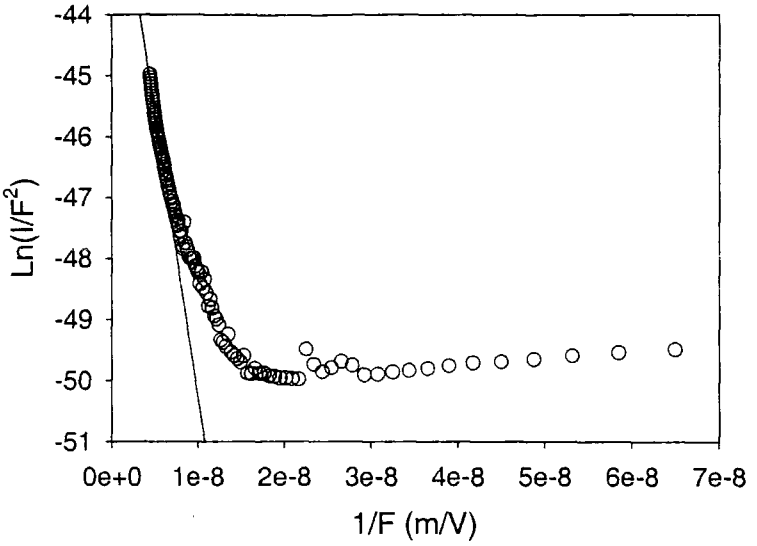

Figure 6-49 *Fowler-Nordheim analysis of a bilayer MEH-PPV/PPY device*

Bilayer MEH-PPV devices with various MEH-PPV to PPY thickness ratios were prepared. A summary of the external quantum efficiency, Schottky barrier height, charge mobility and Fowler-Nordheim barrier height for the bilayer MEH-PPV devices is presented in Table 6-12.

MEH-PPV to PPY Thickness Ratio (r)	Peak EQE (%)	Schottky Barrier Height (± 0.01 eV)	Charge Mobility ($cm^2 V^{-1} s^{-1}$)	F-N Barrier Height (eV)
1.0 ± 0.3	0.0046	0.99	$(8 \pm 2) \times 10^{-7}$	0.30 ± 0.03
1.6 ± 0.3	0.030	1.00	$(2.8 \pm 0.5) \times 10^{-6}$	0.26 ± 0.02
1.9 ± 0.2	0.036	0.80	$(1.2 \pm 0.2) \times 10^{-5}$	0.21 ± 0.01
2.9 ± 0.8	0.030	0.86	$(1.3 \pm 0.3) \times 10^{-6}$	0.27 ± 0.03
3.5 ± 0.8	0.021	0.95	$(1.5 \pm 0.3) \times 10^{-6}$	0.20 ± 0.02
3.8 ± 0.9	0.017	1.06	$(9 \pm 2) \times 10^{-6}$	0.21 ± 0.02

Table 6-12 *Efficiency and device parameters for bilayer MEH-PPV/PPY devices*

The Schottky barrier height for the bilayer devices is higher than the 0.74eV found for a single layer MEH-PPV device. It should be noted that the diode ideality factors for each device are very high and Fowler-Nordheim theory may provide a better framework than Schottky analysis. The use of a PPY layer reduces the charge mobility in the device from the 1.4×10^{-5} $cm^2 V^{-1} s^{-1}$ found for single layer MEH-PPV device and increases the value of the tunnelling barrier which is found to be 0.12eV in the single

layer device. Data supporting the idea of a larger barrier is given by the larger field required for a given current in Figure 6-46.

The efficiency of bilayer devices varies with layer thickness ratio in a similar manner to that found for the PPV bilayer devices. The variation is shown below.

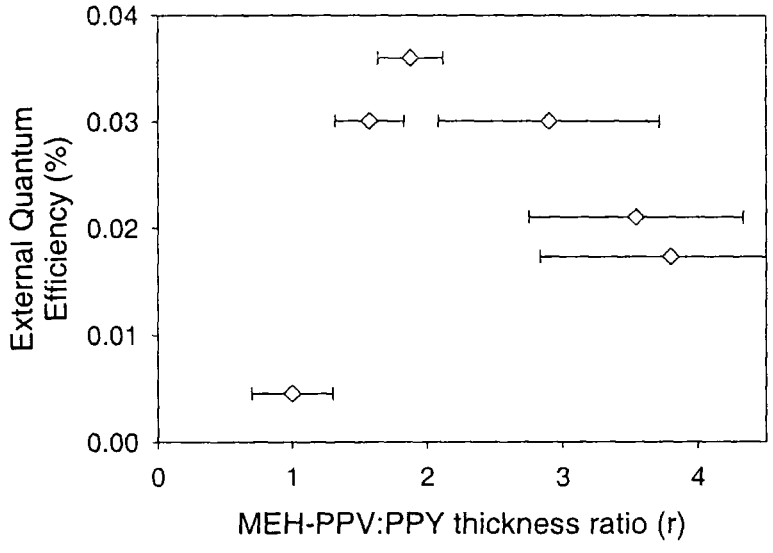

Figure 6-50 *External quantum efficiency as a function of MEH-PPV:PPY layer thickness ratio*

The bilayer MEH-PPV devices have a maximum efficiency for a thickness ratio of r=1.9 and a lower efficiency at thickness ratios smaller and larger than this value.

Summary and Discussion

An increase in the efficiency of operation of MEH-PPV based devices is achieved through the use of a PPY electron-transporting layer. The efficiency of the bilayer devices varies with the ratio of the polymer layer thicknesses. The model of bilayer device operation presented above provides an explanation of the efficiency increase. The increase in efficiency for MEH-PPV devices is not as large as for devices using PPV. This may be a consequence of the barrier to hole injection which arises in MEH-PPV devices (the ITO/PPV contact is thought to be ohmic) preventing the efficient injection and transport of electrons and holes, and hence efficient device operation.

The spectrum of the bilayer MEH-PPV device is very similar to that of the single layer device (Figure 6-44) suggesting the large barrier to hole injection from the MEH-PPV to the PPY (Figure 6-41) largely confines the excitations to the MEH-PPV layer.

BILAYER DEVICES WITH OTHER POLYMERS

A study using PPY as an electron-transporting polymer was carried out by Dr D. Lacey at Cambridge Display Technology (CDT). The study used one of CDT's proprietary PPV derivatives as the hole transporting and emissive layer. In summary, the study found that bilayer devices using a PPY ETL and aluminium electrodes had a similar efficiency to single layer PPV derivative devices with calcium electrodes. In other devices, a PEDOT hole transporting layer [54] was used between the PPV derivative and ITO layers. Using a PPY ETL to form a trilayer device improved the quantum efficiency by a factor 23 over a ITO/PEDOT/PPV/Al device. The efficiency of the device is a half of the efficiency obtained for a PEDOT/PPV device with calcium electrodes.

The efficiency of single layer device structures, examined in Chapter 5, can be greatly enhanced through the use of multilayer structures. Suitable materials can be chosen to act as efficient hole and electron-transporting layers and greatly enhance the operating efficiencies of polymer LEDs.

Thin films of doped polyaniline have been prepared by spin-coating from solutions of volatile acids. Optical characterisation of resulting films has been carried out, and the films have been used as a hole-transporting layer in polymer light-emitting diodes. Commercially available poly(vinyl carbazole) has also been characterised and used as a hole-transporting layer. The inclusion of these hole-transporting layers can produce devices with higher quantum efficiency and lower operating voltages, producing devices with higher power efficiency.

A luminescent polymer, polypyridine, has been used as an efficient electron-transporting polymer, providing an enhancement in efficiency similar to the largest improvements found for other electron-transporting polymers. Such bilayer devices exhibit spectral and efficiency variation with device structure, and a model to describe this variation is proposed. Unfortunately, a significant batch to batch variation of PPY produces significant differences in the performance of bilayer LEDs. Optical, ESR and chemical composition measurements do not provide great insight into the reason for the variation, and further work is required to fully investigate and characterise its origin. The successful elimination of the batch variation should lead to a promising electron-transporting material for polymer LEDs.

PPY is resistant to photochemical [55] and electrochemical [56] oxidation and facilitates the fabrication of efficient devices using less reactive metal electrodes. It has been demonstrated that PPY can produce enhanced device performance with several different polymers, and it's large band gap and orthogonal spinning solvent should allow its use with a range of luminescent polymers.

REFERENCES

[1] D. O'Brien, A. Bleyer, D. G. Lidzey, D. D. C. Bradley and T. Tsutsui, J. Appl. Phys., **82** , 5 (1997), 2662-2670.

[2] T. Yamamoto, T. Inoue and T. Kanbara, Japanese Journal Of Applied Physics Part 2-Letters, **33** , 2B (1994), L 250-L 253.

[3] D. D. Gebler, Y. Z. Wang, J. W. Blatchford, S. W. Jessen, D. K. Fu, T. M. Swager, A. G. MacDiarmid and A. J. Epstein, Appl. Phys. Lett., **70** , 13 (1997), 1644-1646.

[4] D. D. Gebler, Y. Z. Wang, S. W. Jessen, J. W. Blatchford, A. G. MacDiarmid, T. M. Swager, D. K. Fu and A. J. Epstein, Synth. Met., **85** , 1-3 (1997), 1205-1208.

[5] Y. Z. Wang, D. D. Gebler, D. J. Spry, D. K. Fu, T. M. Swager, A. G. MacDiarmid and A. J. Epstein, IEEE Trans. Elect. Dev., **44** , 8 (1997), 1263-1268.

[6] Y. Z. Wang, D. D. Gebler, D. K. Fu, T. M. Swager, A. G. MacDiarmid and A. J. Epstein, Synth. Met., **85** , 1-3 (1997), 1179-1182.

[7] J. S. Huang, H. F. Zhang, W. J. Tian, J. Y. Hou, Y. G. Ma, J. C. Shen and S. Y. Liu, Synth. Met., **87** , 2 (1997), 105-108.

[8] E. Gautier, J. M. Nunzi, C. Sentein, A. Lorin and P. Raimond, Synth. Met., **81** , 2-3 (1996), 197-200.

[9] Y. H. Tak, H. Vestweber, H. Bassler, A. Bleyer, R. Stockmann and H. H. Horhold, Chemical Physics, **212** , 2-3 (1996), 471-485.

[10] H. Antoniadis, J. N. Miller, D. B. Roitman and I. H. Cambell, IEEE Trans. Elect. Dev., **44** , 8 (1997), 1289-1294.

[11] F. Garten, A. Hilberer, F. Cacialli, E. Esselink, Y. vanDam, B. Schlatmann, R. H. Friend, T. M. Klapwijk and G. Hadziioannou, Adv. Mat., **9** , 2 (1997), 127-131.

[12] M. Hamaguchi and K. Yoshino, Jpn. J. Appl. Phys. part 1, **35** , 9A (1996), 4813-4818.

[13] F. Cacialli, R. H. Friend, N. Haylett, R. Daik, W. J. Feast, D. A. Dossantos and J. L. Bredas, Appl. Phys. Lett., **69** , 25 (1996), 3794-3796.

[14] A. J. Epstein, et al., Synth. Met., **78** , (1996), 253-261.

[15] A. J. Epstein, Y. Z. Wang, S. W. Jessen, J. W. Blatchford, D. D. Gebler, L. B. Lin, T. L. Gustafson, T. M. Swager and A. G. MacDiarmid, Macromolecular Symposia, **116** , (1997), 27-38.

[16] R. Osterbacka, A. J. Pal, K. M. Kallman and H. Stubb, J. Appl. Phys., **83** , 3 (1998), 1748-1752.

[17] A. J. Pal, R. Osterbacka, K. M. Kallman and H. Stubb, Appl. Phys. Lett., **70** , 15 (1997), 2022-2024.

[18] H. L. Wang, F. Huang, A. G. MacDiarmid, Y. Z. Wang, D. D. Gebler and A. J. Epstein, Synth. Met., **80** , (1996), 97-104.

[19] H. L. Wang, A. G. Macdiarmid, Y. Z. Wang, D. D. Gebler and A. J. Epstein, Synth. Met., **78** , 1 (1996), 33-37.

[20] S. A. Carter, M. Angelopoulos, S. Karg, P. J. Brock and J. C. Scott, Appl. Phys. Lett., **70** , 16 (1997), 2067-2069.

[21] D. D. Gebler, Y. Z. Wang, J. W. Blatchford, S. W. Jessen, H.-L. Wang, T. M. Swager, A. G. MacDiarmid and A. J. Epstein, J. Appl. Phys., **78** , 6 (1995), 4264-4266.

[22] G. Gustafsson, G. M. Treacy, Y. Cao, F. Klavetter, N. Colaneri and A. J. Heeger, Synth. Met., **57** , 1 (1993), 4123-4127.

[23] S. Karg, J. C. Scott, J. R. Salem and M. Angelopoulos, Synth. Met., **80** , 2 (1996), 111-117.

[24] Y. Yang and A. J. Heeger, Appl. Phys. Lett., **64** , 10 (1994), 1245-1247.

[25] P. N. Adams, P. Devasagayam, S. J. Pomfret, L. Abell and A. P. Monkman, Journal Of Physics-Condensed Matter, **10** , 37 (1998), 8293-8303.

[26] A. J. Epstein and A. G. MacDiarmid, Synth. Met., **69** , (1995), 179-182.

[27] M. Herold, J. Gmeiner, W. Riess and M. Schwoerer, Synth. Met., **76** , 1-3 (1996), 109-112.

[28] M. Greczmiel, P. Posch, H. W. Schmidt, P. Strohriegl, E. Buchwald, M. Meier, W. Riess and M. Schwoerer, Macromolecular Symposia, **102** , (1996), 371-380.

[29] Q. Pei and Y. Yang, Chem. Mater., **7** , (1995), 1568-1575.

[30] S. A. Jenekhe, X. J. Zhang, X. L. Chen, V. E. Choong, Y. L. Gao and B. R. Hsieh, Chem. Mat., **9** , 2 (1997), 409.

[31] T. Yamamoto, H. Suganuma, Y. Saitoh, T. Maruyama and T. Inoue, Jpn. J. Appl. Phys. Part 2, **35** , 9A (1996), 1142-1144.

[32] P. E. Burrows, Z. Shen, V. Bulovic, D. M. McCarty, S. R. Forrest, J. A. Cronin and M. E. Thompson, J. Appl. Phys., **79** , 10 (1996), 7991-8006.

[33] S. A. Vanslyke, C. H. Chen and C. W. Tang, Appl. Phys. Lett., **69** , 15 (1996), 2160-2162.

[34] T. Hattori, T. Taira, M. Era, T. Tsutsui and S. Saito, Chem. Phys. Lett., **254** , 1-2 (1996), 103-108.

[35] E. Aminaka, T. Tsutsui and S. Saito, Jap. J. Appl. Phys., **33** , 2 (1994), 1061-1068.

[36] K. Tamao, M. Uchida, T. Izumizawa, K. Furukawa and S. Yamaguchi, J. Am. Chem. Soc., **118** , 47 (1996), 11974-11975.

[37] D. O'Brien, M. S. Weaver, D. G. Lidzey and D. D. C. Bradley, Appl. Phys. Lett., **69** , 7 (1996), 881-883.

[38] M. S. Weaver, et al., Thin Solid Films, **273** , (1996), 39-47.

[39] D. R. Baigent, A. B. Holmes, S. C. Moratti and R. H. Friend, Synth. Met., **80** , (1996), 119-124.

[40] J. Bettenhausen, M. Greczmiel, M. Jandke and P. Strohriegl, Synth. Met., **91** , 1-3 (1997), 223-228.

[41] M. Meier, E. Buchwald, S. Karg, P. Posch, M. Greczmiel, P. Strohriegl and W. Riess, Synth. Met., **76** , 1-3 (1996), 95-99.

[42] M. Strukelj, T. M. Miller, F. Papadimitrakopoulos and S. Son, J. Am. Chem. Soc., **117** , 48 (1995), 11976-11983.

[43] T. Fukuda, T. Kanbara, T. Yamamoto, K. Ishikawa, H. Takezoe and A. Fukuda, Synth. Met., **85** , 1-3 (1997), 1195-1196.

[44] T. Fukuda, T. Kanbara, T. Yamamoto, K. Ishikawa, H. Takezoe and A. Fukuda, Appl. Phys. Lett., **68** , 17 (1996), 2346-2348.

[45] D. O'Brien, A. Bleyer, D. D. C. Bradley and S. Meng, Synth. Met., **76** , 1-3 (1996), 105-108.

[46] N. C. Greenham, S. C. Moratti, D. D. C. Bradley, R. H. Friend and A. B. Holmes, Nature, **365** , 14 October 1993 (1993), 628-630.

[47] S. C. Moratti, R. Cervini, A. B. Holmes, D. R. Baigent, R. H. Friend, N. C. Greenham, J. Gruner and P. J. Hamer, Synth. Met., **71** , 1-3 (1995), 2117-2120.

[48] Y. Yang and Q. B. Pei, Appl. Phys. Lett., **70** , 15 (1997), 1926-1928.

[49] Y. Yang and Q. B. Pei, J. Appl. Phys., **81** , 7 (1997), 3294-3298.

[50] L. Patterson, To be published, , (1998), .

[51] A. P. Monkman, To be published, , (1998), .

[52] H. Yokoyama, Science, **256** , 3 April 1992 (1992), 66-70.

[53] A. Dodabalapur, L. J. Rothberg, R. H. Jordan, T. M. Miller, R. E. Slusher and J. M. Phillips, J. Appl. Phys., **80** , 12 (1996), 6954-6964.

[54] J. C. Carter, et al., Appl. Phys. Lett., **71** , 1 (1997), 34-36.

[55] M. Halim, I. D. W. Samuel, E. Rebourt and A. P. Monkman, Synth. Met., **84** , 1-3 (1997), 951-952.

[56] T. Yamamoto, et al., J. Am. Chem. Soc., **116** , (1994), 4832-4845.

Chapter 7 Summary and Conclusions

The apparatus required for the measurement of photoluminescence spectra and for the fabrication and characterisation of polymer light-emitting diodes has been assembled. The essential assumptions and calculations required to fully characterise polymer light-emitting diodes have been applied and reported.

POLYPYRIDINE

Polypyridine (PPY), synthesised in Durham, has been characterised by optical spectroscopy. Batch-to-batch variation of the polymer has been investigated using optical spectroscopy, electron-spin resonance (ESR) studies, chemical analysis and molecular weight determination.

The differences in the optical properties of PPY in solution and film have been investigated using optical spectroscopy. Emission from excimer or aggregate states has been discounted, and the differences have been explained in terms of rotations of the pyridine rings out of the plane of the polymer chain, producing a reduced conjugation length in solution. The high degree of order in the polymer film reduces the occurrence of ring rotations, producing a longer conjugation length and hence a lower energy emission. The conjugation length of PPY in solution and film has been probed by disrupting the conjugation along the chain using *meta*-linked monomer units in random copolymers of *meta*- and *para*-linked PPY. From optical measurements of these polymers, the conjugation length has been estimated to be between 3 and 4 repeat units in film and less than 3 repeat units in solution.

The "tuneability" of polymer emission has been demonstrated by the study of the solid state dilution of PPY. Films of PPY and poly(methyl methacrylate) blends have been shown to produce considerable colour tuning, without the requirement for modification of the chemical structure.

DERIVATIVES OF POLYPYRIDINE

Significant colour tuning has also been achieved by altering the chemical structure of PPY. This has been demonstrated by the study of novel derivatives of PPY.

A hexyl substituted PPY derivative with increased solubility, and a *meta*-linked derivative of PPY with a reduced conjugation length have been synthesised and characterised. The addition of a hexyl group appears to increase the ring torsion angle in the polymer, leading to a reduction of the conjugation length and a blue-shift of the absorption in solution and film. The side group also seems to prevent the high ordering observed in PPY films, producing a smaller shift between the photoluminescence of solution and film. The larger torsion angle may increase the probability of intersystem crossing, leading to a reduction in the photoluminescence quantum yield of the polymer.

The *meta*-linked derivative of PPY exhibits blue-shifted absorption and emission in solution and film, which would be expected from a polymer with a reduced conjugation length. The *meta*-links produce a polymer with significantly weaker photoluminescence in solution and film, however.

COPOLYMERS OF PPY

Random copolymers of PPY and hexyl substituted or *meta*-linked PPY derivatives have been characterised using optical spectroscopy. This characterisation has enabled an estimate of the conjugation length in PPY.

Regular copolymers of PPY (and derivatives) and poly(*p*-phenylene) (PPP) (and derivatives) have also been characterised. Blue-shifted absorption and almost pure blue emission is observed from copolymers containing hexyl substituted PPY units, but little change from the optical properties of pure PPY is observed when unsubstituted PPY units are used in the copolymer.

DEVICES BASED ON PPY AND PPY COPOLYMERS

Polymer electroluminescent devices based on PPY and copolymers of PPY exhibit novel charge injection and transport properties and show symmetric current-voltage characteristics, independent of theoretical barriers to charge injection. This represents a departure from the simple model of device operation and is significantly different to devices using PPV and derivatives. Single layer devices using PPY have an efficiency of approximately 3×10^{-3}%, similar to efficiencies found for PPV based devices with aluminium electrodes. The use of lower workfunction metals can reduce the field required for a given current in PPY devices but the efficiency, in contrast to

what is found for PPV devices, is significantly reduced. This could be due to chemical interaction between the reactive metals and the polymer.

Schottky and space charge limited current analysis of the current-voltage characteristics provide some insight into device operation, but the small range over which the models fit and the high diode ideality factors suggest that application of these models to polymer systems is not ideal. Fowler-Nordheim analysis of PPY based devices is inappropriate. Capacitance-voltage analysis of PPY-based devices finds a doping density similar to that of poly(*p*-phenylene vinylene) (PPV).

The efficiency and performance devices using PPY:PMMA blends as the active layer is poor (two orders of magnitude less than single layer PPY devices), and the photoluminescence and electroluminescence spectra exhibit considerable differences. Similar efficiency and spectral variation is found for devices using regular copolymers of PPY. The electroluminescence of one of the regular copolymers is found to be almost white, and not the almost pure blue emission of photoluminescence.

Single layer light-emitting diodes using the random hexyl copolymer have low efficiency and exhibit anomalous current-voltage characteristics. Devices using the *meta*-linked copolymers show no electroluminescence. They exhibit increasingly anomalous current-voltage characteristics with increasing *meta* content, suggesting that the anomalies may be connected to the reduction in the conjugation length of the polymer.

PPV AND DERIVATIVES

Single and bilayer electroluminescent devices using PPV and MEH-PPV have been fabricated and tested. The spectral characteristics of the devices have been measured, and their current-voltage behaviour has been analysed in a Schottky, SCLC and Fowler-Nordheim framework. Single layer devices using aluminium electrodes have an efficiency of approximately 4×10^{-3}% and 9×10^{-3}% for PPV and MEH-PPV respectively. PPV diodes using calcium electrodes have an efficiency of approximately 1×10^{-2}%. Capacitance-voltage measurements of the devices have also been carried out.

The effect of conversion of precursor route polymers on ITO coated substrates was investigated using optical spectroscopy and quasi-static capacitance voltage analysis.

Significant differences were found in the absorption and luminescence spectra of poly(2-methoxy, 5-(2'ethyl-hexyloxy)-*p*-phenylene vinylene) (MEH-PPV), prepared

via thermal conversion of the precursor polymer, on ITO and quartz substrates. In contrast, only minor differences were found for PPV prepared on ITO and quartz substrates. Significant doping of the polymers prepared on ITO substrates by indium chloride is the likely explanation.

Comparison of the capacitance-voltage characteristics of devices using precursor and solution processed MEH-PPV found a doping density 280 times higher in the precursor route device, suggesting substantial doping during the conversion process. A similar doping density was found for PPV prepared via the precursor route.

HOLE-TRANSPORTING POLYMERS

Efficiency improvements using hole-transporting polymers have been demonstrated. Films of commercially available poly(vinyl carbazole) have been optically characterised and applied successfully as the hole-transporting layer in bilayer devices using PPY as the electron-transporting and emissive layer. Thin films of the conducting form of polyaniline (PANi) have been prepared by spin-coating from volatile solvents and their optical properties have been measured. MEH-PPV and PPY devices with a PANi hole-transporting layer show reduced turn-on voltages and devices with MEH-PPV show increased efficiency.

PPY AS AN ELECTRON-TRANSPORTING POLYMER

The novel charge injection properties of PPY devices facilitated the use of PPY as an efficient electron-transporting polymer (ETP). Devices with PPV as the hole-transporting and emissive layer and PPY as an ETP show an increase in efficiency of a factor 60 over single layer PPV devices with aluminium electrodes and a factor 20 over devices with calcium electrodes. The peak efficiency of the bilayer devices is 0.25%. These bilayer devices show an efficiency and spectral variation if the ratio of the thickness of the polymer layers is altered. A model is described to account for the spectral and efficiency variation, and for the efficiency improvements. The improvement in efficiency is thought to be due to the improved balance of injection and transport of electrons and holes, compared to single layer devices, and the displacement of the emissive region into the bulk and away from the metal contact.

An increase in the quantum efficiency of devices using two other conjugated polymers as the hole-transporting and emissive layer, and PPY as an electron-transporting layer is also reported, and a similar variation of efficiency with thickness ratio is measured for one of the polymers.

A large variation in bilayer device performance is produced by batch to batch variation of PPY. Optical, ESR and chemical analysis failed to provide an explanation for the variation, and further work is required to determine the origin of the variation.

SUMMARY

In summary, a wide range of conjugated polymers has been characterised by optical spectroscopy. Single layer electroluminescent devices have been fabricated and characterised, but a significant increase in efficiency can be obtained through the use of multiple polymer layer structures. Analysis of the devices in Schottky, space charge limited current and Fowler-Nordheim frameworks provides some insight into device operation, but the complexity and material dependence of the operation of polymer light-emitting diodes prevents accurate modelling.

SUGGESTIONS FOR FUTURE WORK

Conducting thin films of polyaniline could be used as hole-transporting layers with a range of polymers. Triple layer devices using the structure polyaniline/MEH-PPV/PPY/Al may provide a method of producing stable and efficient devices. The doping of MEH-PPV prepared via thermal conversion on ITO may produce devices with improved efficiency due to the p-doping of the polymer. The spectral characteristics of such devices may be undesirable, however.

Methods to improve the efficiency of electroluminescence from PPY and PPY derivatives could be investigated in an effort to exploit their high photoluminescence quantum yields. Possible structures include a blend of poly(vinyl carbazole) and poly(hexylpyridine) in a single layer structure, and the use of other hole-transporting polymers, for example PEDOT. Further experiments using a poly(vinyl carbazole) layer may also prove useful.

Further characterisation of devices using PPY as an electron-transporting layer may be provided through the measurement of the charge mobility of the component polymers, providing some insight into the layer thickness ratio required to achieve peak efficiency. Further investigation into the nature and amount of impurities that may lead to very efficient electron-transporting polymers for devices is required. Knowledge of the mechanism of the improvement in efficiency following vacuum treatment of PPY may also prove to be extremely useful.

APPENDIX 1 LISTING OF EEXT.XFM

The Jandel Sigmaplot transform file for the calculation of the external quantum efficiency of LEDs is listed below. The transform uses area.xfm, provided with Jandel Sigmaplot, to calculate integrals.

```
;EL QUANTUM EFFICIENCY CALCULATOR VERSION 1.0

;**********FILL IN THESE VALUES*****************
dcurr=                  ;current in polymer diode
volt2=                  ;voltage signal in photodiode
;************************************************
wave=col(1)   ;sets wavelength for T in col 1 (MUST BE IN m)
tint=col(2)     ;sets tint in col 2
planck=6.626076e-34
cee=299792458
solidang=0.0625
elec=1.60217733e-19
pi=3.141592654

;*******2nd order polynomial fit to response curve**********
gcoef=-9.17965e10
hcoef=7.80834e5
icoef=-0.119066
resp=gcoef*(wave^2)+hcoef*(wave)+icoef
col(3)=resp
cell(3,1)="respons a/w"
;*******end of response section*****

;******Calibration******
;rf=2.31e6        ;reference resistor in amp
rf=2.2e6     ;reference resistor in amp
;voltage=(0.987*volt2)
;voltage=(0.989*volt2)
voltage=(0.954*volt2)
;***********************

col(4)=(col(3)*col(2))/col(1) ;intensity proportional to photon energy
x_col=1          ;column number for x data
y_col=4          ;column number for y data
res=5           ;column number for result
;Define x and y data
x=col(x_col)
y=col(y_col)

;*************** CALCULATE AREA ***************
```

```
;Compute the the range of differences between
; x[i] & x[i-1]
xdif1=diff(x)
n=count(x)              ;Delete first value-
xdif=xdif1[data(2,n)]    ;not a difference
;Compute the range of differences between
; y[i] & y[i-1]
ydif1=diff(y)
ydif=ydif1[data(2,n)]    ;Delete first value-
                    ;not a difference
;Use only y values from y[1] to y[n-1]
y1=y[data(1,n-1)]
;Calculate trapezoidal integration
intgrl=y1*xdif+0.5*ydif*xdif
int=total(intgrl)

;******** PLACE RESULTS IN WORKSHEET *********
cell(res,2)=int      ;Put area in result column
cell(res,1)="int TR/L"
col(6)=(voltage/(rf*planck*cee*int))*col(2)
cell(6,1)="norm int"

;*********INTEGRAL NUMBER 2***********
sx_col=1          ;column number for x data
sy_col=6          ;column number for y data
sres=7           ;column number for result
;Define x and y data
sx=col(sx_col)
sy=col(sy_col)

;CALCULATE AREA 2
;Compute the the range of differences between
; x[i] & x[i-1]
sxdif1=diff(sx)
sn=count(sx)              ;Delete first value-
sxdif=sxdif1[data(2,n)]    ;not a difference
;Compute the range of differences between
; y[i] & y[i-1]
sydif1=diff(sy)
sydif=sydif1[data(2,n)]    ;Delete first value-
                    ;not a difference
;Use only y values from y[1] to y[n-1]
sy1=sy[data(1,n-1)]
;Calculate trapezoidal integration
sintgrl=sy1*sxdif+0.5*sydif*sxdif
inttwo=total(sintgrl)

;******** PLACE RESULTS IN WORKSHEET *********
cell(sres,2)=inttwo      ;Put area in column res
cell(sres,1)="int 2:"
Eext=(elec*pi*inttwo)/(dcurr*solidang)
cell(sres+1,2)=Eext
```

```
cell(sres+1,1)="Eext="
cell(sres+1,3)="Eext (%)"
cell(sres+1,4)=Eext*100
```

APPENDIX 2 LISTING OF CANDELA.XFM

The Jandel Sigmaplot transform file for the calculation of the brightness in candela per square metre of LEDs is listed below. The transform uses area.xfm, provided with Jandel Sigmaplot, to calculate integrals.

```
;CANDELA CALCULATOR VERSION 1.0

;**********CONSTANTS***********
wave=col(1)          ;sets wavelength for T in col 1 (MUST BE IN m)
tint=col(2)          ;sets t int in col 2
planck=6.626076e-34  ;Planck's constant
cee=299792458        ;speed of light
solidang=0.0625      ;solid angle of collection
elec=1.60217733e-19  ;charge on the electron
pi=3.141592654       ;pi
areadi=2e-6      ;area of pixel in m2
km=683.002       ;CIE CONSTANT
fit1_dat=10      ;data column for CIE x<555nm
fit2_dat=11      ;data column for CIE x>555nm
wav_col=1        ;wavelength data
res_col=7        ;col for CIE data

;******FILL THESE IN**********************
x_start=         ;start of wavelength col
x_end=           ;end of wavelength col
volt2=           ;voltage signal in photodiode
dcurr=           ;current drawn by polymer diode (for lm/W calc)
dvolt=           ;voltage across polymer diode (for lm/W calc)

;*******2nd order polynomial fit to response curve
gcoef=-9.17965e10
hcoef=7.80834e5
icoef=-0.119066
resp=gcoef*(wave^2)+hcoef*(wave)+icoef
col(3)=resp
cell(3,1)="respons a/w"
;*******end of response section*****

;***********Calibration section***********
rf=2.31e6                ;reference resistor in amp
;rf=2.2e6                ;reference resistor in amp
voltage=volt2*0.987
;voltage=volt2*0.989
;voltage=volt2*0.954
```

```
;*********************************************

col(4)=(col(3)*col(2))/col(1)
x_col=1          ;column number for x data
y_col=4          ;column number for y data
res=5            ;column number for result
cell(4,1)="R*T/E"
;Define x and y data
x=col(x_col)
y=col(y_col)

;**************** CALCULATE AREA ****************
;Compute the the range of differences between
; x[i] & x[i-1]
xdif1=diff(x)
n=count(x)              ;Delete first value-
xdif=xdif1[data(2,n)]    ;not a difference
;Compute the range of differences between
; y[i] & y[i-1]
ydif1=diff(y)
ydif=ydif1[data(2,n)]    ;Delete first value-
                  ;not a difference
;Use only y values from y[1] to y[n-1]
y1=y[data(1,n-1)]
;Calculate trapezoidal integration
intgrl=y1*xdif+0.5*ydif*xdif
int=total(intgrl)

;******** PLACE RESULTS IN WORKSHEET *********
cell(res,2)=int      ;Put area in column res
cell(res,1)="int TR/L"
col(6)=(voltage/(rf*planck*cee*int))*col(2)
cell(6,1)="norm int"

;*********CIE DATA SECTION**********************

;*********CIE CURVE FIT DATA**********
cell(fit1_dat,1)=1.00
cell(fit1_dat,2)=5.5163e-7
cell(fit1_dat,3)=3.5761e-8
cell(fit2_dat,1)=1.00
cell(fit2_dat,2)=5.5880e-7
cell(fit2_dat,3)=4.3678e-8
cell(fit1_dat,4)="CIE curve fit"
cell(fit2_dat,4)="parameters"
;******END OF CIE CURVE FIT*******

for j=x_start to x_end step 1 do
i=if(cell(wav_col,j)<555e-9,fit1_dat,fit2_dat)
acie=cell(i,1)
bcie=cell(i,2)
ccie=cell(i,3)
```

```
xcie=cell(wav_col,j)
ycie=acie*exp((-0.5)*(((xcie-bcie)/ccie)^2))
cell(res_col,j)=ycie
end for

;******END OF CIE GENERATING DATA******

cell(res_col,1)="CIE data"
;s()*e()*c()
cell(8,1)="S*E*C"
col(8)=col(6)*col(7)*planck*cee/col(1)

;*********INTEGRAL NUMBER 2***********
sx_col=1          ;column number for x data
sy_col=8          ;column number for y data
sres=9           ;column number for result
;Define x and y data
sx=col(sx_col)
sy=col(sy_col)
;Compute the the range of differences between
; x[i] & x[i-1]
sxdif1=diff(sx)
sn=count(sx)              ;Delete first value-
sxdif=sxdif1[data(2,n)]    ;not a difference
;Compute the range of differences between
; y[i] & y[i-1]
sydif1=diff(sy)
sydif=sydif1[data(2,n)]    ;Delete first value-
                  ;not a difference
;Use only y values from y[1] to y[n-1]
sy1=sy[data(1,n-1)]
;Calculate trapezoidal integration
sintgrl=sy1*sxdif+0.5*sydif*sxdif
inttwo=total(sintgrl)

;******** PLACE RESULTS IN WORKSHEET *********
cell(sres,2)=inttwo      ;Put area in column res
cell(sres,1)="int 2:"
cell(sres,3)="Cd/m2"
cell(sres,4)=inttwo*km/(areadi*solidang)
cell(sres,6)=cell(sres,4)*pi*areadi
cell(sres,5)="lumens"
cell(sres,7)="lumens/watt"
cell(sres,8)=cell(sres,6)/(dcurr*dvolt)
```

APPENDIX 3 CALIBRATION OF THE DETECTOR

Calibration of the large area photodiode and amplifier, used as the detector in efficiency and brightness measurements, was carried out using a calibrated photodiode of known spectral response in conjunction with an air-cooled argon ion laser. The 514nm line of the laser was used as the light source. A number of neutral density filters were used to reduce and vary the flux incident on the detectors. The intensity measured by the photodiodes was compared and a calibration equation was obtained. The measurements were carried out in the same session and the laser was operated continuously to reduce error due to intensity fluctuation.

The absorbance of the neutral density filters used was measured over a wavelength range of 450 to 800 nm to allow the linearity of the detectors to be checked. The incident light intensity is reduced by the filter by

$$I = I_o \times 10^{-A},$$

where A is the absorbance of the filter, and I_0 is the intensity of light source. This means that a plot of log intensity versus filter absorption should produce a straight line graph if the detector is linear.

The linearity of the large area photodiode and amplifier circuit is compared to that of the calibrated photodiode below.

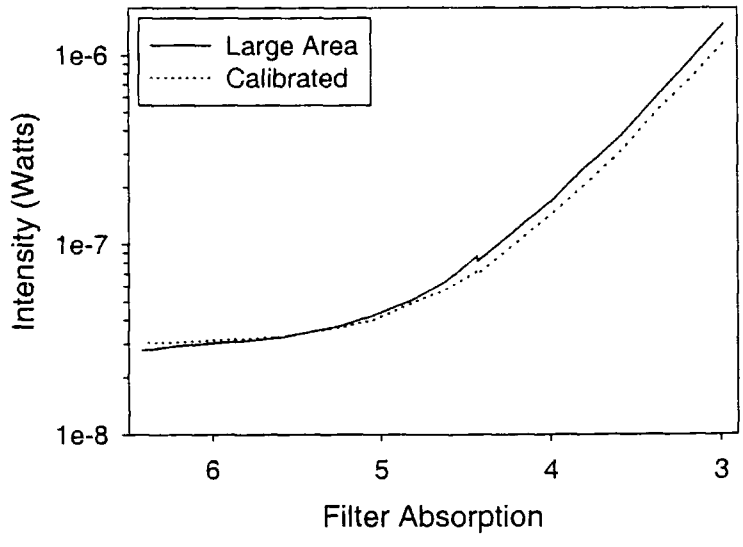

Figure A-1 *Semi-log plot of intensity as a function of added filter absorption*

The response of both detectors is essentially linear at intensities of 5×10^{-7} watts and above. The behaviour below this level is non-linear and similar in both cases.

Three different calibration equations were required to correct the intensity measurement of the large area photodiode and amplifier following changes to the amplifier circuit. Figure A-2 provides calibration data for a period between 1/10/95 and 1/5/97, Figure A-3 for a period between 2/5/97 and 28/10/97 and Figure A-4 for a period between 29/10/97 and 1/10/98.

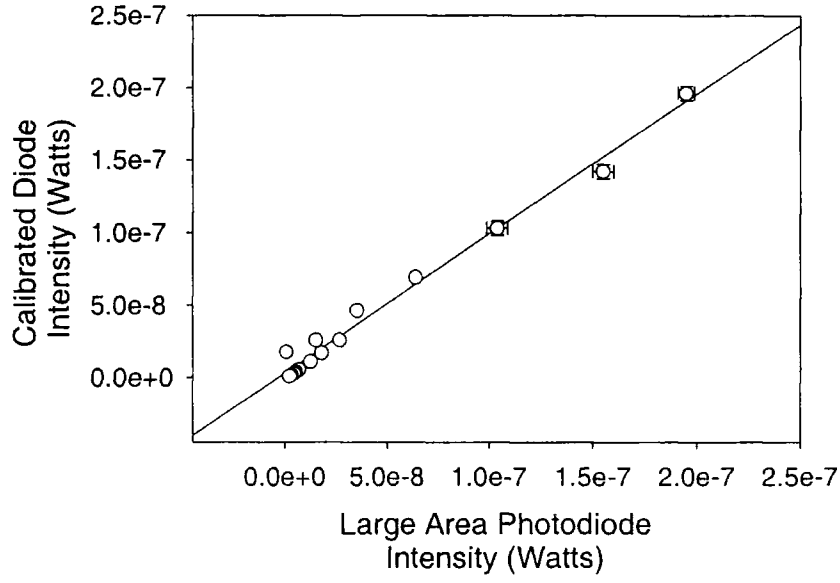

Figure A-2 *Comparison of light intensity measured using a calibrated photodiode and a large area photodiode and amplifier*

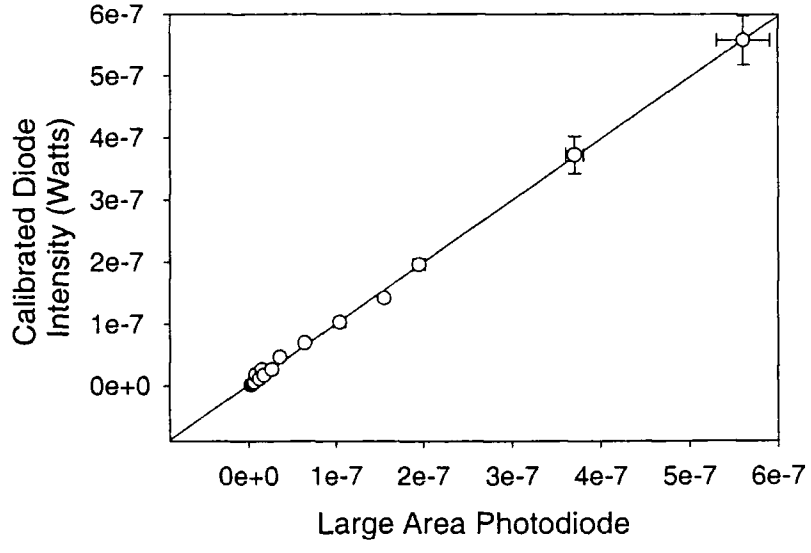

Figure A-3 *Comparison of light intensity measured using a calibrated photodiode and a large area photodiode and amplifier*

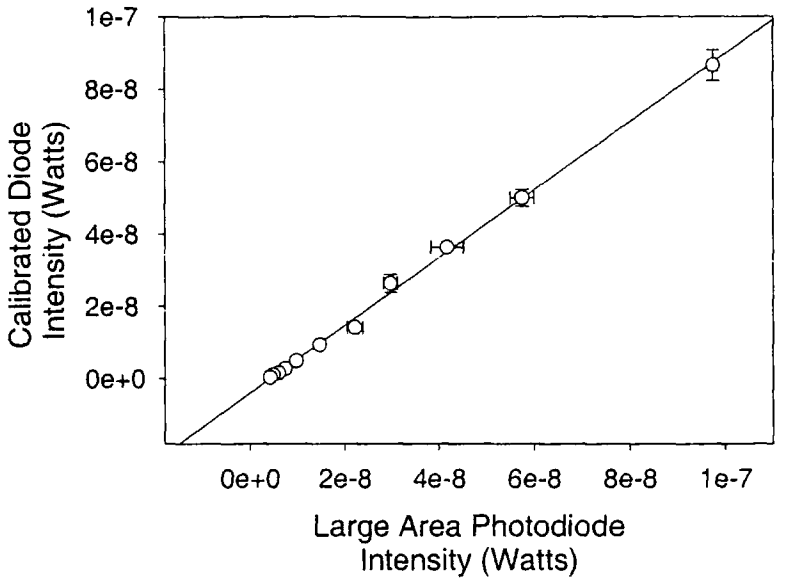

Figure A-4 *Comparison of light intensity measured using a calibrated photodiode and a large area photodiode and amplifier*

The calibration parameter, a, and the value of the feedback resistance in the amplifier circuit which provide the calibration data are listed below. The calibration uses the calibration parameter as a factor by which the voltage signal from the photodiode is multiplied.

Start Date	End Date	A	R_F (MΩ)
1/10/95	1/5/97	0.987	2.31
2/5/97	28/10/97	0.989	2.31
29/10/97	1/10/98	0.954	2.20

Table A-1 *Calibration parameter and feedback resistor used for calibration of the large area detector during certain time periods*

APPENDIX 4 CROSS-CHECK WITH LUMINANCE METER

The brightness values calculated for some organic LEDs from measurements made by the large area photodiode were compared to values measured using a Minolta LS-100 luminance meter, at the time of their testing. In addition, a series of commercial inorganic LEDs and polymer LEDs were used to perform a systematic cross check of the large area photodiode and amplifier measurements, the brightness calculation, candela.xfm, and the some of the measurements therein.

The area of each LED and the solid angle of collection of the emission were measured using a travelling microscope. A white, blue and green inorganic LED were used to vary the spectrum of the emission. A PPV single layer device with calcium electrodes was used as a standard organic LED.

WHITE LED

The brightness of a white LED with an emitting area of 5.31mm^2 was measured using the two systems, as described above. The calculated solid angle for this system is 0.140 steradians. The spectral output of the white LED was measured using a CCD spectrograph and is shown below.

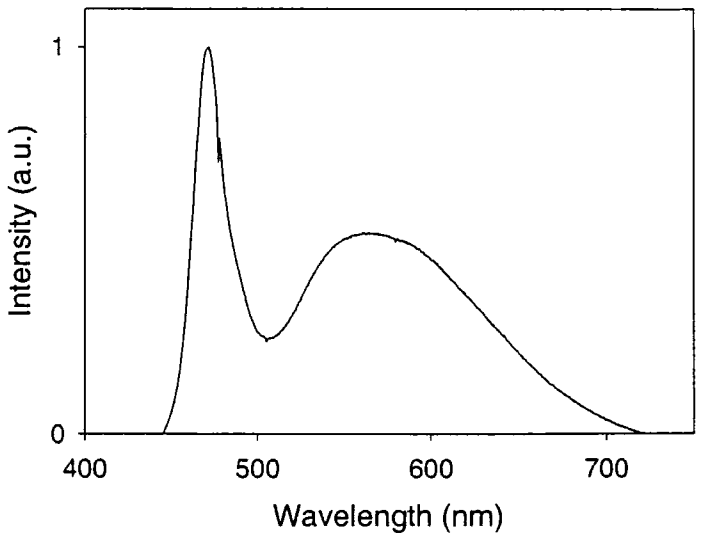

Figure A-5 *Electroluminescence spectrum of an inorganic white LED*

The comparison between the measured and calculated brightness is shown below.

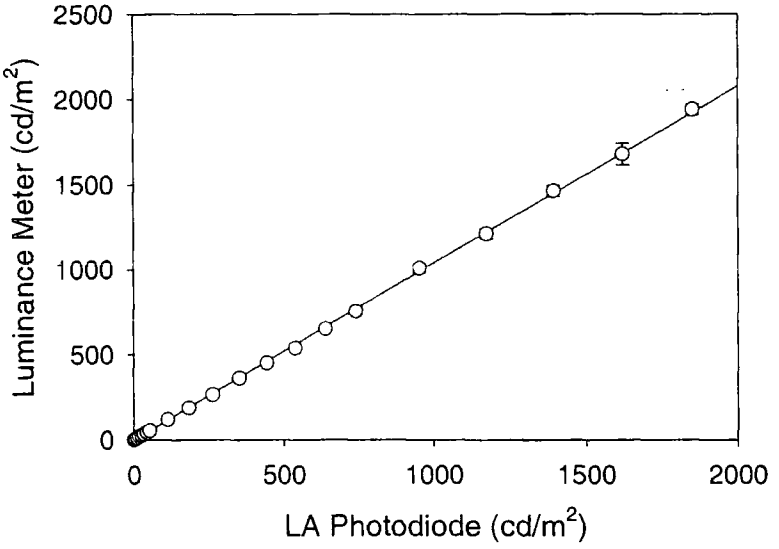

Figure A-6 *Comparison of measured (luminance meter) and calculated (LA photodiode) brightness for a white inorganic LED*

BLUE LED

The total LED emissive area was found to be 18.02mm^2. The solid angle of collection of 0.0866 steradians. The spectral output of the blue LED is shown in the figure below.

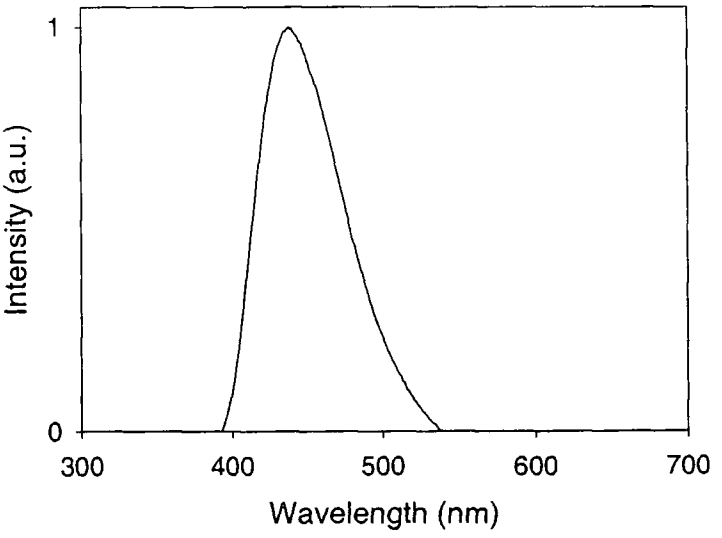

Figure A-7 *Electroluminescence spectrum of a blue inorganic LED*

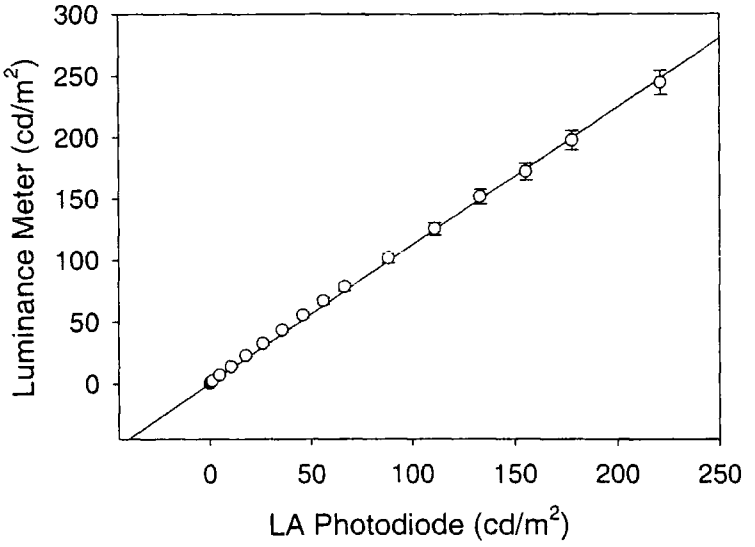

Figure A-8 *Comparison of measured (luminance meter) and calculated (LA photodiode) brightness for a blue inorganic LED*

GREEN LED

The area of the green LED was found to be 10.81mm^2. It defined a solid angle of collection of 0.149 steradians. The spectral output for the LED is shown below.

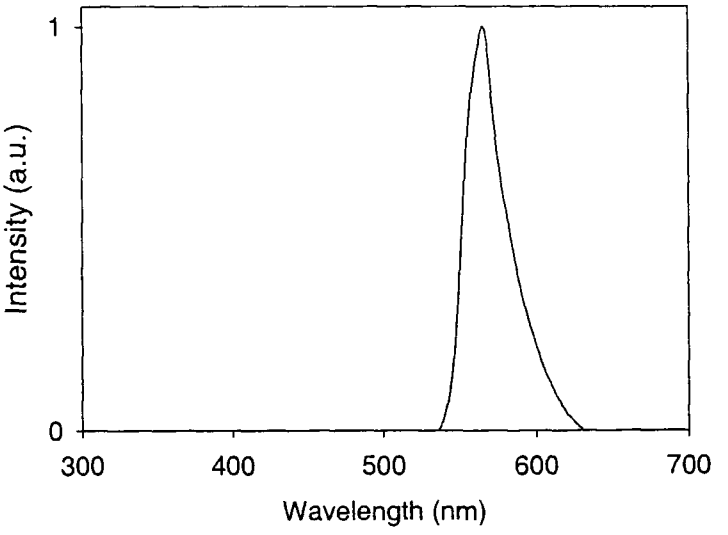

Figure A-9 *Electroluminescence spectrum of a green inorganic LED*

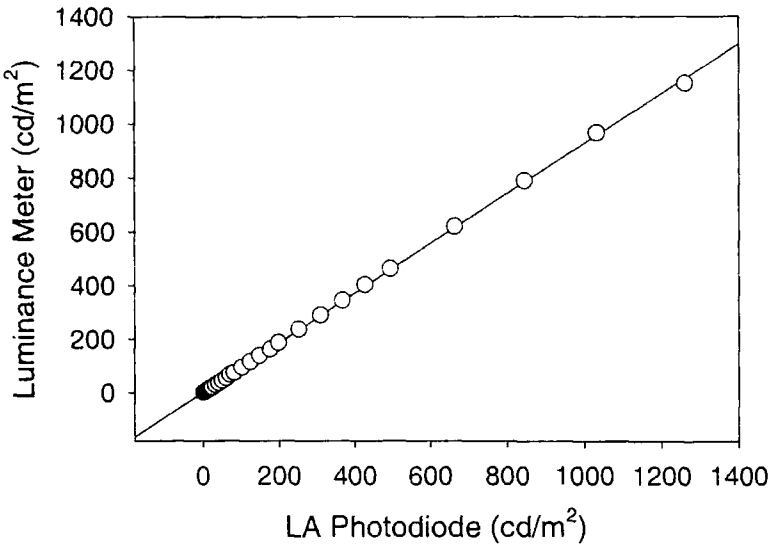

Figure A-10 *Comparison of measured (luminance meter) and calculated (LA photodiode) brightness for a green inorganic LED*

ORGANIC LED

A single layer ITO/PPV/Ca/Al device was also used in the systematic study. The EL spectrum of this device can be found in Chapter 5. The comparison between the calculated and measured intensity can be seen below.

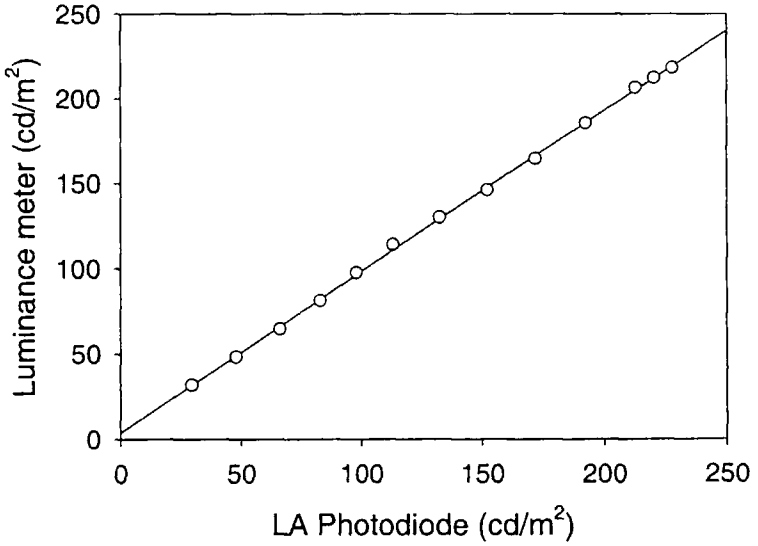

Figure A-11 *Comparison of measured (luminance meter) and calculated (LA photodiode) brightness for an ITO/PPV/Ca/Al device*

The results for the regression lines to the data are shown below. The coefficients are for an equation of the form

$$Int\ (measured) = b(1) \times Int\ (calculated) + b(0).$$

Device	b(0)	b(1)
White LED	-4.1	1.04
Blue LED	1.7	1.10
Green LED	0.3	0.93
ITO/PPV/Ca	3.7	0.95

Table A-2 *Coefficients of the regression lines to the cross-check data for several light sources*

In summary, the cross-check shows there is a small error in the calculation of the brightness of LEDs with a range of spectra. The difference may arise due to the calculation of the solid angle of the system or small variations in the actual emitting area of diodes.

APPENDIX 5 LISTING OF XYZ.XFM

The Jandel Sigmaplot transform file for the calculation of the CIE (X, Y, Z) colour co-ordinates of LEDs is listed below. The transform uses area.xfm, provided with Jandel Sigmaplot, to calculate integrals. The colour matching functions as a function of wavelength (in metres) must be in the first four columns of the worksheet.

```
;COLOUR COORDINATE CALCULATOR
;el intensity should be proportional to photons and interpolated to 5nm steps from 380
;to 780

;**************
planck=6.626076e-34  ;Planck's constant
cee=299792458        ;speed of light
x_dat=col(1)         ;wavelength in col 1
x_bar=col(2)         ;x_bar in col 2
y_bar=col(3)         ;y_bar in col 3
z_bar=col(4)         ;z_bar in col 3
el_int=col(8)        ;EL spectrum in col 8
col(8)=col(8)*planck*cee/col(1)
res_col=9
x_EL=x_bar*el_int
y_EL=y_bar*el_int
z_EL=z_bar*el_int
col(res_col)=x_EL
col(res_col+1)=y_EL
col(res_col+2)=z_EL

;*********************************************
;x_el integral
x=col(1)
y=col(res_col)
xdif1=diff(x)
n=count(x)           ;Delete first value-
xdif=xdif1[data(2,n)]    ;not a difference
ydif1=diff(y)
ydif=ydif1[data(2,n)]    ;Delete first value-
y1=y[data(1,n-1)]
intgrl=y1*xdif+0.5*ydif*xdif
a=total(intgrl)
col(res_col+3)=a     ;Put area in column res
;*********************************************

;y_el integral
xa=col(1)
ya=col(res_col+1)
```

```
xadif1=diff(xa)
na=count(xa)              ;Delete first value-
xadif=xadif1[data(2,na)]    ;not a difference
yadif1=diff(ya)
yadif=yadif1[data(2,na)]    ;Delete first value-
ya1=ya[data(1,na-1)]
intgrla=ya1*xadif+0.5*yadif*xadif
ab=total(intgrla)
col(res_col+4)=ab      ;Put area in column res

;***********************************************
;z_el integral
xb=col(1)
yb=col(res_col+2)
xbdif1=diff(xb)
nb=count(xb)              ;Delete first value-
xbdif=xbdif1[data(2,nb)]    ;not a difference
ybdif1=diff(yb)
ybdif=ybdif1[data(2,nb)]    ;Delete first value-
yb1=yb[data(1,nb-1)]
intgrlb=yb1*xbdif+0.5*ybdif*xbdif
ac=total(intgrlb)
col(res_col+5)=ac      ;Put area in column res
;***********************************************

sumo=col(res_col+3)+col(res_col+4)+col(res_col+5)
xs=col(12)/sumo        ;x=X/(X+Y+Z)
ys=col(13)/sumo        ;y=Y/(X+Y+Z)
zs=col(14)/sumo        ;z=Z/(X+Y+Z)
cell (15,1)="x :="
cell (15,3)="y :="
cell (15,5)="z :="
cell (15,2)=xs
cell (15,4)=ys
cell (15,6)=zs
```